Computational Modelling of Gas Turbine Aerodynamics with Endwall Contouring

Schreiner, Buchan Deneys Jeremy

Award date:
2020

Awarding institution:
University of Bath

Computational Modelling of Gas Turbine Aerodynamics with Endwall Contouring

submitted by

Buchan Deneys Jeremy Schreiner

for the degree of Doctor of Philosophy

of the

University of Bath

Department of Mechanical Engineering

2019

Abstract

Industrial gas turbines form an integral part of electricity generating networks, providing base load at high efficiencies. This high efficiency has been developed over time through both aerodynamic improvements and increased turbine entry temperatures. While materials science has improved the high temperature performance of many components it is still beneficial, and in some cases necessary, to protect these parts from the high temperatures to prevent oxidation and creep. This is achieved through the use of component cooling technology and can take a myriad of forms.

A key cooling technology is the use of cold gas bled from the compressor to seal the turbine wheelspace from hot gas ingestion, protecting the turbine disc from exposure to high temperatures. Minimising the amount of gas bled from the compressor is essential to maintaining high cycle efficiency, which must be balanced with the need for a fully sealed condition. A major drawback of this is that coolant gas escapes through the turbine rim seal into the mainstream flow, negatively affecting the mainstream flow through a blockage effect and a strengthening of secondary flows in the blade passage. These are both unsteady phenomena.

A number of authors have successfully utilised non-axisymmetric endwalls to increase turbine stage efficiencies by weakening or controlling the secondary flow features seen in a blade passage. This has primarily been achieved through the use of steady state computational fluid dynamics and a thorough understanding of the desired flow field. However, it has also been shown that these non-axisymmetric endwalls are more sensitive to the introduction of purge flow egress than the cylindrical baseline and any benefit is quickly eroded. This is due to the interaction between purge and mainstream flows, which contributes additional losses in the stage. This

has driven industry to pursue a combined approach to endwall design, encompassing rim-seal, seal clearance profile and contoured endwalls. Non-axisymmetric endwall contouring in the presence of purge flow forms the focus of this thesis, with emphasis on the application of numerical methods to the design of novel endwalls.

The new experimental facility at the University of Bath is described in detail. This facility is intended to provide researchers with the opportunity to investigate the fundamental fluid dynamics of purge-mainstream interactions. The design of the facility inlet is presented, with emphasis on the delivery of well-conditioned flow to the turbine stage. The iterative design process introduced several features that enabled this to be achieved, as validated by test data.

A numerical model of the turbine stage was developed for a selection of geometric representations. This model was used to demonstrate grid and timestep sensitivity, assess iterative convergence and provide validation against test data. It was found that the inclusion of the full wheelspace extent prevented the solution from achieving periodic behaviour when purge flow was present. However, when purge flow was removed, periodic behaviour was achieved. Periodic behaviour for purged cases was obtained for reduced wheelspace extent models.

The interaction characteristics of purge and mainstream flows was numerically investigated. Results are presented that enhance the understanding of both geometric effects and purge flow on the evolution of secondary flow structures. Flow in the blade passage matches the classical secondary flow structure for annulus only calculations. The flow becomes modified by the inclusion of rim-seal geometry, with both ingress and egress present for an unpurged case. Finally, for the purged case, a plume of egress is seen to exit the rim-seal near the blade suction-surface. This interacts with the secondary flow structures, causing the pressure-side leg of the horseshoe vortex to increase in strength. Radial displacement of the vortical structures occurs and the suction-side leg of the horseshoe is suppressed. The egress plume becomes entwined with the passage vortex as it lifts off the hub endwall.

A novel method for endwall design was developed and presented. Discrete features are implemented to obtain specific influences on the flow structures in the blade passage. These features were investigated in isolation and then combined, result-

ing in a notable improvement to stage efficiency. The suction-side trough was used to control the position of the egress plume and reduce unsteady fluctuations. The leading-edge feature was used to weaken the horseshoe vortex formation at the blade leading edge.

Dedication

To Nicole, for her patience through the hard yards.

To Heather and Deneys, for their unwavering support.

Acknowledgement

I would like to express my appreciation to both my academic supervisors, Dr Carl Sangan and Dr Mike Wilson, for their support, knowledge, and advice throughout this research project. Their encouragement through the lows and celebration of the highs kept me motivated, which is no mean feat. I thank them for the opportunity to undertake my PhD as part of the Turbomachinery Research Centre at the University of Bath.

Peter Smith, formerly of Siemens, is thanked for his constructive criticism and guidance during the early part of this project. His input to the grid generation process and simulation setup was essential to the progress of the project.

This research made use of the Balena High Performance Computing Service at the University of Bath. My thanks go to the HPC support team, Dr Steven Chapman and Roshan Mathew for their help in troubleshooting issues that arose.

I would also like to thank my colleagues in 4E2.27 who provided support, enthusiasm, and light relief. They all contributed to make the office a positive research environment in which to spend our time. I should also mention the occupants of Trouble Corner who were willing to lend an ear when needed.

The research programme and supporting iCASE scholarship was funded by the Engineering & Physical Research Council (under grant EP/M026345/1) and by Siemens Industrial Turbomachinery Ltd.

slender adjective

Selected definitions from the Oxford English Dictionary [1]:

1. Of things: Small in diameter or width in proportion to length; long and thin; attenuated.
2. Having little thickness or solidity in proportion to extent of surface; slight or slim in size or structure.

Contents

List of Figures

Nomenclature

b	hub radius
C	gas concentration
c	chord length
C_f	flow coefficient
C_p	pressure coefficient
C_w	non-dimensional mass flow rate
d	trough depth
f	frequency
F_s	GCI factor of safety
k	turbulent kinetic energy
p	order of convergence
G	gap ratio
h	Leading Edge Feature height
$\dot{m}$	mass flow rate
M	Mach Number
N	number of cells
P	pressure
Q	Q criterion
r, θ, z	Cylindrical coordinates
Re	Reynolds Number

Re_ϕ	rotational Reynolds Number
$\dot{S}'''_{visc}$	viscous entropy generation rate
S	inner wheelspace axial spacing
s	span
s_a	axial spacing between two discs
s_c	seal clearance
S_{ij}	strain rate tensor
s_{ov}	seal lip overlap
T	temperature
U	bulk mean radial seal velocity
u, v, w	Cartesian velocity components
u_r, u_θ, u_z	Cylindrical velocity components
V	volume
x, y, z	Cartesian coordinates
y^+	Non-dimensional first cell height
$\vec{u}$	Velocity vector

Greek Symbols and Mathematical Operators

β	swirl ratio
δ	boundary layer thickness
$\Delta\eta_{mix,ISO}$	stage efficiency unsteady fluctuations
$\eta_{mix,ISO}$	stage efficiency
γ	heat capacity ratio
λ_T	turbulent flow parameter
μ	dynamic viscosity
ν	kinematic viscosity
Ω	angular speed of rotating disc
ω	turbulent frequency
ϕ_0	sealing flow rate

ϕ_{min}	minimum sealing flow rate
ρ	density
τ_{ij}	Shear stress in j direction on face normal to i
τ_w	wall shear stress
θ	azimuthal coordinate in degrees
ε	sealing effectiveness or viscous dissipation rate
ε_C	concentration effectiveness
$\vec{\omega}$	vorticity
δ_ν	turbulent length scale
δ_{ij}	Kronecker Delta
∇	del operator
sgn	signum operator
tr	matrix trace
u_τ	friction velocity

Abbreviations

2D	two dimensional
3D	three dimensional
AD	Annulus Domain
ADGT	Aero-Derivative Gas Turbines
AMG	Algebraic Multigrid
BP	baffle plate
bpp	blade passing period
CD	Chute Domain
CD	conical diffuser
CFD	Computational Fluid Dynamics
CI	Combined Ingress
DB	double baffle
DNS	Direct Numerical Simulation

EI	Externally Induced
EPSRC	Engineering and Physical Sciences Research Council
EWC	EndWall Contour
FFT	Fast Fourier Transform
FWD	Full Wheelspace Domain
GCI	grid convergence index
GGI	General Grid Interface
HSV	horseshoe vortex
HSV-PS	pressure-side leg of horseshoe vortex
HSV-SS	suction-side leg of horseshoe vortex
LAR	Large Annulus Rig
LE	leading edge
LEF	Leading Edge Feature
LES	Large Eddy Simulation
LGT	Large Gas Turbines
MF	mass fraction
MGP	main gas path
N_a	Attachment point
N_s	Separation line
NGV	nozzle guide vane
NS	Navier-Stokes
PID	proportional-intergral-derivative
PIV	particle image velocimetry
PLIF	CO_2 planar laser induced fluorescence
PS	pressure-side
PSTR	Pressure Side TRough
RANS	Reynolds-Averaged Navier-Stokes
RB	rotor blade

RD	radial diffuser
RI	Rotationally Induced
rpm	revolutions per minute
S_p	Saddle Point
SC	settling chamber
SD	Stub Domain
SKE	secondary kinetic energy
SS	suction-side
SST	shear stress transport
SSTR	Suction Side TRough
TE	trailing edge
URANS	Unsteady Reynolds-Averaged Navier-Stokes
VV	volumetric velocimetry

Subscripts

0	purge flow
1	nozzle guide vane leading edge
3	rotor blade trailing edge
a	annulus
$eddy$	turbulent or eddy parameter
eff	effective
in	inlet
max	maximum
min	minimum
s	stator surface
T	turbulent or eddy parameter

Chapter 1

Introduction

The Industrial Revolution of the early 19^{th} century marked mankind's transition from unpowered, hand production techniques to recognisably modern methods of manufacture. The foundations for mechanical power extraction had been laid much earlier with the use of water and windmills, though the development of new technology and materials meant that the introduction of the steam engine was possible. The drive for new and improved methods of harnessing energy sources had begun.

John Barber is credited with the earliest patent for a gas turbine in 1791, though Hunt [2] suggests that many engineers of the Industrial Revolution period knew of the concept, citing a number of engineers and inventors. These individuals were responsible for a number of unsuccessful patents and prototypes that followed over the next century and a half, adding to the body of knowledge on which the next generation could be built.

It was not until 1939 that materials research could be combined with axial compressor technology to produce the first successful gas turbine for electricity generating purposes. This was a 4 MW machine was built by Brown Boveri Company for the municipal power station in Neuchâtel, Switzerland. This unit achieved a turbine efficiency of 89% and a thermal efficiency of 17.4% with a turbine entry temperature of 823 K, near the material limit at that time. From there, the growth in power output of Brown Boveri machines was immense: within a decade, 27 MW units were produced and within four decades, 118 MW units were produced.

The post-war period saw a number of manufacturers enter the industrial turbine market

from across the world. In the US, the General Electric Company and Westinghouse led the field; in Europe, Siemens produced many successful engines with ever increasing efficiency. By the turn of the 21st century, thermal efficiencies of 38.6% were achieved with units in excess of 300 MW. These modern, high efficiency gas turbines had surpassed steam turbines for power generation by the 1980's and continue to form the backbone of electricity networks across the globe.

1.1 Gas Turbine Theory and Efficiency

In its most basic form, the gas turbine consists of three main components: a compressor, a combustion chamber and a turbine (Figure 1-1). Air, the working fluid, is drawn into the compressor which raises the pressure through one or more stages. Heat is added in the combustor in the form of fuel and an ignition source provides energy and increases the temperature of the gas. Finally, the hot, high pressure gas is expanded through the turbine to extract work for two purposes: compressor power and output power.

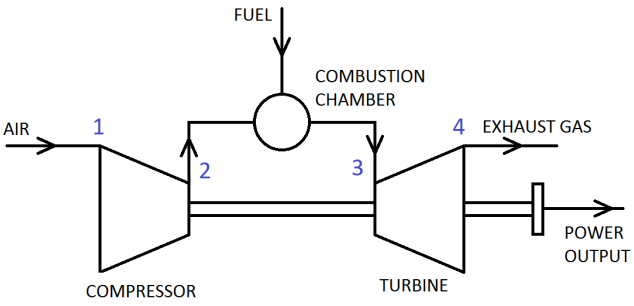

Figure 1-1: Gas turbine with shaft-work output schematic

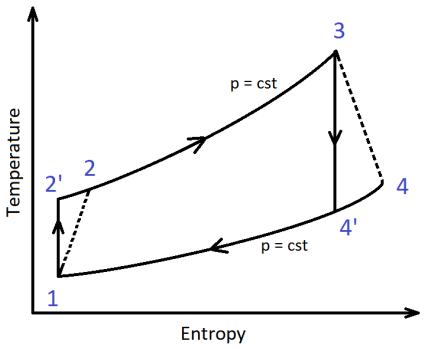

Figure 1-2: Temperature-Entropy diagram for a Brayton cycle

In an ideal cycle, compression and expansion are both reversible and adiabatic, thus isentropic. In addition, pressure losses in connecting duct work are ignored, as are kinetic energy changes within a component. The working fluid is assumed to have constant composition throughout, effectively replacing the combustion process with a perfect heat exchanger. The mass flow of working fluid is also assumed to be constant.

However, in a real cycle we cannot ignore losses throughout the system. This is especially true of the compression and expansion processes, which are non-isentropic. The

effect of this on the Temperature-Entropy (T-s) diagram can be seen in Figure 1-2. The ideal cycle follows $1-2'-3-4'$, while the non-isentropic cycle follows $1-2-3-4$, allowing the lost work to be quantified. By defining the efficiency of the cycle as the ratio of net work output to heat supplied, the ideal cycle efficiency is found to be a function of pressure ratio ($PR = p_2/p_1 = p_3/p_4$) only.

As noted for real cycles, losses cannot be ignored and thus the cycle efficiency is not purely dependent on the pressure ratio. The specific work output can be shown to be a function of both pressure ratio and temperature ratio ($t = T_3/T_1$). If the Turbine Entry Temperature (TET $= T_3$) is considered fixed by material constraints and the inlet temperature (T_1) is fixed by ambient conditions, then it is possible to find the optimum PR to maximise the specific work output. Thus for a real cycle, the TET must also be increased if the maximum efficiency is to be reached.

Returning to the early Brown Boveri engine, we can see that the TET was low at 823 K, allowing the use of commonly available materials. Saravanamuttoo, Rogers and Cohen [3] show that Westinghouse successfully drove development of their 501 series engine from 42 MW in 1968 to 160 MW in 1993. Aerodynamic developments produced an increase in pressure ratio from 7.5 to 14.6, a significant improvement, but this was accompanied by an increase in TET from 1153 K to 1533 K.

1.2 Cooling

Developments in materials technology after the war led to a significant increase in TET (Figure 1-3), initially through the use of high grade, heat resistant alloys and later single crystal casting methods. These improved materials would still be inadequate to survive the TET of a modern aero-engine, which can be in excess of 2000 K, or even an industrial engine, typically ~100 K lower. In order to combat this, the turbine vanes and blade must be actively cooled using air bled from the compressor to prevent oxidation, creep or fatigue of critical parts.

Air in the compressor is significantly cooler than the TET at around 900 K and, in the high pressure stages, is at a slightly higher pressure than the turbine entry pressure due to losses in the combustor. This cool, high pressure air is supplied to the critical turbine components through an internal system of ducts shown in Figure 1-4, known as the internal or secondary air system. This gas, referred to as secondary air, is primarily used to for film

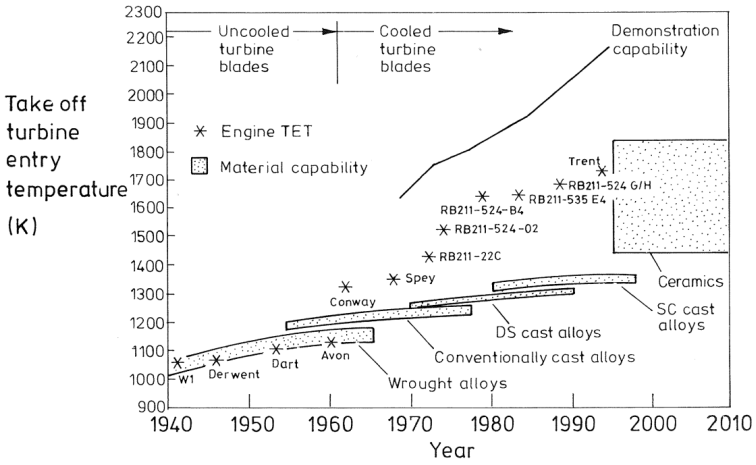

Figure 1-3: Turbine Entry Temperature trends, from [4]

cooling of the vanes and blades. To do so, air is fed through channels that contain ribs and pins to increase the heat transfer. This ensures that the material temperature limits are not exceeded for components exposed to the mainstream gas and high TET.

An additional use of the secondary air is to seal the cavity or wheelspace that exists between the stationary disc to which the vanes are mounted (known as the stator) and the rotating disc to which the blades are mounted (known as the rotor). Here, gas is introduced to the wheelspace at low radius and exits through the non-contact rim seal at high radius. This prevents the possible ingestion of hot gas, which would have a detrimental impact on the discs. The driver for this ingestion is the circumferentially varying static pressure between the stator and rotor as seen in Figure 1-5. Here, the pressure in the annulus may be locally higher or lower than inside the cavity, leading to ingress and egress respectively. This is known as externally-induced ingress.

It is possible to have ingress in the presence of an axisymmetric external flow field. The flow structure in the wheelspace is dominated by rotational effects, leading to a radial pressure gradient that can drop below the external pressure. The rotating disc causes egress of flow near the rotating disc due to the disc pumping effect. In order to conserve mass flow, fluid is ingested near the stator. This is known as rotationally-induced ingress. Both forms of ingress are discussed in detail in Section 2.2.3.

The rim seal forms a labyrinthine path for the purge gas to navigate, leading to a pressure drop across the seal. The intricate seal has key two functions. The first is to

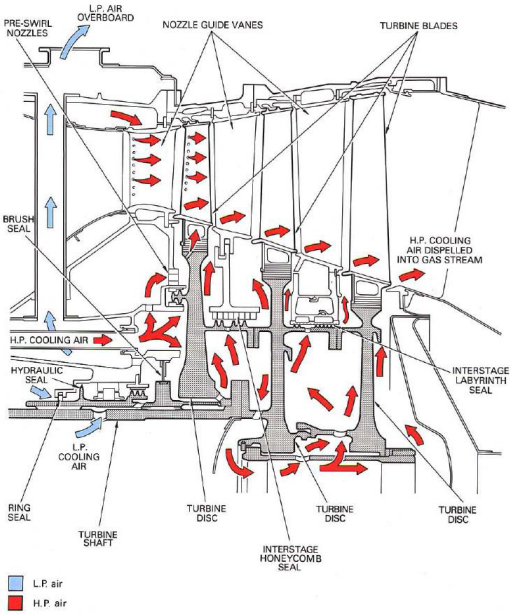

Figure 1-4: Internal air system (aero engine), from [5]

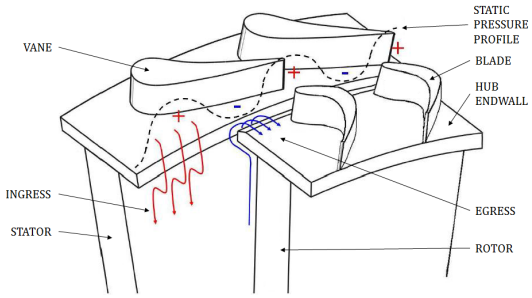

Figure 1-5: Circumferential variation in static pressure as the driver for ingress and egress across a rim seal, adapted from [6]

prevent the hot mainstream gas from reaching the stator and rotor discs, which reduces overheating and thus lowers the amount of purge gas needed. The second is to limit the egress of purge gas in to the annulus, which has a detrimental effect on the aerodynamics of the turbine stage with reductions of 0.8% reported per 1% of purge flow (Regina *et al.* [7]).

Secondary air also has a direct impact on the cycle efficiency as mass flow is removed once work has been done in raising its pressure. For modern, high efficiency turbines, with combined efficiencies above 60%, secondary air can be as much as 20-25% of the mainstream mass flow. This has led to the drive to accurately predict the required purge gas mass flow to ensure that none is superfluous: Mirzamoghadam [8] reports that a 1% reduction in sealing gas increases the thermal efficiency by 0.4%.

1.3 Non-axisymmetric Endwall Contouring

Improvements in cycle efficiency have not been obtained through focussing solely on increasing pressure ratio and TET. Aerodynamic losses in the compressor and turbine can be addressed directly by design and have led to huge gains in efficiency. Advances in computa-

tional power and techniques (see Section 2.5) have provided engine designers with the tools that can provide comprehensive flow field data, especially suited to comparative analysis. Blade stacking and blade lean are now widely used to improve the aerodynamic performance and can be optimised using Computational Fluid Dynamics (CFD), as reported by Dorfner *et al.* [9].

A principal area of research effort in gas turbine efficiency is focussed on hub endwalls, identified in Figure 1-5. This research has looked at both the compressor and turbine, though the aerodynamics differ significantly between these components. Rose [10] refers to the use of a cylindrical endwall as an unnecessary constraint on the engine design. It has been proposed by a number of authors (see Section 2.4) that the shape of the endwall can be designed in such a way that the aerodynamic losses can be reduced and an example can be seen in Figure 1-6.

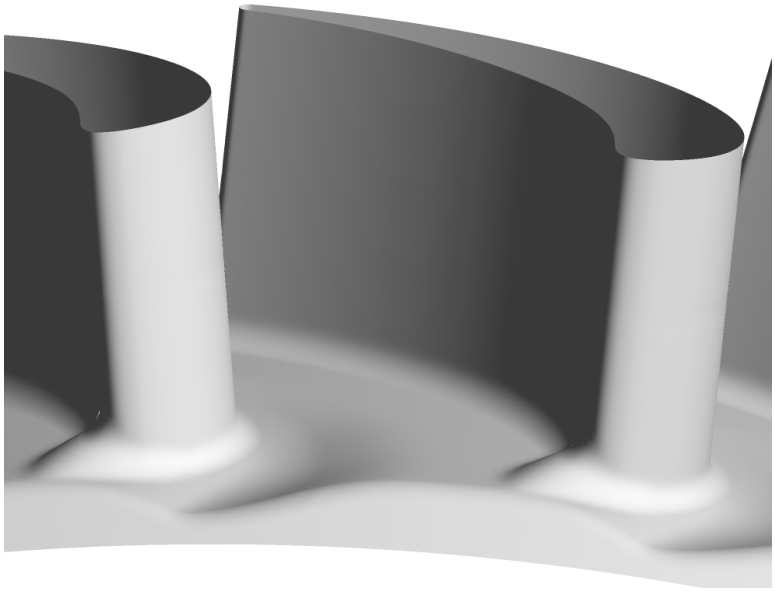

Figure 1-6: Contoured Turbine Hub Endwall

In the compressor, the endwall can be shaped to reduce separation and control the flow features which cause loss [9]. While far from a simple design process, their use in the compressor is less complex than the turbine. In the turbine, their design is significantly complicated by the presence of purge gas egress. Egress of purge gas has been shown to alter the mainstream flow field through two key mechanisms, discussed in Section 2.2.4.

Entropy is generated throughout a blade passage due to viscous effects, leading to aerodynamic loss. A large portion of this loss is due to the secondary flow features that

are present, features which can be controlled and manipulated to reduce the magnitude of loss. Denton [11] highlights that the jet of egress will lead to high shear rates and thus entropy generation, which is less readily eliminated.

1.4 Aims and Objectives

This thesis will attempt to answer the following research questions:

1. How can the unsteady interactions between mainstream flow and purge gas be modelled using Reynolds-Averaged Navier-Stokes CFD solvers?
2. How does the unsteady behaviour interact with a non-axisymmetric contoured endwall and what effect does this have on the flow structures we wish to control?
3. How can a non-axisymmetric endwall be developed using instantaneous or time-averaged flow field data that is robust across a range of purge rates?

The main aim of this thesis is to develop a robust design methodology for contoured endwalls that will produce improved aerodynamic performance in the presence of purge flow egress.

In order to achieve this aim and answer the questions posed above the following objectives have been identified:

1. To generate a suitable computational domain for the baseline, cylindrical endwall. This domain shall be used to perform mesh sensitivity studies as well as determine appropriate simulation parameters for later work.
2. To conduct a three dimensional (3D), viscous and unsteady CFD simulation of the baseline case to obtain the time-accurate flow field from which an endwall can be developed. This will be used to develop an understanding of the unsteady interaction between mainstream and egress flow.
3. To design and develop novel non-axisymmetric endwall geometries that improve aerodynamic performance in the presence of purge flow.
4. To critically analyse the endwall designs to gain an understanding of the altered flow fields and any effect on the mainstream-egress interaction.

5. To support the concurrent experimental campaign by producing flow field data, thus informing rig design and locating flow structures to be examined.

1.5 Thesis Overview

Chapter 1 has provided an introduction to gas turbine development, the theory of their operation and the governing parameters for their efficiency. The impact of turbine cooling has been outlined, providing substantial benefit but also presenting challenges. The concept of non-axisymmetric endwalls was introduced as a method by which stage efficiency might be increased.

Chapter 2 presents a literature review of the design of gas turbines, from historical to modern. The flow physics of gas turbines is explored in depth, covering mainstream flow features, cavity flows and the interaction of egress and mainstream gas. The current state-of-the-art for contoured endwalls is presented, along with the challenges for endwall design. The role of CFD in turbomachinery is also explored.

Chapter 3 describes the design and development of the new Large Annulus Rig facility at the University of Bath. The design of the rig inlet is presented, detailing the CFD method used in the process, the design decisions taken and the final design reached.

Chapter 4 introduces the numerical framework for the CFD solver, the computational model and geometric representations of the rig utilised in the calculations. The setup of the model is explored, covering boundary conditions and turbulent closure, as well as the computational grid generation. Grid independence studies are presented with validation based on rig data. Finally, unsteady calculations are explored.

Chapter 5 contains results for the baseline, cylindrical endwall, for both purged and unpurged cases. The flow structures are described and the impact of purge flow investigated. The implications for the design of contoured endwalls are presented.

Chapter 6 develops the novel endwall generation approach and applies it to the previously described flow field. The influence of each feature is quantified and improvements to stage efficiency are achieved.

1.6 Publications

The research documented in this thesis has resulted the following publications for the author:

Schreiner, B.D.J., Wilson, M., Li, Y.S., and Sangan, C.M., 'Effect of purge on the Secondary flow-field of a Gas Turbine Blade-row' *Journal of Turbomachinery*, In Press 2019. [12]

Schreiner, B.D.J., Wilson, M., Li, Y.S., and Sangan, C.M., 'Design of Contoured Turbine Endwalls in the presence of Purge Flow: A Feature-Based Approach' In: *Proceedings of ASME Turbo Expo 2019: Turbomachinery Technical Conference and Exposition, 17-21 June 2019, Phoenix, Arizona*. ASME GT2019-90443, 2019. [13]

Jones, R.R., Pountney, O.J., Cleton, B.L., Wood, L.E., Schreiner, B.D.J., Carvalho Figueiredo, A.J., Scobie, J.A., Cleaver, D.J., Lock, G.D., and Sangan, C.M., 'A New Single-Stage Turbine Facility For Investigating Non-Axisymmetric Contoured Endwalls In The Presence Of Purge Flow' In: *Proceedings of ASME Turbo Expo 2019: Turbomachinery Technical Conference and Exposition, 17-21 June 2019, Phoenix, Arizona*. ASME GT2019-90377, 2019. [14]

Carvalho Figueiredo, A.J., Schreiner, B.D.J., Mesny, A.W., Pountney, O.J., Scobie, J.A., Li, Y.S., Cleaver, D.J., and Sangan, C.M. 'Volumetric Velocimetry Measurements of Purge-Mainstream Interaction in a 1-Stage Turbine' Manuscript in preparation for ASME Turbo Expo 2020

Chapter 2

Literature Review

2.1 Gas Turbine Design

2.1.1 One-dimensional Design

The design of a gas turbine has never been a trivial exercise. Both the technology and design process have developed significantly since Whittle's early prototypes, providing the designer with extra information, intricate detail and new challenges. Saravanamuttoo, Rogers and Cohen [3] detail the typical process, noting that preliminary studies would be undertaken to assess the type of cycle desired, the layout of components and the number of stages. Thermodynamic cycle analysis of the design point would follow, using loss coefficients to assess the expected stage efficiency and pressure losses throughout the machine.

Mean-line calculations and velocity triangles, as outlined by many authors including Saravanamuttoo *et al.* [3] and Dixon and Hall [15], at the component level would then be used to establish basic geometric parameters for Nozzle Guide Vanes (NGVs) and Rotor Blades (RBs), such as flow angles, chord and height. The loss coefficients used in these calculations are ubiquitous in taught undergraduate courses on the subject, often presented as fact in the problem statement, though it is not always clear how they are obtained. These correlations were heavily relied upon to design the gas turbines of the post-war period [16].

2.1.2 Empirical Loss Estimation

An early blade row correlation model, which can be traced back to an unpublished 1949 document from the Gas Turbine Laboratory at the Massachusetts Institute of Technology [15], collated performance data for individual blade row stagnation pressure loss for a wide range of gas turbines. This was correlated with physical parameters such as space-chord ratio, blade aspect ratio, blade thickness-chord ratio and the Reynolds number (Re) in order to derive an equation that modelled the relationship. Known as the Soderberg correlation, it still finds use today as a rapid estimate method that is accurate to within ±3% [15]. A later empirical correlation method by Ainley and Mathieson [17] related loss to the deflection angles and pitch-chord ratio, with steam turbine cascades providing the experimental data [16, 17]. These authors also began to associate the loss to specific physical phenomena within the blade passage, namely:

i. a profile loss;

ii. a secondary or endwall loss;

iii. a tip or shroud clearance loss.

The mechanisms and predictions of loss form the focus of Section 2.3 and will be expanded upon therein.

A Reynolds Number correction to the Ainley and Mathieson correlation was presented by Craig and Cox [18] in 1970, while in 1982 Kacker and Okapuu [19] further refined the resulting model by treating the trailing edge loss as a separate source of loss with a new correlation. More recently, Wilson [20] presented an improved method for converting the loss factors of previous authors in to a total pressure loss, yet still relied on empirical data. *A priori* prediction of losses for a new design has improved but remains a challenge for modern computational techniques.

2.1.3 Two- and Three-dimensional Design

When applied directly, free-vortex flow calculations allow for the analysis of the spanwise variation in flow angle of a blade. However, when applied indirectly it is possible to determine the required blade shape from a desired velocity distribution. These lead to a twisted blade design where the stagger angle varies from root to tip. These methods first appeared

in the 1950's [15, 16], being some of the first two-dimensional design tools available. From the 1960's detailed aerodynamic design of axial turbomachines began to rely on the use of two-dimensional throughflow calculation tools [15, 21], providing more detail regarding the fluid dynamics within a turbine.

These tools also signalled the introduction of computational codes to the design process [16], finding use in the earliest streamline curvature methods. While capable of producing machines with excellent aerodynamic performance, these tools still relied on empirical correlations and an iterative design process. Design iterations followed by physical testing was costly in both time and hardware, driving a need for faster and cheaper design tools. As such, the use of computational tools has expanded significantly. Horlock and Denton [16] note that the design of modern, three-dimensional turbomachinery relies almost exclusively on Computational Fluid Dynamics (CFD). Section 2.5 deals with the current state-of-the-art for CFD in turbomachinery and highlights some of the relevant theory.

Following thermodynamic and aerodynamic calculations, the designer would consider the mechanical design of the turbine. This would include stress and vibration analyses that can often have conflicting requirements to those of the aerodynamics. Additionally, the off-design performance needs to be assessed and a control system must be developed. Finally, the detailed design would be undertaken, balancing the needs of aerodynamics and mechanics with those of the manufacturing engineers.

2.2 Flow Physics

The turbine designer is only able to predict, in granular detail, the flow expected through a blade passage using powerful computational techniques. However, it is still essential to have a full understanding of the *expected* patterns of flow through a turbine, both in the mainstream annulus and any secondary air system cavities or seals. The literature for mainstream flows, Section 2.2.1, is built on both experimental studies and computational work in linear cascades and rotating rigs. Flow in cavities is covered in Section 2.2.2. In addition, these two flows interact when purge air is ejected into the mainstream, leading to modified flow fields which are discussed in Section 2.2.4.

2.2.1 Mainstream Flow

Turbine annulus flow fields are unsteady [3, 15, 21]. All time-dependent behaviour that is linked to the shaft rotational speed is said to be *deterministic*, while unsteady behaviours that are not linked is said to be *non-deterministic*. A machine with stationary NGV rows and rotating RB rows will give rise to a flow field with characteristic, *deterministic*, variations due to their interactions with wakes as they move through the annulus. Moreover, the local effect of the blade is often dependent on the spanwise position of interest, leading to a highly complex flow field especially close to the hub and shroud. Remote from the endwalls, the flow field of high aspect ratio blading can be treated as quasi-two-dimensional as the radial velocity component is in most cases negligible, although the deterministic unsteadiness remains. This mid-span flow follows the blade profile, forming boundary layers that are responsible for the profile loss noted previously.

Secondary Flows

Secondary flow can be defined as any flow travelling along a vector not aligned with the bulk flow vector. The physical mechanism by which these arise in turning flow is undeniably simple. Radial equilibrium for the pressure gradient normal to any curved streamline gives the familiar result:

$$\frac{\partial p}{\partial r} = \frac{\rho u^2}{r} \tag{2.1}$$

In equation 2.1, the pressure gradient is proportional to the square of the velocity magnitude tangential to the streamline and is balanced for uniform flows. For *non-uniform* flows, any velocity deficit will cause the fluid to follow a smaller radius of curvature. Thus it can be seen that for any turning flow with boundary layers, there will be a near-wall region of flow which does not travel in the same direction as the mainstream, forming a secondary flow.

In contrast to the turbine mid-span region, hub endwall flows are dominated by these three-dimensional effects. The picture of these flows has developed over time: Sieverding [22] produced the first comprehensive review of secondary flows, Langston [23] collated more recent results and expanded on boundary layer separation while Simon and Piggush [24] provided additional insight on the impact of secondary flow on heat transfer. The classical structure of secondary flows around a blade is shown in Figure 2-1.

In the case of the turbine, the formation of secondary flows due to deflection by the blade leads to overturned flow at the hub with flow tending towards the suction-side, known

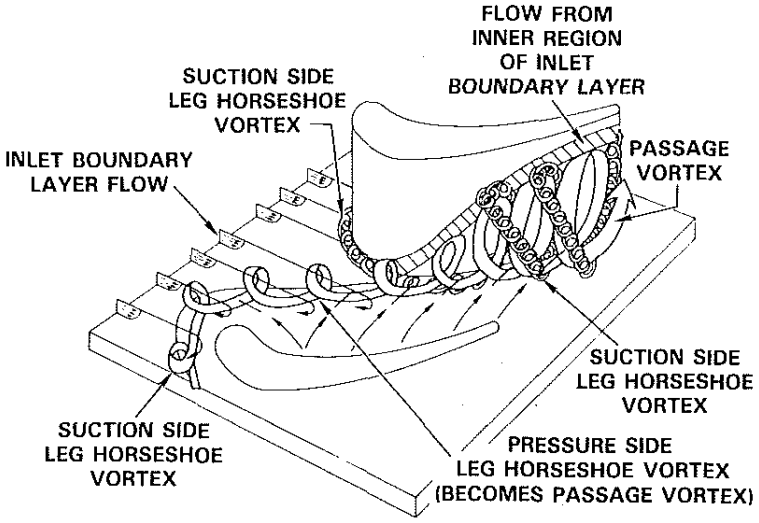

Figure 2-1: Classical Secondary Flows from [25]

as the cross-passage flow. In addition, there exists a strong blade-to-blade pressure gradient, known as the cross-passage pressure gradient. This pressure gradient, due to the presence of the blades, only serves to enhance the cross-passage flow and leads to highly skewed flow in the boundary layer as shown in Figure 2-2.

The direction of the wall shear at the hub can be seen to have a significant deviation compared to the flow outside the boundary layer and the resulting velocity profile appears twisted in the wall normal direction. A significant body of work is dedicated to turbomachinery endwall boundary layers, for example Horlock and Perkins's [28] comprehensive text. Johnston and Flack [27] review the experimental data and consider the modelling issues that arise in their prediction. Anderson and Eaton [26] note that for a purely two-dimensional boundary layer, no mean longitudinal vorticity is present. This is not the case for a three-dimensional boundary layer, which might lead to a stabilising effect on turbulence in the near-wall region. This simple picture of the boundary layer is complicated by additional flow structures.

It is well known that a HorseShoe Vortex (HSV) forms at the junction of a flat plate and an isolated obstacle, often appearing in Civil Engineering applications such as bridge piers [29]. In simple flows, these vortices occur when the incoming boundary layer experiences a static pressure variation normal to the flat plate as the flow stagnates against the obstacle Leading Edge (LE). This spanwise pressure gradient drives flow from the midspan towards the endwall, causing a rotation. This roll-up results in a three-dimensional separation line

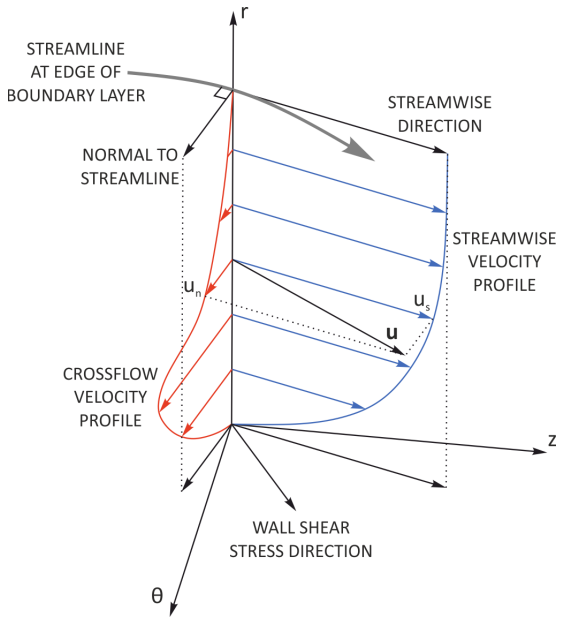

Figure 2-2: Three-dimensional boundary layer flow, after [16, 26, 27]

around the obstacle as the HSV is bent around the obstacle. This bending causes the crosswise boundary layer vorticity to become streamwise. The surface flow pattern seen in Figure 2-3a are taken from Baker's [29, 30] experimental work on turbulent HSV formation.

Eckerle and Langston [31] performed detailed experimental investigations of this simple configuration, utilising surface flow visualisation as well as static and total pressure measurements in turbulent flow for a thick boundary layer. They described a single, symmetrical main vortex forming fully within the boundary layer thickness. This vortex is split by the cylinder in to two legs that move only slightly away from the endwall as it is convected downstream. Figure 2-3b details this idealised, symmetrical flow pattern around a cylinder, highlighting the presence of the saddle point and separation line on the endwall which can be used to identify the vortex limits.

Sieverding [22] attributes the first description of a HSV in a turbomachinery context to Klein's 1966 paper, but notes that it was not until the experimental work of Sjolander in 1975 and Langston, Nice and Hooper in 1977 [32] that the role of the HSV in the secondary flows of a turbine began to be understood. Langston *et. al.* [32] describe the flow due to the presence of the HSV in detail using velocity and pressure measurements and surface flow visualisation in a large-scale cascade. By referring to the legs of the HSV using the blade surface which they initially follow, the authors describe the paths taken through the

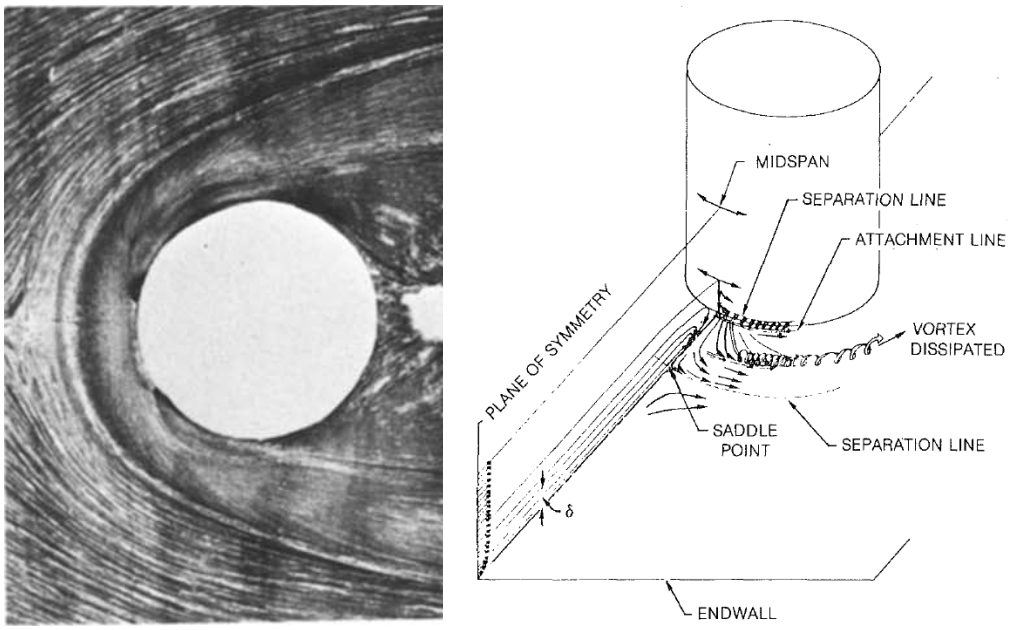

(a) Oil-flow visualisation. From [29] **(b)** Idealised formation. From [31]

Figure 2-3: HorseShoe Vortex formation

blade passage and this is the naming convention which shall be followed in this thesis: the Pressure-Side leg (HSV-PS) and the Suction-Side leg (HSV-SS). For a given geometry, the location of the saddle point and attachment line is determined primarily by the incoming flow impingement point, meaning the HSV roll-up location is not constrained to the blade's physical LE.

Langston *et al.* [32] found that, due to their complementary sense of rotation, the cross-passage flow feeds the HSV-PS as the latter is convected downstream of the Blade Leading Edge (BLE). Additionally, this causes a pitchwise migration towards the adjacent suction surface. When the HSV-PS impinges on the suction surface, the vortex is deflected away from the hub endwall and moves in a spanwise direction. As the HSV-PS is no longer considered hub-bound from this point, it is subsequently referred to as the Passage Vortex (PV). The HSV-SS has the opposite sense of rotation, leading to a continuous reduction in strength as it is convected downstream.

For low-speed, high-turning blades in a cascade, Sieverding and Van den Bosche [33] showed experimentally that the HSV legs are convected into adjacent passages, with the HSV-PS moving towards and interacting with the HSV-SS of the next blade. This was achieved using coloured smoke, released near the endwall, to distinguish between source

regions. Figure 2-4 shows the cross-passage migration of the HSV-PS before it impinges on the adjacent blade. This lifts the HSV-SS off the endwall, leading to the two vortices becoming entwined. This leads to a reduction in lift for the blade.

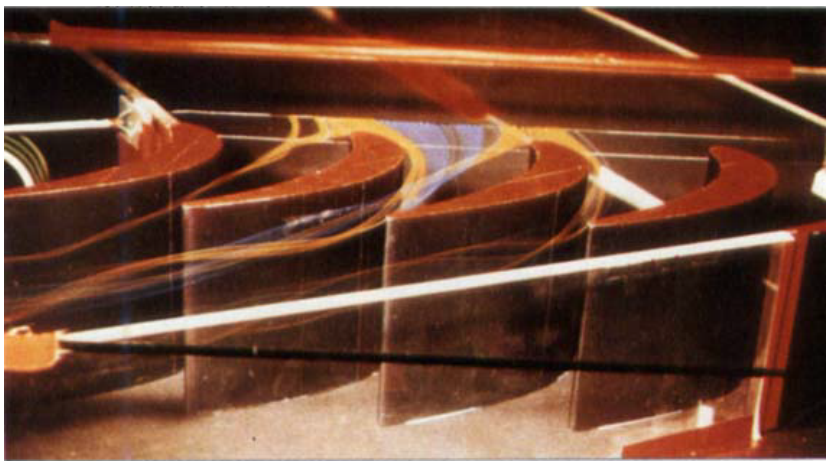

Figure 2-4: HSV vortex leg interaction, from [33]

Sharma and Butler [25] produced experimental data that agreed with Sieverding and Van den Bosche's vortex wrapping, leading to the idealised structure seen in Figure 2-1. Snedden *et al.* [34, 35] applied computational techniques to a rotating blade-row, also capturing the vortex wrapping. Langston notes that additional structures have been proposed in the literature, including corner vortices, which lead to a more complex picture of the flow. An example of this is the experiments undertaken at low Re by Wang *et al.* [36]. These revealed the presence of a multiple horseshoe system at the leading edge with periodic changes to both position and vortex number, however, the low Re suggests these may be transitional or laminar features.

2.2.2 Cavity Flow

The study of rotating flows covers such a wide range of applications and scales that entire books are dedicated to the topic [37, 38]. Suffice to say, this literature review shall not attempt a comprehensive study of rotating fluid dynamics, rather it shall be limited to presenting four key governing parameters for a simple free disc (Figure 2-5) and discussing the most relevant configuration: the rotor-stator system (Figure 2-6).

A free disc rotating in a stationary fluid at constant angular velocity (Ω) will develop boundary layers on both surfaces. For simplicity and due to symmetry, only one side shall

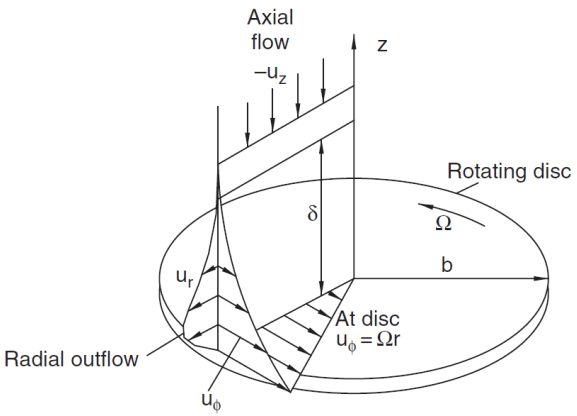

Figure 2-5: Flow near a free disc, from [37]

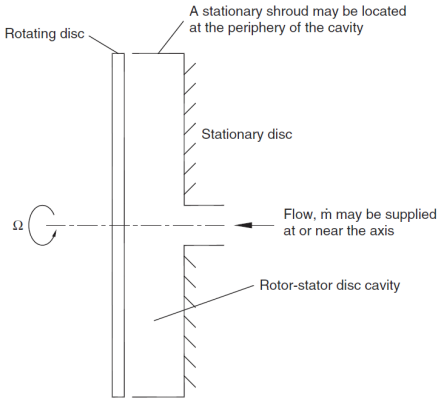

Figure 2-6: Shrouded rotor-stator disc cavity, from [37]

be considered. The no-slip condition requires that the fluid at the disc surface moves with tangential velocity $u_\theta = \Omega r$, while the radial (u_r) and axial (u_z) components remain zero, creating a shear between the free stream fluid which is at rest and the fluid in the disc boundary layer. The centrifugal forces arising from this shear drive a radial outflow of fluid in the boundary layer, which must be balanced by axial inflow from the freestream. This is known as the disc pumping effect. The rotational Reynolds number (Re_ϕ) is defined in the usual manner as the ratio of inertial to viscous forces. For a rotating disc, the characteristic length is radius (b):

$$Re_\phi = \frac{\rho(\Omega b)b}{\mu} \tag{2.2}$$

This definition can be considered in a local frame by replacing the disc radius with the local radius (r). It follows that flow at the centre will always be laminar while at the disc rim the flow may be turbulent. As Re_ϕ increases with the square of the radius, transition may occur at low radius with Childs [37] providing a figure for the critical value of $Re_\phi = 2 \times 10^5$.

The second parameter to consider is the non-dimensional mass flow rate (C_w):

$$C_w = \frac{\dot{m}_0}{\mu b} \tag{2.3}$$

Here, the mass flow rate of fluid entrained by the disc may be taken to be any superposed axial flow, becoming a non-dimensional sealing flow rate for a purged turbine system.

The final two parameters are the swirl ratio (β) and the turbulent flow parameter (λ_T).

The swirl ratio is the ratio of tangential velocity to disc surface angular velocity at the same radial position. The turbulent flow parameter combines the rotational Reynolds number and the non-dimensional mass flow rate.

$$\beta = \frac{u_\theta}{\Omega r} \tag{2.4}$$

$$\lambda_T = \frac{C_w}{Re_\phi^{0.8}} \tag{2.5}$$

A rotor-stator system (Figure 2-6) closely describes the common arrangement of a turbine disc and stationary casing: the arrangement of a stator, some axial gap and a rotor forms a cavity or wheelspace. In addition to the free disc case, the prevailing flow conditions between the discs is now also dependent on geometric parameters such as the axial distance between the discs (s_a).

Early theoretical studies proposed two models of flow for the cavity, known as Batchelor and Stewartson flow regimes. In 1951 Batchelor proposed the existence of an inviscid core region rotating at a constant swirl between boundary layers on both the stator and rotor. The rotor boundary layer would behave differently to that found on a free disc, as the free disc entrains fluid at all radial positions as seen in Figure 2-5. The stator boundary layer would behave like a stationary disc in a rotating fluid: flow would be radially inwards and axially away from the disc at low radius, thus feeding the core with the required fluid to conserve mass. In 1953 Stewartson proposed that the cavity flow would be similar to the free disc case, with no boundary layer on the stator. Typical velocity profiles for both can be seen in Figure 2-7.

Experimental work showed that both cases can exist, under specified conditions. Batchelor flow accurately describes the flow for a closed system with little or no superposed flow. As the superposed flow rate increases, core rotation is seen to decrease (i.e. $\beta \to 0$) and the flow becomes more like Stewartson flow. A system lacking the shroud shown in Figure 2-6 is known as an open or unshrouded system and Stewartson flow is typical [37].

Experimental work by Daily & Nece [39] on an closed cavity determined that four flow regimes exist depending on the gap ratio ($G = s_a/b$) and Re_ϕ. The conditions for these regimes can be seen in Figure 2-8 and are described as:

Regime I: Laminar flow in small gap ratio cavities, leading to merged boundary layers.

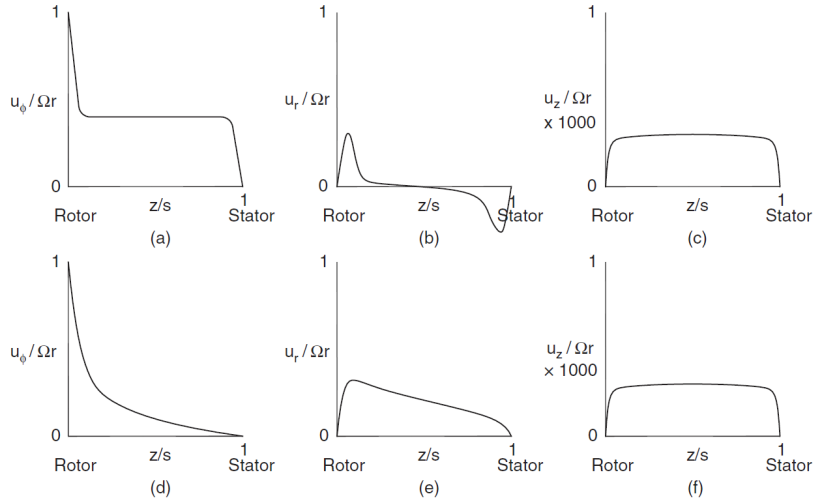

Figure 2-7: Batchelor flow (a-c) and Stewartson flow (d-f), from [37]

Results in Couette type tangential component flow.

Regime II: Laminar flow in larger G cavities. Discrete boundary layers on rotor and stator.

Regime III: Turbulent flow in small G cavities with merged boundary layers. Turbulent Couette flow profile for tangential component.

Regime IV: Turbulent flow in large G cavities with discrete boundary layers.

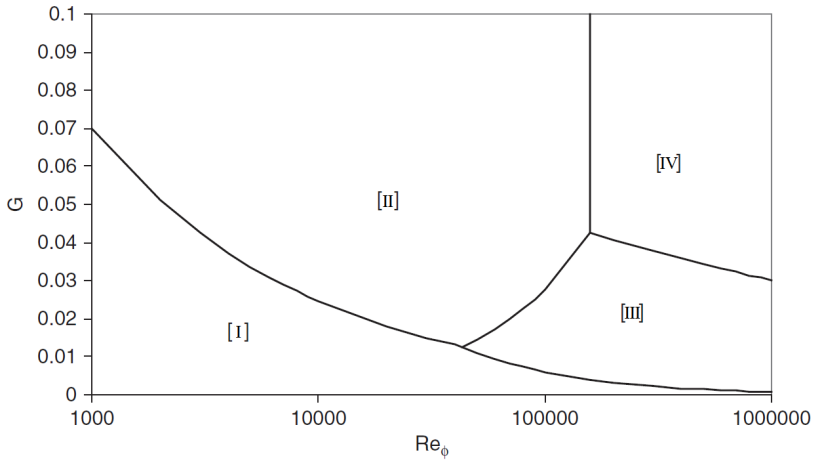

Figure 2-8: Cavity flow regimes, from [37]

2.2.3 Ingestion

For real systems such as turbine wheelspaces it is clear that no cavity can be completely physically enclosed without some exotic sealing arrangement. Designers have avoided contacting seals by using a variety of rim seal arrangements to try and limit the flow from cavity to mainstream. In addition, purge flow is supplied near the axis of rotation to provide further sealing. While possible to fully seal any arrangement using purge flow, there is a balance between component life and cycle efficiency as the purge flow is taken from the compressor for this purpose. It is thus important to consider the two key mechanisms by which hot gas may be ingested across the rim seal, as well as any additional factors that may have an impact.

In Part I of a two part paper, Owen [40] defines Rotationally-Induced (RI) ingress as the ingress that occurs across a rim seal in the presence of an axisymmetric external flow field. The fluid in a rotor-stator cavity experiences a radially increasing pressure due to the core rotation. This pressure gradient can result in a lower internal pressure than the external flow. The flow structure in the cavity, as described above and shown in Figure 2-7 a-c, has flow radially outwards on the rotor and radially inwards on the stator for a closed system with small superposed flow. These conditions result in egress of purge gas near the rotor and ingress of external air near the stator (Figure 2-9). As the sealant flow rate is increased, the internal pressure can be increased to the point where it is in equilibrium with the external pressure, allowing the system to be "purged". If the flow rate is increased yet further, a condition with only egress flow can be achieved.

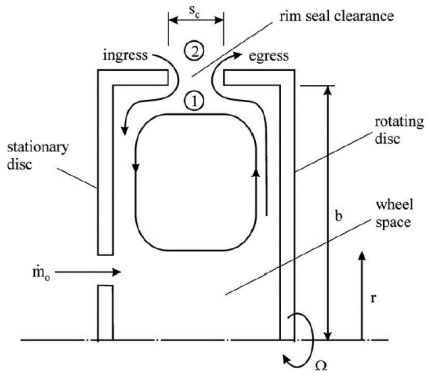

Figure 2-9: Ingress and Egress through a simple rim seal, from [40]

The same author defines Externally-Induced (EI) ingress as the ingestion of fluid across a seal due to a non-axisymmetric external flow field. Typically, this takes the form of an

unsteady 3D flow field in a turbine annulus. The stator vanes introduce a stationary non-axisymmetric pressure field, where the external pressure may be higher or lower than the cavity pressure. In addition to this, the rotor flow field is non-axisymmetric and unsteady, rotating with the blade row. Thus the two pressure fields combine, resulting in ingestion. This ingestion is unsteady in nature. Figure 2-10 shows the instantaneous pressure field between the NGV and RB of a high pressure turbine simulation by Elliott *et al.* [41], with the circumferential variation clearly visible. The pressure peaks correspond to the RB leading edges, with the trough at mid passage.

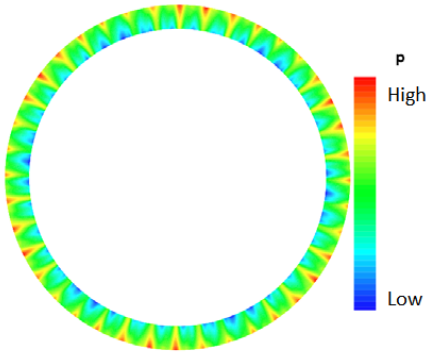

Figure 2-10: Instantaneous pressure field downstream of NGV, adapted from [41]

Owen [42] also defines Combined-Ingress (CI) where both RI and EI effects are present. In part II of his paper [42] a mathematical model is proposed, known as the Orifice Model, by which the minimum flow rate (ϕ_{min}) required for complete sealing can be predicted based on an assumed circumferential pressure profile and empirical constants. Typically, purge flows in the range of 0.7 – 1.0% of the mainstream mass flow rate can be used to fully seal the wheelspace [43].

Johnson *et al.* [44] provide a thorough summary of ingestion mechanisms found in experimental work spanning three decades. In addition to RI and EI ingress, which they term disc pumping and periodic vane/blade pressure field respectively, they identify the following factors affecting ingestion:

- 3D geometry in the rim seal region,
- Asymmetry in the rim seal geometry,
- Turbulent transport in the platform overlap region, and

- Flow entrainment

The first two factors are significant when the focus of the study is EndWall Contouring (EWC), the former referring to axisymmetric contours and the latter to non-axisymmetric. **This is the first indication that the design of contoured endwalls must take into account the turbine rim seal and appropriate levels of purge flow.**

2.2.4 Interaction of Egress and Mainstream Flows

The previous sections have established that in order to avoid ingestion of hot gas to the wheelspace, thus preventing the exposure of the turbine disc to unacceptably high temperatures, the cavity is purged with gas that exits via the rim seal. This purge gas is supplied at a rate and pressure from the compressor to ensure that the rim seal minimises ingestion. However, the pressure distribution in the annulus varies circumferentially and, for the non-sealed case, will lead to regions of ingestion where the annulus pressure is higher than the cavity pressure or egress where the opposite is true. For the fully sealed case, the designer sets the conditions such that the cavity pressure always exceeds the annulus pressure, thereby ensuring a fully sealed wheelspace. The result is egress through much of the rim seal. This egress interacts strongly with the mainstream flow and thus any full analysis of the mainstream must include purge flow in a realistic manner. Some of the key interactions are discussed here.

Barigozzi *et al.* [45] undertook experimental work on a linear cascade, studying the influence of purge flow rate and gap geometry on both the aerodynamic and thermal performance of a rotor blade. They simulated rotational effects by introducing a "tangential" flow component using (variable) angled fins in the seal gap. They discuss the influence of rotation on the incoming boundary layer, highlighting that when moving from the absolute frame of reference (in the stator) to the relative frame (in the rotor) the boundary layer is negatively skewed by the rotation. This can be seen in the endwall cross-flow and is seen to be a driver for the generation of secondary flows. Thus the addition of purge flow with a negative skew component is shown to have a strengthening effect on the cross-flow and the associated secondary features.

The authors conclude that for all geometry combinations, an increase in the purge flow rate had a corresponding increase in mixed-out loss for the blade row - primarily due to the increased negative skew of the purge flow enhancing the HSV-PS. This can be seen

in Figure 2-11, which compares the size and location of the PV for two purge flow rates. By using non-dimensionalised vorticity and secondary flow vectors, the increased size and change in radial position can clearly be seen on a plane downstream of the blade trailing edge. Importantly, a key conclusion from the work is that when the tangential component of the purge flow is neglected, the secondary flow loss is significantly underestimated.

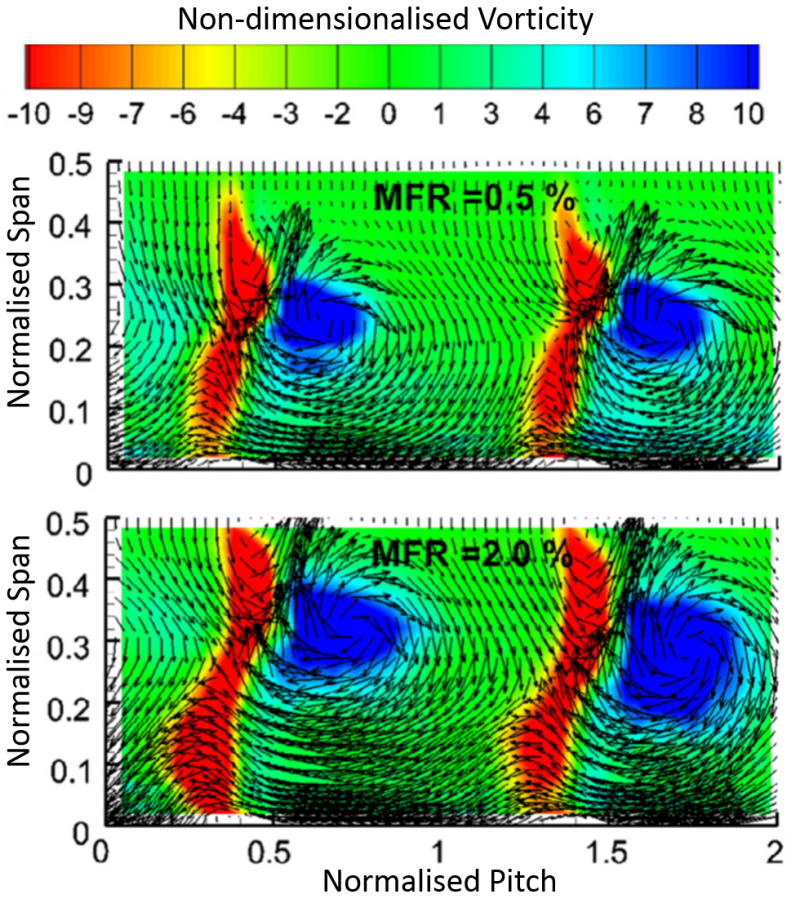

Figure 2-11: Effect of purge on secondary flow vorticity, adapted from [45]

Schrewe *et al.* [46] studied the spoiling effects of purge flow in the Large Scale Turbine Rig at Technische Universität Darmstadt, a 2-stage low speed installation running at $Re_{in} = 5.4 \times 10^5$. The temperature of the mainstream and purge air were independently controlled, allowing for a temperature difference of 15-20° C to be maintained. Temperature measurements were then used to track the trajectory of the purge air, showing that the majority was entrained into the HSV-PS. They observed four sources of loss associated with the purge flow: 1) increased blockage of the annulus as purge air entered the turbine;

2) increased purge flow rates intensified the secondary flow features; 3) incidence angles at the downstream blade row were disturbed and 4) the losses in the stator increased due to an altered downstream flow field.

Other studies include two by Schuepbach and co-authors. The first of these, Schuepbach *et al.* [47] is an experimental study that found the radial extent of hub secondary flows increased with the presence of egress through the rim-seal. The second paper by Schuepbach *et al.* [48] presents both computational and experimental studies of egress interaction, conducted in the LISA research turbine at ETH Zurich. Their findings generally agree with the studies discussed above. In addition, they note that the purge flow leaving the rim seal initially carries normal vorticity, which subsequently and progressively becomes streamwise vorticity as it is bent around the BLE. The purge flow vorticity was in the same sense of rotation as the HSV-PS. When considered together with the findings of Schrewe *et al.* [46] there is strong evidence to show that the the purge flow is entrained into the HSV-PS, with consistent conclusions that that purge flow also directly strengthens the HSV-PS. Schuepbach *et al.* [47] also report that a drop in total-to-total efficiency was found at increased purge flow rates; a similar drop in efficiency was shown by Barigozzi *et al.* [45].

Regina *et al.* [7] present another experimental study from the LISA rig, this time with a focus on aerodynamic performance and measurements of stage efficiency in the presence of egress. A purpose-built fast-response aerodynamic probe is used to make measurements of the unsteady flow field at a frequency up to 48 kHz; measurements with the probe are presented at two measurement planes. In addition, time-averaged results were also presented for purge flow injection rates ranging between -0.1% (a nominal sucking condition) to 1.2% (engine representative blowing) of the mainstream mass flow-rate. The results showed that the stage efficiency was sensitive to purge flow, reducing by 0.8% per 1% of purge flow injection rate. The reduction in efficiency was greatest near the rotor hub, seen in Figure 2-12, where the authors concluded that the cause was an increased strength of the HSV-PS - which lifted off earlier in the passage when purge flow was injected at higher rates.

In contrast to these studies, which look at egress through rim seals, Simon & Piggush [24] review the studies investigating the secondary flow field from a turbine heat transfer perspective. A number of authors find that when purge flow is introduced through the hub or through a slot upstream of the vane or blade, it is possible to re-energise the boundary

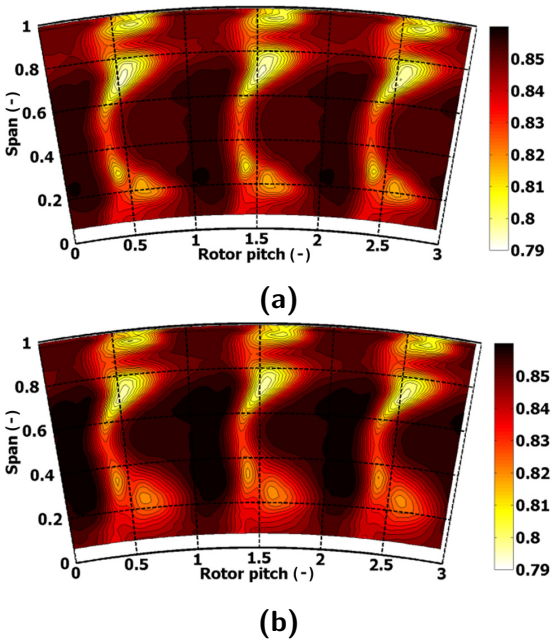

Figure 2-12: Effect of purge on relative total pressure at rotor exit for (a) nominal sucking and (b) engine representative blowing, from [7]

layer. By doing so, the secondary flow structures are weakened rather than strengthened. This paper is included here to demonstrate that the competing design requirements faced by the engine designer can often produce conflicting results. Attention must therefore be given to the specific injection location and momentum ratio of purge flow and its introduction into the mainstream gas path.

2.2.5 Vortex Identification

To visualise the secondary flow structures (or vortices) directly and begin to understand their size it is useful to employ derived variables. The most common of these is vorticity, which can be defined as the curl of the velocity field:

$$\vec{\omega} = \nabla \times \vec{u} \tag{2.6}$$

This has the same units as angular velocity and can be non-dimensionalised using $c_{NGV/RB}/w_{in}$. Here, $c_{NGV/RB}$ is the axial chord of the rotor blade or nozzle guide vane as appropriate and w_{in} is the mass-averaged axial flow velocity at the inlet.

As vorticity is a vector and thus has direction, it can be used to identify the direction

of rotation for a vortex. In order to bring this in to a 2D visualisation, it is possible to utilise the sign of one of the components to deliver both positive and negative vorticity *magnitude*, which in itself does not differentiate. Contours of vorticity are presented throughout this work in this manner:

$$|\vec{\omega}| \cdot \frac{c_{RB}}{w_{in}} \cdot sgn(\omega_x) \tag{2.7}$$

This is particularly useful in identifying and tracking individual vortical structures as they develop through a vane or blade passage, however, this measure alone is not sufficient for identification of coherent vortices. This is particularly true in regions of high shear, such as the boundary layer [49].

Hunt *et al.* [50] introduced the Q-criterion as a method for identifying coherent vortical structures. They defined *eddy zones* as regions with vorticity and strong swirling, but excluded near-straight shear layers and irrotational swirling. Two criteria were applied for a vortex to be present:

1. irrotational strain is small when compared to the vorticity and;
2. a pressure minimum exists somewhere in the zone.

The former is evaluated by taking the second invariant of the deformation tensor, specifically:

$$Q = \frac{1}{2}\left[\left(tr\left(\nabla\vec{u}\right)\right)^2 - tr\left(\nabla\vec{u}\right)^2\right] \tag{2.8}$$

and evaluating where this is positive. The latter is evaluated by interrogating the pressure field.

2.3 Loss

All of the methods for estimating loss factors described in Section 2.1.2 for total pressure are *a posteriori* design tools in that the correlations are based on the data collected from previous designs. While accurate for preliminary work, they do not allow the analysis of novel designs. In order to better attempt to understand loss, Denton [11] viewed loss in terms of its origin and the associated increase in entropy, where loss is unambiguously defined as:

"any flow feature that reduces the efficiency of a turbomachine will be called

loss, but this does not include any factors that affect the cycle efficiency as opposed to the turbine or compressor efficiency."

The profile loss, as defined by Denton [11], is any loss due to boundary layers on the vane or blade remote from the endwalls where the flow is assumed to be two-dimensional. This includes additional losses that occur at the trailing edge. The secondary losses occur when the boundary layers of the incoming annulus flow encounter a blade row, resulting in secondary flows near the endwalls. It is generally accepted that conventional boundary layer theory is not appropriate for describing these endwall flows due to their highly three-dimensional nature and complex separation patterns [16]. Tip losses arise from the leakage flow between blade tip and the shroud. Denton [11] notes that for many turbomachines these three sources each contribute around $^1/_3$ of the total loss.

Zlatinov *et al.* [51] use entropy as a measure of loss when considering the impact of sealing flow. They argue that the entropy generation must be broken down into *thermal mixing* and *viscous* effects, with the thermal mixing contributing to a drop in cycle efficiency while the viscous effects contribute to the turbine efficiency, the latter is of interest to this work. Two conclusions are drawn: firstly, qualitative analysis of loss distribution is best carried out using contours of volumetric entropy generation rate (equation 2.9) and secondly, quantitative comparisons should utilise cumulative lost work. The former can be transformed into a coordinate system of streamwise, cross-flow and radial directions, which agrees with Langston's [23] definition of vortices being aligned to the throughflow. The second equation utilises mass-averaged temperatures and work-averaged pressures to account for the multi-stream flow. It should be noted that entropy generation rate can be used as a proxy for visualisation of vortex structures, though it does not differentiate between vortices and shear layers.

$$\dot{S}'''_{visc} = \frac{1}{T}\tau_{ij}\frac{\partial u_i}{\partial x_j} \tag{2.9}$$

Further mixing losses originate from the re-introduction of purge air, bled from the compressor, into the mainstream flow in the turbine. Purge air, the details of which have been described in Section 2.2, emerges from a rim-seal immediately upstream of the blade endwall. The interaction of egress flow with the secondary flow field in the turbine annulus can enhance the secondary features; the egress core becomes entwined with the passage vortex as shall be demonstrated in this work.

Designers use geometric shaping of the turbine endwalls to minimise secondary flow loss; this process is known as EndWall Contouring (EWC). The objective of EWC is to manipulate, and control, the annulus pressure field such that the growth of passage flow features is reduced. More recently, the interaction between EWC and the upstream rim-seal has become an increasingly important consideration – this will be discussed further in Section 2.4.

For the purposes of this study, stage efficiency is used as a relative measure of stage performance and to quantify overall losses. Turbine stage efficiency is defined as follows, using mass-averaged values:

$$\eta_{mix,ISO} = \frac{T_{mix,ISO} - T_{0,3}}{T_{mix,ISO} \times \left[1 - \left(\frac{P_{0,3}}{P_{0,1}}\right)^{\gamma - 1/\gamma}\right]} \tag{2.10}$$

$$T_{mix,ISO} = \frac{\dot{m} T_{0,1} + \dot{m}_p T_{0,p}}{\dot{m} + \dot{m}_p} \tag{2.11}$$

where location 1 is evaluated at the vane leading edge and location 3 is at the blade trailing edge. Subscript p denotes purge flow variables, evaluated at the purge inlet. All other mass-averaged variables are defined in the nomenclature. This definition does not account for losses due to the non-uniform exit flow, however, this formulation does allow for a consistent comparison for the purposes of this study. The use of infinitesimally small arcs mixed out over an infinite length would address this, with most authors agreeing on a consistent distance downstream over which to measure the efficiency.

The stage efficiency (Equation 2.10) is averaged over one full sector pass for each calculation. In conjunction with this, the unsteady fluctuation over one full sector pass, $\Delta\eta_{mix,ISO}$ (defined in Equation 2.12) was also used as a measure of the interaction between secondary flow features. As noted by Manwaring and Wisler [52], the periodic unsteadiness experienced by turbomachinery blading typically originates from upstream blade rows. The blades and vanes exposed to these fluctuations thus experience unsteady loads. This can lead to vibration and reduced fatigue life of the components. As will be demonstrated in this research, the magnitude of the unsteadiness can be increased by the introduction of purge flow. Subsequently, it will be demonstrated that this can be mitigated using endwall contouring.

$$\Delta\eta_{mix,ISO} = [\eta_{mix,ISO}]_{MAX} - [\eta_{mix,ISO}]_{MIN} \tag{2.12}$$

2.4 Endwall Contouring

The structure of flow in a blade passage has been described in increasing detail over half a century, resulting in the comprehensive picture we have today shown in Figure 2-1. Alongside this, computational techniques have improved and developed to the point where useful 3D flow field data can be obtained at a cost and time scale that is accessible to the turbine designer. These tools, described in Section 2.5, can be leveraged to pursue increasingly complex design features such as EWC. However, it will be shown in this section that for a design to be considered successful the engineer must combine this with an appreciation for the physical processes they are intending to modify.

As reported by both Ingram [53] and Snedden [54], early studies of axisymmetric EWC exist though limited success was achieved, These studies are not covered here. The ground breaking study in this field was presented by Rose in 1994 [10], discussed in detail below, and since that time a large body of work has been produced, gaining increasing traction in recent years. The following section will examine some of the key approaches to non-axisymmetric EWC, evaluating the various design processes and objectives, as well as the validation work and sensitivity studies that have been undertaken.

The use of EWC to minimise stage loss is widely documented. However, until recently, most studies have sought to develop endwalls that were optimised without consideration of the egress flow through the upstream rim-seal. The review presented here is organised into two sub-sections: Section 2.4.1 considers the performance of EWC without the introduction of purge flow (i.e. egress) while Section 2.4.2 considers the interaction between egress and EWCs. Within the first section, the discussion follows the work of Rose and the Durham group (as this forms a comprehensive body of work), before presenting the work of other groups.

2.4.1 Endwall Contouring without Egress

Rose [10] employed EWC to control the static pressure field on the endwall of a stator vane passage. This influential work investigated the static pressure field of a NGV and proposed that by altering the stator hub geometry in a non-axisymmetric fashion, the pressure field (and thus the driver for EI ingress) could be controlled in such a way that egress of coolant could be minimised. This numerical study employed a CFD solver to obtain the full 3D viscous flow field for a subsonic turbine stator row, known as the Moore Elliptical Flow

Programme, which was designed specifically for turbomachinery. This solver incorporated the Baldwin-Lomax mixing length model and a second order accurate upwind numerical scheme that minimised numerical diffusion. The computational grid should be considered with a historical perspective: 37 000 cells were used per stator passage, with the domain extending two chords downstream of the trailing edge. In spite of this low spatial resolution and basic turbulence model, Rose showed a significant reduction in the circumferential variation of static pressure for a contoured endwall compared to a cylindrical baseline. This conclusion was later supported experimentally by Hartland *et al.* [55].

Three non-axisymmetric endwalls were simulated, aimed at reducing the circumferential variation in static pressure at the stator platform trailing edge. One of these endwalls, identified as NAXI3, is presented in Figure 2-13. By introducing features to cause streamline curvature, the pressure could be increased (endwall concavity) or decreased (endwall convexity) respectively. The pressure field in the circumferential direction was found to be approximately sinusoidal, leading to the choice of a similar geometric profile for the endwall with a period of one vane pitch. The axial geometric profile combined a parabolic curve and a sinusoid, with the intersection occurring upstream of the peak. The control of such an endwall was found to be quite simple, requiring only four parameters: axial locations of the platform trailing edge, maximum height, height of protrusion and a phase shift between the vane pitch and endwall sinusoid. The blade-hub intersection was modelled without a blend radius, which was shown by two groups (Hawes *et al.* [56] and Germain *et al.* [57]) to have a significant negative impact on the accuracy of computations as real geometries have a radius at the root.

Figure 2-13: Example of contoured endwall by Rose (NAXI3), from [10]

It was shown that most of the flow field was unaltered by the profiled endwalls, with

no change in blade loading at the mid span. Variations were seen closer to the endwall, with significant differences present along the suction surface at 0.48% height, while the whirl angle showed variation up to 10% span. Overall loss through the NGV was unaffected by the endwall. This is a key aspect to the paper: reducing loss was not a goal and thus no attempt was made to identify or quantify the sources of loss in the passage. Of the three endwalls, two were considered successful in reducing the variation in circumferential pressure distribution at the platform trailing edge, with the best giving a 70% reduction compared to an unprofiled endwall. Rose concluded that axisymmetric endwalls placed a constraint on the turbine design that was unnecessary.

Hartland *et al.* [55] conducted an experimental campaign to validate Rose's original approach. The Durham Linear Cascade, a large-scale low-speed installation, was modified to incorporate endwall designs following Rose's method. Static pressure data showed good agreement with the CFD, allowing them to conclude that the design of contoured endwalls using numerical results is possible. Total pressure and velocity data was also recorded and the impact of contoured endwalls on the secondary flow was deemed to be small. However, they did observe that secondary losses had increased, but no reason was given. This showed that Rose's approach, use of streamline curvature to alter the static pressure field, was both valid and successful: this is thus the first approach to be so.

EWC has also been optimised to reduce secondary flow losses. In the first part of their two part paper, Harvey *et al.* [58] present a linear design system for non-axisymmetric EWC in a stator passage. Their proposed methodology was based on the reduction of the cross-passage pressure gradient and thus secondary losses, specifically the blade exit whirl angle deviation, caused by the PV. This was achieved in the same manner as Rose's work, that is control of the static pressure field using streamline curvature, but with an increased scope for variation of the geometry. Here, the entire blade passage endwall was parametrised using six axial control points, connected using B-splines, and six circumferential points controlled with a three-term Fourier series. Periodicity was preserved by locking the circumferential end points while the axial points extended upstream and downstream of the blade.

This use of an optimisation type approach allowed the authors to set limits on the design envelope and have the endwall constructed for them which satisfied the target function. This allows for a large number of possible solutions to be tested in a short period of time. The authors conclude that it was possible to significantly reduce the secondary flows and secondary kinetic energy, however, only a small reduction in loss was predicted

overall. Additionally, they showed that the use of profiled endwalls could be compared favourably to combined lean and skew of the aerofoil. This is due to the rapid decay of static pressures away from the endwall, leaving the mid span flow mostly unchanged and the simpler mechanical implementation of EWC.

In the second part of the paper, Hartland *et al.* [59] present the experimental validation work undertaken on the Durham cascade with the selected endwall. The cascade was operated in the incompressible range ($M = 0.1$) and $Re = 4.0 \times 10^5$. Static pressure measurements in the blade passage showed good agreement with the design prediction, though the CFD pressure field under-predicted the reduction in cross-passage pressure gradient upstream of the throat. The presence of a strong corner vortex in the latter part of the passage was predicted by CFD due to an endwall ridge extending downstream of the passage and this was found to be present in the velocity field measurements. Overall, secondary flow strength was reduced in the early part of the passage, which was found to lead to a 30% reduction in secondary loss at the exit plane. The authors concluded that the new endwall was successful in reducing the secondary losses and whirl angle deviation, closely matching the predicted performance. The magnitude of loss was significantly over-predicted at the mid-span. They also noted that the turbulence model used would have contributed to the discrepancies between CFD and experimental data.

Gregory-Smith *et al.* [60] developed a second generation of endwall using Harvey *et al.*'s [58] inverse design method. By imposing new design constraints, they hoped to improve on the previous results, specifically the study aimed to reduce the strength of the suction-side leg of the horseshoe vortex (referred to by the authors as the counter vortex). The extent of the profiling was limited to within the blade passage itself, which can be considered a more realistic envelope for a turbine. The computational grid employed for the calculations provided significantly finer spatial discretisation than Rose's original work: 100 000 cells were used in a single passage for half of the span. A symmetry boundary was implemented at the mid span to reduce computational expense. In addition, they presented experimental data from the Durham cascade to validate the design, again showing good agreement for the static pressure field and velocity data. They concluded that the numerical methods were not yet able to predict the loss with sufficient accuracy for this to be used as the target function, attributing this to a poor turbulence model (Prandtl's mixing length model) and no transition model.

The successful approach developed at Durham was extended to engine representative

conditions in a subsequent pair of papers. Brennan *et al.* [61] presented the design of an endwall for the Trent 500-HP single stage turbine using a forward and inverse 3D design program called FAITH. This was based on a similar principle to the previous linear design system but allowed for significantly more complex perturbations in the circumferential direction, incorporating up to third order harmonics in the Fourier series. The CFD solver used was a development of the Moore Elliptical Flow Programme known as sz02, while the computational grid contained 150 000 cells per NGV passage. While the previous studies had excluded the rotor blade row, this study included the downstream blade row using 70 000 cell per blade passage. The design process required 72 steady state CFD runs to performed for each blade row using a manual iterative process. Turbulent closure was again obtained using the Prandtl mixing length model.

Brennan *et al.* [61] proposed the use of secondary kinetic energy (SKE) as proxy for secondary loss based on both Hartland *et al.* [55] and Gregory-Smith *et al.* [60] finding correlation between CFD predictions of SKE and experimental results for secondary loss. They note, however, that to define SKE accurately, the ideal streamwise flow direction must be known which can be problematic for highly 3D blading, leading edge and trailing edge regions. To counteract this, they suggest that the dot product of SKE and Helicity (SKEH) be used to focus on the vortical components of the flow. Helicity can be defined as the flux of streamwise vorticity and is zero where the vorticity is orthogonal to the streamlines. SKEH was thus used as a design parameter with the goal of minimising both SKEH and whirl angle deviation. Endwall contours at the hub and shroud were generated for both stator and rotor.

The selected endwall design for the NGV led to both an increase and decrease in the cross-passage pressure gradient, dependent on the location. Upstream and at the throat saw an increase, while downstream the gradient was reduced. A 30% reduction in SKEH was seen at the mid-plane of the rotor-stator gap, which was assumed to produce an equivalent reduction in secondary loss. In stage efficiency terms, this was estimated to be ±0.24%. Whirl angle was seen to improve everywhere except at the hub and stator. The rotor with contoured endwalls saw the opposite effect on cross-passage pressure gradient: a decrease early in the passage followed by a strengthening later. A 17% reduction in SKEH was predicted, equating to ±0.16% stage efficiency gain. The improvements to whirl angle followed the same pattern as the NGV, but to a reduced extent.

In the part II of the paper, Rose *et al.* [62] applied this EWC to an engine-representative

turbine rig, based on a Rolls-Royce Trent 500. Unsteady CFD simulations were compared to experimental data obtained from a cold flow test with $Re = 6.8 \times 10^5$. The authors concluded that the predicted improvement to performance due to the endwall was successfully demonstrated for the given flow conditions, where stage efficiency gains were predicted as 0.4% and measured at 0.59% (±0.25%), respectively; contouring was applied to both the vane and blade endwalls. They also note that the use of EWC concentrates the secondary losses nearer to the endwalls, leading to more uniform flow at the turbine exit. However, they caution that this could negatively impact on any downstream blade rows and that this should be taken into account at the design stage.

These Rolls-Royce funded efforts clearly demonstrate that endwall contouring is a powerful tool that can be leveraged by the turbine designer. However, it should be reiterated that Rose's original approach was aimed at reducing ingestion of hot gas between blade rows and none of the subsequent studies included any purge or coolant flows. The development of inverse design methods has been successfully applied in the reduction of secondary flows, but there remains the risk of blind application by designers without a true appreciation for the mechanisms by which the physical features have improved performance. Ingram *et al.* [63] address this in a paper by looking specifically at the development of loss and secondary flows in the presence of EWC. A comprehensive experimental campaign was undertaken using the Durham cascade and both generations of contoured endwalls from [58] and [60].

Using a combination of surface flow visualisation and five-hole probe pressure data, they found that the primary effect of the profiled endwalls was to weaken the cross-passage pressure gradient. This follows directly from the desired target function used in the endwall design: reduction of whirl angle deviation at the exit plane. The fundamental driver for these deviations is known to be the HSV-PS initially generated at the blade leading edge. In turn, this vortex is fed by the cross-passage flow and cross-passage pressure gradient. In addition to satisfying the target function, the reduced cross-passage pressure gradient reduces the secondary flow velocities. This leads to a reduction in secondary losses near the endwalls. A fundamental difference between the first and second generation endwalls was the axial extent of the profiling. The first generation extended both upstream and downstream of the blade passage, with a ridge present near the leading edge. The feature can be considered similar to the aerodynamic separator presented by Dorfner *et al.* [9] in compressor applications and endwall fences discussed by Snedden [54], in that it serves to control the path of secondary flows directly. This does, however, result in a large saddle point on the upstream face of the ridge.

Later studies include Gregory-Smith *et al.*'s [64] experimental work investigating combined effects of EWC, blade lean and leading edge extensions. They found that the leading edge extension reduced secondary flows by reducing underturning of the incoming boundary layer and reduced horsehoe vortex strength. Hawes *et al.* [56] investigated the blade root fillet influence on secondary flows numerically. They incorporated optimisation of the fillet which was allowed to vary along the root, leading to a large radius at the leading edge and pressure side which reduced towards the trailing edge. The suction side fillet reduced in size up to near the mid-chord before increasing toward the trailing edge. This combination was found to limit the horseshoe vortex generation and growth, as well as limiting the migration of the HSV-PS and subsequently the PV up the blade span.

Other collaborations on EWC research include the MTU and ETH Zurich group. Their work includes the previously mentioned Germain *et al.* [57] computational work used to develop endwalls for the LISA rig and relies on a non-linear optimisation algorithm, DONLP2. The endwalls were parametrised in an object oriented manner, such that protrusions and depressions could be added, removed or controlled independently, as described by an axial decay function and a circumferential shape function. They paid particular attention to ensuring the geometrical representation of blade root fillet was captured accurately during grid generation. Comparison of data showed that the lack of a root fillet led to a large under-prediction of loss across the normalised span.

The objective functions used were total pressure loss and SKE, with an additional limitation on the averaged exit whirl angle, producing contoured endwalls for the stator hub and shroud and rotor hub. The computations used for the study were time-accurate URANS, however, it is not clear whether the flow fields were processed in any way before being passed to the optimiser. They determined both numerically and experimentally that contoured endwalls influence the flow field in a number of ways:

1. endwall curvature influences the static pressure field;
2. changes in blade cross-section which influenced flow over the full span and
3. changes to blockage will alter the axial pressure gradients.

They concluded that the improved stage efficiency obtained using EWC was not limited to improvements to the secondary flows: mid-span losses were noticeably reduced. This had not been reported previously as a benefit, Hartland *et al.* [55] reported that the CFD had

over predicted loss in this region while Rose's original work reported the mid-span flow as unaltered.

MTU have also collaborated with RWTH Aachen, producing a two part design and validation paper on EWC and 3D blade profiling. Poehler *et al.* [65] adopted a downhill simplex optimisation algorithm with stage efficiency as the target function. This group used the DLR TRACE code in steady state mode and employed a mixing plane at the stage interface. The design space for this study was large due to the inclusion of blade profiling, covering 27 parameters, with optimisation requiring 150 – 200 CFD results. Blade root fillets were excluded during optimisation, but were implemented for final analysis using URANS. Contoured endwalls were produced for the stator hub and shroud as well as the rotor hub. Importantly, by linking the stator and rotor optimisation, they found that while the optimised stator saw an increase in loss and secondary flow, the vane exit flow angle deviations were improved. This reduced downstream blade row losses, which compensated for the "worse" vane performance. It was seen that the stator secondary flows were re-positioned in such a way that reduced losses due to the rotor secondary flows.

Niewoehner *et al.* [66] performed experiments on the 1.5-stage test rig at RWTH Aachen to validate Poehler *et al.*'s [65] endwall designs. They found good agreement with efficiency gain (experiment: 0.38%, CFD: 0.24%). Additionally, they found that the benefit due to EWC was not lost when running at off-design conditions, although reduced mass flow rates saw smaller efficiency gains. The mechanism of increased efficiency was confirmed to be homogenised stator exit angle, especially near the endwalls.

Siemens have also collaborated with a number of research institutions to investigate EWC. Panchal *et al.* [67] performed a design and analysis type study at Virginia Tech. They focussed on a transonic turbine blade passage in a cascade format, thus excluding rotation and upstream guide vanes. A commercially available optimisation package was employed to minimise the total loss coefficient at a specific axial location downstream of the blade TE. The endwall itself was parametrised using control points (25) joined with B-splines. These splines were then lofted together to form the surface extending from 1.25 chords upstream of the blade LE to the TE.

Computations were carried out using the ANSYS CFX v12.1 solver and SST turbulence model on a grid containing 1.8×10^6 cells. 350 calculations were required to obtain an optimised endwall. They included analyses for baseline geometry, optimised and two alternative endwall selections. They reported limited success, with the total pressure loss

showing only a small improvement. However, they did report secondary losses reduced by 66%. They conclude that the contribution of SKE to total pressure loss is not large, rather that reduction in SKE improved flow distribution at blade exit.

2.4.2 Endwall Contouring with Egress

The few studies that consider EWC in the presence of egress flow raise concerns over the robustness of conclusions drawn in the absence of egress.

It is believed that Schuepbach *et al.* [48] were the first researchers to examine the performance and sensitivity of contoured endwall profiles – designed in isolation from purge flow – when exposed to egress introduced upstream of the turbine blades. Their results showed that the improvements offered by the EWCs diminished as purge flow was introduced. The uncontoured case experienced a drop in efficiency of -0.6% per 1% increase egress; the contoured endwalls were significantly more sensitive, returning -1.2% and -0.7% for the two tested.

Using time-resolved computational data, they found this to be due to the blockage introduced by the egress, which causes streamline curvature and alters the pressure field. In addition, they noted that the egress became entrained in, and subsequently strengthened, the passage vortex; this finding corroborated the conclusions drawn by Schrewe *et al.* [46]. They conclude that it is important to include the egress flow when designing endwalls and aim to obtain a uniform static pressure field at the rim seal exit. This ties closely with Rose's original purpose for EWC and is a key finding.

Regina *et al.* [68] present a further study from the large-scale turbine test rig at ETH Zurich with a focus on the robustness of EWC in the presence of egress using fast response aerodynamic probes. Profiled endwalls for the stator (hub and shroud, 26 parameters) and rotor (hub, 41 parameters) were designed for the LISA facility using an optimisation system utilising a commercially-available time-averaged CFD solver. The target function was stage efficiency and cavity purge gas was not included in the optimisation work to improve convergence behaviour.

Measurements at large purge flow rates showed EWC to be disadvantageous compared to a cylindrical baseline. Their investigation considered both steady and unsteady aerodynamic effects in order to quantify the sensitivity of the stage efficiency to increased egress. The authors reported that both the cylindrical and contoured cases experienced a drop in

efficiency when purge flow was introduced, with a near linear trend over the flow rates tested. The contoured endwall was seen to be more efficient at zero purge flow, proving that the optimised design was a success, however it was also found to be more sensitive than the cylindrical case and all benefit had been eradicated at engine representative conditions.

They conclude that while the efficiency difference at intermediate purge flow injection rate was negligible, the flow fields were noticeably different. This was particularly apparent near the endwalls. Time-resolved measurements indicated that the PV evolves differently in the presence of egress. Unsteadiness was seen to increase, and interaction between the stator secondary flows and purge flow become dominated by the rotor flow field for a contoured endwall. They propose one key design guideline for endwall designs where purge flow effects are present: the unsteady interaction of purge and mainstream flows should form the primary focus, including quantifying the upstream extent of this effect.

The key conclusion drawn from this work was the requirement for EWCs to be designed (or optimised) in the presence of purge flow. Such was the sensitivity of the purge flow to the enhancement of secondary flow structures, and vice-versa the potential for EWCs to affect the performance of rim-seals, that the authors recommended a substantial change to the design strategy: EWCs and rim-seals optimised in combination.

Finally, Jain *et al.* [69] used the transonic cascade facility at Virginia Tech to perform validation work on the endwalls designed by Panchal *et al.* [67]. This facility was operated at design conditions for the blading and, crucially, incorporated purge flow capability. The found that for a planar endwall, the introduction of 1% purge flow resulted in a 2% increase in loss. For the contoured endwall, a 3% increase was reported.

2.5 CFD in Turbomachinery

The following section examines the current state-of-the-art in turbomachinery CFD. This is important as the focus of this work is the accurate prediction of the mainstream flow field in order to design contoured endwalls, which have been described in Section 2.4. Dorfner *et al.* [9] note that it is the advances in CFD, specifically the development of high-fidelity codes, that has enabled the designer to consider complex, 3D designs including contoured endwalls and blades. CFD provides the designer with a data rich flow field which, while not yet suitable for absolute performance prediction, is ideal for comparative analysis of designs. The following section will present literature detailing the available computational

techniques and their suitability for the application at hand as well as considering the relative computational cost.

2.5.1 Steady Techniques

Numerical methods for the prediction of fluid flow have been developed since the early 20th century [70], predating the advent of modern electronic computing. These early methods made simplifying assumptions, such as axisymmetric flow or inviscid fluid, to reduce the computational effort required to obtain a solution. In the early post war years the application to turbomachinery applications began to develop, with Wu's [71] S1 (blade-to-blade) and S2 stream surfaces viewpoint coming to dominate. The modern turbomachinery designer still relies on simple 1D calculations to determine annulus shape and mean blade angles, followed by an axisymmetric throughflow (S2) calculations to provide spanwise velocity distributions. Subsequently, a quasi-3D blade-to-blade (S1) calculation can be used to develop the blade profile [21, 72]. These tools do not explicitly resolve or predict many of the fully 3D flow features present in a turbomachine and thus are limited in application to the early design phases.

It was not until the latter part of the 20th century that the computational power available to both researchers and designers allowed for fully 3D methods such as the finite volume method to be implemented [54]. The extension to 3D allows the analysis of more complex geometry and physics, including tip gaps and leakage, blades with lean and secondary flows. Indeed the use of viscous 3D CFD to predict the impact of these real world flows is essential and can now be routinely be found in the design process either as a final check of the S1/S2 design or as a primary tool for applications where 3D effects dominate [21]. Denton argued as early as 1994 that the full 3D flow field should be used as the primary tool for all blading design and notes that useful comparisons can be drawn between solutions on grids of 100 000 cells for a single blade passage.

2.5.2 Turbulence Modelling

Computational fluid mechanics concerns itself with the numerical prediction of complex flow fields. The governing equations for fluid mechanics are known as the Navier-Stokes (NS) equations, relating the pressure, velocity, temperature and density of the fluid. The NS equations consist of three parts (conservation of mass, momentum and energy), leading to a coupled system of partial differential equations which must be solved simultaneously.

A comprehensive derivation for these equations falls outside of the scope of this work but can be found in various forms in textbooks such as Versteeg & Malalasekra [73], Kundu [74], Anderson [75], Wilcox [76] and Pope [77].

Prediction of a wall bounded flow field using the full NS equations at high Re is made challenging by the wide range of length scales present. The Reynolds-Averaged Navier-Stokes (RANS) equations attempt to circumvent this by concerning themselves only with mean flow and the effects of turbulence on mean flow properties. This is done by time-averaging the flow variables to decompose them into mean and fluctuating components, which introduces additional terms to the previously closed NS equations. An alternative averaging process, useful for compressible flows, is the density weighted Favre-Averaging process.

These additional terms are known as the Reynolds stresses. These additional terms require closure and are modelled using a variety of turbulence models. Examples of popular and successful models include the one-equation Spalart-Allmaras model [78] and two-equation Menter's $k-\omega$ Shear Stress Transport (SST) formulation [79]. These are both complete models in that they are self-contained, though they do have a set of model constants which have been developed empirically to give good performance for certain flow conditions. These are computationally efficient, requiring a limited number of additional, linear equations to be solved but are limited in accuracy due to the assumption that turbulence is isotropic. They also provide limited information regarding the turbulent flow, with the SST model providing only length scale, frequency and eddy viscosity.

More advanced models exist, such as the seven-equation Reynolds Stress model. These models will contain more information about the flow and allow the consideration of anisotropic turbulence, however, the introduction of seven additional equations comes at a significant computational cost. These are discussed in more detail with reference to the computational model in Section 4.3.1.

Physical Limitations

For prediction of more than one blade row, such as a turbine with a stator and rotor or a multi-row compressor, the flow field becomes fundamentally unsteady in nature. For design purposes the use of a "mixing plane" between rows allows steady techniques to be used and has produced reasonable data for overall machine performance [21, 80]. As expected for a real mixing process, entropy must increase and this is reflected in a step change seen

across the mixing plane especially at Mach numbers approaching unity where the unsteady effects are strong.

This approach does not, however, provide accurate predictions of boundary layer growth or secondary flow features, nor does it provide time-accurate solutions. For example, the flow downstream of a blade with non-zero trailing edge thickness is always unsteady and characterised by vortex shedding, a source of loss which will not be captured by steady state simulations. RANS simulations are still useful and concise as the output from a steady calculation is a single flow field of time-averaged quantities which can be obtained at low computational cost.

Jia & Liu [81] performed steady computations on the ETH Zurich research turbine, LISA. While their aim was to predict rim seal ingestion, they provide a significant amount of detail regarding their validation of mainstream flow with experimental data. The flow solver employed was *ANSYS CFX* v12.0 with the SST turbulence model. The computational domain was simplified to a single passage with 3×10^6 cells. The flow conditions were matched to experimental data, with $Re = 7.1 \times 10^5$ and known inlet total pressure profile. It is unclear whether the second stator row was modelled, but based on cell count it is assumed that this was excluded. Their results show a poor agreement between CFD and experiment for flow angle at stator and blade exit.

2.5.3 Unsteady Techniques

The previously discussed computations of turbomachinery rely on the assumption that the unsteady flow field can be treated as steady when analysed in the rotating reference frame, allowing the use of RANS. However, as the design of turbomachines has driven efficiencies higher and higher, the gains available to exploitation become smaller and harder to find. The computational cost of Unsteady RANS (URANS) simulations starts to become justified where no further gains are available from the steady state methods: Montomoli *et al.* [72] report that an unsteady calculation requires two orders of magnitude increase in iterations when compared to a steady calculation.

Montomoli *et al.* [72] investigated the Cranfield University low-speed research compressor, comprising four identical stator-rotor stages with constant hub and shroud radii. This is an ideal case for comparison work as a wealth of experimental data is available. While this allows quantification of the losses due to unsteady effects such as wake passing,

it must be noted that the rotor pitch was scaled to take advantage of periodicity for the computational domain. Both steady and unsteady calculations were performed using HYDRA, a fully 3D viscous solver. The computational grid was a structured multi-block mesh, comprising an O-grid around the blade with H-blocks elsewhere, which is a simple blocking arrangement best suited to the thin blades with low turning angles found in compressors. The domain contained three NGVs and four RBs per stage, with 4.4 × 10^6 and 3 × 10^6 cells per row respectively for Re = 2.9 × 10^6. The one-equation Spalart-Allmaras turbulence model was employed for this compressor application. They conclude that while prediction of flow field losses improves for the unsteady case, the concordant increase in computational cost is prohibitive for routine use.

Holmes *et al.* [82] present computational results for a low pressure turbine stage in order to further explore the impact of steady or unsteady calculations. They simplify an existing turbine test rig geometry, reducing stage count and taking advantage of periodicity by adjusting blade counts. This still results in an extremely large domain, being $\frac{1}{14}^{\text{th}}$ of the annulus and four stages for a total of 67 blade passages and the cell count is correspondingly large at 200 × 10^6. TACOMA, a structured, multiblock solver was employed for the calculation, with the SST turbulence model, including a transition model. Accurate boundary conditions were obtained from experimental results, specifying total temperature, total pressure and swirl angle at the inlet. No details are given regarding the operating conditions. They conclude that while the steady calculation provides a reasonable solution for the overall performance of the turbine, the individual stage efficiencies can be seen to be considerably different from the unsteady solution. This result might be masking large errors in the flow field for the steady state solution and highlights the need to include unsteady effects in any high fidelity solution. The authors draw attention to one of the drawbacks of unsteady calculations: large data output both in terms of file numbers and file size.

Germain *et al.* [57] performed unsteady calculations of the flow through the LISA turbine test rig. They used the TRACE solver, developed by DLR and MTU, which is specifically for the steady and unsteady analysis of turbomachinery. The computations utilised the standard two-equation Wilcox $k-\omega$ model and incorporated a transition model. The structured multi-block grid contained 1.5 × 10^6 nodes per stage for Re = 7.1 × 10^6 and M = 0.54. These calculations were performed with the aim of predicting loss and secondary flow features in order to develop a contoured endwall. Results indicated that the solution was sensitive to 1) geometric fidelity, specifically accurate representation of the blade root fillet, 2) transition model and 3) inlet turbulence levels.

2.5.4 Advanced Turbulence Modelling

All RANS and URANS based studies include some form of turbulence model. As no single model is applicable to all flows the analyst must be wary of using these models to predict flows for which they have not been tailored. The empirical constants within these models can be adjusted to suit a new application, though this is a long process which requires accurate validation data for the desired flow [77]. Clearly, the turbulence model is and will remain the fundamental weakness in any CFD solvers based on using RANS. However, the equations developed over 100 years ago are not the only available formulation for CFD. The modern analyst has access to two other key techniques: Large Eddy Simulation (LES) and Direct Numerical Simulation (DNS).

DNS can be considered as a numerical experiment, where the full range of length scales are resolved in a time accurate manner. The full, unsteady NS equations must be solved on a grid which allows the resolution of the smallest eddies. These are of the order of the Kolmogorov length scale, defined as the length at which viscous and inertial effects are equal in magnitude. The computational grid for DNS scales with $Re^{(9/4)}$ for non wall-bounded flows [73]. When combined with the requirement that computations be run in a time-accurate manner, the computational cost of DNS precludes its use for most engineering applications for the immediate future. It usually finds application in the field of turbulence model development and validation as well as in specialist cases used for software development.

LES is an alternative to DNS which was developed for weather prediction, providing time accurate data and resolving some features of turbulent flow unavailable to RANS. Here, a spatial filtering is applied to the governing equations, limiting the range of scales to be resolved and thus relaxing the grid requirements somewhat. It assumes that the smallest eddies are isotropic in nature and can be modelled using a sub-grid scale model to account for energy dissipation. In this way, a reasonably coarse grid can be developed that captures the larger, anisotropic eddies which are of interest. As we shall see, this is still a computationally expensive technique but is beginning to find traction for engineering applications and wall-bounded flows where DNS remains unaffordable.

It is clear that both of these methods present a significant improvement over classical turbulence modelling. Recent advances in computational power and the developing field of parallelisation has enabled researchers to begin to apply both techniques to turbomachinery.

O'Mahoney *et al.* [83] performed both URANS and LES computations on a single stage turbine rig geometry utilising the Rolls Royce HYDRA code. By taking advantage of periodicity, a single NGV passage and two RB passages were meshed, including the rim seal and wheelspace. Grid cell counts ranged from 5.5 × 10^6 for URANS and a coarse (or under-resolved) LES simulation to 23 × 10^6 for their final LES run, which should be considered a more appropriate grid for the technique. Flow conditions were chosen to match available experimental data, with Re = 1.3 × 10^6 and Re_ϕ = 2.2× 10^6. They were able to compare result from the two techniques and grid levels. The LES produced higher quality results than the URANS as expected, with the fine grid giving an improvement over the coarse grid. However, it is essential that we now consider the computational cost of this technique. The URANS simulation required 10 752 CPU hours to produce results. The coarse LES required 122 880 CPU hours while the fine LES required 614 400 CPU hours. This is an exceptionally high cost which does not, yet, justify the method for regular use.

Sandberg *et al.* [84] performed compressible DNS using the HiPSTAR solver on a linear cascade rig. While this is not a true turbomachinery application as there is no rotation, it is still interesting to see DNS being applied to wall bounded flows of this type. They considered two flow conditions, Re = 60 000 and Re = 100 000, both at M =0.4. The cell counts for coarse grids were 18.1 × 10^6 and 75.6 × 10^6 respectively. The results produced using this technique are exceptional, very closely matching experiment for both blade loading (Figure 2-14) and wake loss.

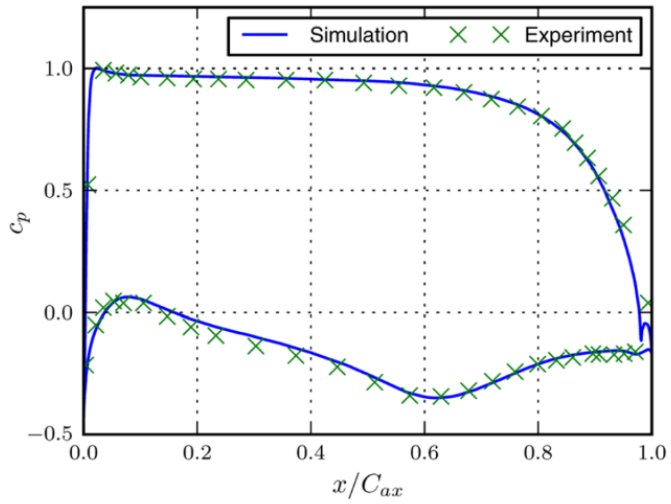

Figure 2-14: Comparison of DNS and experiment blade pressure coefficient at Re = 60 000, from [84]

2.6 Summary

Secondary flows in the main gas path of a turbine contribute directly to loss through the stage. These secondary flows have also been shown to be responsible for exit angle deviations, causing an off-design incidence angle for any downstream rows. The use of EWC has been demonstrated to successfully reduce both of these losses.

EWC is only possible through the use of CFD to inform the design. Solver and computational power developments mean that the current design process can begin to include URANS, though DNS and LES remain too costly. These time-accurate simulations are particularly important for the unsteady phenomena found in the rim seal, as a result of ingress and egress.

Egress interacts with the mainstream in an unsteady manner, causing two direct detrimental effects. These can be accurately predicted by unsteady CFD. Additionally, the purge flow has been found to interact strongly with the secondary flow features. EWC has been shown to be more sensitive to purge flow than a cylindrical endwall. This is expected for highly optimised endwall designs which might be at the limit of an available design envelope. Thus the design of an endwall must include both a realistic purge flow rate and the unsteady effects of any interactions.

The intersection between these three areas of research provides a focus for this work. Where endwalls have been successfully designed computationally, they have shown sensitivity to off-design conditions with purge flow. The design process can now be supported by CFD that is sufficiently capable to provide time-accurate flow field data of acceptable accuracy. The next generation of contoured endwalls must take into account as much of the expected flow physics as possible in order to be considered practically useful and successful.

Chapter 3

Large Annulus Rig

3.1 Research Programme

In order to study, in detail, secondary flows in the presence of purge flow, the University of Bath is collaborating with Siemens Industrial Turbomachinery Ltd to design and build a new, bespoke experimental facility with funding from the EPSRC (grant EP/M026345/1). This Large Annulus Rig (LAR) forms the focus of a research programme of experimental and computational work aimed at revealing the fundamental flow physics and interaction phenomena present in a rotating, single turbine stage. While the present body of work focuses on the computational aspects of the project, it is essential to contextualise the work within this larger framework.

The parallel application of novel experimental measurement techniques will provide a wealth of validation data for CFD studies of the stage, while the CFD will be used to provide additional insight. The study of secondary flow phenomena has been presented in Sections 2.2.1 and 2.2.4, detailing the underlying structures and the influence of purge gas on those structures. Additionally, it has been demonstrated in Section 2.4.1 that turbine efficiency can be increased through the use of contoured endwalls. The open literature notes the limitations of designing endwalls in isolation of the purge gas flow, which this programme aims to address. The novel endwall design methodology, detailed in Section 6, takes a deterministic approach to control secondary flows in a desired manner.

This project falls within a global Siemens project on endwall contouring. The LAR

provides the opportunity to validate endwall designs proposed by three separate research groups. The first group is Siemens Large Gas Turbines (LGT), based in the USA and Germany. They applied commercial CFD solvers and optimisation techniques to the challenge. The LGT team considered both steady and unsteady CFD in the presence of purge flow, however, they did not model the wheelspace in order to reduce the computational effort. The second group is Siemens Aero-Derivative Gas Turbines (ADGT), based in Montreal, Canada, applied the proprietary Rolls-Royce Hydra CFD code within an optimisation routine. The ADGT team accurately modelled the wheelspace, however, they did not model the vane or blade root fillets.

The third group comprises the University of Bath and Siemens Small Gas Turbines (SGT), based in Lincoln, UK. The approach used in this collaboration was to employ commercial CFD solvers but avoid optimisation routines, preferring to identify and generate specific endwall features. These features are intended to control the secondary flow structures in a distinct manner, rather than reducing objective functions. Geometric modelling used within the group was the highest level of fidelity, including both vane and blade root fillets, as well as the wheelspace.

The new facility is described in detail in Section 3.2, providing a thorough overview of the LAR and its operating conditions. The author's contribution to the design and development of this facility is then detailed in Section 3.3.

3.2 New Facility

The LAR is a new, one-stage axial turbine rig facility at the University of Bath. This facility has been designed specifically for investigations of the fundamental fluid dynamic phenomena controlling the interaction between purge and mainstream flows. The following sections describe the rig capabilities, operating conditions and design of the inlet section. Figure 3-1 shows the six key sub-assemblies of the rig: feed pipework, inlet (red), working section (green), exhaust system (purple), and drivetrain and support system (blue). The measurement apparatus are not shown in this figure. A detail view of the working section is shown in Figure 3-2.

The facility has been designed around state-of-the-art optical measurement techniques in order to reveal the fundamental fluid dynamics of the secondary flow structures and the interaction mechanisms of mainstream and purge gases. Pressure (total and static) and gas

concentration measurements can be made at select locations throughout the wheelspace. Static pressure measurements can be made at three radial locations on the NGVs and at selected positions on the hub and shroud. Finally, torque and five-hole probe measurements are planned for the facility, but are yet to be implemented.

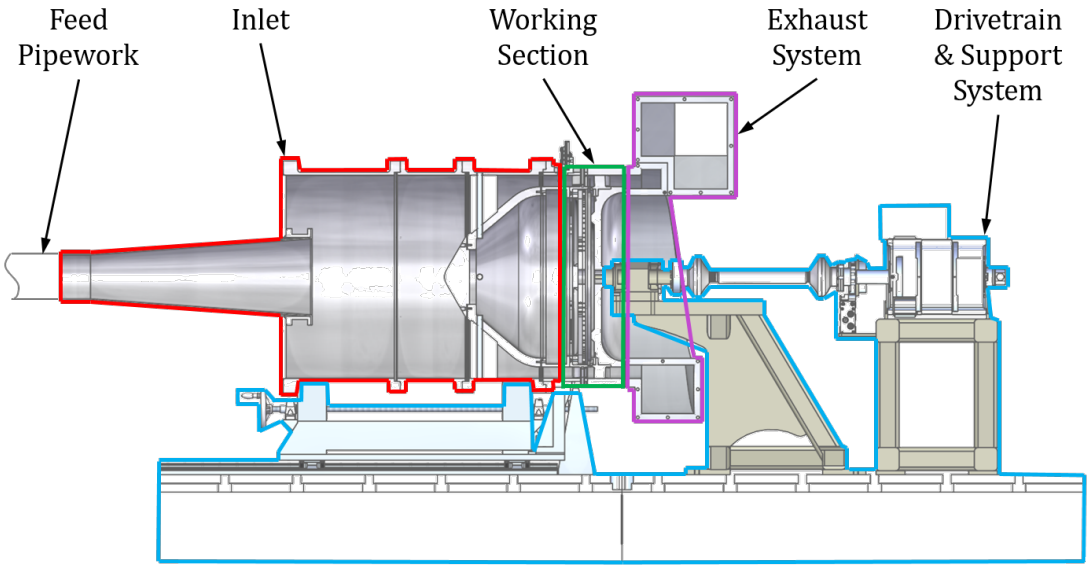

Figure 3-1: Section view of the LAR, adapted from unpublished work by R Jones, 2016

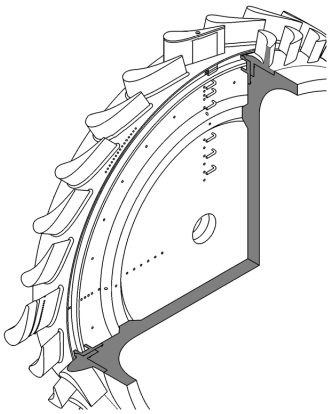

Figure 3-2: LAR working section, adapted from [14]

The experimental facility is shown mounted on its bedplate to allow for lateral translation and access to the working section. Air, the working fluid, is delivered to the inlet drum (red) through a conical diffuser and supply pipework by a remotely located compressor. The maximum sustainable mass flow rate ($\dot{m}$) for the LAR is 1.5 kg/s at 1.2 bar. Control of $\dot{m}$ is achieved using a proportional-integral-derivative (PID) control loop for a variable

speed drive, where $\dot{m}$ is measured using an in-line thermal mass flow meter. In addition, the PID control allows for thermostatic control of the mainstream flow temperature using a water-cooled heat exchanger; 298 K is the target condition. For experiments documented in this thesis, the design conditions for the rig were: 1100 rpm ($Re_\phi = 7.2 \times 10^5$) and a mass flow rate of 1.4 kg/s ($C_f = 0.38$). The axial Reynolds number, based on vane chord is $Re_{ax,NGV} = 2.8 \times 10^5$ and vane exit Mach number $M = 0.14$.

Bayley and Owen [85] report that values of Re_ϕ up to 10^7 are common for gas turbines. However, the cavity flow conditions are governed by λ_T as the superposed purge mass flow has a first order impact as shown by Owen and Rogers [38]. In this parameter, there is a close match between typical engine values and this facility ($\lambda_T \sim 0.1$)[14]. This ensures that the cavity flow is representative of engine conditions. In addition, the critical Re_ϕ to ensure turbulent flow in a cavity of this type is 3.5×10^5 [37]. Barringer *et al.* [86] report that a typical aero-engine has $Re_{ax,NGV} = 3 \times 10^5$. This compares favourably with the current facility. However, they also report typical blade inlet Mach numbers of 0.65, where the current facility remains incompressible ($M_{RB,in} = 0.21$) and thus compressibility effects will not be captured.

The low speed, low aspect ratio turbine stage (green) features 24 NGVs and 36 RBs. Vane and blade profiles (Figure 3-3) are scaled from a current industrial low-pressure turbine design with the aerodynamic profiles specified at 10% span. This design was selected to artificially enhance secondary flows in order to aid detection with experimental techniques. The span (s) is 40.0 mm with a NGV axial chord (c_{NGV}) of 50.0 mm; the RB axial chord (c_{RB}) is 54.1 mm. The hub radius (b) of 312.0 mm gives a hub-to-tip ratio of 0.886, typical of the first stages of many gas turbines. Both NGV and RB have a fillet of 0.0875 s (3.5 mm) at the hub root, with a rotor tip gap to the casing of 0.0125 s (0.5 mm). The axial offset between NGV trailing edge (TE) and RB leading edge (LE) is 0.5 c_{NGV}, providing sufficient space for a double chute seal arrangement. These parameters are summarised in Table 3.1.

Purge flow is introduced at low radius through the bore of the stator disc. The inner wheelspace (i.e. the separation between stator and rotor discs) has an axial dimension ($S_{IWS} = 0.52\ c_{NGV}$, feeding an outer wheelspace via an inlet seal at $r/b = 0.62$. The outer wheelspace extends from $r/b = 0.68$ to 0.90. Purge gas is metered independently of the main gas and can be seeded with up to 100% CO_2, providing up to 0.061 kg/s. For the design point, a purge mass fraction (compared to the mainstream flow) of 1.7% was

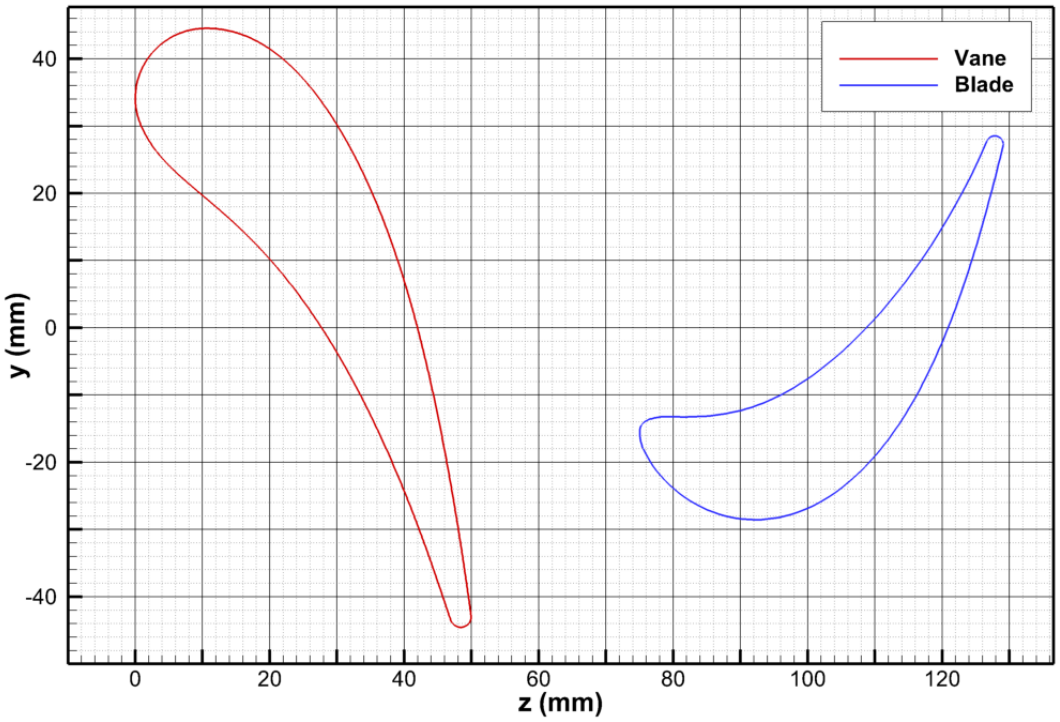

Figure 3-3: Vane and blade profiles

used, ensuring fully sealed conditions in the wheelspace (i.e. there was no ingress through the rim-seal). The rim seal selected for the rig is a double-clearance chute seal, shown in detail in Figure 3-4 with the key geometric parameters presented in Table 3.1.

Performance characteristics for the double rim-seal are presented in [14] and are summarised briefly here. Typically for ingress purposes, the purge mass flow supplied to the rig is expressed as the non-dimensional sealing flow parameter:

$$\phi_0 = \frac{U}{\Omega b} \tag{3.1}$$

where $U = \dot{m}_0/2\pi\rho_0 s_c b$ is the bulk mean radial seal velocity, calculated using purge mass flow, density, seal clearance s_c and seal hub radius b. Ω is the angular disc speed. Sealing effectiveness can be defined as the ratio of the purge mass flow rate ($\dot{m}_0$) to the sum of the purge mass flow rate and ingested annulus mass flow rate ($\dot{m}_i$):

$$\varepsilon = \frac{\dot{m}_0}{\dot{m}_0 + \dot{m}_i} \tag{3.2}$$

however, this definition of effectiveness is difficult to measure directly and thus proxy meas-

ures are employed.

For the LAR, the purge flow is a blend of CO_2 and air. A varying concentration of CO_2 can be achieved, from the atmospheric level of 0.4% through to 100%. This allows a useful measure of effectiveness, the concentration effectiveness, to be defined as:

$$\varepsilon_C = \frac{C_s^* - C_a^*}{C_0^* - C_a^*} \tag{3.3}$$

where:

$$C_s^* = \frac{\rho_{CO_2}}{\rho_{air} \cdot (C_0 - C_s) + \rho_{CO_2} \cdot C_s} \cdot C_s \tag{3.4}$$

$$C_a^* = \frac{\rho_{CO_2}}{\rho_{air} \cdot (C_0 - C_a) + \rho_{CO_2} \cdot C_a} \cdot C_a \tag{3.5}$$

and

$$C_0^* = \frac{\rho_{CO_2}}{\rho_{air} \cdot (1 - C_0) + \rho_{CO_2} \cdot C_0} \cdot C_0 \tag{3.6}$$

Here, the mass based concentrations C^* are calculated from the gas analyser measured volumetric concentrations. The subscripts s, a and 0 refer to the stator surface measurement location, annulus values and purge flow values.

Concentration effectiveness has been shown to be dependent on seal geometry, radial measurement position and sealing flow rate. Two positions are typically reported for double seal arrangements: the inner seal cavity ($r/b = 0.9$ for the LAR) and the outer seal cavity ($r/b = 0.979$). The minimum value for ϕ_0 at which $\varepsilon_C = 1$ is defined as ϕ_{min}. For the LAR, ϕ_{min} is 0.040 for the inner cavity and 0.120 for the outer cavity. The endwall aspect of the project specifically requires designs to be carried out in the presence of egress, as such calculations are performed with a purge mass flow above ϕ_{min}, with the 1.7% of main gas flow rate mentioned previously corresponding to $\phi_0 = 0.134$.

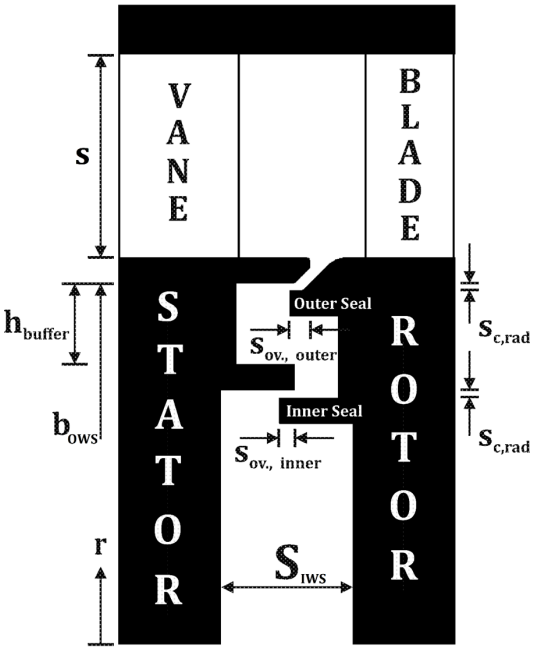

Figure 3-4: Double Lip Seal Profile, from [14]

Parameter	Dimension (mm)
s	40.0
c_{NGV}	50.0
c_{RB}	54.1
r_{root}	3.5
$tipgap$	0.5
$r_{a,min}$	312.0
$r_{a,max}$	352.0
h_{buffer}	16.0
b	312.0
b_{OWS}	307.0
S_{IWS}	26.0
$s_{c,chute}$	2.1
$s_{c,rad}$	1.5
$s_{ov,outer}$	4.0
$s_{ov,inner}$	3.0

Table 3.1: Rig Geometric Parameters

The LAR is specifically designed to enable the deployment of two state-of-the-art optical fluid measurement techniques: volumetric velocimetry (VV) and CO_2 planar laser-induced fluorescence (PLIF). The application of both techniques to a rotating rig is novel [14] and will provide a validation data set for CFD studies in the near future. A brief description of both non-intrusive techniques follows.

VV is a well-known particle tracking technique, effectively an extension of 2D particle image velocimetry (PIV) to a three-dimensional volume and both techniques share many elements. Particle tracking requires that the flow is seeded with trace particles which move with the flow, using a droplet generator. Using a known timestep, these particles are illuminated using a pulsed laser sheet (PIV) or cone (VV). A setup with one, two or three CCD cameras can be used to capture frames at each illumination pulse, depending on the method and desired velocity components. VV utilises three cameras and captures one frame from each per timestep, providing six high resolution images which are then post processed to compute the displacement in space of particles. The processing method specific to the LAR is described by Carvalho Figueiredo *et al.* in [87] with respect to successful application in the study of film cooling kidney vortices. All three instantaneous components of velocity

are provided for the illuminated region, which can be interpolated to a structured grid using a Gaussian weighted average.

PLIF takes advantage of the phenomenon of laser-induced fluorescence, whereby a laser sheet is used to excite molecular transitions of gas species. The photons released by the induced transition have a wavelength that depends on the gas and laser wavelength and can be captured in a single frame using a carefully selected image sensor. The concentration of the gas is proportional to the fluorescence intensity. PLIF has found application in combustion research, where flames naturally provide a source of CO_2. In the LAR, the purge flow is seeded using CO_2 as previously discussed. This provides a means by which the egress plume can be imaged directly, obtaining both location and concentration data.

The application of both techniques to a rotating flow field such as the LAR provides additional challenges. Due to the movement of the rotor disc, the two illuminations required by the VV method must be closely spaced to avoid significant dislocation of the blade in each step. The acquisition frequency of both techniques is low (~10 Hz) in comparison to the design rotational frequency (~23 Hz) and thus the expected frequency of flow interaction phenomena which are highly unsteady. This resulted in a reduction of the expected rig operating speed from 1375 rpm to 1100 rpm and enabled the implementation of phase-locked ensemble-averaging to produce time-averaged, periodic flow fields.

3.3 Inlet Design Study

Preliminary designs for the LAR included a simple, spherical nosecone in a tapered drum for inlet ducting. The final design of the facility required an inlet to be designed in order to ensure steady, uniform flow in the turbine stage inlet. CFD was employed for this purpose, developing geometry to transition between existing, 6 inch pipework to the much larger diameter annulus to achieve a smooth, flat radial velocity profile which was axisymmetrical while minimising pressure drop. For the given design envelope, it was decided that various features could be advantageous such as the use of baffle plates. In order to evaluate these features and to compare performance, the following CFD study was undertaken.

3.3.1 Design Envelope

The key limitations on the design envelope were:

- LAR stator and rotor design;
- Existing pipework size and flange location;
- Available laboratory size;
- Access required for optical system and safe operation.

Based on these, the envelope is shown as red hatching in Figure 3-5. The allowable maximum internal diameter was 704 mm and maximum internal length was 2050 mm. In addition to the size limitation, the incoming pipework had been previously installed with a series of three 90° elbows immediately upstream of the flange. Initial calculations based on mass flow rate revealed a large difference in velocity between the feed pipework (76 m/s) and the annulus working section (16.6 m/s). The presence of short radius elbows in the pipework is expected to cause the formation of Dean vortices [88, 89], requiring the addition of honeycomb straighteners in the pipework immediately preceding the rig entry.

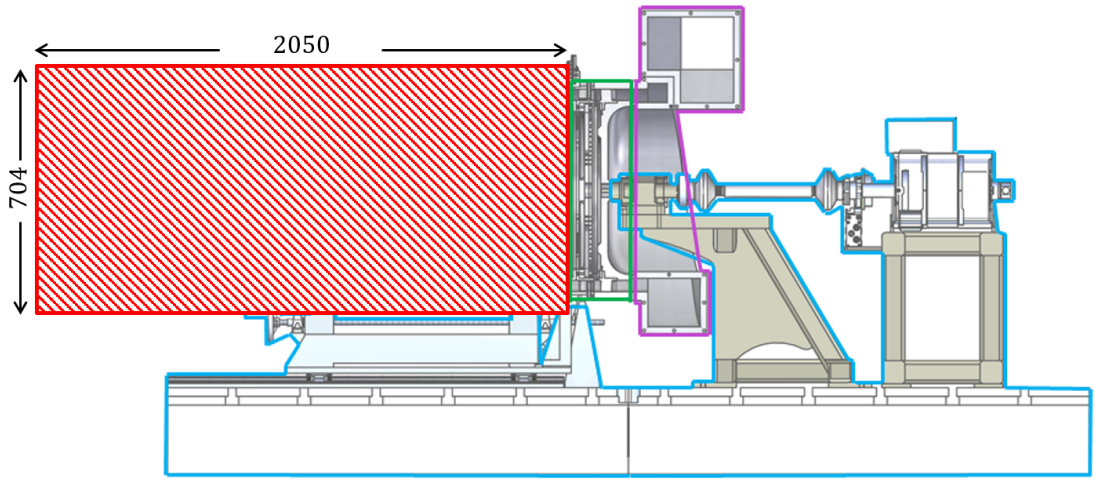

Figure 3-5: Inlet design envelope

In addition, the desire for a settling chamber would require that the air be decelerated further before accelerating towards the annulus. It was proposed that for simplicity, the settling chamber be a cylinder with ⌀ 704 mm to match the annulus. With these parameters and constraints defined, a series of designs were proposed before being simulated and compared using CFD.

3.3.2 Computational Model and Baseline

The commercial solver used for the study was *ANSYS Fluent v15.0*. *Fluent* is a general purpose CFD solver which finds application in the literature for both external [90, 91] and internal flows [56, 92–94]. The design of the inlet is an internal flow considered in a non-rotating domain. This is a cell-centred solver, as discussed in Section 4.1. The $k-\omega$ SST turbulence model was employed. *Fluent* allows the use of wall functions and, as accurate skin friction and heat transfer data was not desired, the non-dimensional first cell height was set to $y^+ \geq 11$ in accordance with the requirements of the model [95]. A nominal refinement ratio of 1.4 was used between grid levels, providing a difference in size that is in accordance with Stern's guidelines [96].

A grid sensitivity study was carried out using Roache's [97] grid convergence index (GCI) using a Richardson extrapolation for the pressure drop in lieu of experimental data. The use of three grid levels allows the factor of safety to be set to the recommended $F_s = 1.25$. The calculated order of convergence was $p_{GCI} = 1.86$ compared to the strictly second order scheme employed, where differences can be attributed to grid deficiencies and turbulence model. The GCI was calculated to be 0.314% from the coarse to medium grid and 0.086% from medium to fine. This confirms that the results are in the asymptotic range of convergence. In order to visualise this, Figure 3-6 shows the pressure loss through the simple radial diffuser for three grid levels. The extrapolated value is shown in red. The grid levels are represented using non-dimensional cell size, calculated using Celik *et al.'s* method [98]:

$$h = [\frac{1}{N}\sum_{i=1}^{N}\Delta V_i]^{\frac{1}{3}} \tag{3.7}$$

A baseline design for testing was chosen to be a primitive radial diffuser, designated RD1, shown in Figure 3-7. This was considered the simplest case type of design, though it had successfully been employed on a previous rig by Sangan [99] and was thus considered a known quantity. A cross section of this is shown in Figure 3-7, showing half of the symmetrical profile. The vane position is indicated with a yellow box and the rotational axis lies at the at the lower edge. The total pressure loss for this design was calculated to be ~10.1 kPa.

The computational model for the inlet took advantage of the axisymmetric nature of the designs to reduce the domain from a cylindrical volume to a sector. However, due to the need to model the feed pipe and, indeed, any settling chamber as a full cylinder,

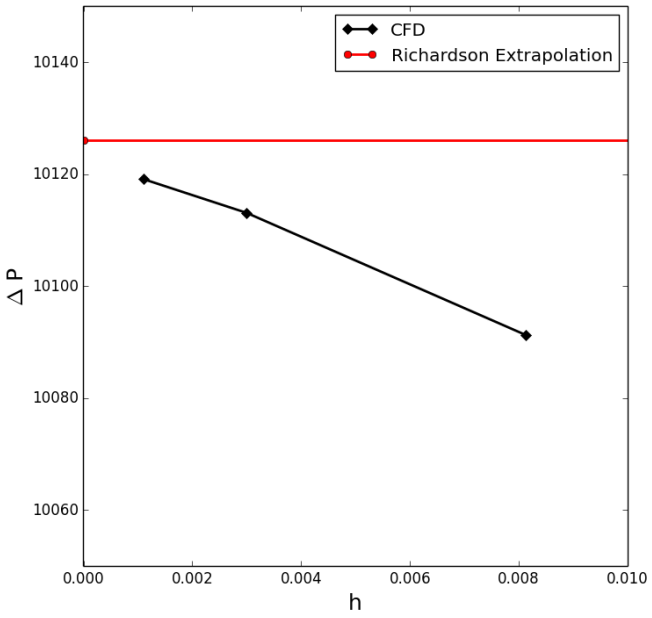

Figure 3-6: Grid Convergence for Inlet Design Study

the sector formed a tight wedge at the centre, as seen in Figure 3-8. Thus the use of a structured mesh for the domain became problematic with the cells becoming vanishingly small at the centre. Two approaches were considered to address this:

1. introduce an inviscid wall at the centre at some small radius r to avoid the vanishing cell height or
2. utilise an unstructured grid.

Cell quality at the centre was poor using both approaches, however, the unstructured

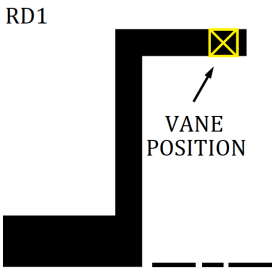

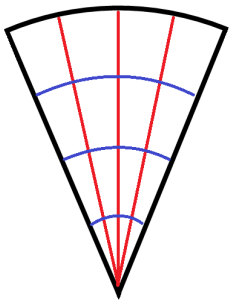

Figure 3-7: Simple Radial Diffuser RD1 **Figure 3-8:** Structured Grid for a Sector

grid was found to give an advantage over the structured approach due to the presence of a single tetrahedral element at the axis of symmetry. The minimum angle was thus defined by the sector size, allowing a sector size to be chosen that allowed for reasonable cell quality. In contrast, the structured grid retained the circumferential cell count, specified at the annulus outer radius, throughout the domain. In this case, the minimum angle is a function of both sector size and circumferential cell count. Circumferential cell count is itself a function of sector size, so no improvement to cell quality at the inviscid wall is possible without compromising cell quality at the annulus outer radius.

Three sector sizes (10°, 30°, 45°) were considered. The 30° was chosen for three reasons:

1. this matches the minimum sector size for a 24:36 blade count periodicity,
2. 10° was deemed to give poor quality unstructured cells at the centre and
3. it afforded a 30% reduction in domain volume compared to the 45°sector with no discernible change to the flow field.

3.3.3 Inlet Development

The final design, designated DB25, can be seen in Figure 3-9 and includes a number of key design features such as the shaped nose and settling chamber arrangement. Again, the vane position is shown as a yellow box. A green box indicates the presence of a lip feature. The red boxes enclose the double baffle arrangement. This design was selected based on performance against three criteria: axial velocity distribution at one NGV chord upstream of the NGV LE, total pressure loss and overall length. Other criteria, such as total pressure distribution, flow angle distribution and peak tangential velocity were also considered where necessary. Key families of designs and the progression between designs are shown as a flowchart in Figure 3-11.

Figure 3-10a presents the non-dimensional axial velocity profile (w/w_{mean}) against non-dimensional span ($(r-b)/s$) for three designs, with RD1 shown in black. Negative w/w_{mean} corresponds to a region of recirculation or separation. The flow field for the baseline RD1 (profile shown in Figure 3-7) design was dominated by a region of separation downstream of the transition from radial flow to annulus flow extending to 37.5% span. This was accompanied by a region of accelerated flow near the shroud where the peak

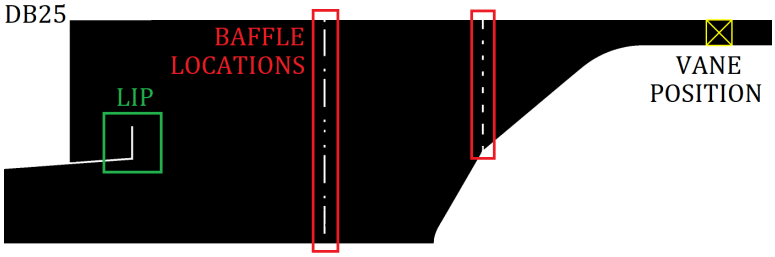

Figure 3-9: DB25 inlet design

velocity reaches over 3.2 w_{mean}. In addition to the large pressure drop experienced by this arrangement, this makes the radial diffuser an unacceptable design.

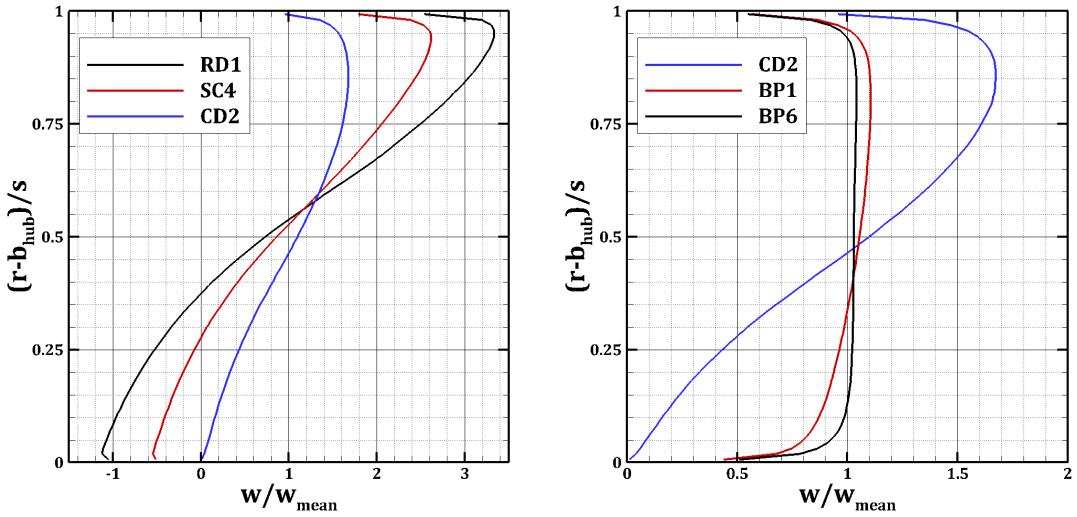

Figure 3-10: Effect of (a) settling chamber and diffuser and (b) baffle plate on the radial distribution of axial velocity

The first extension to the baseline RD1 was the addition of a settling chamber, as shown in Figure 3-11. No attempt was made to reduce the incoming jet velocity prior to discharge into the settling chamber. This discharge velocity remained high and although the velocity profile improved, the design was still not acceptable as it displayed recirculation at the measurement plane. This can be seen in the non-dimensional axial velocity profile for SC4 plotted in red in Figure 3-10a, where the recirculation again reaches above 25% of span. The magnitude of this reversed flow is significantly reduced, as is the accelerated flow near the shroud. The pressure drop also remains high for this design at ~9 kPa.

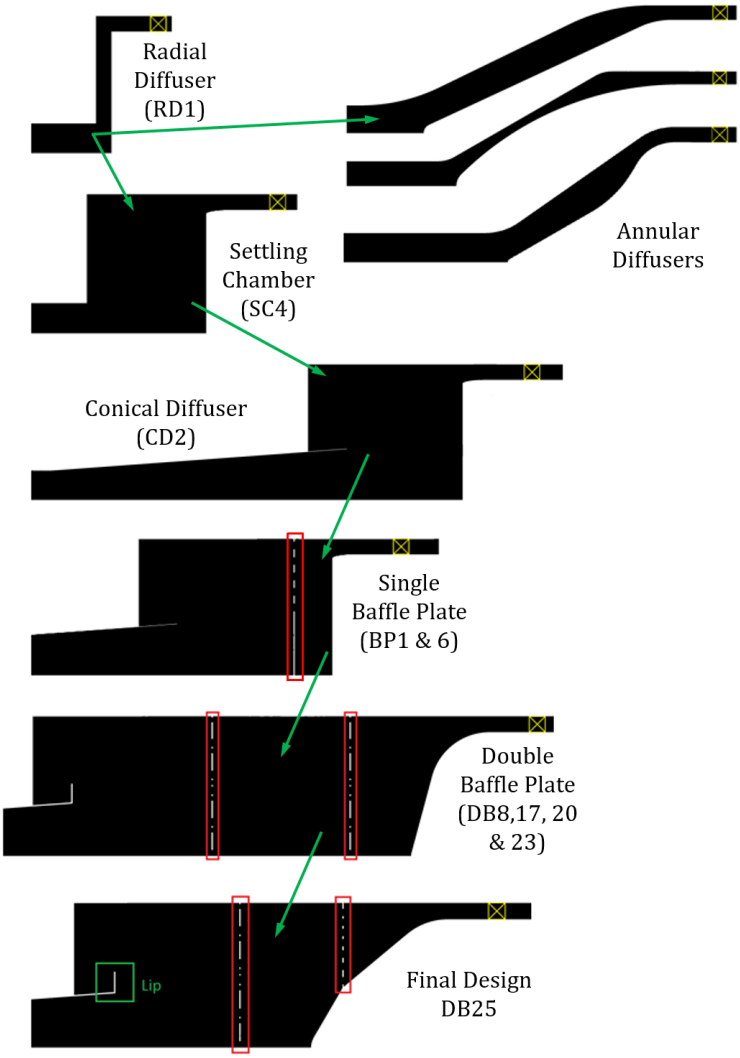

Figure 3-11: Inlet design families

Figure 3-11 shows the conical diffuser extending to the left of the inlet which was used to reduce the air velocity in the pipe. Sovran and Klomp [100] provide guidelines for efficient conical diffuser design to avoid separation. They define diffuser performance in terms of inlet area, outlet area, working length and inlet radius. Using an inlet to outlet area ratio of three to obtain an exit jet velocity of one third inlet velocity, a non-dimensional length of 10 is required. The introduction of the diffuser significantly improved the total pressure loss, reducing this to ~2 kPa while the diffuser discharge velocity was found to be ~25 m/s. This produced a concordant improvement to the velocity distribution and can be seen for CD4 shown in blue in Figure 3-10a. No recirculation is present as the velocity

profile remains positive across the span. This in turn reduces the velocity at the shroud, though the peak velocity is within the outer 20% of the annulus.

A single baffle, highlighted in red in Figure 3-11, with a blockage ratio of 0.5 was found to provide another improvement to velocity distribution. This is evidenced by the red solid curve for BP1 in Figure 3-10b, while the BP1 profile is shown in Figure 3-12. Modelling the baffle plate using large holes (⌀ 20 mm), allowed for the the total hole count to be kept low in order to reduce computational cost. Figure 3-10b reveals that a velocity peak remained at around 80-85% span. This was improved somewhat by addressing the recirculation present behind the baffle plate using a contoured or shaped nose (Figure 3-13) to direct the flow. While the overall length was short (less than 1.4 m) the complicated nose shape was considered to be a costly feature and alternatives were sought. The total pressure loss for the baffle plate designs was found to be 1.3 to 1.8 kPa.

Figure 3-12: Bluff nose inlet

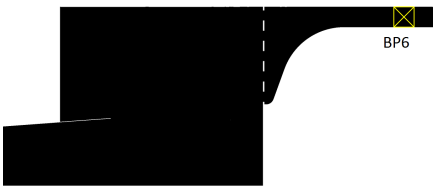

Figure 3-13: Shaped nose inlet

Doubling the length of the settling chamber facilitated the introduction of a second baffle plate as seen in Figure 3-11. This was found to improve the velocity profile slightly, providing a smoother profile with a peak at 25% span (curve DB8 in Figure 3-14a). An unexpected benefit from the introduction of a second baffle was that total pressure loss reduced (11.9%), however, this was at the expense of a 50% increase in total length. The positions of the baffles relative to each other and the diffuser exit were found to have a detrimental effect when the separation between the features became small, though increasing the spacing to fill the envelope did not provide a completely acceptable solution.

By combining the double baffle and the shaped nose of BP6, a series of composite designs were produced. Initially, a single angle cone was introduced with the baffle at the half way point (DB17) though this produced an unacceptable velocity peak near the hub (15% span, Figure 3-14b). Setting the up- and downstream cone angles to different values (as can be seen in Figure 3-9) allowed the velocity profile to be tuned and progressively improved. The final three successful designs (DB20 – large blend radius to annulus, DB23

– small blend radius, and DB25 – small blend radius with a diffuser lip) showed that no further improvement could be obtained for the velocity profiles (Figure 3-14b). These three designs gave a velocity profile with a slight bias towards the shroud with the peak velocity lying at $(r-b)/s = 0.6$.

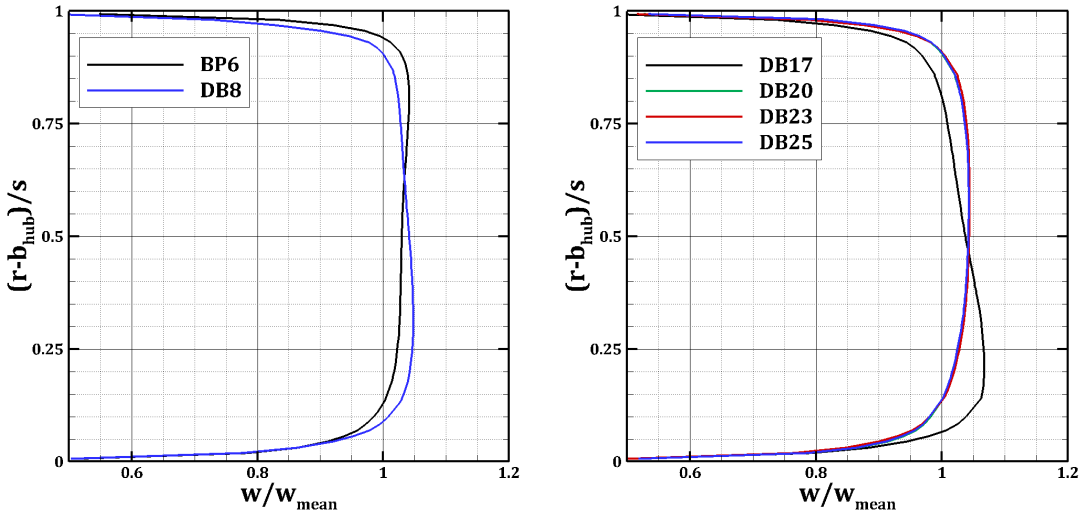

Figure 3-14: Effect of (a) double baffle and (b) shaped nose on the radial distribution of axial velocity

Of these three final designs, DB20 did not provide a meaningful benefit for the increased overall length, achieving a total pressure loss of 1.2 kPa. DB23 and DB25 differed in the presence of the diffuser exit lip, which was found to allow the jet to continue expansion in the first settling chamber by altering the recirculating flow pattern. Both designs achieve a total pressure loss of 1.16 kPa. The presence of the lip was found to be beneficial for manufacturing purposes and thus DB25 was selected for the final design.

3.4 Inlet Validation

Full details of the calibration and commissioning experimental campaign are published in the open literature in [14] with some key results presented here for completeness. Experimental validation (Figure 3-15) of the inlet design was possible with the final DB25 design being taken forward for manufacture early on in the project cycle.

The metric for pressure loss was not replicable in the rig due to limited access for

total pressure measurements outside of the annulus region. However, steady total pressure data was obtained one axial chord upstream of the vane leading edge in order to assess the flow conditioning and to characterise the boundary layer. A radial traverse was performed using a Pitot probe connected to a differential pressure transducer, both with and without a turbulence grid in place. Additional boundary layer velocity data was obtained using a hot-wire probe, however, this was taken with the turbulence grid in place and thus does not present a fair comparison with the CFD as it introduces additional velocity deficit in the near hub-wall region. The hot wire data was used to confirm the profile found for the case with the turbulence grid in place and showed good agreement with respect to the near hub-wall velocity deficit region, giving additional confidence in the total pressure data.

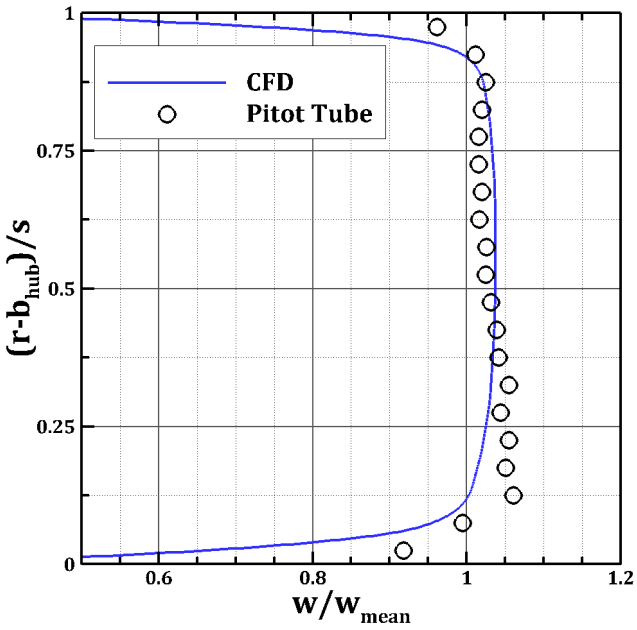

Figure 3-15: Radial distribution of axial velocity

Validation of the CFD and design was assessed using the Pitot tube measurements of the radial distribution of axial velocity one axial chord upstream of the NGV LE, without the experimental turbulence grid installed as no turbulence grid was modelled in the simulations. Remote from the wall, the CFD results presented in Figure 3-15 demonstrate good agreement with the pitot tube data with deviations of less than 10%. The computed mass flow rate differed from the measured mass flow rate by less than 1.8%. However, Figure 3-15 indicates that the velocity profile in the near hub-wall region is not exactly captured, suggesting that the use of wall functions was not fully justified. The slight bias towards

the hub-wall was unexpected and shows that the DB25 overcorrected the shroud bias in the velocity profile present in early designs. The key criteria of a flat velocity profile for the LAR was achieved and the measured turbulence intensity at the vane LE was determined to be 5% [14], with the profile shown in Figure 3-16.

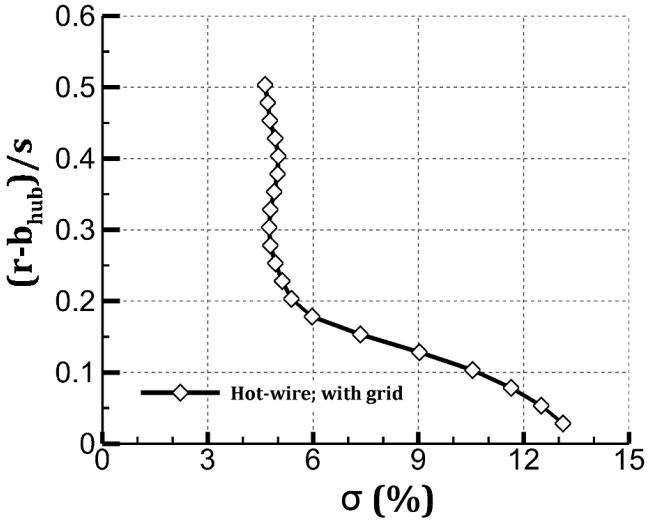

Figure 3-16: Radial distribution of turbulent intensity, adapted from [14]

3.5 Summary

The LAR is a new experimental facility at the University of Bath, forming part of a global Siemens research effort and is the focus of this body of work. Turbine vane and blade geometry has been taken from an industrial design, scaled to enhance secondary flow structures in this low-speed rig. A turbine rim seal of a double-lip arrangement is present between the stator vanes and rotor blades, where purge flow egress can exit the wheelspace into the annulus. This purge flow can be tracked using PLIF, while the velocity field can be imaged using VV.

An inlet has been designed for the LAR using CFD, starting from a simple baseline with the aim of reducing total pressure loss and providing a flat velocity profile at the vane LE. The diffuser section was introduced to reduce incoming velocity, while a settling chamber reduced pressure losses. Baffle plates were introduced to further improve the design before a shaped nose was used to fine-tune the velocity profile. The selected design was validated using experimental data obtained during rig commissioning and was found to perform as per expectations.

Chapter 4

Computational Method

4.1 Solver

The calculations undertaken for this research employed the commercial CFD package *ANSYS CFX 17.0*. This package is used widely in the published turbomachinery literature, with examples such as [65, 67, 101, 102] relevant to this study of rotating turbomachinery. *CFX* is a Reynolds-Averaged Navier-Stokes (RANS) solver for both steady-state and unsteady (URANS) calculations. Unless stated otherwise, all results presented in this thesis are time-averaged variables obtained from URANS calculations.

CFX uses the finite-volume method for the solution of the governing NS equations and any applicable scalar transport equations. The spatial domain is discretised using a computational mesh, which is used by the solver to create finite volumes as shown in 2D in Figure 4-1. The nodes or mesh vertices are the storage locations for all variables and fluid properties. The vertex-centred or cell-vertex control volume approach employed by *CFX* has both advantages and disadvantages when compared to the cell-centred approach used by *Fluent*. While the discretisation accuracy of both approaches is second order or higher accurate on smooth grids, only a vertex-centred approach maintains first order accuracy on distorted grids [103]. The cell-centred approach depends on the smoothness of the grid, as distortion can cause face midpoints to fail to lie along the line joining cell centres, affecting the calculation of averages and fluxes. In contrast, a cell-centred scheme has discretisation advantages at boundaries as the control volume respects the shape exactly. For calculations on the same size mesh, the vertex-centred approach has fewer degrees of freedom [103,

104], which is computationally less costly in CPU time and memory allocation. Morton and Sonar [105] note that cell-centred approaches result in more reliable shock capturing.

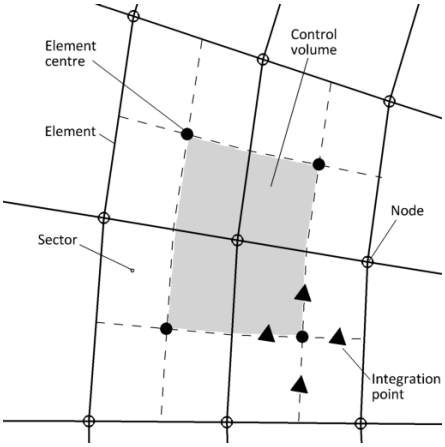

Figure 4-1: Vertex-centred control volume (2D)

CFX discretises the integral form of the NS equations using integration points for surface integrals and sectors for volume integrals. The surface and volume integrals are locally conservative using this method. The integration of the advection term requires that the solution variable at the integration point be approximated using the data stored at the nodal locations. The general form for this approximation at an integration point for a scalar, ϕ, can be written:

$$\phi_{ip} = \phi_{up} + B\nabla\phi \cdot \vec{r} \tag{4.1}$$

where ϕ_{up} is the upwind node value, $\vec{r}$ is the vector from the integration point to the upwind node. The choice of B, a weighting, and $\nabla\phi$, the scalar gradient calculation, can be varied to give a number of numerical schemes. The choice of B $= 0$ results in a first order upwind difference scheme, while B $= 1$ gives a second order central difference scheme. The former is robust but causes diffusive errors that smear sharp gradients. The latter combats the diffusion error but introduces dispersive errors or oscillations to the solution. This does result in a scheme which is not strictly second order accurate, however.

The *CFX* High Resolution Scheme first computes maximum and minimum values for the solution variable at all nodes surrounding the integration point, using a specified stencil. Then equation (4.1) is solved for B for each integration point surrounding a node, in order to prevent oscillatory behaviour. This allows the value of B to be as close to one as possible, while avoiding creating extrema. This combats the issues of both upwind and central scheme, providing *up to* second order accuracy while remaining non-oscillatory in

nature. In one-dimensional situations, the scheme can be shown to be Total Variation Diminishing [106].

CFX utilises a co-located grid, providing identical control volumes for all transport equations. Decoupled solutions can arise from this methodology if implemented without redress. Here, a pressure-redistribution term is used to modify the continuity equation discretisation to prevent a chequerboard solution. Spurious velocity fields can still arise from this formulation in cases where discontinuous body-forces are present, such as free surface interfaces or porous region boundaries.

A Second Order Backward Euler scheme is employed for the transient terms. This scheme is robust, implicit and conservative in time. The scheme is second-order accurate in time and no limit is placed on the time-step size. However, the scheme is not bounded which can lead to non-physical solution oscillations. A modified scheme is used for quantities where boundedness is required, for example volume fractions. The first timestep of a transient calculation employs a first order scheme, with each subsequent step using the second order scheme.

All equations are solved as a single system, known as a coupled solver, utilising a fully implicit discretisation of the equations for all timesteps. In transient calculations, all non-linear equations are linearised and solved using an Algebraic Multigrid (AMG) method. The AMG is employed to accelerate and improve the behaviour of the matrix inversion technique, with iterations being carried out on progressively coarser (virtual) grids. The solution is then passed back through the grid levels to the original grid. One significant advantage of this is the reduction in errors with longer wavelength than the original grid size, due to the change in grid size with iteration. Coarse, virtual grids are created through the summation of finer grid control volumes, while the linearisation is only performed for the finest grid. This is computationally efficient. This process is iterated within the physical timestep and then advanced to the subsequent timestep. In steady-state mode, the timestep is a pseudo-time parameter acting to guide the solution and reduce the number of iterations required for convergence.

4.2 Model and Domains

The computational model is broken down in to two discrete regions, based on the frame of reference as follows: the stator or S1 (red in later figures) is a stationary frame of reference

(no model rotation); the rotor or R1 (blue in later figures) is placed in a rotational frame of reference. For this work, this ensures that the wheelspace and seal geometry are always contained in the rotating frame (R1) and thus avoids a known issue in *CFX* where β and ingress of mainstream gas was incorrectly predicted for steady-state computations. This is achieved by locating the stator-rotor interface 0.2 c_{NGV} downstream of the NGV TE and 0.079 c_{NGV} upstream of the stator hub platform TE.

Additionally, this removes the sliding plane domain interface from the regions of expected unsteadiness. The implementation of mesh connections within *CFX* allows for both matched and non-matched node positions on connected mesh faces. In the current study, a matched node interface was not possible for two reasons:

1. the periodic faces for S1 and R1 were generated in different software, leading to a geometric difference and;
2. the circumferential cell count would match only one timestep in transient calculations, preventing an accurate analysis of temporal resolution.

The sliding plane interface between S1 and R1 is thus of the non-matching type known as a General Grid Interface (GGI) in *CFX*. At the beginning of each timestep, the relative position of both sliding faces is computed. Surface fluxes are then discretised along both sides (local and interface) of the mesh face, giving rise to balance equations between the nodal (local) variables and control surface (interface) variables. Where a cell face overlaps with more than one control surface, a weighting factor is applied to the fluxes. The resulting set of linear equations is solved to provide nodal variable values that are conservative in nature, however, some data resolution is lost. Thus placing the interface upstream of the regions of expected unsteadiness (in the seal gap and near the rotor platform leading edge) ensures that no resolution is lost in regions of interest.

The NGV to RB spacing is 0.5 c_{NGV} to allow for instrumentation access in the experimental facility. The sector size was chosen to take advantage of the 2-3 periodicity of the vanes and blades, resulting in a matched 30° sector. The numerical error associated with the treatment of a non-matched pitch leads to a large decrease in accuracy and can lead to non-physical transient interactions. Additionally, calculations were performed on a double sector domain (60°) to test the impact of a larger sector and justify this choice. Results from these calculations can be seen in Section 4.6

In order to develop understanding of the flow physics occurring during mainstream-egress interaction, a number of different computational models of increasing complexity were utilised. The simplest computational domain features only the main gas path (MGP) with no egress flow or seal geometry included, referred to here as the Annulus Domain (AD). This domain was primarily used for testing the boundary conditions and model parameters, as well as for some early grid validation studies. Some results from this domain are presented in Chapter 5 in order to quantify the undisturbed secondary flow field, free from all flow effects due to the seal and wheelspace geometry such as disc pumping [37].

The first extension to the computational domain was the inclusion of a chute representing the outermost part of the rim-seal as shown in Figure 4-2, referred to as the Chute Domain (CD). This development facilitated the introduction of egress flow from below the hub. This significant simplification of the physical arrangement limits the influence of the main gas-path flow field on the egress plume. Here, the purge gas inlet is an annular plane of height 1.5 mm at $r/b = 0.98$ and a single axial location. An axisymmetric velocity profile with appropriate β was applied to the inlet.

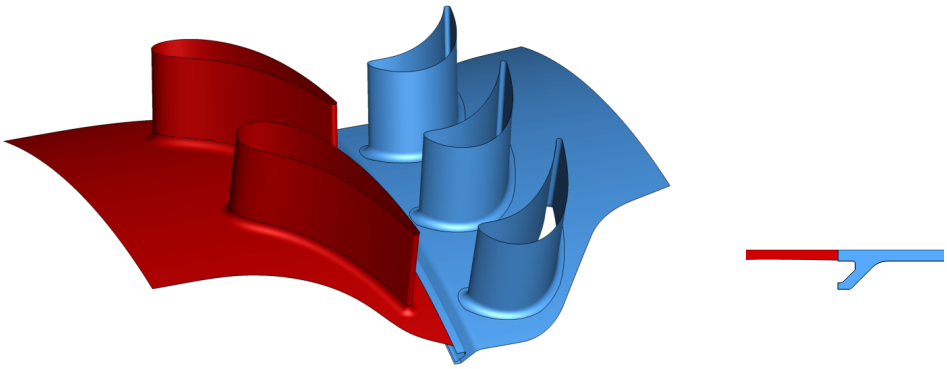

(a) **(b)**

Figure 4-2: Chute Domain (CD) (a) Isometric and (b) Elevation views

A further extension of the model is shown in Figure 4-3, which includes both the outer chute and double lip rim-seal; this model is designated as the Stub Domain (SD). While still a simplification of the physical test rig, it is a more accurate representation of the region where the purge-mainstream interaction occurs. This is essential for the purposes of this research as the interaction phenomena must be accurately and physically resolved to allow for robust endwall designs to be implemented.

By including the inter-seal gap, significant distortion of the velocity field at and below $r/b = 1.0$ occurs, with damping of pressure fluctuations taking place in the enclosed volume. This is due to the velocity field at $r/b = 0.98$, in the seal chute, becoming distorted and indicating that the placement of the SD purge inlet moves the interaction zone further in to the seal. The purge inlet is again an annular plane of height 1.5 mm at $r/b = 0.92$ and a single axial location. Again, an axisymmetric velocity profile was applied at the inlet with representative β taken from Full Wheelspace Domain calculations (see below).

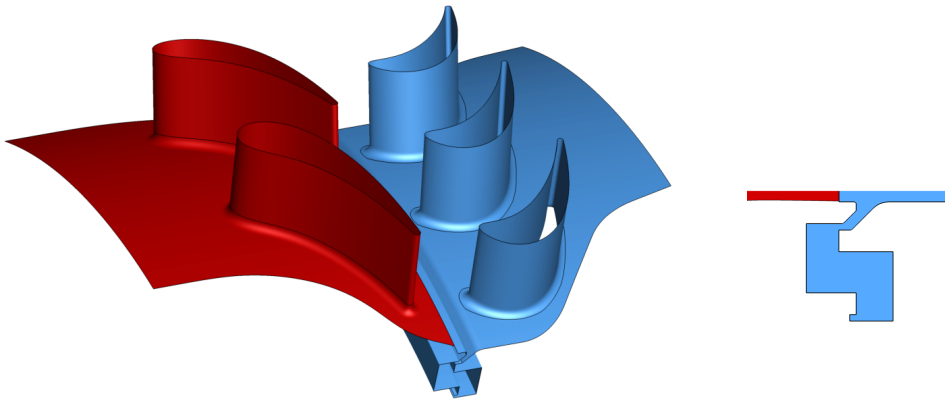

(a) **(b)**

Figure 4-3: Stub Domain (SD) (a) Isometric and (b) Elevation views

The Full Wheelspace Domain (FWD) was an extension of the model including the wheelspace below the double-clearance rim-seal, terminating at the inlet seal at the base of the wheel-space, as shown in Figure 4-4. In this arrangement the purge inlet is formed by a cylinder at $r/b = 0.65$ with an axial extent of 2 mm. This is the mid-height of the so-called inlet seal, a physical feature of the rig that allows Couette flow to develop before entry to the main wheelspace. The test rig extends below this inlet seal, where the purge flow is fed through a 2 inch pipe at the bore of the stator disc. This was modelled separately in order to provide a velocity profile for the purge gas at entry to the FWD (Section 4.3.3); these simulations also confirmed Couette flow conditions at entry to the wheel-space.

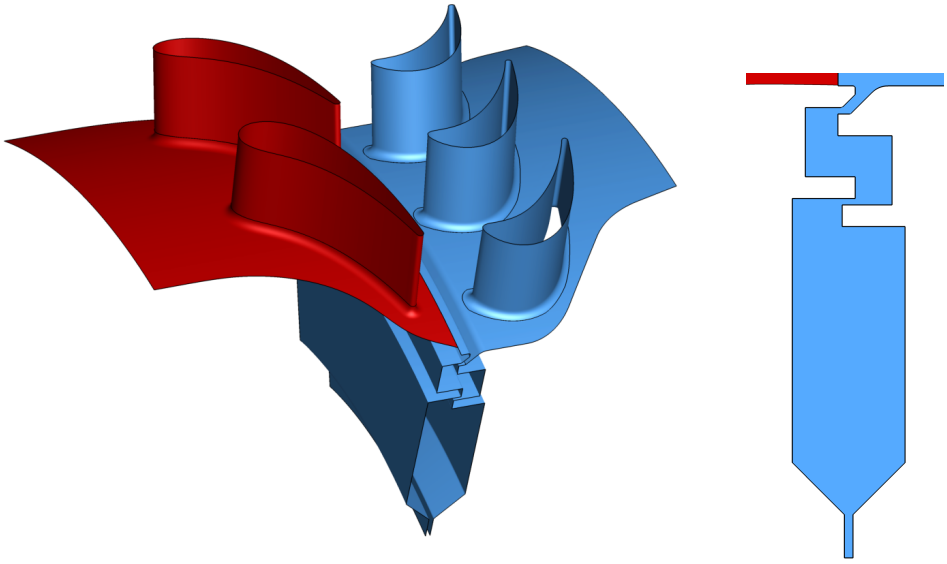

(a) (b)

Figure 4-4: Full Wheelspace Domain (FWD) (a) Isometric and (b) Elevation views

4.3 Boundary Conditions and Setup

Specifying well-posed boundary conditions presents a challenge to any CFD study. For this work, no experimental data was available until late in the program, requiring reliance on industrial best-practice and robust initial testing of the computational model. Typical turbomachinery applications consist of single inlet, single exit problems and this forms the starting point for the problem at hand. The operating conditions for the LAR have been discussed previously (Section 3) and from this data and the known annulus area, mean velocities can be calculated. Similarly, based on the blade geometry, rotational speed and assuming exhaust to ambient, the pressure drop across the stage can be estimated. Three preferred combinations for inlet and outlet exist [95]:

1. mass flow rate and total temperature specified at inlet, average static pressure specified at outlet;
2. total pressure and temperature at inlet, average static pressure at outlet;
3. total pressure and temperature at inlet, mass flow rate at outlet.

Each of these has advantages and disadvantages. The first is recommended by *ANSYS* literature as the most robust. Here, the mass flow rate is known and an average static

pressure at the outlet can reasonably be estimated. If needed, velocity and temperature profiles can be specified at the inlet. The total pressure at inlet and pressure drop across the stage is an explicit output of the solution.

The second is sensitive to the initial estimate of inlet total pressure, which must be determined *a priori* by hand calculation or from rig data (if available). If the calculation is inaccurate, the solution mass flow rate will be incorrect and might need to be re-run with an adjusted inlet condition. However, this is a physically realistic combination as the mass flow rate will not be controlled at, or even close to, the rig.

The third combination is somewhat sensitive to the initial estimate for total pressure, but avoids the possibility of needing adjustment. This would be difficult to obtain experimental data for as the measurement of mass flow at the outlet would need to be inferred from upstream data. In addition, the extra mass flow from the purge would need to be included.

For the reasons listed above, and in collaboration with industrial partners, the second option was selected and implemented. At the main gas inlet shown at left in Figure 4-5 the total temperature, CO_2 mass fraction (MF) and turbulence intensity were prescribed. The total pressure profile, obtained from the hot wire experiments of Jones *et al.* [14] was also applied at this inlet. This profile, shown previously in Figure 3-15, displays a relatively thick incoming boundary layer of nearly 15% of span. This was expected to increase the strength of the horseshoe vortex in the stationary domain. An average static pressure was specified at the outlet. Total mass flow rate was monitored at the outlet plane location for convergence purposes.

The purge gas inlet was prescribed a mass flow rate, total temperature, CO_2 mass fraction and turbulence intensity, again closely matching the actual operation of the LAR. Velocity profiles for the purge inlets were generated through the use of a separate calculation for the lower radius inner wheelspace, ensuring the correct swirl and momentum for fluid entering through this boundary. More detail on this can be found in Section 4.3.3 below.

The annulus flow was modelled as air at 298 K and the purge flow was modelled as 100% CO_2, matching the expected rig conditions. This was realised in *CFX* using a multi-component mixture material for the fluid, allowing for a variable composition throughout the domain. The code calculates averaged physical properties for each control volume, according to the computed mass fractions for each component, and the velocity field is

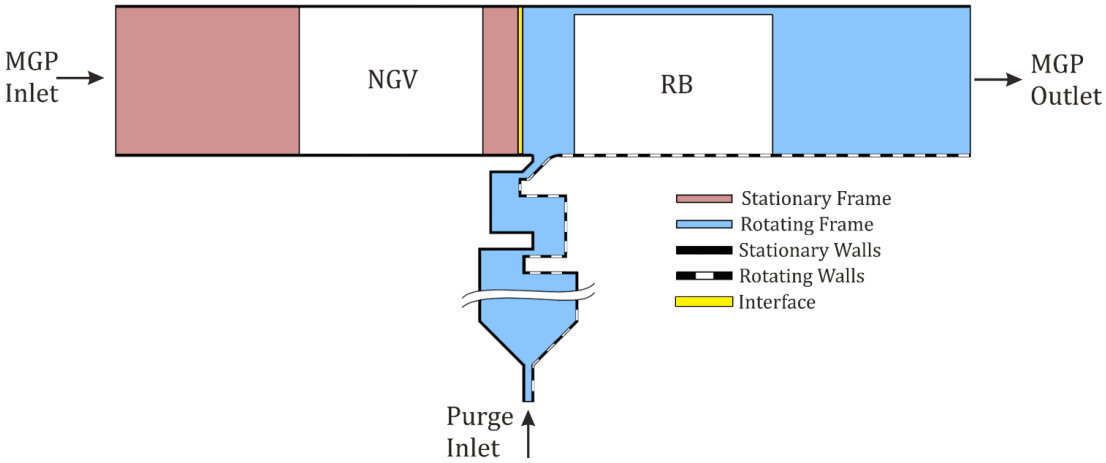

Figure 4-5: Boundary Locations

calculated for each component throughout the domain. The transport and diffusion are calculated for one component (in the present case CO_2); air then makes up the remaining mass fraction as a constraint.

Initial conditions for the time-marching calculations made use of steady-state flow field data. These steady-state results were obtained using a mixing plane interface between the domains. While frozen rotor calculations were found to reduce the initial transient when tested, these required significant additional computing time. A mixing plane breaks down the interface between domains into circumferential bands which are used for circumferential averaging of the fluxes. *CFX* treats the average static pressure for both upstream and downstream side of a band as the average band pressure. This approach can also be applied to the velocity (known as Stage Average Velocity constraint) or can be dealt with in total pressure terms (known as Constant Total Pressure constraint). Due to an implementation error in the specific version of *CFX* being used, the Constant Total Pressure option resulted in an incorrect flow field and thus could not be utilised for the calculations.

4.3.1 Turbulent Closure

Closure of the RANS equations requires a model for the Reynolds stresses (τ_{ij}), as introduced in Section 2.5. A wide range of models are available, with varying degrees of suitability for different flows. While a full analysis of all turbulence models is beyond the scope of this work, it is important to consider some of the models available and justify the selected model.

Wilcox [76] notes that turbulent kinetic energy models have come to dominate the field of turbulence modelling research since the 1960's. This class of model assumes that the Reynolds stress tensor can be modelled as some linear function of the mean rates of deformation. This is the assumption that action of the Reynolds stresses are analogous to those of the viscous stresses. For most two equation models, the Boussinesq approximation is used to relate the Reynolds stresses to the turbulent or eddy viscosity (ν_T), the strain rate tensor (S_{ij}) and the turbulent kinetic energy (k) as follows:

$$\tau_{ij} = 2\nu_T S_{ij} - \frac{2}{3}k\delta_{ij} \tag{4.2}$$

where δ_{ij} is the Kronecker delta. This equation contains three unknowns, however, eddy viscosity can be determined using k and a dissipation term. It should be emphasised here that the Boussinesq approximation assumes *isotropic* turbulence. The limitations of this assumption shall be discussed later.

The transport equation for k introduces the rate of dissipation of turbulent kinetic energy or the viscous dissipation rate (ε). An exact equation for ε contains further unknowns and unmeasurable terms, so it is desireable to model this using a transport equation. The $k-\varepsilon$ family of two equation models, originally developed by Launder and Spalding in 1974 [73], develop transport equations for ε in terms of existing variables. This leads to a set of closed equations (for continuity, momentum in the n dimensions of interest, energy, turbulent kinetic energy and viscous dissipation) with a number of adjustable constants for the latter two. These are complete models in that they do not require any additional or *a priori* data to be provided to the model [76, 77].

Pope [77] notes that the standard form $k-\varepsilon$ model is one of the simplest, complete models available and thus is applicable to a broad range of flows. However, while it performs admirably for simple flows, it is not suited for complex flows and can give rise to qualitatively incorrect flow patterns. Adverse pressure gradients cause the model to predict unreasonably high levels of turbulent shear stresses, leading to partial or complete suppression of separated flow regions. It is also poorly suited for near-wall flows in the standard form and can require wall-damping functions. The constants can be adjusted to more accurately predict the particular flow of interest but this is not a desirable characteristic for a complete model and model modifications have been proposed.

An alternative to the $k-\varepsilon$ family is the $k-\omega$ family proposed by Wilcox at the end of

the 20th century [73, 77], which replace the dissipation term with the turbulent frequency ($\omega = \varepsilon/k$). The transport equation for ω still contains constants. These models addressed the near-wall limitations of the $k-\varepsilon$ models, but introduced issues in the freestream region where both k and ω tend to zero, leading the eddy viscosity to become indeterminate. This limits the applicability of pure $k-\omega$ models to internal flows [77].

In order to address this shortcoming, Menter introduced a hybrid model known as $k-\omega$ SST [79] which allows for a transformation between the $k-\omega$ model near the wall and the $k-\varepsilon$ in the freestream. This model has been developed over time, with model constants becoming refined and more stable blending functions being introduced. The over production of eddy viscosity under adverse pressure gradient conditions and in wake regions remains, but production limiters can be used to improve performance [73].

All two equation models assume isotropic turbulence, that is the Reynolds stress tensor is symmetric and the effect of turbulence is the same in all directions as k is scalar. This cannot be guaranteed for all real flows of engineering interest and requires that the Boussinesq approximation be abandoned if anisotropy is to be resolved. Cases where this can occur are rotating flows and flows with strong streamline curvature. For this purpose, stress-transport models have been developed that contain a transport equation for each component of the τ_{ij} and directly accounts for the directional effects. This leads to six transport equations for the six unique components of τ_{ij}; a seventh equation is required for the length scale closure increasing the computational cost significantly. These models are known as Reynolds Stress Models and can address some of the shortcomings of one- and two equation models. However, extensions to the two-equation models exist to address specific shortcomings, such as the inability to deal with streamline curvature, without resorting to computationally costly models.

The standard form of two-equation models are generally insensitive to both streamline curvature and rotating systems. In order to address this, Spalart and Shur [107] proposed a modification to one-equation Spalart-Allmaras model. This entailed modification of the production term using an empirical function which varies between zero (in the case of stabilised flow with no turbulent production, such as convex curvature) and 1.25. The upper limit corresponds to cases with enhanced turbulence production or tight concave curvature. Smirnov and Menter [108] successfully applied this correction term to the $k-\omega$ SST model and showed significantly improved results for cases with streamline curvature (2D flow in a U-turn) and for flows with rotating frames of reference (centrifugal compressor). Results

produced with the curvature correction compared favourably with both experimental results and those produced with the more computationally costly Reynolds Stress Model. Those authors concluded that the correction was both computationally efficient and robust, adding a penalty of less than 1% to computational time.

The $k-\omega$ family of two equation models find widespread use in the turbomachinery literature, some pertinent examples are included here as further justification for the choice of model. These references also provide further justification for the choice of *CFX* for rotating calculations and *Fluent* for the stationary inlet study.

Georgiou *et al.* [92] investigated the aerodynamics of HSV development around a bluff body. This study did not consider rotational effects and made use of an open loop wind tunnel to collect experimental data at $Re = 2.6 \times 10^5$. The computational aspect employed *Fluent* and the $k-\omega$ SST model. THe authors reported that the HSV trajectory around the bluff body predicted by the CFD closely matched the experimental data. Further, Hawes *et al.* [56] used the Durham Cascade as a test case to computationally investigate blade root fillets. This research also employed *Fluent* and the $k-\omega$ SST model for the non-rotating cascade. The authors found that, in comparison with experiment, the yaw and loss coefficient data were not captured well in absolute terms, but the relative changes between geometries was comparable.

In a rotating frame, Coull *et al.* [101] studied the flow in an unshrouded turbine annulus in great detail using *CFX* with the $k-\omega$ SST model, focusing aerothermal performance of tip gap winglets. They report over prediction of heat transfer coefficients compared to experiment but consider the validation to be favourable as the correct flow physics are captured in the tip gap and main gas path. In a later study, Coull [109] utilised the HYDRA code with the k–ω SST model to study secondary flows for varying blade geometry. Validation of the numerical method used experimental from two sources, reporting less than 11% error in endwall losses.

Da Soghe *et al.* [102] applied *CFX* and various turbulence models, including $k-\varepsilon$ and $k-\omega$ SST, to the study of a rotating disc cavity. This geometry is similar to the study performed in Section 4.3.3. Turbulence model performance was compared with experimental velocity profiles. They conclude that the two equation models provide good agreement with experiment and that the $k-\omega$ SST model presents a good compromise between accuracy and cost.

The previously discussed studies by Poehler *et al.* [65] and Panchal *et al.* [67] applied both *CFX* and the $k-\omega$ SST model to the study of contoured endwalls. Snedden *et al.* [35] also used the $k-\omega$ SST model to this field. Further to this, Dunn *et al* [110] applied the $k-\omega$ SST model to endwall contouring using a URANS approach.

For the purpose of this research, turbulent closure is achieved through the use of Menter's [79] $k-\omega$ SST turbulence model. This is in accordance with the literature and the best practice of the industrial sponsor who desired that the modelling approach used should be replicable in any of their future design work. In order to combat some of the shortcomings of the baseline model highlighted above the following modifications were used. The Kato-Launder production limiter reduces the excessive generation of turbulent energy at stagnation points. The re-attachment modification addresses the under prediction of turbulent stresses in separating shear layers. The curvature correction modifies the production term to increase the sensitivity to streamline curvature.

4.3.2 Wall Functions

The presence of boundary layers near no-slip walls requires that the wall-normal grid spacing to be of sufficient resolution to resolve the boundary layer profile. The viscous effects on transport processes are large near the wall and the wall-normal variation in the flow variables is rapid. The most significant gradients [74, 77] occur within the first 20 to 30 turbulent length scales (δ_ν), in what are known as the viscous sublayer and buffer layer regions of the boundary layer. Further away from the wall a logarithmic layer is present where turbulent processes dominate. It is possible to calculate this length scale from the kinematic viscosity of the fluid and the friction velocity:

$$\delta_\nu = \frac{\nu}{u_\tau} \tag{4.3}$$

where

$$u_\tau = \sqrt{\frac{\tau_w}{\rho}} \tag{4.4}$$

which contains the wall shear stress and density. It is possible to calculate a Reynolds number for this length scale ($Re = u_\tau \delta_\nu / \nu$), which is unity. In order to present this in useful form, the turbulent length scale can be converted to a wall normal distance (y) through the use of the non-dimensional wall distance parameter or y^+:

$$y^+ \equiv \frac{y}{\delta_\nu} = \frac{u_\tau y}{\nu} \tag{4.5}$$

It can be seen that the form of y^+ is similar to the local Reynolds number, and at $y^+ = 1$, the wall normal distance is the same as the turbulent length scale and will be of the order 1×10^{-6} m. In order to resolve the boundary layer with a reasonable growth rate of 1.2 in the wall normal direction, a minimum of 13 cells would be required. The thickness of 13 near wall layers would be of the order 5×10^{-5} m. This causes wall-resolved grids to contain very large cell counts. In order to combat this, wall functions can be employed.

Wall functions, such as the Automatic Near-Wall Treatment implemented in *CFX*, take advantage of the logarithmic behaviour of the flow outside of the buffer layer. The boundary layer velocity profile can be reasonably approximated in this way, allowing the numerical computation of the shear stresses as a function of velocity and wall normal distance. In this way, the near wall spacing can be increased, modelling the high gradient regions with a relatively coarse mesh. The $k-\omega$ SST formulation within *CFX* employs Automatic Near-Wall Treatment, which are required to match the wall function to the AMG which changes the grid resolution. This enables *CFX* to smoothly transition from resolving the near wall gradients to modelling them as required. This wall treatment results in a solver that is insensitive to the choice of y^+.

4.3.3 Purge Inlet Profile

A separate CFD study was performed on the central plenum (Figure 4-6) to obtain useful velocity profiles to be used as a boundary condition for FWD simulations at the inner seal purge inlet. For this purpose, the plenum was modelled to the inner seal exit ($r/b = 0.68$), slightly beyond the desired profile location and an inviscid wall was implemented at the centre to avoid the vanishing angle at the centre as discussed in Section 3.3. Initially three, but later five grid levels (Table 4.1) were tested to obtain grid independence based on rotor torque. This was due to the intention to obtain accurate skin friction values for the torque, thus the finest mesh had $y^+ \approx 0.45$, though it was noted that the velocity profile did not change from the coarse grid level and the torque changed less than 0.2% from medium to extra fine.

Grid	cells	refinement ratio	y^+
very coarse	42 994	-	2.2
coarse	120 640	1.41	1.6
medium	345 600	1.42	1.0
fine	968 000	1.41	0.67
extra fine	2 711 632	1.41	0.44

Table 4.1: Central Plenum Grid Levels

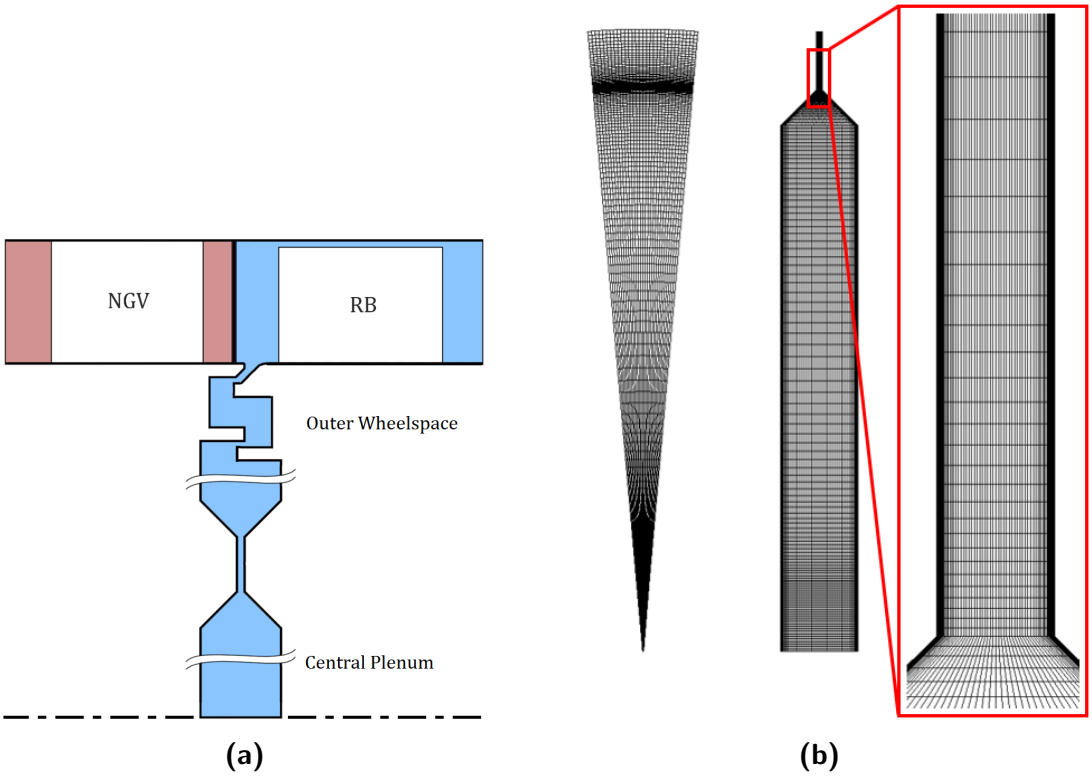

Figure 4-6: Central Plenum (a) location and (b) medium grid, axial and side elevation. Detail of inner seal in red.

A range of flow rates from $\phi_0 = 0$ through to the design egress condition of $\phi_0 = 0.134$ were calculated allowing velocity profiles to be generated using the medium grid. Figure 4-7 shows the profiles for circumferential velocity, normalised by the local surface speed of the disc, taken at $r/b = 0.68$ which lies within the inner seal. Figure 4-8 shows the profiles for radial velocity at the same location. Not shown is the axial velocity as this was a small fraction of the other two components.

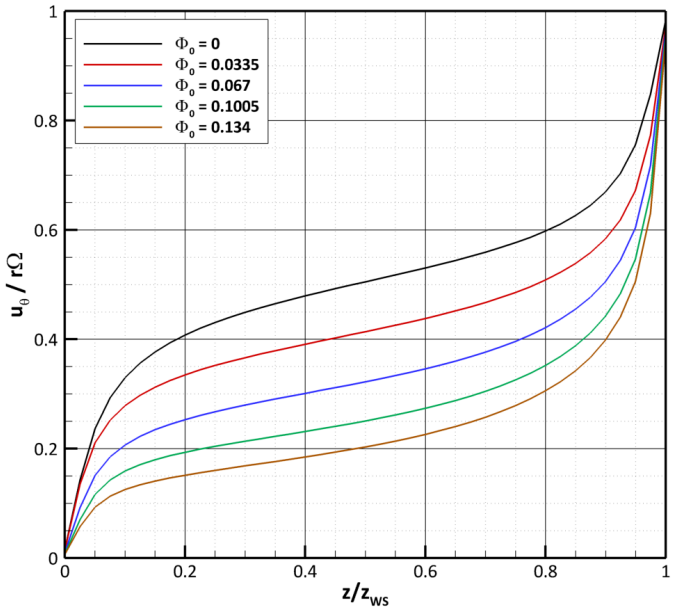

Figure 4-7: Axial Distribution of Swirl in the Inner Seal

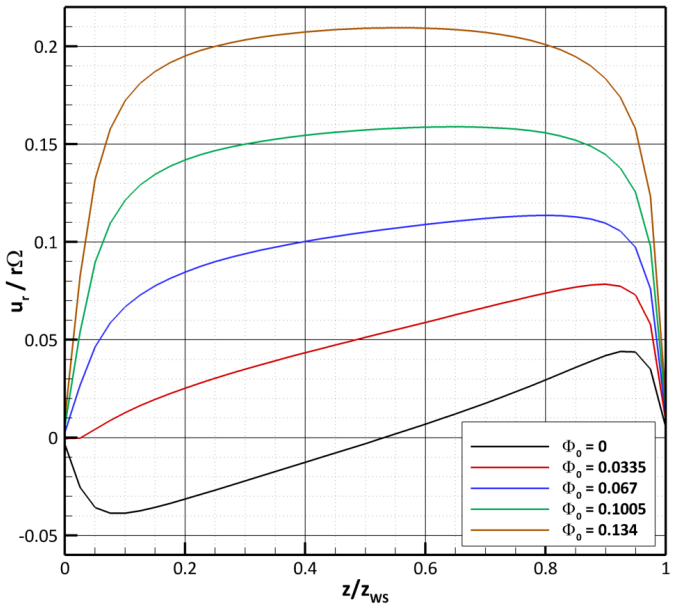

Figure 4-8: Axial Distribution of Radial Velocity in the Inner Seal

The case with no purge flow is shown in black in Figure 4-7, where the non-dimensionalised circumferential velocity or swirl ($\beta = u_\theta/r\Omega$) profile shows merged boundary layers with no core region and a mid-gap swirl ratio of $\beta = 0.5$. This is as expected for the small gap ratio ($G = 0.01$) and the local rotational Reynolds number ($Re_\phi = 8.5 \times 10^5$) when compared to Daily & Nece's [39] regimes and those detailed by Childs [37]. It can also be compared to the velocity profile for Couette flow, however, there is no analytical solution for turbulent Couette flow for direct comparison. Increasing the purge flow rate causes a decrease in the swirl at the mid-gap point, reaching $\beta = 0.2$ at the maximum flow rate, indicated by the tan line in Figure 4-7. This indicates that the tangential flow component is becoming dominated by the increasing radial component, as seen in Figure 4-8.

At zero purge, shown in black in Figure 4-8, the radial velocity profile shows radial outflow on the rotor and inflow on the stator. This matches the expected Batchelor flow profile for merged boundary layers as shown in Figure 2-7 and indicates that disc pumping is occurring. Increasing the purge flow rate superposes a radial flow to the profile, causing a small radial shift in the profiles seen in Figure 4-8, for example compare the black ($\phi_0 = 0$) and red ($\phi_0 = 0.0335$). At high purge rates, the flow becomes dominated by the radial outflow component, producing a velocity profile which more closely matches flow between two stationary plates. When considered in conjunction with the swirl, it can be seen that as the flow becomes dominated by the radial outflow, the circumferential component decreases.

4.4 Grid Generation

The computational domain takes advantage of rotational periodicity to reduce computational expense. With each vane passage repeating over 15° and each blade passage over 10°, a ratio of 2:3 results in a fully matched sector of reasonable size. However, this does limit the maximum size of the flow structures that can be resolved by CFD and thus places a limit on the solution in that flow structures that may be larger than 10 or 15° become locked to the sector size.

This is an important consideration. Jackoby *et al.* [111] performed full 360° simulations of a turbine wheelspace and found there to be large scale structures present, confirmed by measurements taken at the University of Aachen. This was characterised as a stable pressure disturbance with a tri-lobed appearance rotating at around 80% of the rotor speed,

which would require a 120° sector to resolve correctly. They found that the feature was only present at low purge flow rates, though this was dependent on seal configuration and geometry. It was decided that the increase in sector size required to resolve these structures would lead to an unacceptably large mesh for this project considering that they are not likely to be present at the high purge flow rates expected or with stub and chute domains.

Blocking topology around a blade depends on a number of factors, including turning angle and blade thickness. A number of topologies are possible that maintain 1:1 matching across periodic faces, here H- (Figure 4-9a) and J-grids (Figure 4-9b) are shown. The H-grid is simplest, retaining cell-ordinate direction throughout the blade passage, i.e. cells on the inlet face retain a 1:1 matching with their counterparts on the outlet face. Where a tip gap is present, this also retains 1:1 matching in that zone. However, for large turning angles very poor quality cells can be generated. To combat this, the more complex J-grid can be used. Here, the cells are turned around the blade at the LE, TE or both to enhance cell quality. Periodic matching is maintained from side to side, however, within the passage matching is lost. This poses a problem where a tip gap is present, requiring a non-matching interface to be created. This will result in a loss of information in this region.

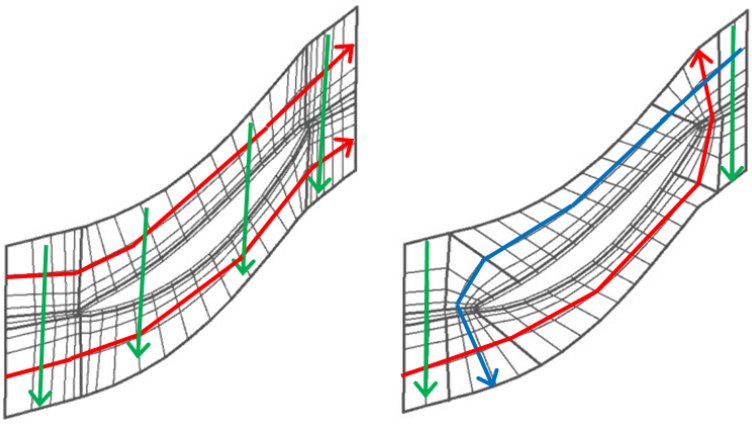

(a) **(b)**

Figure 4-9: Blocking Topologies: (a) H-grid and (b) J-grid, adapted from [95]

Stator grids (Figure 4-10) were generated using the NUMECA Autogrid software, which follows a block structured approach and has been developed specifically for turbomachinery applications. This package allows for relatively fast grid generation from minimal fixed data inputs through the use of on-board optimisation routines to improve mesh quality. H-grid topology was selected for the stator based on the low turning angle. A near-wall O-grid

region was implemented in order to capture the large gradients of the boundary layer. The vane root fillet utilised a butterfly grid arrangement, allowing the hub boundary layer blocks to transition smoothly in to the vane O-grid blocks without resulting in excessively skewed cells or a hard break line in the mesh. For the medium grid, the non-dimensional first cell height was set to $y^+ \leq 10$ throughout the main gas path. Cell counts in the radial (r), circumferential (θ) and axial (z) directions were 65 × 50 × 76, while the vane O-grid contained 18 layers.

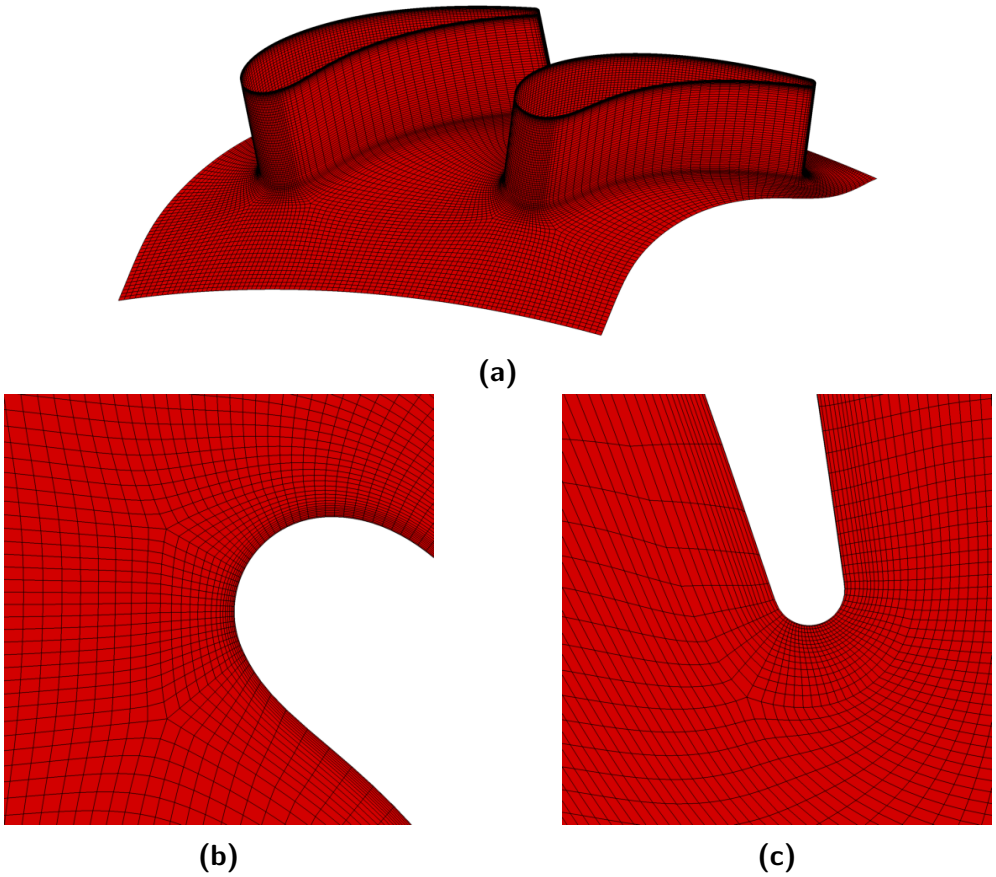

Figure 4-10: Stator surface mesh: (a) Isometric view, (b) LE detail and (c) TE detail

ANSYS ICEM v17, a generic multi-block grid generation package that accommodates both structured and unstructured approaches, was used to generate structured grids for the rotor domain (Figure 4-11). J-grid topology was used around the blade due to the high turning angle, which necessitated a non-matching generalised grid interface in the tip gap. This compromise was considered preferable to when compared to H-grid topology with no interface for cell quality reasons near the suction surface and in the wake region.

13 cells were placed in the tip-gap, with bunching at both solid walls to reflect the required resolution in the highly sheared and merged boundary layers. For the medium grid, the first cell height matched that of the stator at the hub and shroud, with 68 × 59 × 132 cell counts (r, θ, z). For all geometry below the hub, a $y^+ \leq 1$ was set, while in the annulus $y^+ \leq 10$ was achieved. The rotor grid also utilised a butterfly blocking structure to ensure continuity of boundary layer cells, containing 18 cells in order to match the stator mesh.

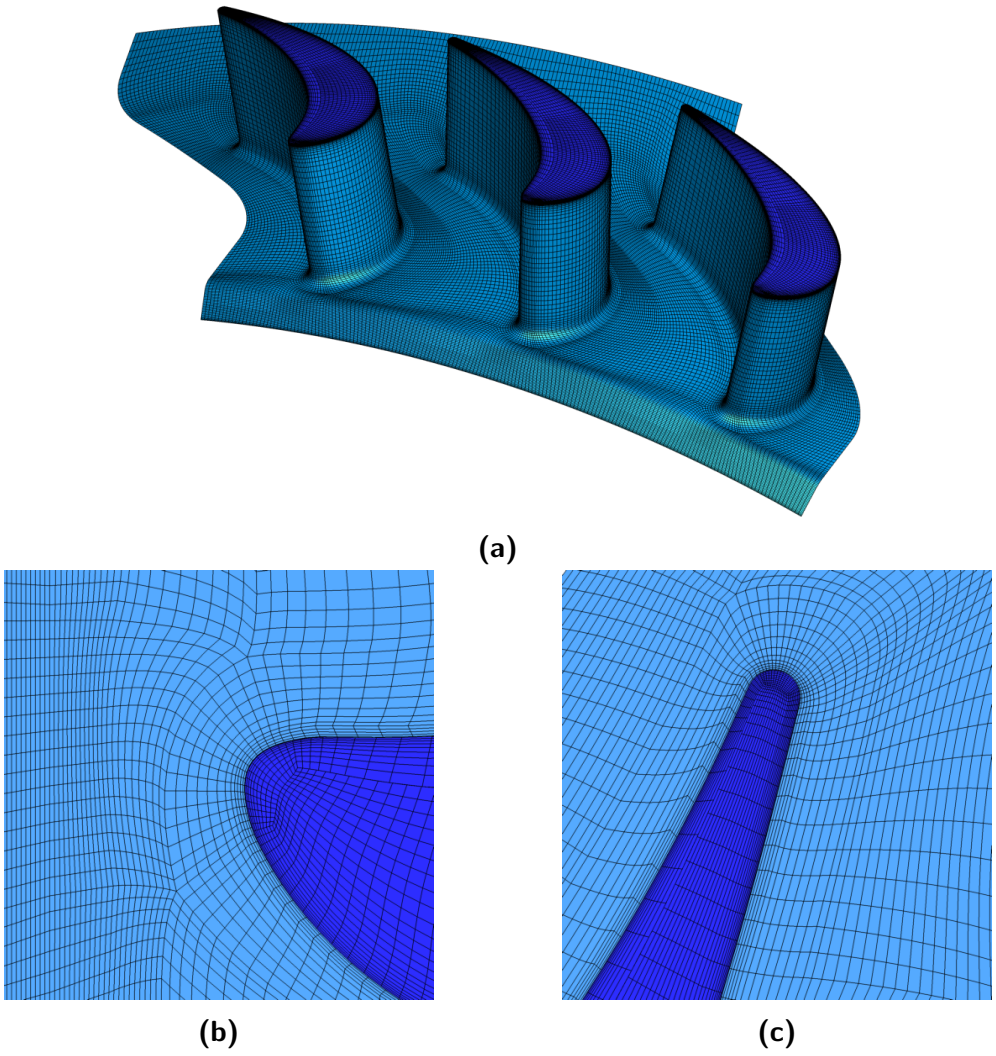

Figure 4-11: Rotor surface mesh: (a) Isometric view, (b) LE detail and (c) TE detail

The rotor wheelspace provided a meshing challenge due to the smooth transition between seal and hub, designated X in Figure 4-12. Here, the two surfaces intersect with an angle of 45°. The interaction of a boundary layer capturing block in proximity to

the wall in both the wheelspace and the annulus can be handled in one of two ways:

1. the blocks can pass through one another, remaining separate, used where two walls meet at or close to a right angle or join at a heard break;
2. the blocks can form one continuous near-wall block, used where the walls intersect at an angle approaching zero or a smooth transition.

As can be seen from the figure, both of these cases have merit. The angle is not close to zero which points to option 1, yet the transition is smooth pointing to option two. In order to avoid poor quality cells near the wall in this region, option two was chosen, although this causes some cells immediately adjacent to the boundary layer blocks to be skewed up to 45°. This option choice results in continuity of the near-wall block from the seal through to the blade tip. One unavoidable side effect of this continuity was the constraint that the boundary layer blocks all contain the same number of nodal points. In order to ensure a constant y^+ and growth rate in the annulus, the block height became a fixed parameter. At the transition point, X, however, the block height required reduction to ensure the required y^+ could be achieved in the wheelspace. Thus between the cylindrical annulus hub immediately above X in 4-12 and the transition to the conical surface of the chute, the y^+ reduced rapidly from ~10 to 1.

Three grid levels were generated using the blocking structure outlined above. Initial steady-state testing on the AD informed the cell count for the medium grid annulus, which was then refined and coarsened to obtain the additional grids. Extending the grid into the wheelspace maintatined the pitchwise cell counts. Due to the use of wall functions, the first cell heights were maintained across the grid levels. Stern's [96] guidelines were followed for refinement ratios, targeting $r = \sqrt{2}$ in each ordinate direction. This provides for a large step between grid levels while avoiding excessive cell counts. Take, for example, a unit cube with ten cells per edge. A simple doubling or halving of the count along each edge would provide grids with total cell counts as seen in Table 4.2:

cells per edge	edge ratio	total cells	grid ratio
5	0.5	125	0.125
10	1	1000	1
20	2	8000	8

Table 4.2: Unit Cube Refinement

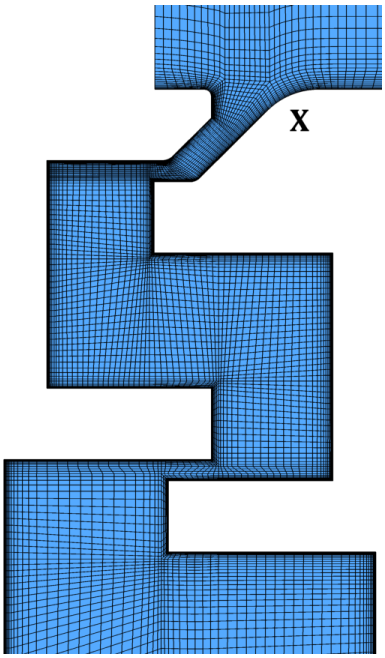

Figure 4-12: Wheelspace mesh detail

Thus the choice of a refinement ratio of two for three dimensional grids could result in grid levels that are either too coarse to reasonably resolve the desired flow features or too fine to compute in a timely manner. The final three grids used for the grid convergence study achieved $r \approx 1.4$, as desired, with cell counts and ratios can be seen in Table 4.3 below:

grid level	stator passage	blade passage	domain	refinement ratio	grid ratio
coarse	178 678	511 395	1 891 541	-	-
medium	505 412	1 557 564	5 683 516	1.45	3.03
fine	1 085 274	4 421 182	13 808 818	1.38	2.62

Table 4.3: Grid Level Details

Grid generation for non-axisymmetric endwall geometries for the rotor domain relied on the basic blocking structure developed for the baseline, above. The use of *ICEM* allowed for the surfaces that differed between baseline (Figure 4-13a) and non-axisymmteric (Figure 4-13b) cases to be imported directly to the existing model to replace, specifically the rotor hub, blade and blade root fillet. The adaptation of the surface mesh can be seen in Figure 4-13, where the root fillet position is changed due to the presence of a leading edge feature. Block nodes in the affected regions were adjusted where needed to maintain mesh quality.

Cell counts were not adjusted.

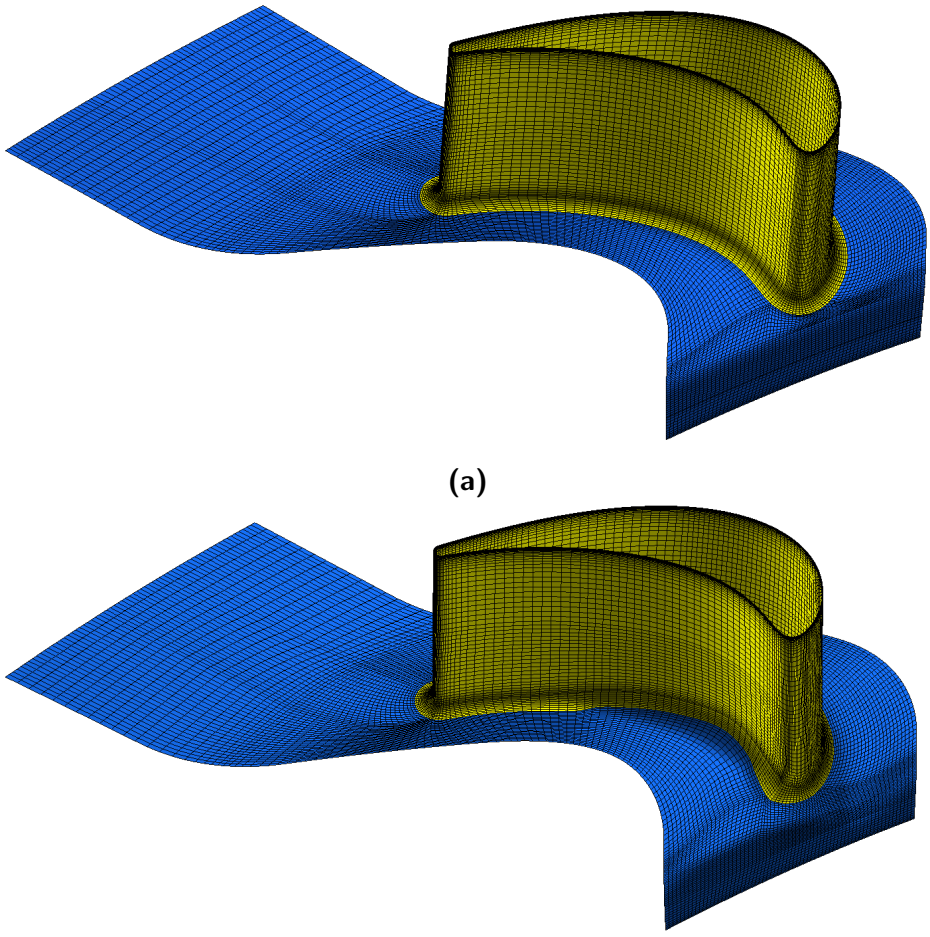

(a)

(b)

Figure 4-13: Surface mesh adaptation between (a) cylindrical baseline mesh and (b) typical contoured endwall

4.5 Validation

4.5.1 Grid Sensitivity

Grid sensitivity was investigated using the same approach as Section 3.3, that is Roache's GCI [97] and Richardson extrapolation, using the Stub Domain shown in Figure 4-3. The blending functions employed in *CFX* do complicate the GCI calculations somewhat as the solver is not *strictly* second order and at worst, the solver can be first order ($p_{solver} = 1.0$). The calculated order reflects this blending, with $p_{GCI} = 1.752$ being significantly lower than

second order. Typically, discrepancies between the scheme order and calculated order are due to grid quality and turbulence model effects. The parameter selected for the calculation of GCI is the stage efficiency (defined in equation 2.10) as this is the primary measure of endwall performance. As detailed in Section 4.4, three grids levels were generated, allowing the factor of safety to be set at 1.25. Details of these grids can be found in Table 4.3.

Steady-state, mixing plane calculations were performed for the three grid levels to establish grid sensitivity. The calculated GCI from coarse-to-medium was 0.394% and 0.117% from medium-to-fine. Figure 4-14 presents the Richardson extrapolated value in red and the computed stage efficiency values in black. The results are monotonic but show that an extension to finer grids could be beneficial, however, the additional computational cost was deemed prohibitive. It was deemed that the medium grid was an acceptable grid resolution to take forward to unsteady computations.

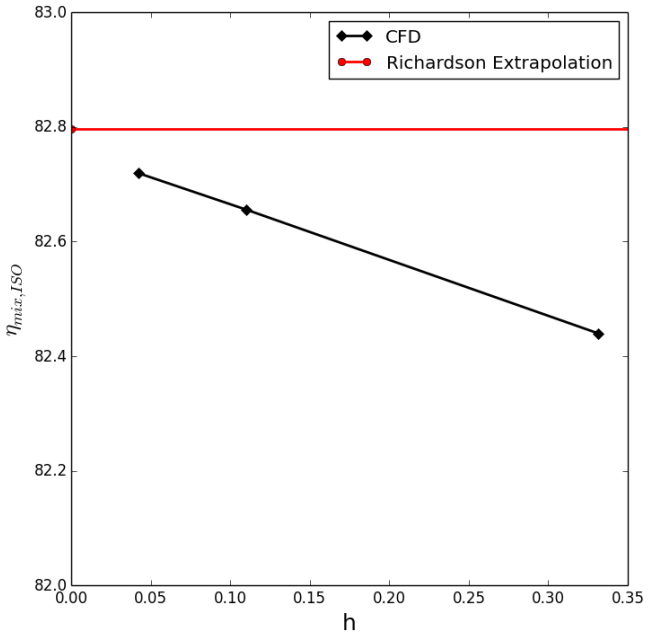

Figure 4-14: Grid Convergence

4.5.2 Iterative Convergence

Due to the iterative nature of CFD calculations, a determination must be made as to whether a calculation has reached a solution during an iteration before advancing to the next. For steady-state calculations, each iteration takes place in a pseudo-time step with the size of the step related to the cell size by the Courant-Friedrichs-Lewy number, starting

from some initial flow field. For a well posed problem, the initial flow field does not effect the final solution, only the number of iterations required to reach it. Iterative convergence can be assessed using the following criteria.

The difference in a flow field variable can be assessed between two iterations, this change is termed the *equation residual* and is typically scaled and normalised. *CFX* calculates residuals for a variable as the local imbalance of each control volume equation which is normalised using control volume coefficients and the range of the variable in the domain. This allows comparative analysis of residuals between the variables. Additionally, residuals are presented in both maximum and root mean square values which can then be compared to a desired target level or reduction. Steady-state calculations for this work, while used primarily as initial conditions for transient calculations, targeted maximum residuals of ~1 x 10^{-4} and RMS residuals ~1 x 10^{-6}. A typical residual trace taken from a grid convergence calculation can be seen in Figure 4-15. This shows an initial reduction in residual level over the first 1000 iterations, followed by a period of oscillatory residuals. This is typical of a simulation which has reached a converged solution in steady-state, but may have some unsteady or periodic behaviour inherent in the simulation. In this case the flow is expected to be unsteady, showing periodic behaviour due to the rotational nature.

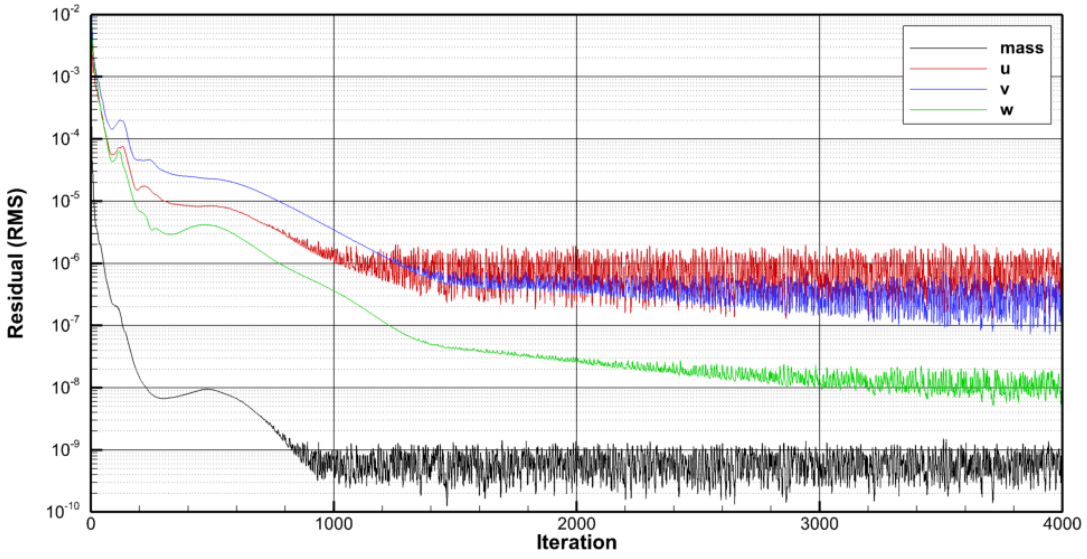

Figure 4-15: Steady-state Residual Behaviour

It is also desirable to monitor quantities of interest, tracking the change with each additional iteration. This is closely related to grid convergence, as a solution which has not converged *iteratively* cannot be accurately assessed for grid effects if the measure is

still fluctuating. The behaviour is typically an initial period of rapid change followed by a period of slow change. For steady-state calculations, the stage efficiency was found to be changing less than 0.01 percentage points per iteration within 100 iterations and less than 0.0001 percentage points from 750 iterations. This shows that using residual convergence is a more strict criteria for this problem.

4.5.3 Time-step Sensitivity

The medium grid and SD was used to assess timestep sensitivity. Grid sensitivity has well-established guidelines for assessment, such as the works by Roache [97], Celik *et al.* [98] and Stern [96]. Additionally, NASA provides online resources such as Slater's Examining Spatial (Grid) Convergence [112], based on the published work by Slater [113]. For temporal sensitivity, formal guidelines are less well established and thus a pragmatic approach is taken here. Four time-steps were tested, corresponding to 20, 40, 80 and 160 time-steps per blade passing period (bpp).

Each of the calculations was assessed against four criteria, both using stage efficiency as the quantity of interest:

- Time-averaged stage efficiency ($\bar{\eta}_{mix,ISO}$) assessed over one sector passing period at the end of one revolution,
- Number of revolutions required to reach periodic fluctuations,
- Frequency ($f/f_{\text{vane pass}}$) of unsteady fluctuations of stage efficiency compared to the expected frequency and
- Magnitude ($\Delta_{\text{peak to trough}}$) of unsteady fluctuations.

It was found that for the largest time-step, 20 steps/bpp, truly periodic behaviour was not achieved in the first five revolutions, after which the calculation was not progressed. This hinders the analysis of the data in Table 4.4 as only the frequency of the vane passing period was found to match the expected frequency. This did highlight a deficiency in the choice of time-steps tested: all levels were increasing harmonics of one another. In addition, the 2:3 matching of vanes to blades meant that any choice of an even number of steps/bpp would result in an exact frequency match. With hindsight, using prime numbers or at least odd numbers for the time-step levels might have been more informative for this activity.

steps/bpp	$\bar{\eta}_{mix,ISO}$	revolutions	f/f$_{\text{vane pass}}$	$\Delta_{\text{peak to trough}}$
20	80.21%	-	1.0	1.00%
40	80.47%	1	1.0	0.41%
80	80.48%	1	1.0	0.40%
160	80.48%	1	1.0	0.40%

Table 4.4: Grid Level Details

The 40 step/bpp case showed periodic behaviour within the first 1080 steps (Figure 4-16), with 1440 steps required per revolution. The instantaneous stage efficiency trace (black) shows an initial transient lasting half a revolution, followed by a quarter revolution of increasingly regular fluctuations. This is tracked by the rolling time-average stage efficiency (red), which can be seen to reflect the initial transient. There is a slow excursion at the half revolution mark where the time-averaged value drops below the final settled value, with the step-to-step change being of the order 0.002 percentage points. The time-averaged value at iteration 1440 (i.e. the end of the first revolution) is within 0.001 percentage points of the value at iteration 2880.

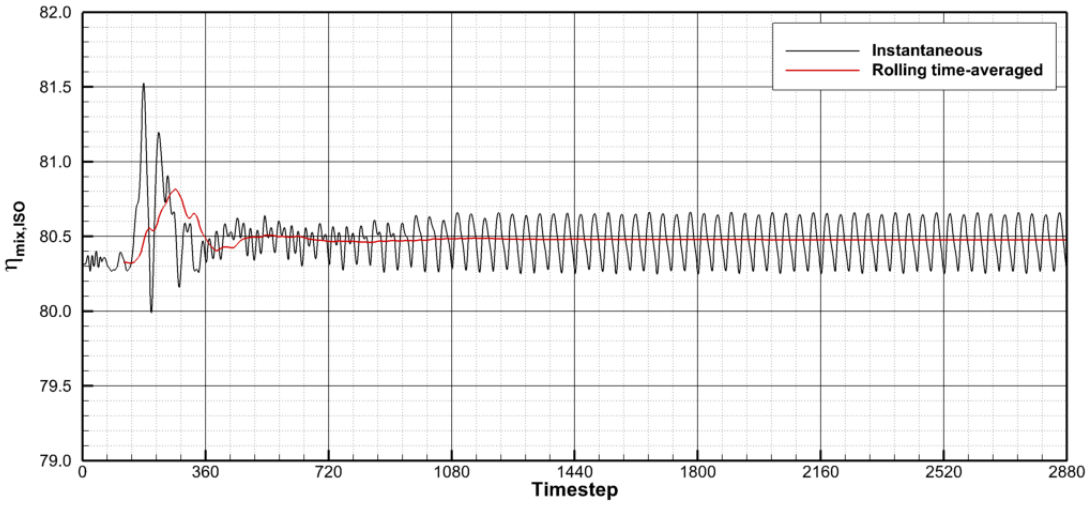

Figure 4-16: Evolution of Stage Efficiency over two revolutions

The behaviour for the 80 step/bpp case shows similar features to the 40 step/bpp case, that is an initial transient lasting approximately half a revolution. The time-averaged stage efficiency settled to a slightly higher value when compared to the 40 step/bpp case, but required twice as many calculation steps. The unsteady fluctuations were found to be

slightly smaller, with 0.4% peak-to-trough magnitude recorded. Increasing the count to 160 steps/bpp doubled the computational cost again but did not reveal any further changes to the time-averaged stage efficiency value or fluctuation magnitude. Based on this analysis, the 40 step/bpp case was taken forward.

4.5.4 Experimental Comparison

In addition to grid and time-step independence studies, experimental validation was undertaken through comparison of steady and unsteady Stub Domain calculations with time-averaged measurements. Data collected on the LAR during calibration activities is documented in detail in Jones et al. [14] and selected results are reproduced here.

The pressure coefficient around the NGV can be defined as:

$$C_{p,n} = \frac{P - P_{0,a}}{\frac{1}{2}\rho_a \Omega^2 b^2} \tag{4.6}$$

where the total pressure ($P_{0,a}$) is taken as a mass-average at the NGV leading edge.

Figure 4-17 presents the vane loading at mid-span for the rig operating point described in Section 3.2; the data presented here are for a case without purge flow. The agreement between CFD (—) and experiment (◇) is broadly good, bar a local region of disagreement at the trailing-edge of the pressure surface. The large overshoot at the trailing edge of the blade is a well-known shortcoming in CFD simulations and can be due to either an overly dissipative numerical scheme or artificial viscosity introduced by the turbulence model. It is believed that the *CFX* High Resolution Scheme weighting (B, equation 4.1) approaches zero at the vane TE due to the high gradients. This becomes the first order upwind scheme, a scheme known to be dissipative in nature [106, 114]. The suction-surface shows a slight disagreement between $z/c_{NGV} = 0.3$ to 0.7 that is attributed to transitional effects, which were not included in the CFD model.

The pressure coefficient in the annulus was defined as:

$$C_{p,a} = \frac{P - \overline{P}_a}{\frac{1}{2}\rho_a \Omega^2 b^2} \tag{4.7}$$

and

$$\Delta C_{p,a} = C_{p,max} - C_{p,min} \tag{4.8}$$

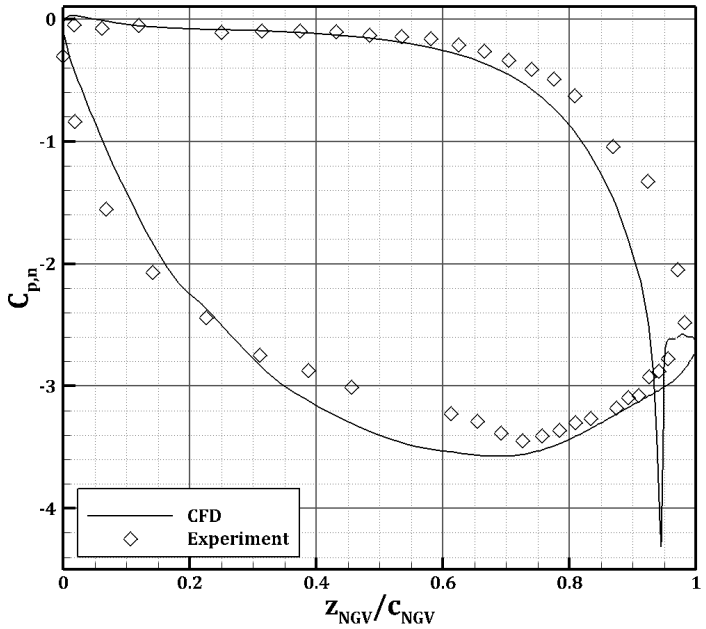

Figure 4-17: NGV loading at the midspan location

evaluated across one vane pitch. The non-dimensional azimuthal coordinate is defined as $\overline{\theta}$ = θ/θ_{NGV}. Comparisons with computations are shown in Figure 4-18, where five data sets are shown:

◇ Experiment, $\phi_0 = 0.0$

○ Experiment, $\phi_0 = 0.134$

—RANS, $\phi_0 = 0.0$

—URANS, $\phi_0 = 0.0$

—URANS, $\phi_0 = 0.134$

For all purge levels, $\Delta C_{p,a}$ is seen to decay with axial distance from the trailing-edge of the NGV (Figure 4-18a) This trend is captured well by the steady CFD, although it can be seen in Figure 4-18b that the local circumferential maxima, $C_{p,max} \approx 0.38$ (shown here at $z_{NGV}/c_{NGV} = 1.1$) is a slight under-prediction of the experimentally-measured value of 0.41 using steady CFD.

In contrast, the unsteady data over-predict $\Delta C_{p,a}$ at all positions. The spoiling effect of purge, seen as a reduction in $\Delta C_{p,a}$ at each station, is captured using URANS. This is

important as it provides confidence for the assessment of the effect of purge in Chapter 5. Additionally, the shape-profile of the static pressure field is captured well, although the CFD predicts a more slender peak than the experiment and lower trough magnitudes. It is likely that at least some of the discrepancy between the experimental and computational pressure data stems from the dissipative overshoot seen in Figure 4-17. This would result in an incorrect vane exit flow angle on the pressure side.

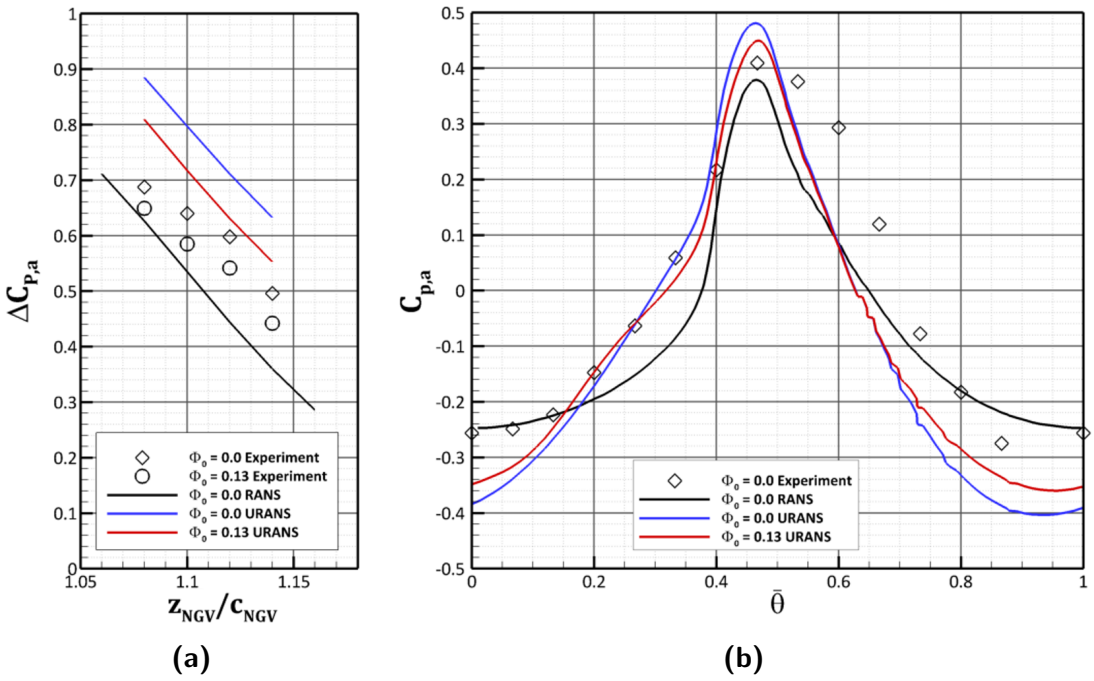

Figure 4-18: Experimental comparison of (a) axial decay of $\Delta C_{p,a}$ and (b) circumferential distribution of $C_{p,a}$ at $z_{NGV}/c_{NGV} = 1.1$

4.6 Unsteady Computations

Unsteady computations have been carried out in previous studies to understand the interaction between the mainstream and purge flows, especially where ingestion is present. In this study, time-varying traces of static pressure are presented for the specific monitor point locations shown in Figure 4-19. These results help to describe the development of flow interactions over time. Results are compared for each of the different domain configurations described in Section 4.2.

The first comparison is made between the SD and CD domains, shown in Figure 4-20; the monitor point is located at 1.0 r/b on the rotor endwall (shown in Figure 4-19

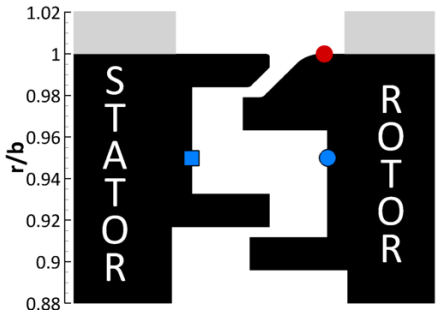

Figure 4-19: Locations of monitor locations in seal and wheelspace region

as a red circle). The monitor point is positioned at the exit of the rim-seal and is in the rotating domain. Due to the rotating frame of reference, the expected periodicity is that of a vane (rather than a blade) passing period. The initial transient pressure fluctuations in Figure 4-20a settle down within the first quarter revolution, at which point a periodic cycle is established for both the SD and CD domains. The period of the pressure peaks exactly matches the vane passing period, as expected. Figure 4-20b shows the final two sector passing periods and illustrates the small difference between the results for the two domains: the stub domain (solid line) shows true periodicity for all cycles, while the chute domain (dotted) shows a very minor amplitude variation every other peak, indicating a sector periodic cycle.

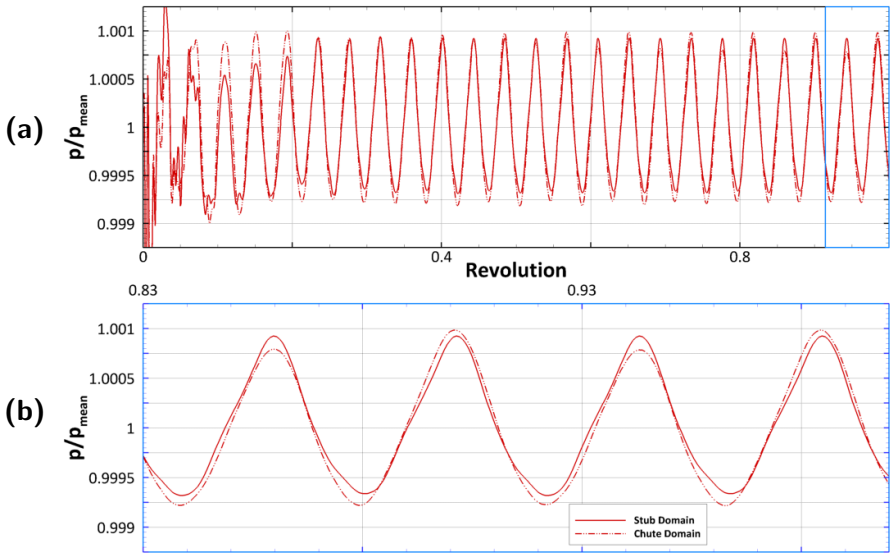

Figure 4-20: Time trace of pressure at 1.0 r/b: (a) first complete revolution and (b) last two sector passing periods for the Stub Domain (—) and Chute Domain (- -)

Figure 4-21 illustrates the computed unsteady behaviour for the SD model at the radially inward monitor points shown in Figure 4-19; these are located in the wheelspace at 0.95 r/b on the stator (the blue square) and on the rotor (the blue circle). Both monitor points are located in the rotating domain. Periodic behaviour at both locations can be seen to develop towards the end of the first revolution, with the initial transient disturbance present for the first quarter of the revolution. This development is slower than that seen in Figure 4-20 for $r/b = 1.0$ and is believed to be indicative that the flow in the wheelspace is interacting with the main annulus flow. Figure 4-21b highlights the sector periodicity of the flow.

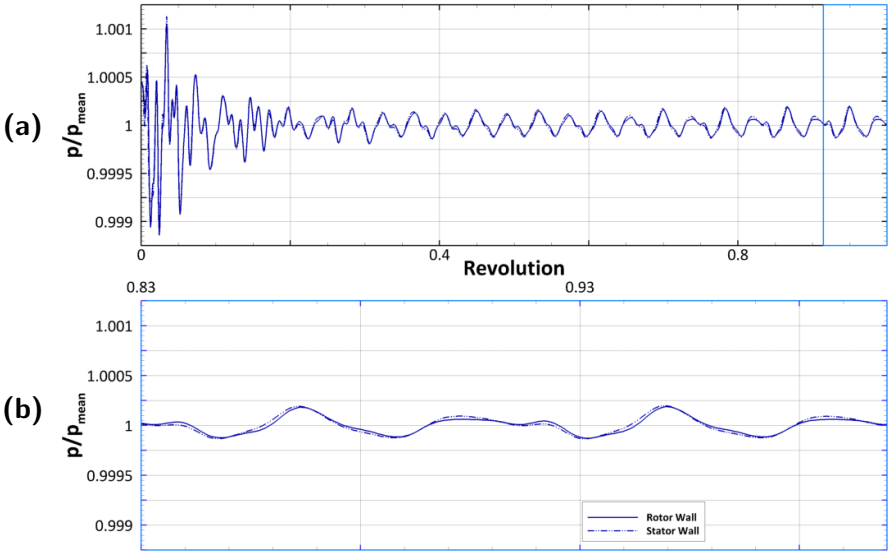

Figure 4-21: Time trace of pressure at $r/b = 0.95$: (a) first complete revolution and (b) last two sector passing periods for the rotor wall (—) and stator wall (- -)

Figure 4-22 shows the unsteady behaviour at the $r/b = 1.0$ location (red circle in Figure 4-19) for the FWD model over two revolutions. Periodicity is not achieved, and the two revolutions shown are taken from a simulation which accumulated 20 total revolutions without improvement in terms of repeatability; Figure 4-22b shows typical behaviour over two sector passing periods. The expected four peaks corresponding to the four vane passes can be noted, however with significant additional fluctuations present.

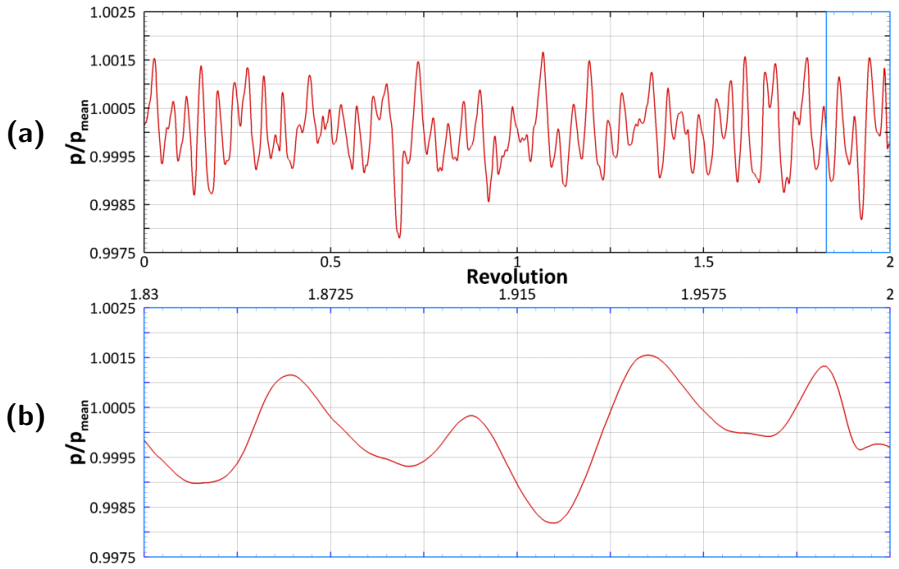

Figure 4-22: Time trace of pressure at $r/b = 1.0$: (a) six complete revolutions and (b) last two sector passing periods for FWD

4.6.1 Effect of Sector Size and Purge Flow Rate

In an effort to understand the source of the unsteady fluctuations described for the FWD additional calculations were performed. The first of these involved increasing the sector size to determine if the periodicity enforced by the 2-3 matching or 30° extent had a significant impact. By doubling the domains to obtain a four vane and six blade model, it was hoped that any flow structures or instabilities larger than the original 30° size would be able to form more readily. The unsteady fluctuations present a significant challenge to analysis of the flow field; in order to address this two sets of data are presented. The first is circumferential pressure distribution on the stator hub, which is a known driver for ingress and thus is expected to have an influence on the mainstream-egress interactions. The second is the pressure fluctuation frequencies in the wheelspace to ascertain whether any significant changes in flow structure can be detected.

In Figure 4-23, the circumferential pressure distribution ($c_{p,a}$ as defined in equation 4.7) is plotted for both sector sizes against non-dimensionalised vane pitch. The measurement location on the stator hub is 14% c_{NGV} downstream of the vane TE, close to the platform TE. The 2-3 sector distribution is shown in red with symbols (▲), while the 4-6 sector distribution is shown in green with symbols (●). Due to the unsteady fluctuations, these data are taken from a time-average over three sector passing periods. For the 2-3 sector,

the two vane passages were then compared to each other, revealing that the data was not perfectly periodic, with a 1.23% difference at the peaks and 0.96% difference at the troughs. The same comparison for the 4-6 sector indicated a 1.70% difference at the peaks and a 6.13% difference at the troughs. To combat this, the pressure distribution was spatially averaged and this is presented in Figure 4-23. The data shows a very small discrepancy at peak and trough with $\Delta c_{p,a}$ of 0.520 recorded for the 2-3 sector and 0.525 for the 4-6 sector. There is excellent matching across the vane pitch, with the two curves being almost indistinguishable away from the extrema.

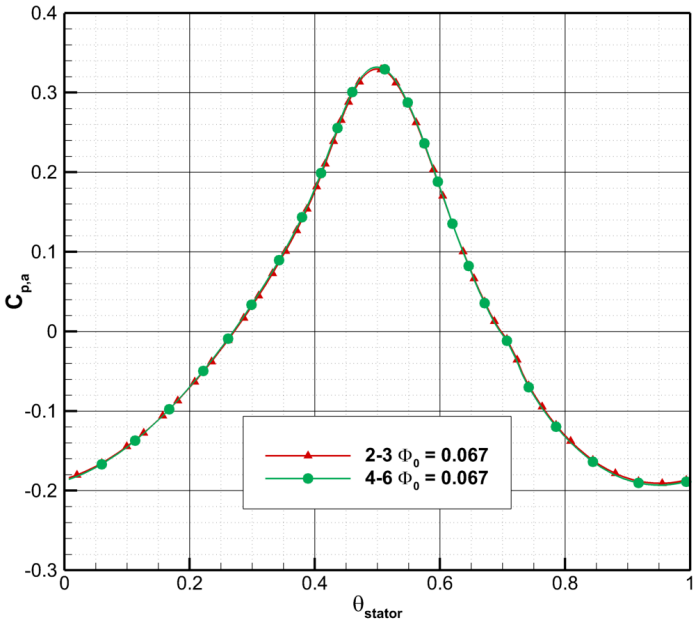

Figure 4-23: Effect of sector size rate on the circumferential distribution of pressure on the stator hub

Figure 4-24 presents a FFT of time-accurate data recorded in the wheelspace at r/b = 0.95 on the rotor wall, thus all data corresponds to the rotating frame of reference. This location lies in the outer wheelspace. Two revolutions of data were recorded for both 2-3 and 4-6 sector sizes, however, the signal remains noisy and this can be seen in the indistinct peaks. The overall frequency profiles do not match exactly, however, the highest peak positions match well. The principal frequency corresponds to the vane passing period, while the next highest is a harmonic related to the vane blade interaction frequency. Both these peaks show excellent frequency agreement despite the noisy data and show close agreement in magnitudes. The two peaks at the lowest frequencies and magnitudes do not match frequencies exactly but the wide spread at this location indicates these peaks may

not be exact. The magnitudes of these peaks are closely matched. It can be concluded that there is no significant change to the flow structure in the outer wheelspace.

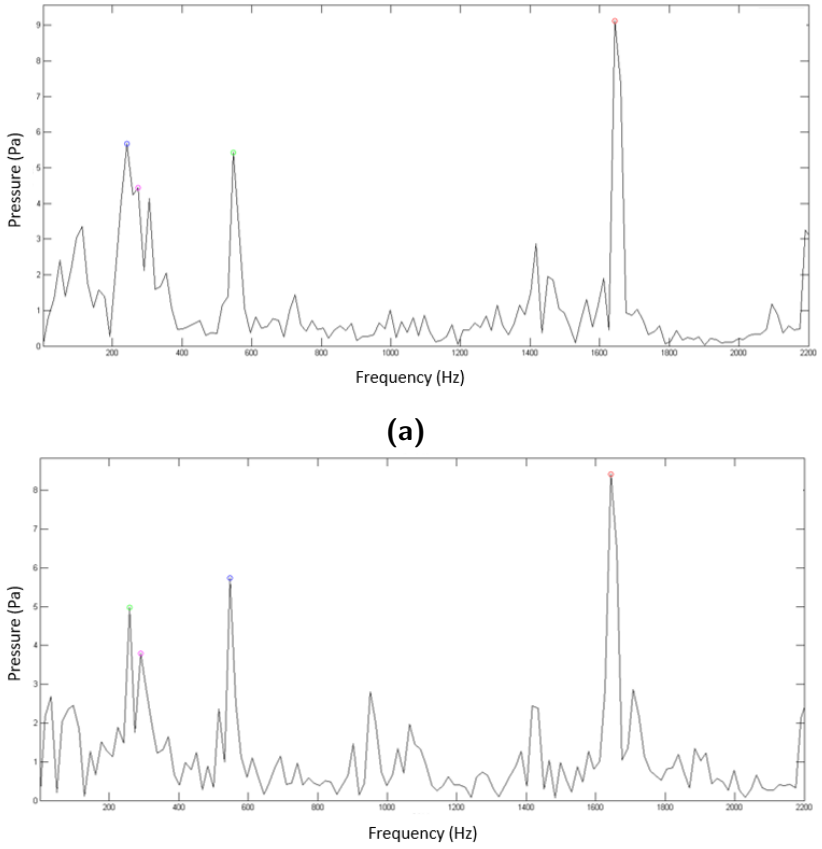

Figure 4-24: Effect of sector size on the frequency of pressure fluctuations in the wheelspace (r/b = 0.95)for (a) 2-3 and (b) 4-6 sector

Figure 4-25 presents a FFT of time-accurate data recorded in the wheelspace at r/b = 0.72 on the rotor wall, which lies in the inner wheelspace. Two revolutions of data were recorded for both 2-3 and 4-6 sector sizes and the data is again noisy. The overall frequency profiles show discrepancies, including an region of increased pressure fluctuations in a range around 1000 Hz for the larger sector size. The highest frequency peak still corresponds to the vane passing period, however, as the pressure pulses due to the stator flow field are significantly damped out by the double seal the magnitude is significantly reduced. The lowest frequency peaks again do not match exactly but still show a wide spread at this location. The largest peaks are contained below 400 Hz, indicating that low frequency unsteadiness dominates the inner wheelspace.

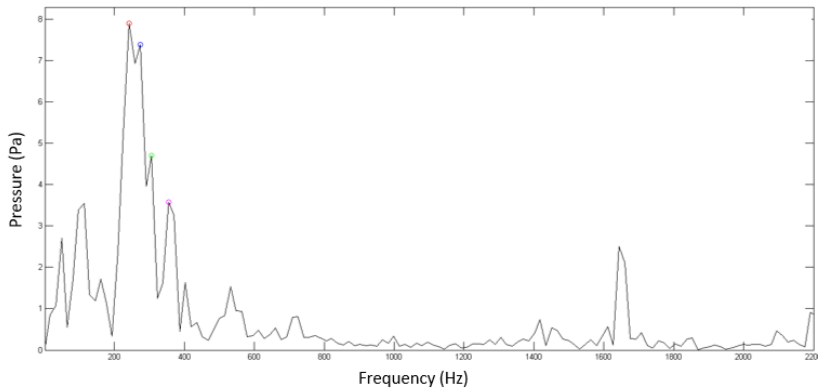

(a)

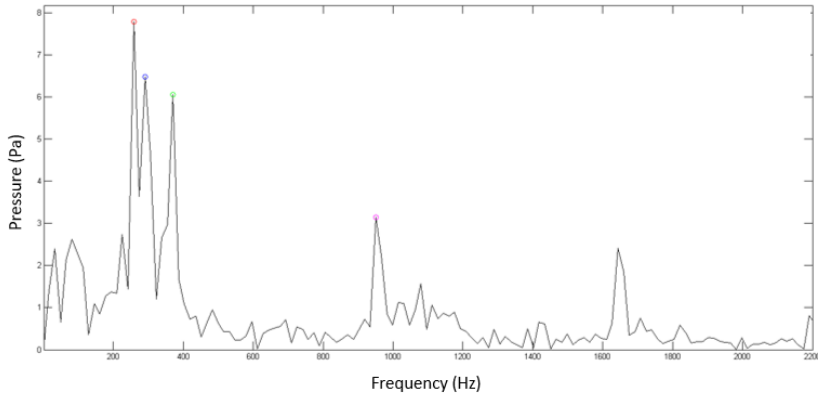

(b)

Figure 4-25: Effect of sector size on the frequency of pressure fluctuations in the wheelspace ($r/b = 0.72$) for (a) 2-3 and (b) 4-6 sector

It is noted here that the fluctuations in stage efficiency were also monitored for all domains and used as a measure of endwall performance in Chapter 6. For the FWD, the fluctuation over each revolution was found to be greater than 1.5% irrespective of sector size. Using a moving average to calculate the stage efficiency over one revolution this mean value was found to be reasonably steady, with excursions of the order 0.1%. Applying an FFT to a time-trace of stage efficiency yielded little in the way of useful information, providing distinct frequency peaks only at the vane and blade interaction frequencies. In comparison, the SD (with purge) fluctuated ±0.2% around the mean, with the average taken over one sector while the AD (with no purge) showed fluctuations of ±0.11% indicating that at least some of the unsteadiness was due to the presence of purge.

Calculations were also performed over a range of purge flow rates, from $\phi_0 = 0.134$ (design condition) through to zero, a completely unpurged case. This was intended to reveal

the effect of purge flow rate on the unsteadiness found in the FWD but not in the reduced domains. First, the effect of purge on the circumferential pressure distribution ($c_{p,a}$) can be seen in Figure 4-26, plotted against non-dimensionalised vane pitch. Here, the zero purge case is shown in black while two purged cases are shown in red ($\phi_0 = 0.067$) and blue ($\phi_0 = 0.134$, design condition). The distributions show very similar trends, with a narrow peak and wide trough, but differ in extrema. The unpurged case shows the highest $\Delta c_{p,a}$ of 0.592, while the design condition shows the lowest with 0.499. This indicates that the increased purge flow rate shows a suppression of the circumferential pressure distribution at the platform trailing edge, which could be related to the blockage reported by Schrewe *et al.* [46]. This "spoiling" effect on the C_p distribution was confirmed experimentally as reported in Jones *et al.* [14].

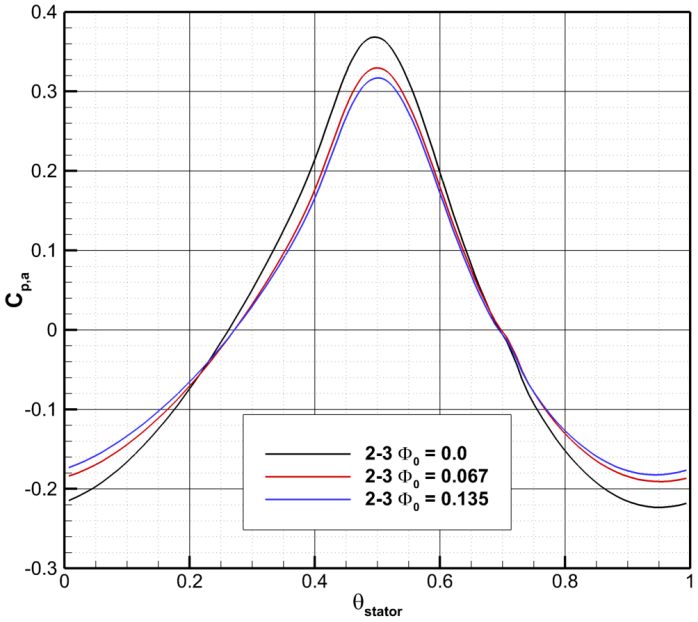

Figure 4-26: Effect of purge flow rate on the circumferential distribution of pressure on the stator hub

It is also informative to compare the evolution of stage efficiency over time for the different levels of purge flow. Figure 4-27 shows the evolution of stage efficiency over time (in revolutions) for unsteady calculations. Two cases are shown, Figure 4-27a shows the behaviour over one revolution for a calculation for the FWD without purge gas while Figure 4-27b shows the behaviour with purge gas over three revolutions. Introduction of purge flow gas is expected to cause a reduction in stage efficiency as noted by a number of authors in Section 2.2.4 and is seen here. Also present is the expected initial transient. However,

the increasingly unsteady behaviour for the purged case shown here and in Figure 4-22 previously is not replicated for the unpurged case.

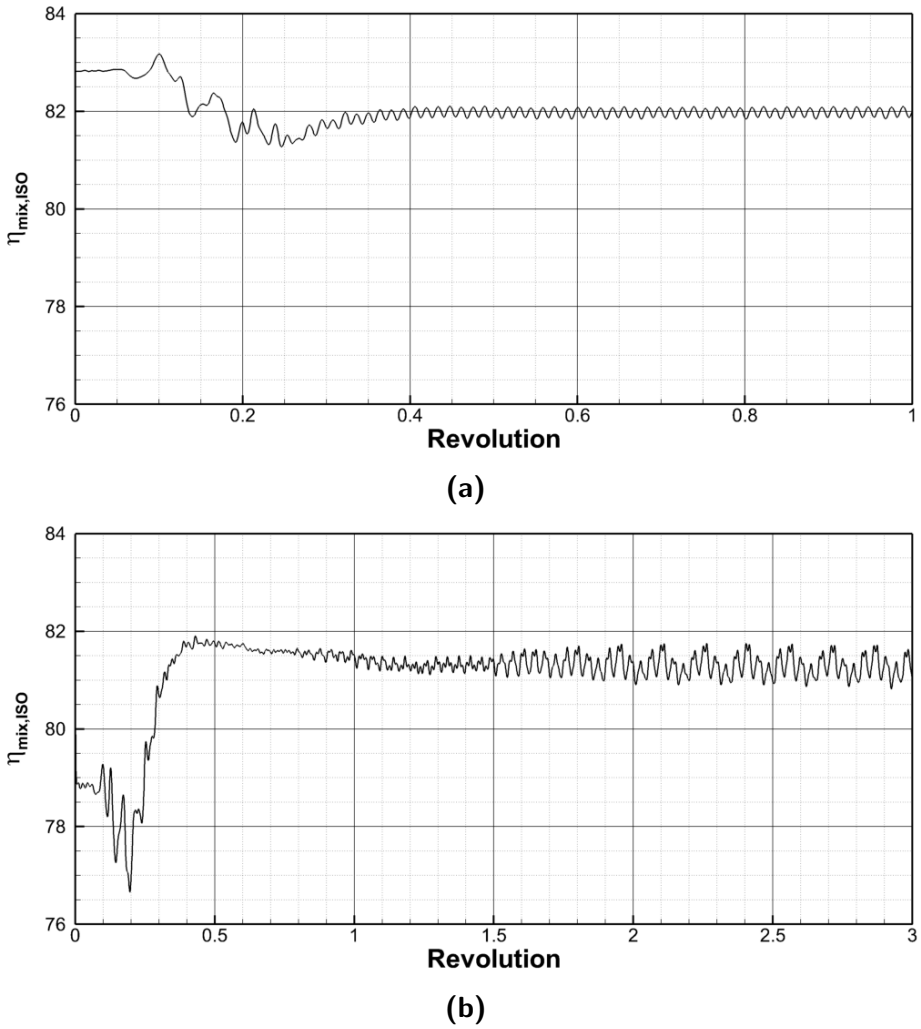

Figure 4-27: Effect of purge flow rate on stage efficiency over time for (a) $\phi_0 = 0.0$ and (b) $\phi_0 = 0.034$

These results for the FWD indicate that the non-periodic behaviour can be attributed to the complex interaction between egress in the seal region and the annulus flow. However, the unsteady effects on the flow in the wheel-space are only experienced when the wheel-space (inboard of the double rim-seal) is included in the computations. This was found to be a significant issue when attempting to include the full wheelspace in calculations including endwalls; the levels of unsteadiness in stage efficiency due to the FWD in the presence of purge were significantly larger than the expected gains due to the introduction

of endwalls. It was concluded that in order to progress, the FWD was not viable for endwall calculations. Investigation of the development of secondary flow structures using the *Stub Domain* in the turbine annulus and the interaction between the structures and purge flow is described in Chapter 5.

4.6.2 Computational Cost

Computations were performed on the Balena High Performance cluster at the University of Bath. Balena has a Linux operating system with a *Simple Linux Utility for Resource Management* or SLURM scheduling system to provide workload management. The cluster contains 196 physical nodes with 16 cores per node.

CFX documentation [106] notes that for hexahedral meshes scalability is good up to a minimum of 75 000 nodes per core. For the SD medium mesh used in this research this results in an optimum number of cores of 80 based on cell count and node size. Typically, steady state and initial condition calculations for the 30° stub domain, using a medium mesh, required 130 CPU hours to reach convergence. For a typical transient calculation, 4600 CPU hours were required per revolution when using 40 steps per blade pass.

4.7 Summary

This chapter described the computational framework and solver numerics employed in the generation of result data. The computational model was described at length, justifying the levels of geometric representation for the S1 and R1 domains as well as the choice of sector size. Options for boundary conditions were presented and justified, as well as expanding upon key details, such as the generation of purge inlet velocity profiles.

A discussion of turbulent closure was presented, noting the development and assumptions behind the widely used two-equation models and their relative strengths and weaknesses. Modifications to the models were discussed relating to specific weaknesses allowing for the justification of the choice of $k-\omega$ SST with wall functions.

Grid generation was presented, along with a discussion of the selected blocking topology and the resulting mesh features. Problems encountered were noted, such as the transition between annulus and seal geometry, as these are relevant to the decisions taken. Cell counts for the medium mesh were provided in detail and overall cell counts were

provided for the three grid levels. The grid sensitivity study was presented, showing that the medium mesh was an acceptable resolution. Iterative convergence was discussed for steady-state, while time-step sensitivity was presented for unsteady calculations. Comparisons with experimental data were provided.

Results from the different domain extents were presented for time-marching computations. These showed the increasingly chaotic, unsteady behaviour that arose from the inclusion of wheelspace geometry, as well as the inclusion of purge flow. It was concluded that the unsteadiness was due to the introduction of the purge flow, rather than the wheelsapce geometry, as it was possible to turn off the random fluctuations by removing the purge flow. It can also be concluded that the introduction of purge has a spoiling effect on the circumferential pressure distribution, in agreement with other authors and the experimental data for the rig.

Chapter 5

Effect of Egress

This chapter investigates the interaction characteristics in the LAR, a single-stage experimental turbine facility at the University of Bath. Details of the LAR can be found in Section 3. The effect of domain extent is presented through comparison of Annulus Domain (AD) data with that of the Stub Domain (SD). Purge gas is applied to the Stub Domain to understand the influence of this interaction. Secondary flows are visualised using different variables in order to provide a platform for later contoured endwalls and new variables are introduced. The work presented in this chapter expands on the results presented in Schreiner *et al.* [12] by presenting both stator and rotor flow fields, establishing visualisation methods for use in later analysis and introducing additional, derived variables.

5.1 Annulus Domain

In order to describe the effects of purge flow on the secondary flow structures in the vane and blade passages, it is first necessary to identify and characterise the flow in the *absence* of any purge flow. The AD excludes all physical features outside of the annulus, notably the seal and wheelspace. The inclusion of these physical features would themselves generate egress through rotor pumping, even in the absence of superposed egress. Thus while the AD provides the least complex flow field for investigation, it must be noted that this flow structure is not seen in reality as all engines in the field have some form of seal between the stator and rotor. Transient data, averaged over one sector pass, are presented here for the AD case.

5.1.1 Stator Flowfield

Consider first the stator. Streamlines are released close to the inlet at the midspan (Figure 5-1) using the time-averaged velocity field. These are coloured by spanwise position in order to highlight the bulk flow behaviour far from the endwalls. Upstream of the NGV, the bulk flow is 2D in nature, as expected. Moving in to the passage the flow becomes deflected by the NGV. However, deviations from the midspan become apparent especially near the suction surface where a positive radial migration is seen. The opposite occurs at the pressure surface with flow moving towards the hub. Within the vane passage this migration is limited to ± 0.05 s. Near the trailing edge, the positive migration close to the suction surface approaches 0.07 s. From this it is clear that the secondary flow structures remain near the hub and shroud walls. The small displacement near the walls is expected: the cross passage pressure gradient causes a flow from pressure to suction surfaces at the hub, which in turn causes a spanwise flow along the blade. This spanwise flow on the suction surface is from mid-span outward, while on the pressure surface this is from the endwalls towards midspan. These flows are wall bound.

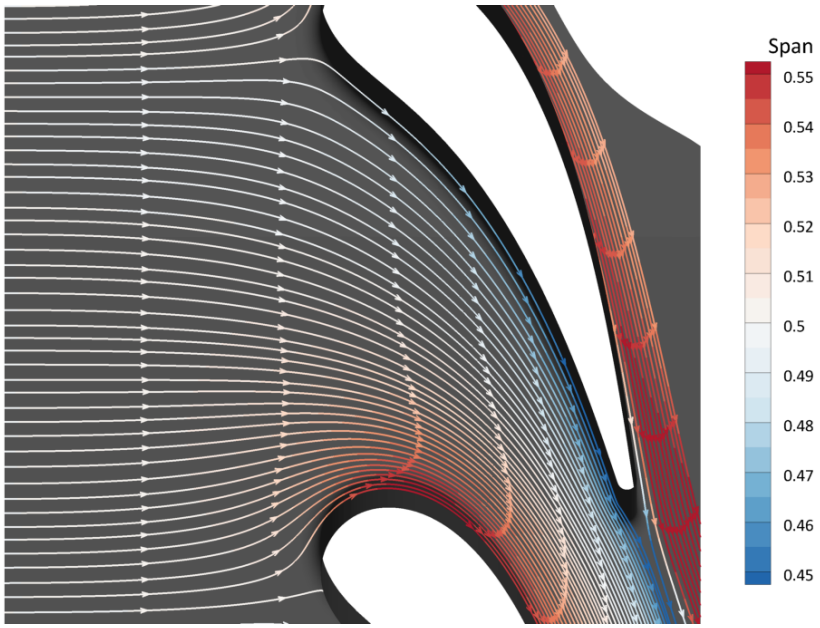

Figure 5-1: Streamlines in the stator released at midspan, coloured by spanwise position, for a case with no superposed flow

The pressure coefficient ($C_{p,n}$) is defined in Equation 4.6 and presented in Figure 5-2a as a contour on the hub and blade. A typical pressure gradient is present with both axial and circumferential components. The overshoot in pressure seen in Figure 4-17 is noted

as a small region of low pressure and strong gradients on the pressure surface close to the trailing edge. The circumferential gradient from pressure-side to suction-side, across the passage, drives a cross-passage flow at the hub which is visible as a pitchwise migration of surface streaks in Figure 5-2b. The hub flow pattern is significantly different to the bulk flow, with *Saddle Points* (S_p) upstream of the NGV LE revealing the presence of a leading edge horseshoe vortex (HSV) in agreement with the surface flow patterns of Baker [30] in Figure 2-3a.

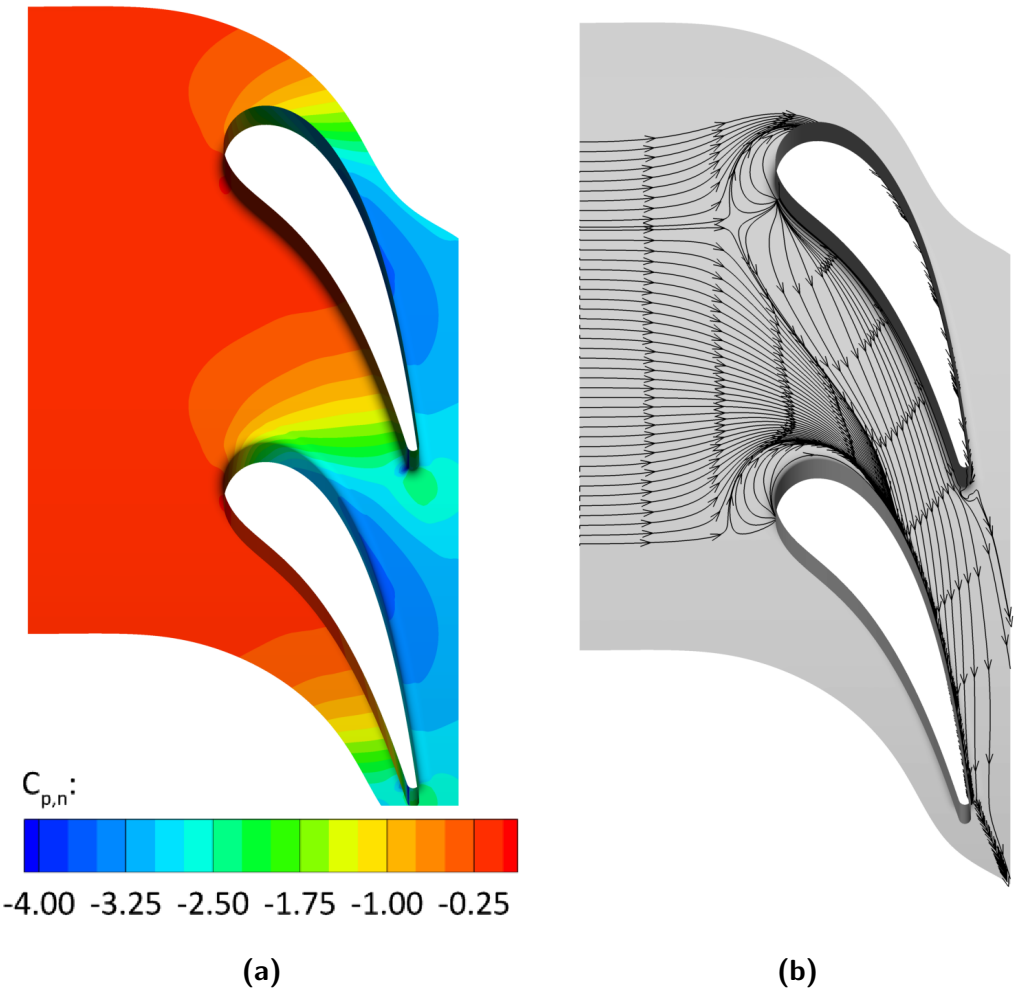

Figure 5-2: AD stator (a) contours of $C_{p,n}$ and (b) surface streaklines in the stator

Secondary flow structures can also be understood by considering their impact on the total pressure in the stator passage. Regions of reduced total pressure are indicative of lost work and disturbed flow. A plane located at 0.8 c_{NVG} (Figure 5-3a) shows local minima in total pressure near both hub and shroud. These minima features correspond

to the maximum spanwise extent of two vortical structures, one at the hub and one at the shroud, migrating across the passage but remaining close to their respective endwalls. Boundary layers at this location are still thin due to the favourable pressure gradient seen in Figure 5-2a. However, downstream of 0.8 c_{NVG} an adverse pressure gradient on the suction surface causes thickening of the boundary layers.

At the NGV exit plane (Figure 5-3b) both vortices have grown in size and their rotation is indicated for clarity. The structure at the hub has a radial extent of 0.25 s, while the structure at the shroud extends 0.35 s. This agrees with the spanwise migration seen in Figure 5-1 as the vortex near the shroud has a stronger influence at the midspan. The thick boundary layer on the pressure surface is due to the pressure overshoot. This presents as an artificially strong adverse pressure gradient and results in an underturning of the NGV wake.

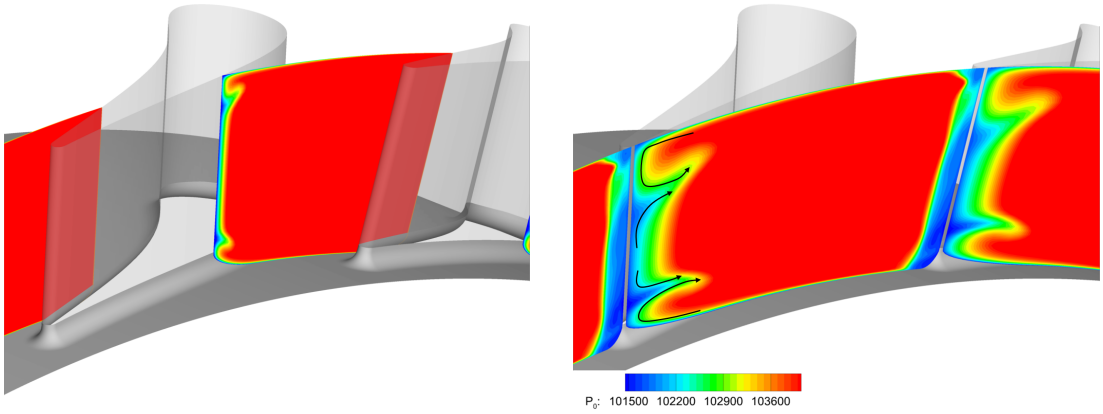

(a) **(b)**

Figure 5-3: P_0 in stator passage showing secondary flow and wake development for a case with no superposed flow on axial planes at (a) 0.8 c_{NVG} and (b) 1.0 c_{NVG}

To more clearly visualise the HSV roll-up at the NGV LE and subsequent convection downstream, the visualisation technique of Sieverding and Van den Bosche [33] is particularly useful. Releasing streamlines at the inlet, from 0.0375 s, reveals the incoming boundary layer rolling up at the LE (Figure 5-4). Streamlines have been isolated in two regions using the LE bifurcation and the approximate mid θ; black indicates the pressure side (HSV-PS) and orange indicates the suction side (HSV-SS). The pressure side streamlines move with the cross-passage pressure gradient, wrapping underneath as seen in Figure 5-4b. This lifts and weakens the HSV-SS due to the opposing rotation. The HSV-PS impinges on the

adjacent suction surface and moves up the vane, aided by the smooth transition between blade and hub created by the vane root radius. As the point at which HSV-PS is no longer hub-wall bound and migrates radially, it is known as the Passage Vortex. This point is not clear in the stator.

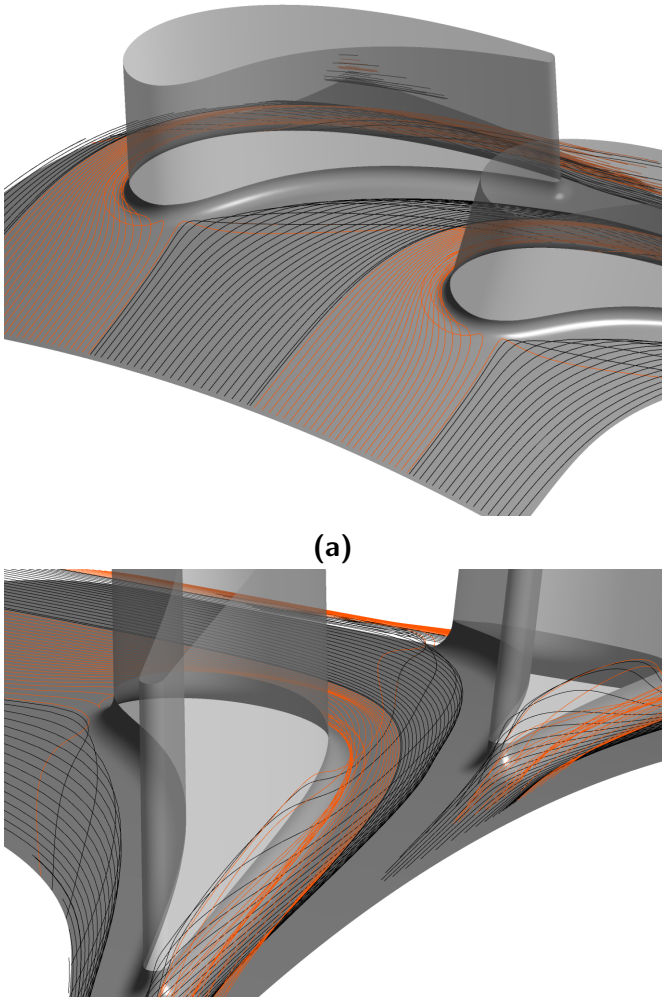

(a)

(b)

Figure 5-4: HSV roll-up at NGV LE and interaction for a case with no superposed flow, view from (a) upstream and (b) downstream

Figure 5-5 presents contours of non-dimensional vorticity on axial planes, limited to $s \leq 0.5$ in order to highlight secondary flow structures near the hub endwall. The inset at bottom left of Figure 5-5b shows the location and sequential numbering for the axial planes in the stator. Positive z-component vorticity corresponds to a clockwise rotation when looking downstream.

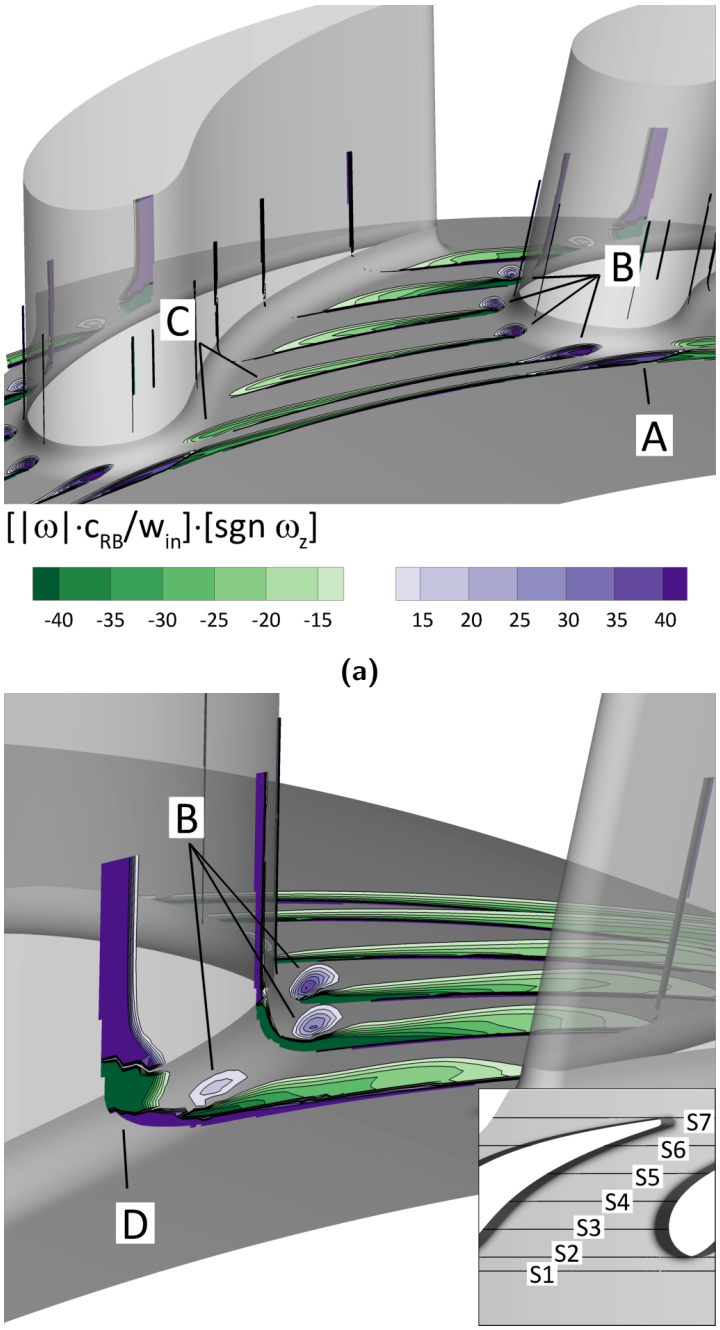

Figure 5-5: Distribution of non-dimensional vorticity in the stator for a case with no superposed flow, view from (a) upstream and (b) downstream

Figure 5-5a shows planes S1 through S6 from an upstream viewpoint. The roll-up of the HSV at the LE is highlighted and noted 'A'. The HSV bifurcates at the vane LE, with the HSV-SS noted 'B' and HSV-PS noted 'C'. The boundary layer in the blade passage experiences shear due to the cross-passage pressure gradient, leading to the wide vorticity distribution seen. Combined with the HSV-PS failing to form a tight vortex core, this leads to poor discretion of the HSV-PS as a specific vortex. The HSV-SS, however, is clearly visible as it moves downstream. By plane S4, the HSV-SS is being lifted from the endwall by the cross-passage flow, which also weakens the vortex. This is in agreement with both Sieverding and Van den Bosche's [33] and Sharma and Butler's [25] findings.

Figure 5-5b shows the same planes, but from a downstream viewpoint. The HSV-SS is again noted 'B' and can be seen to be displaced radially by the cross-passage flow. At plane S6 it is clear that the HSV-SS and HSV-PS are no longer travelling in a generally axial direction, which leads to the poorly defined feature 'D'. A streamwise coordinate system for vorticity would avoid this issue, however, alternative vortex identification variables exist.

5.1.2 Rotor Flowfield

Building an understanding of the rotor flow field in the absence of purge follows a similar approach to that taken for the stator. New plane locations are specified and feature numbering will be restarted for the rotor.

The time-averaged flow field is used to release streamlines at the domain inlet on a midspan surface (Figure 5-6). These are coloured using spanwise position. Incoming flow bifurcates around the blade, however, the impingement point is not at the metal LE and appears on the pressure surface at 0.05 c_{RB}. 2D flow far upstream of the RB is shown, however, by the RB LE a positive spanwise migration to 0.52 s is present across the passage. This increases with axial distance, rising to 0.55 s at 0.3 c_{RB} and 0.57 s at the mid-chord. Downstream of the mid-chord a negative migration near the pressure surface occurs, approaching 0.41 s. Within the blade passage the flow is highly 3D in nature, indicating that the secondary flows are large.

In the rotating domain, the pressure coefficient can be defined as:

$$C_{p,r} = \frac{P - P_{0,in}}{\frac{1}{2}\rho_{in}\Omega^2 b^2} \tag{5.1}$$

Here, the subscript in indicates mass-averaged variables assessed at the RB LE, i.e. the

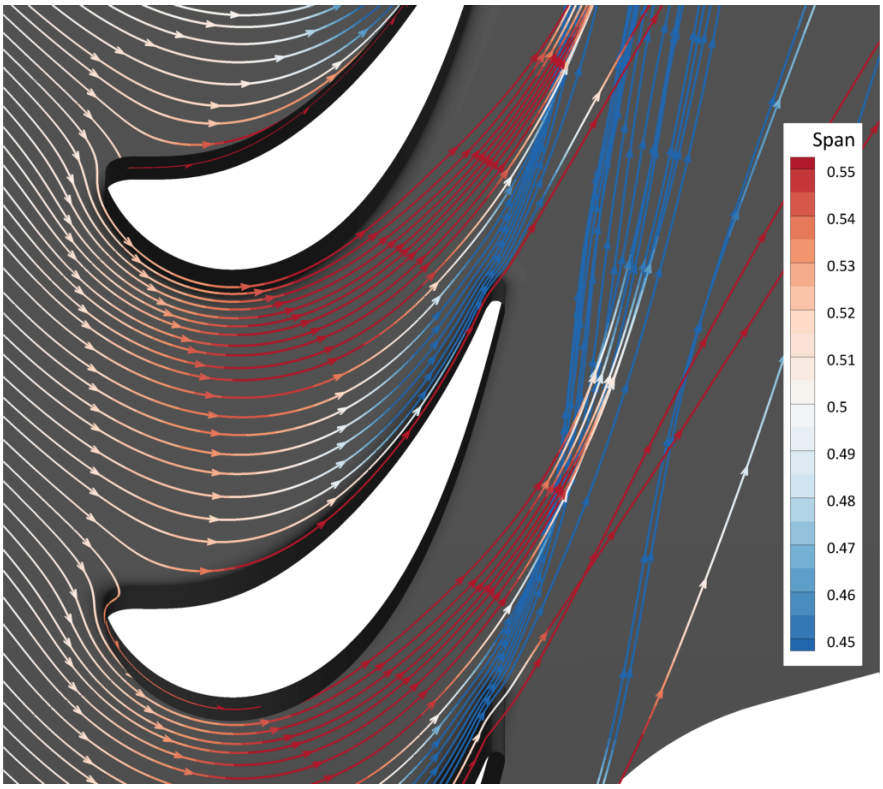

Figure 5-6: Streamlines in the rotor released at midspan, coloured by spanwise position, for an AD case with no superposed flow

inlet to the blade passage. Contours of $C_{p,r}$ are presented in Figure 5-7a for the cylindrical hub surface, displaying a more complex pattern than in Figure 5-2a. Both axial and circumferential pressure gradients appear, however, a clear dividing feature (marked with a dashed line) is present. On the pressure side of this line, a circumferential gradient dominates, while on the suction side, an axial gradient dominates. This low pressure intrusion indicates increased strength of secondary flow features in the rotor.

Surface streaks are plotted on the hub and rotor blades (Figure 5-7b). Saddle points are visible upstream of the RB LE, occurring at 0.35 θ/θ_{RB}, indicating the presence of the HSV. In contrast to the stator, the rotor cross-passage flow is dominant throughout the passage with axial flow present in one small triangular region only, extending to 0.15 c_{RB}. The formation of the HSV-SS is very clear in the surface streaks, with a bunching of the streaklines present on the suction side of the RB LE which curve from the saddle point in to the adjacent blade passage.

It is clear that the secondary flow structures are larger in the rotor domain. Using Siev-

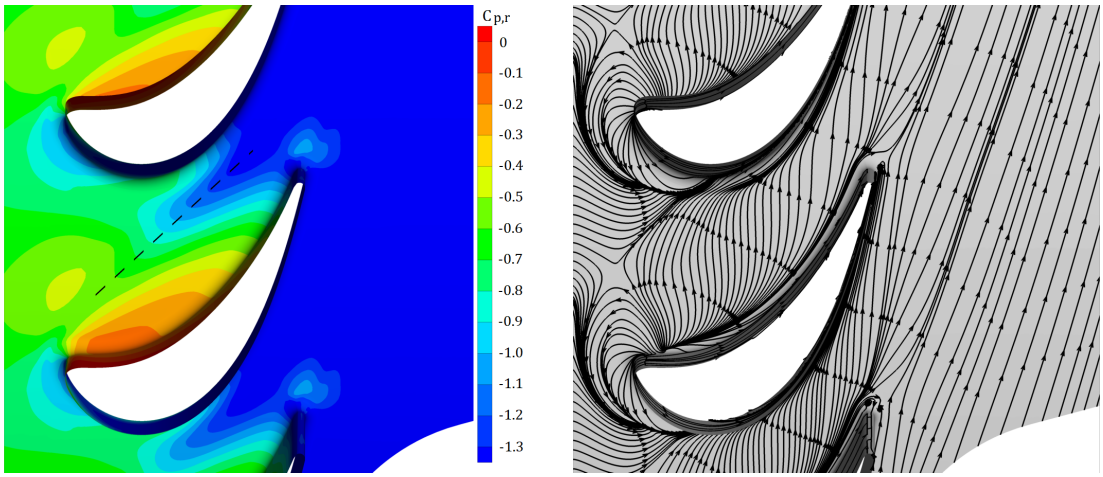

(a) **(b)**

Figure 5-7: AD rotor, case with no superposed flow, (a) contours of $C_{p,r}$ and (b) surface streaklines

erding's coloured smoke technique in Figure 5-8, the pitch-wise migration of the secondary flow features can be understood: HSV-SS (gold) and HSV-PS (blue). The cascade view (5-8a) shows the HSV-PS interacting strongly with the HSV-SS, passing under the latter near 0.4 c_{RB} and displacing it upwards. This corresponds to the radial migration near the suction surface in Figure 5-6. The HSV-PS impinges on the suction surface of the adjacent blade at 0.6 c_{RB}, becoming the PV and migrating rapidly towards the shroud.

Figure 5-8b shows the HSV roll-up close to the blade leading edge and the initially straight trajectory of the HSV-PS. Both Figure 5-8a and b reveal that the HSV-PS trajectory becomes deflected by the interaction with the HSV-SS as the HSV-PS streamlines become bunched as the HSV-SS passes back underneath the former. Looking from downstream (Figure 5-8c), the wrapping of the HSV-SS around the HSV-PS is clearly visible.

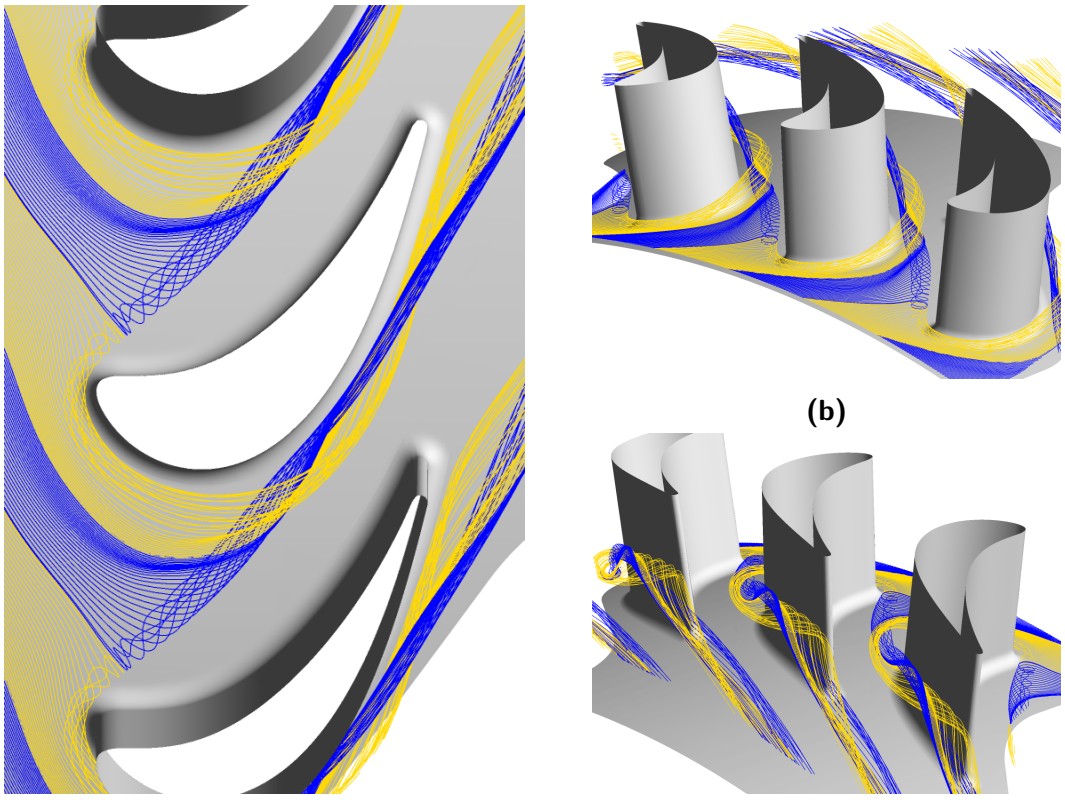

Figure 5-8: Streamlines tracing the secondary flows for a case with no superposed flow, (a) cascade, (b) upstream and (c) downstream views

Finally, the streamlines can be viewed in the $r-z$ plane to accurately map their radial displacement. Figure 5-9 shows the HSV-PS rising significantly from 0.5 c_{RB} onwards. This indicates that it has impinged on the adjacent RB suction surface and, therefore, become the PV. It passes under the HSV-SS, lifting the latter to 0.25 s at 0.4 c_{RB}. Both vortices reach 0.5 s by 1.0 c_{RB}. This is also clearly seen in the inset, where the blade streaklines show a large upwash. The downwash at the blade tip corresponds to the tip vortex, which is not of interest to this study and thus not visualised further.

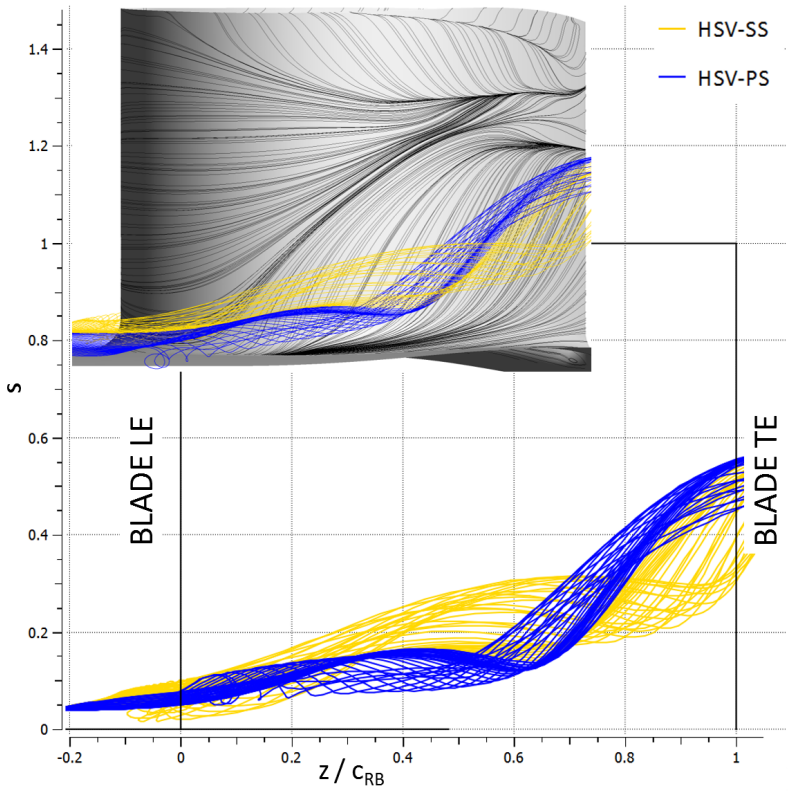

Figure 5-9: Streamlines and streaklines tracing the secondary flows for a case with no superposed flow, view on the radial-axial plane

Figure 5-10 presents contours of non-dimensional vorticity on axial planes limited to $s \leq 0.7$ in order to highlight secondary flow structures near the hub endwall. The inset at top left of Figure 5-10b shows the location and sequential numbering for the axial planes in the rotor. Positive z-component vorticity corresponds to a clockwise rotation when looking downstream.

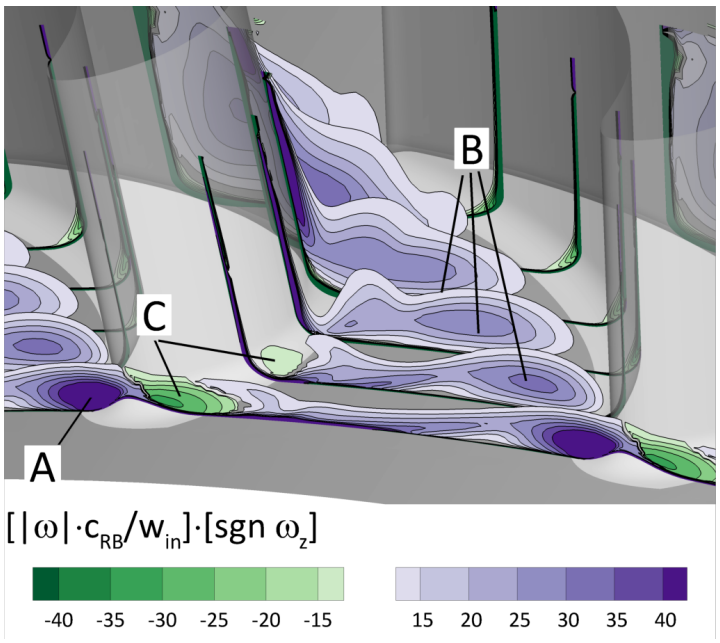

(a)

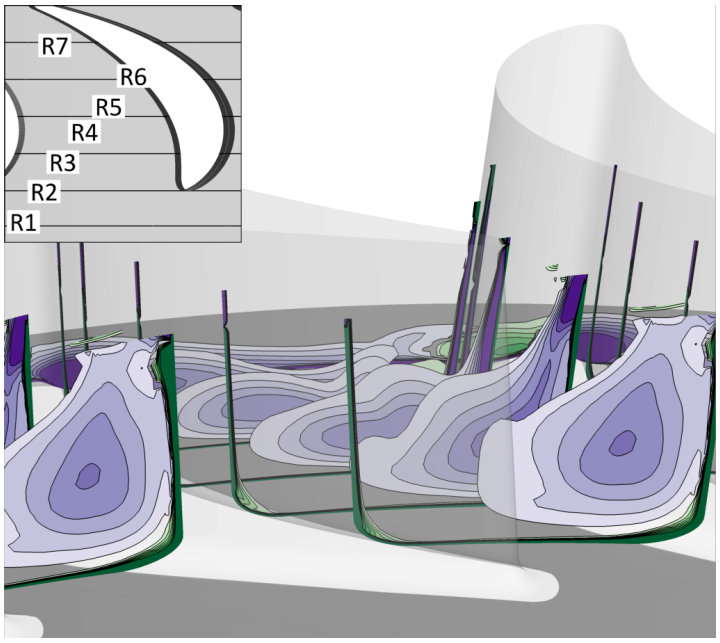

(b)

Figure 5-10: Distribution of non-dimensional vorticity in the rotor for a case with no superposed flow on axial planes, view from (a) upstream and (b) downstream

Figure 5-11 shows the distribution of non-dimensional vorticity on a surface at 0.05 s. Feature 'A' identifies the shape of the HSV as it is bent around the BLE. Here, negative y-vorticity corresponds to flow that turns radially downward towards the endwall: regions of negative y-vorticity can be seen in the boundary layer and in the HSV. This highlights that the HSV-PS is enhanced by the cross-passage flow. The HSV-SS ('C') is very weak in comparison to the HSV-PS ('B') as expected.

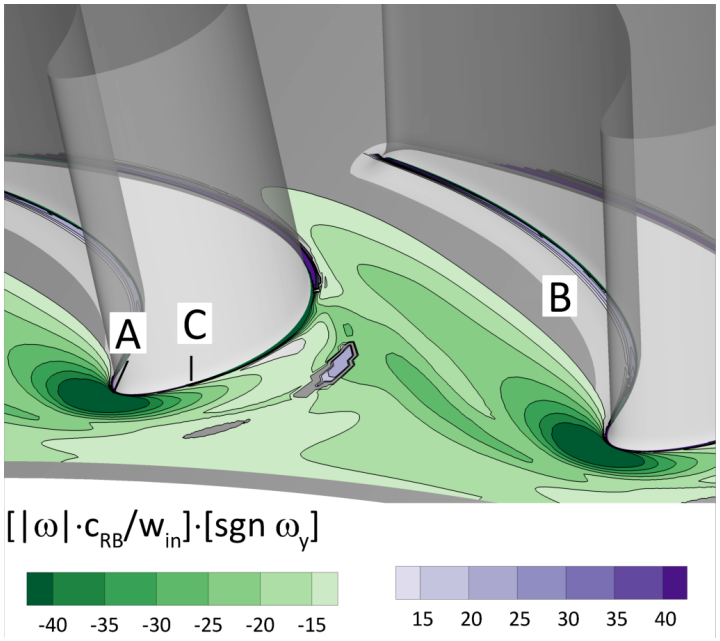

Figure 5-11: Distribution of non-dimensional vorticity in the rotor for a case with no superposed flow on a cylindrical surface 0.05 s, view from upstream

The evolution of the stage efficiency (Equation 2.10) for the AD, over the first computational revolution, can be seen in Figure 5-12. Both instantaneous (red) and moving, sector averaged data (blue) are presented. An initial transient lasting 0.45 revolutions is followed by periodic behaviour. The periodic behaviour shows peaks corresponding to the expected vane-blade interaction frequency. The moving average stage efficiency remains constant at 82.12% from 0.6 revolutions, with fluctuations in instantaneous efficiency of ±0.13% around the mean value.

In general, the flow fields described here for both the stator and rotor closely match that shown in Figure 2-1. A HSV rolls up at the aerofoil leading edge due to the boundary layer velocity deficit. The HSV legs are convected downstream by the bulk flow. The cross-passage pressure gradient moves the HSV-PS pitchwise towards the suction surface. The

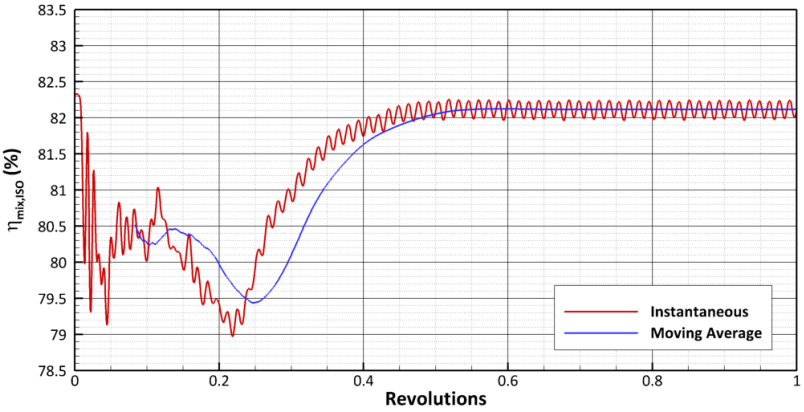

Figure 5-12: Time trace of $\eta_{mix,ISO}$ for AD case with no superposed flow over the first revolution. Instantaneous data in red, sector-pass average in blue.

HSV-SS is lifted, initially only slightly by the cross-passage flow and later more aggressively by the HSV-PS as the latter impinges on the suction surface. Impingement of the HSV-PS on the suction surface causes the vortex to move up the blade, away from the endwall, becoming the PV.

5.2 Stub Domain without Purge Gas

The stator flow field was found to be unchanged due to the addition of the stub domain wheelspace and closely matches that shown in the early part of Section 5.1. For this reason, no additional details are shown for the stator.

The rotor, by contrast, shows subtle changes due to the addition of the stub cavity. Here again, the time-averaged flow field is visualised using streamlines released at the domain inlet on a midspan surface (Figure 5-13), coloured using spanwise position. Incoming flow bifurcates around the blade with the impingement point on the pressure surface near 0.05 c_{RB}. The 2D flow upstream of the RB seen in Figure 5-6 remains so with the addition of the seal geometry. At RB LE a positive spanwise migration is present across the passage. This increases with axial distance, rising to 0.56 s at 0.3 c_{RB} and 0.58 s at the mid-chord. Downstream of the mid-chord a negative migration near the pressure surface occurs, approaching 0.4 s. Within the blade passage the flow is highly 3D in nature, indicating that the secondary flows remain large.

Contours of $C_{p,r}$ are presented in Figure 5-14a for the Stub Domain cylindrical hub

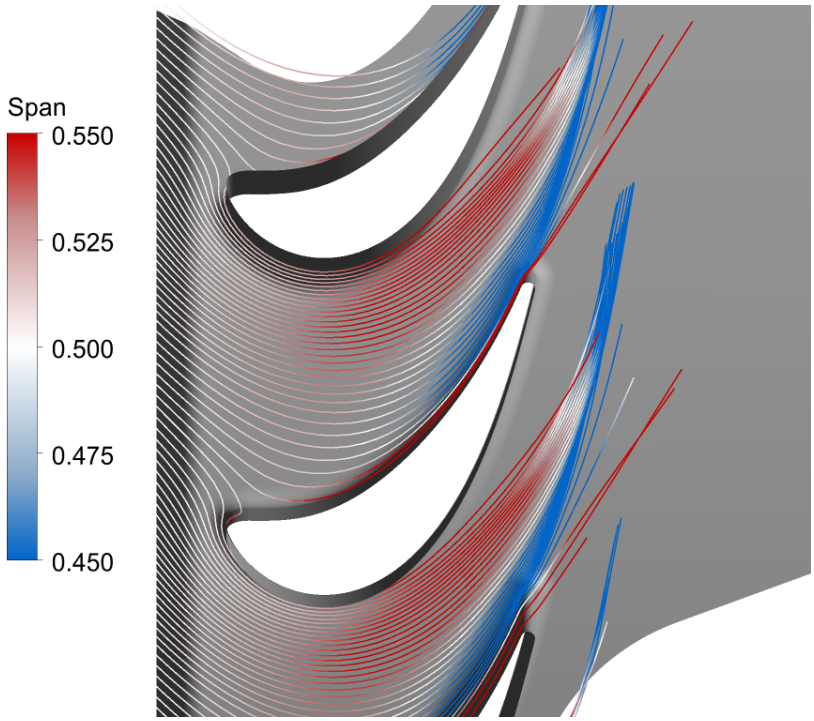

Figure 5-13: Streamlines in the rotor released at midspan, coloured by spanwise position, for a SD case with no superposed flow

surface, displaying a very similar pattern to that seen in Figure 5-2a. Axial and circumferential pressure gradients appear in the blade passage. The low pressure feature is still present though the axial extent does not match. This indicates a change in the secondary flow structure size, specifically the HSV-PS. On the pressure side of this feature, the circumferential gradient dominates, while on the suction side, the axial gradient dominates.

Surface streaks are plotted on the hub and rotor blades (Figure 5-14b). Saddle points are present upstream of the RB LE (0.36 θ/θ_{RB}), the lift off point for the HSV which has not significantly moved. A significant change to the surface streaks occurs upstream of the HSV lift off: the presence of the chute seal geometry interrupts the clear HSV-SS formation shown in Figure 5-7b. A secondary effect of this change to the HSV-SS formation is that the cross-passage streaklines are deflected axially.

The visualisation technique used in Figure 5-4 and Figure 5-8 is repeated here in Figure 5-15. The HSV roll-up at the RB LE present as expected with both HSV-SS (gold) and HSV-PS (blue) legs clearly visible. Figure 5-15a supports the previous assertion that the HSV-SS formation has been affected by the introduction of the seal geometry as

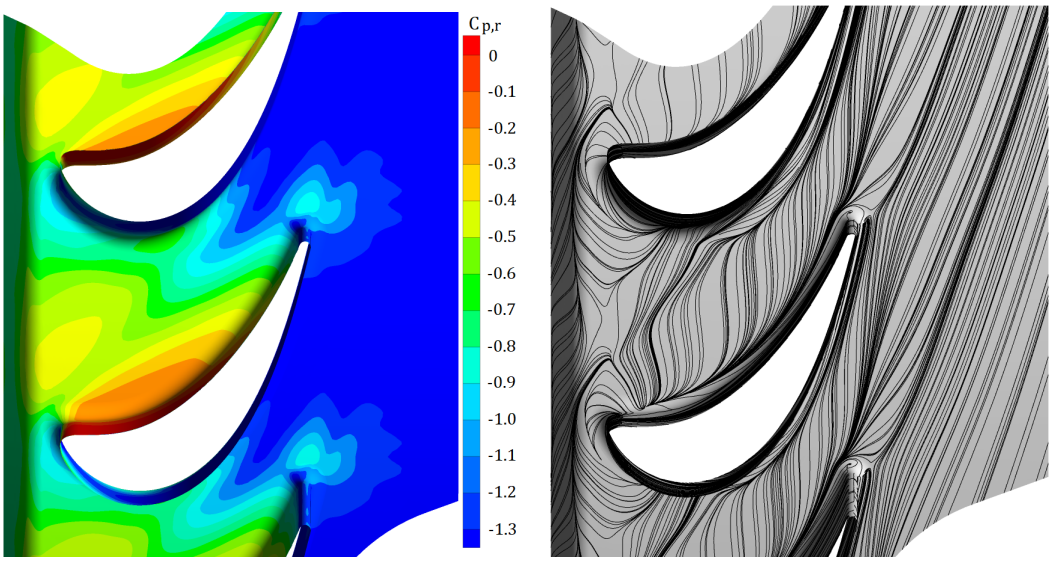

Figure 5-14: SD rotor, case with no superposed flow, (a) contours of $C_{p,r}$ and (b) surface streaklines

the streamlines passing around the leading edge are displaced pitchwise, increasing their footprint towards the pressure side. Two factors cause this change and are covered in detail below.

The bulk flow convects the vortical structures downstream, while the HSV-PS is migrated pitchwise towards the suction surface. The HSV-SS remains close to the suction surface until it is lifted by the cross-passage flow and the HSV-PS as the latter impinges blade surface. The HSV-SS can be seen to wrap around the HSV-PS in Figure 5-15c, in agreement with the experimental results of both Sieverding and Van den Bosche [33] and Sharma and Butler [25], as well as the computational results of Snedden *et al.* [34, 35].

The AD case has no seal and thus no gap between stator and rotor hub surfaces, while the SD has an axial gap at the hub of 12.7% c_{RB}. This disrupts the boundary layer progression in the SD case and introduces a zone of shear between the annulus flow and the mostly quiescent fluid in the seal gap. Vortex shedding from the stator platform TE makes this a region with unsteady flow features.

The introduction of the wheelspace creates a disc pumping effect, whereby the rotor imparts both swirl and radial velocity to the fluid. The swirl component across the seal gap varies with both axial position, reaching unity on the rotor wall and zero on the stator wall,

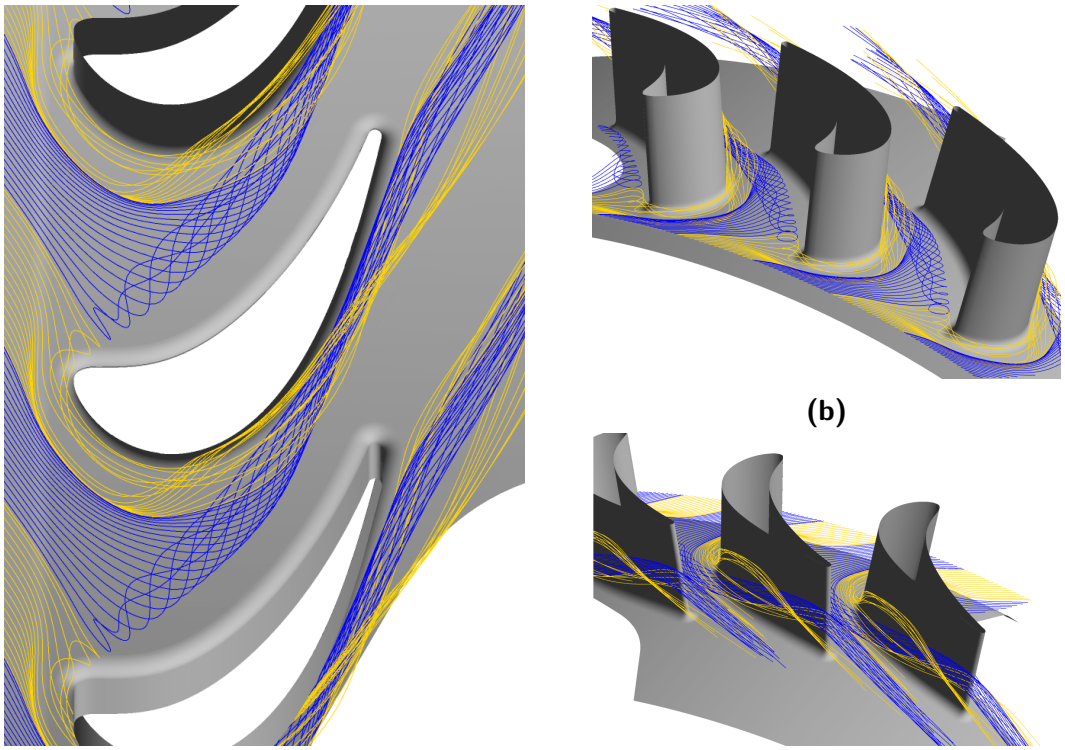

Figure 5-15: Streamlines tracing the secondary flows for a SD case with no superposed flow, (a) cascade, (b) upstream and (c) downstream views

and with circumferential position as shown in Figure 5-16a. Additionally, Figure 5-16b shows the non-dimensional radial velocity in the seal gap which highlights zones of both ingress and egress. This presents the fluid upstream of the RB LE with highly variable conditions: egress zones present a blockage causing deflection, ingress will remove low momentum fluid from the boundary layer region. These combined effects cause the alteration of the HSV-SS and can be attributed to the presence of the seal geometry alone.

The evolution of the stage efficiency for the SD *without* superposed flow, over the first computational revolution, can be seen in Figure 5-17. Both instantaneous (red) and moving, sector averaged data (blue) are presented. An initial transient lasts 0.4 revolutions, followed by periodic behaviour. Peaks corresponding to the expected vane-blade interaction frequency are again present. The moving average stage efficiency remains constant at 82.26% from 0.5 revolutions, with fluctuations in instantaneous efficiency of ±0.06% around the mean value. The introduction of the seal geometry has had a negligible impact on the overall stage efficiency.

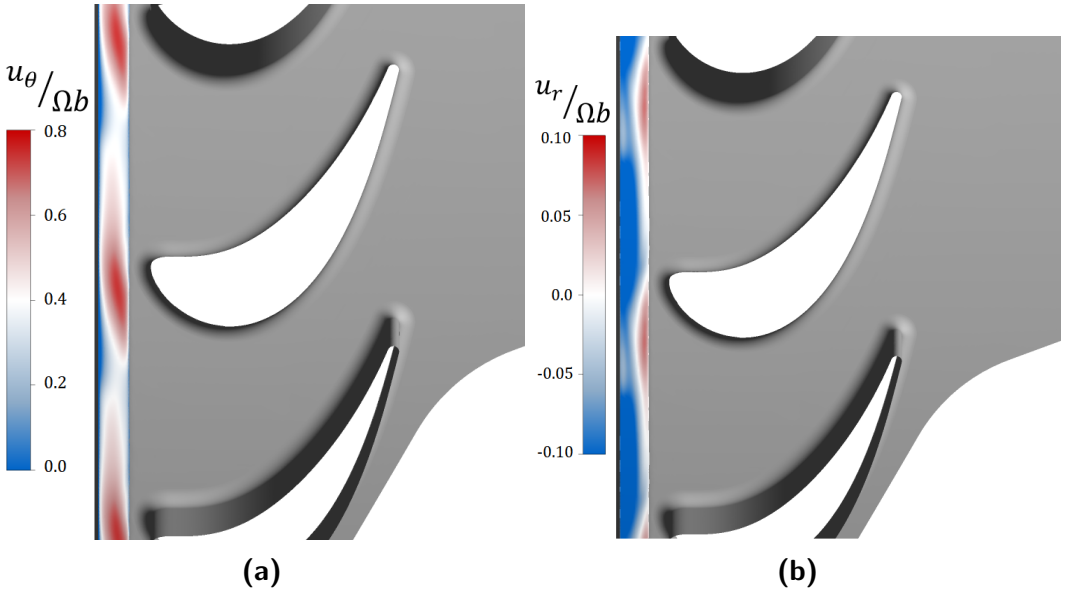

Figure 5-16: SD rotor, case with no superposed flow, (a) swirl and (b) radial velocity in the seal gap

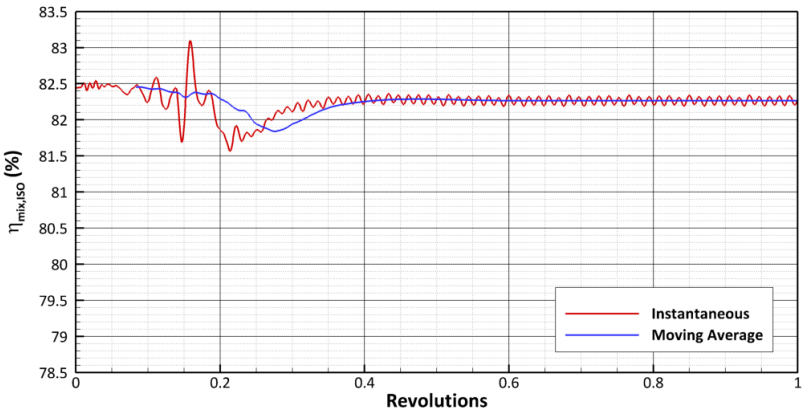

Figure 5-17: Time trace of $\eta_{mix,ISO}$ for SD case without superposed flow over the first revolution. Instantaneous data in red, sector-pass average in blue.

5.3 Stub Domain with Purge Gas

It was shown that the introduction of the seal and outer wheelspace geometry had an impact on the flow field in the rotor. This impact is small, but important and provided a useful insight prior to the analysis of the flow field with purge flow present. The following section presents simulations where a superposed purge flow is introduced through the rim-seal at the periphery of the wheel-space; the purge mass fraction is 1.7% of the mainstream flow. The purge flow is CO_2; the mainstream flow is air, as detailed in Chapters 3 and 4.

Midspan flow is presented in Figure 5-18 using streamlines released at the 0.5 s position and coloured by s. The incoming 2D flow is deflected radially towards the shroud on the suction side of the blade from 0.1 c_{RB} upstream of the blade. This is significantly earlier than seen in Figure 5-13, with no purge flow present. The spanwise migration reaches 0.58 s at 0.3 c_{RB} and exceeds 0.61 s by the mid-chord position; this represents a 3% shift in spanwise migration due to the introduction of purge flow near the suction surface. The radial shift towards the hub near the pressure surface has also increased, reaching 0.34 s towards the RB trailing edge. The secondary flow structures have significantly increased in size, causing distortion of the midspan flow field that covers a larger axial and radial range than previously seen. This has a detrimental impact on the stage efficiency, reducing from 82.25% to 80.46%. The cause of this increase in secondary flow structure size must still be determined. In order to do so, the purge flow is examined below.

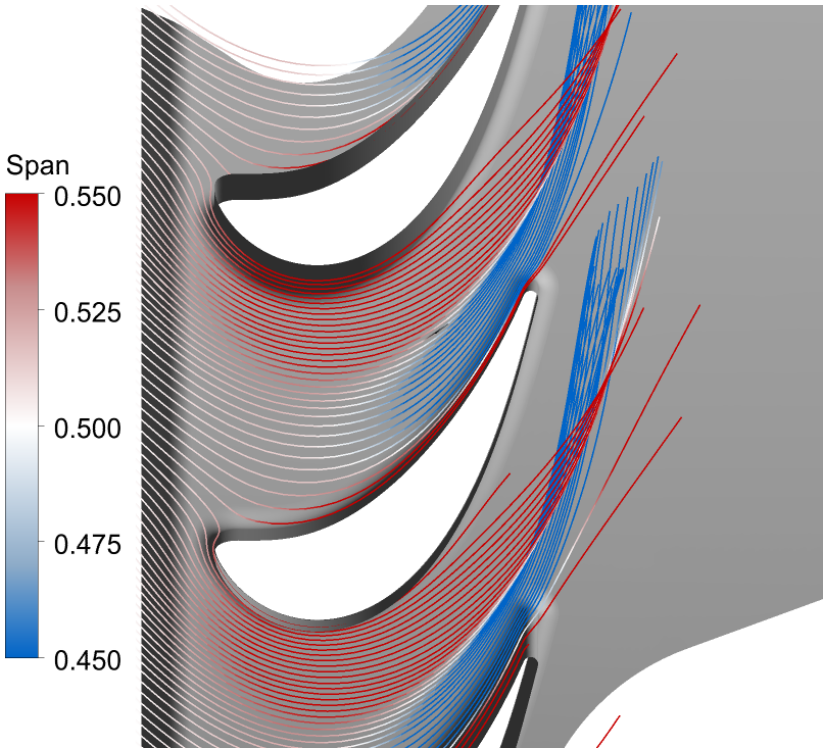

Figure 5-18: Streamlines in the rotor released at midspan, coloured by spanwise position, for a SD case with superposed flow

5.3.1 Visualising the egress plume

In order to visualise the egress plume as is emerges from the wheelspace, the ejected fluid can be traced as a region of increased CO_2 concentration moving through the blade passage. Contours of CO_2 are shown in Figure 5-19 for a series of axial planes. The contours have been limited to a minimum mainstream Mass Fraction (MF) of 9% in order to best visualise the main path of the egress plume. Plane R1, located in the seal gap, shows a relatively high MF of CO_2 across the whole of the blade pitch. A clear peak is seen slightly upstream of the BLE, corresponding to the low pressure region associated with the suction surface of the blade.

Plane R2, located at the BLE, shows that the CO_2 plume is now concentrated near to the SS. However, the plume is not tightly bound in a circular profile, suggesting the interaction of vortices. Indeed, once the locus of maximum CO_2 MF is extracted, it becomes clear that this does not necessarily coincide with the vortex centre.

As the egress plume moves downstream through the blade passage it migrates radially,

coinciding with a continuing reduction in MF as the purge flow mixes with, and is hence diluted by, the mainstream flow. Around the mid-chord (Plane R4) the plume is no longer wall-bound and is an indication that the HSV-PS has crossed the passage and impinged on the suction surface of the adjacent blade.

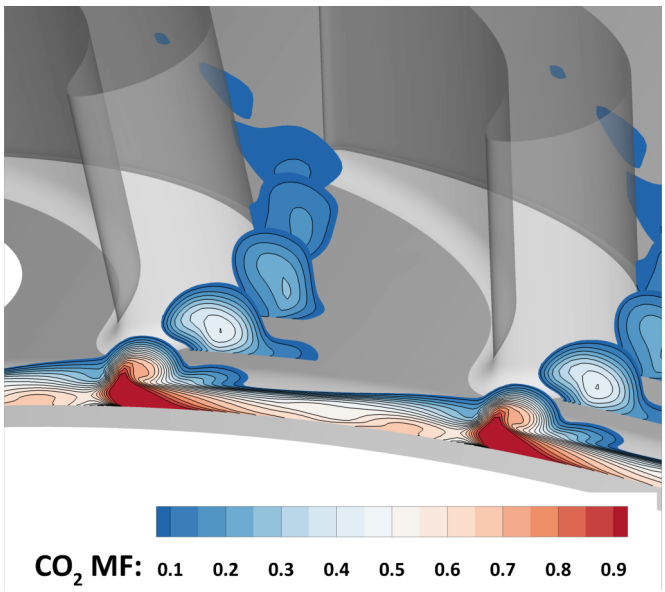

Figure 5-19: Contours of CO_2 MF (where > 9%) through the turbine blade passage

5.3.2 Vorticity

Contours of non-dimensional vorticity, coloured by signum z-vorticity, are provided in Figure 5-20a for Planes R2-7. This allows for the evolution of the HSV-PS ('B') to be visualised. The sense of rotation remains the same as for the unpurged case (Figure 5-10a). It is immediately clear, however, that the egress plume ('D') has a relatively large vorticity and inherits the same sense of rotation as the HSV-PS. This large, clockwise rotating structure dominates the smaller, counter-clockwise HSV-SS ('C'), subsequently reducing its size and strength. Additionally, the HSV-SS appears to be pressed against the suction-surface of the blade by the egress plume, which also causes radial migration of the HSV-SS.

A fourth region of high vorticity, 'E', is present, although further analysis - using Q-criterion - shows that this is not a coherent vortical structure and is composed of shear rather than rotation. The impending merger of the HSV-PS ('B') and the egress plume ('D') is apparent as the structures travel downstream of the plane at mid-chord (Plane R6). This is consistent with the behaviour predicted by Sharma and Butler [25].

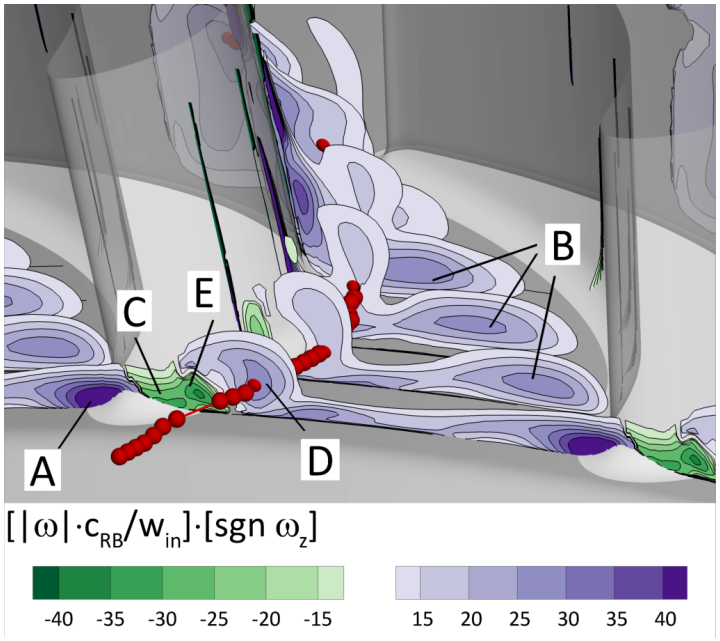

(a)

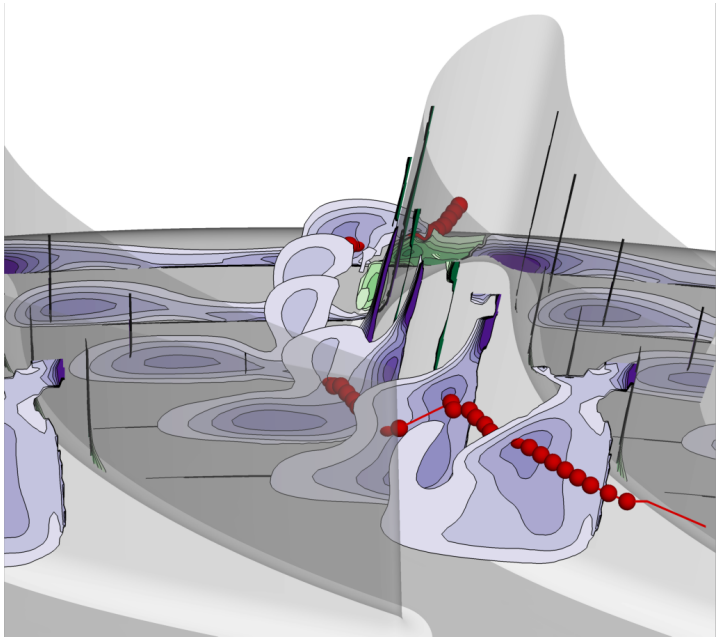

(b)

Figure 5-20: Distribution of non-dimensional vorticity in the rotor for a case with superposed flow (1.7% MF), view from (a) upstream and (b) downstream. The locus of max CO_2 is shown (in red spheres), corresponding to the path of the egress plume

The locus of maximum CO_2 MF is shown as a series of red spheres, calculated across a series of sequential axial planes; the spheres are connected by a series of short linear lines in order to aid the reader. The spheres allow the independent tracking of the egress plume in comparison to the vortical secondary flow structures in the annulus. It is clear that the maximum locus of CO_2 remains closer to the endwall than the centre of the suction-side vorticity; this is consistent for all axial planes. Figure 5-20b provides the reversed view. This enables the merger of plume and HSV-PS to be seen on Plane 7. Neither remain as a distinct feature; a single passage vortex is present.

Figure 5-21 shows the distribution of non-dimensional vorticity on a surface at 0.05 s, coloured using signum y-vorticity; the locus of maximum CO_2 is shown as a red sphere on each axial plane. The roll-up of the HSV ('A') and subsequently the HSV-PS ('B') are clearly visible, as before. The HSV-SS is not as easily distinguishable at this radial position due to its radial migration once the HSV-PS reaches the adjacent blade by mid-chord. The shear structure, 'E', is again visible. The boundary layer, signified by a region of increased vorticity ('F'), is again dominant throughout the passage, promoting rotation of the HSV-PS and the egress plume. This is likely a contributor to the rapid dilution of CO_2 in the egress plume.

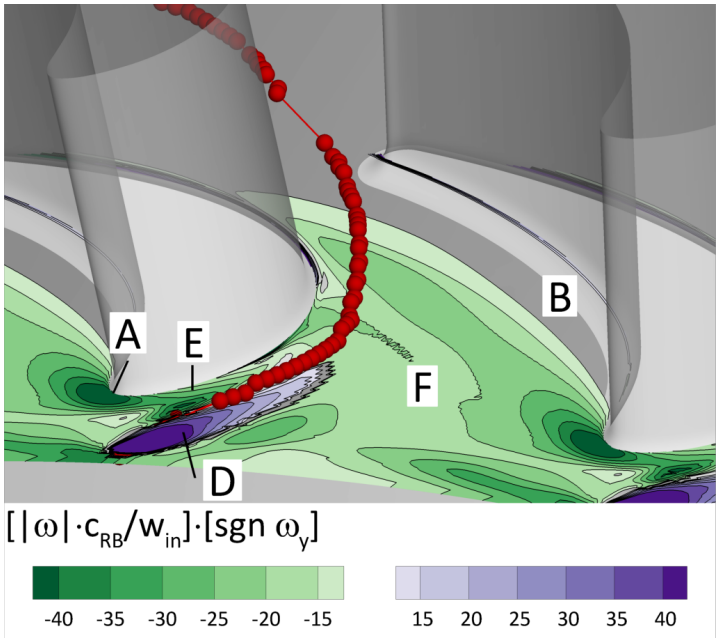

Figure 5-21: Distribution of non-dimensional vorticity in the rotor for a case with superposed flow (1.7% MF), view from upstream on a cylindrical surface. The locus of max CO_2 is shown (in red spheres), corresponding to the path of the egress plume

5.3.3 Q-Criterion

Figure 5-22 introduces the use of the Q-criterion (Hunt *et al.* [50]) as a way of defining coherent vortical structures. The first column is vorticity on planes R2, R4 and R6. The second column shows Q-Criterion and the third shows CO_2 MF using the previously established parameters.

Direct comparison is made between vorticity (1st column), Q-Criterion (2nd column) and the MF of CO_2 (3rd column). Results are shown for axial Plane R2 (1st row), Plane R4 (2nd row) and Plane R6 (3rd row); the location of the axial planes are shown inset. The secondary flow features are identified using a consistent lettering to that used in Sections 5.1.2 and 5.2.

Consider first the plane at the BLE ($z/c_{RB} = 0$, Figure 5-22a–c). The disappearance of feature, 'E', is apparent when considering Q-Criterion; here, a clear separation exists between 'C' and 'D'. The shear between these two separate vortical structures is therefore revealed as the source of the high vorticity noted 'E' in Figure 5-22a. The egress plume, however, is distorted by this shear phenomena, as noted by the lobed profile ('E') seen in Figure 5-22c.

Now consider the plane at $z/c_{RB} = 0.14$ (Figure 5-22d–f). The vortical structures 'C' and 'D' can be readily identified when considering vorticity, with two clear peaks in the vorticity contour. The larger vortex ('D') contains all of the CO_2 at this location, allowing it to be clearly identified as the egress plume; the smaller of the two vortices – the HSV-SS, 'C' - contains negligible CO_2. It should also be noted that the peak CO_2 concentration does not correspond with the peak vorticity, as seen in Figure 5-20. The Q-criterion is unable to detect the HSV-SS at this location as it has weakened considerably compared to the plane at $z/c_{RB} = 0$; however, the HSV-PS is now visible as it begins its excursion across the blade passage.

Finally, consider the furthermost downstream plane at $z/c_{RB} = 0.55$ (Figure 5-22g–i). The distinction between two discrete vortical structures is less pronounced, however two lobes of high vorticity are detectable; the increase in Q-criterion suggests that the two vortices are mixing. The CO_2 mass fraction, however, remains reasonably coherent and shows the radial migration of the egress plume ('D') away from the endwall. The interaction characteristics of these structures, occurring once they reach the mid-passage, are shown more clearly by considering the streamlines and streaklines in the turbine annulus.

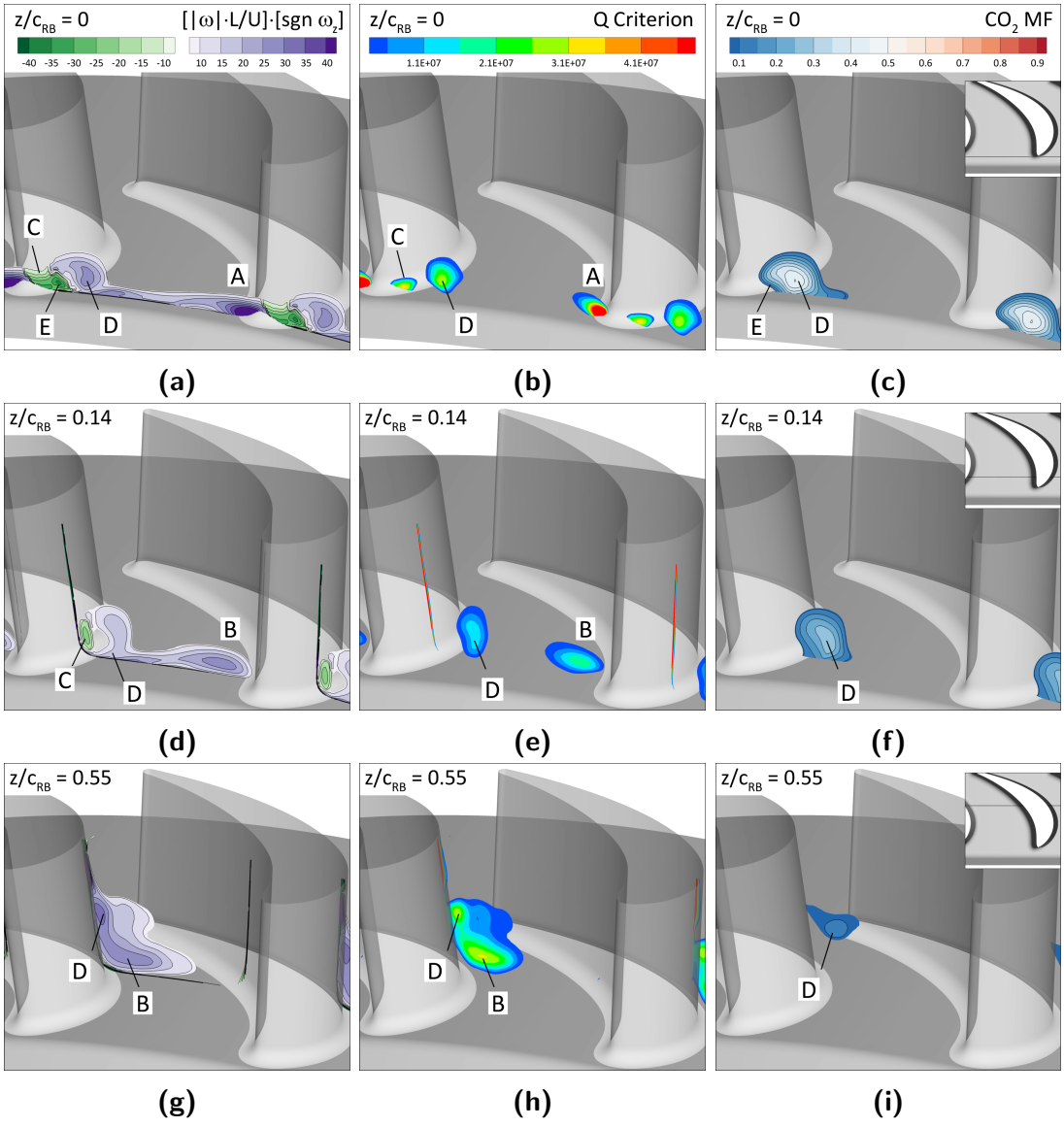

Figure 5-22: Vorticity (1st column), Q-Criterion (2nd column) and CO_2 mass fraction (3rd column) at z/c_{RB}=0 (1st row), z/c_{RB}=0.14 (2nd row) and z/c_{RB}=0.55 (3rd row)

5.3.4 Streamlines and streaklines

Figure 5-23 shows the span-wise migration of both the HSV-SS (gold) and HSV-PS (blue) using typical streamlines at their centres, produced from the time-averaged flow field. The HSV-PS remains endwall-bound until at least $z/c_{RB} = 0.49$ before rapidly migrating up the blade suction-surface, inducing a similar radial translation of the locus of maximum CO_2 (shown as black circles) that occurs upstream of the passage vortex. The HSV-SS (feature 'C') does not remain endwall-bound and is likely forced away from the hub by the corner vortex, which is not shown here. The radial migration of the HSV-SS and CO_2 peak follow similar trajectories but are not co-located. The inset shows the surface streaklines on the blade surface, relative to the three vortical features. The passage vortex (formerly the HSV-PS) is seen to migrate radially, reaching 70% of the blade span by the blade trailing-edge.

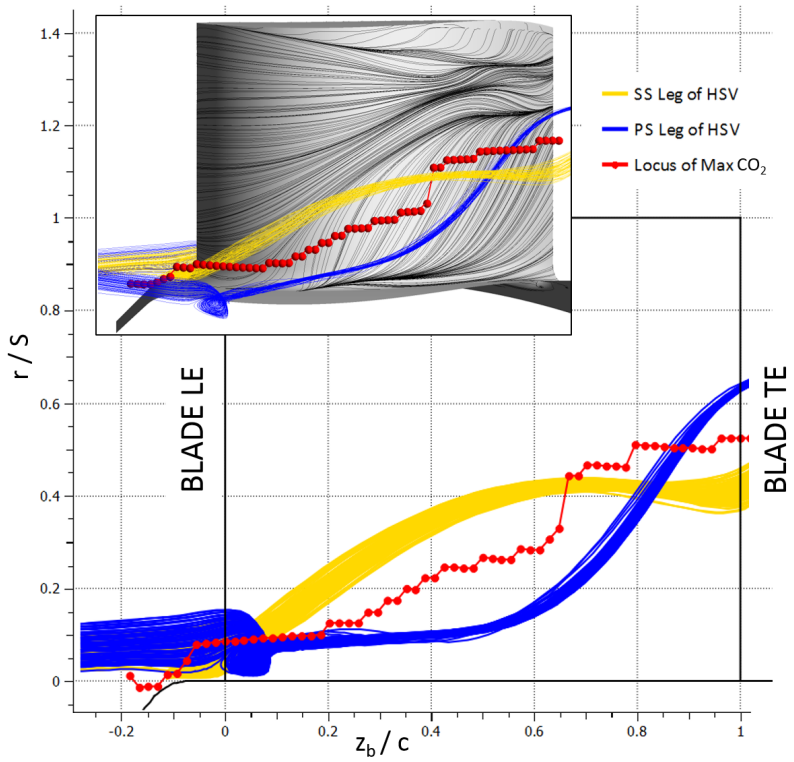

Figure 5-23: Streamlines and streaklines tracing the secondary flows for a case with superposed flow (1.7% MF), view on the radial-axial plane; the locus of maximum CO_2 is shown as red circles

Figure 5-24 shows the pitch-wise migration of the secondary flow features identified in previous figures: HSV-SS (gold); HSV-PS and passage vortex (blue); and egress plume

(red). The pitch-wise migration of the HSV-PS is clearly visible, impinging of the suction-surface of the adjacent blade by $z/c_{rb} \approx 0.5$. The HSV-PS can be seen to pass under the HSV-SS and egress plume (Figure 5-24b), forcing the latter to migrate radially. The plume can be seen to be turned rapidly by the annulus flow as it exits the rim seal before lifting the HSV-SS.

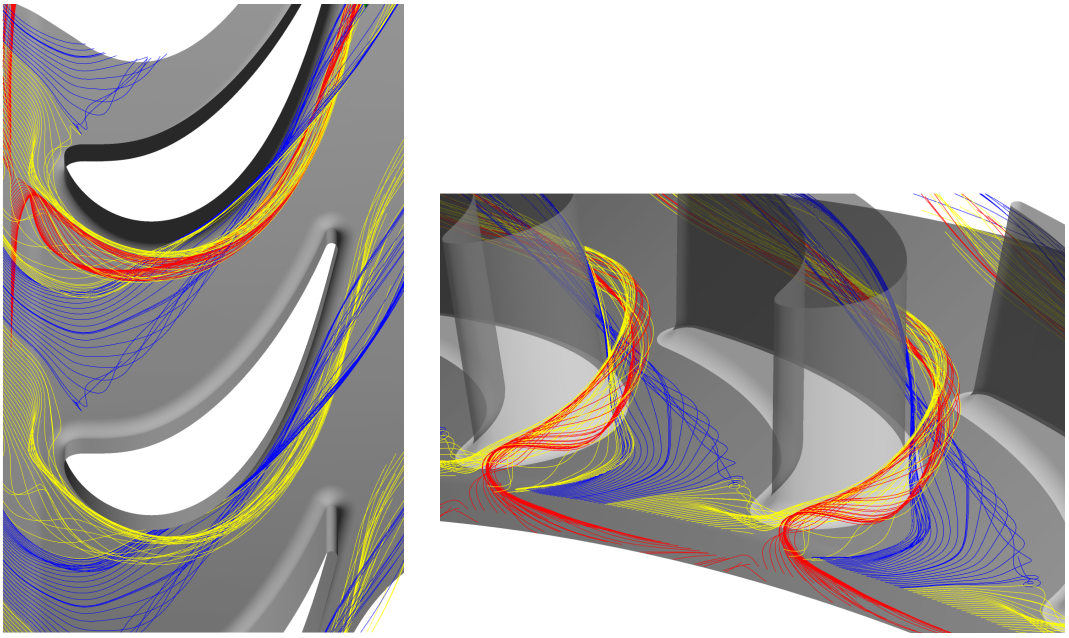

(a) **(b)**

Figure 5-24: Streamlines tracing the secondary flows for a case with superposed flow (1.7% MF), (a) cascade and (b) upstream view

Surface streaklines on the endwall are shown in Figure 5-25, superimposed over a map of the local pressure at the endwall surface. The surface streaklines highlight the dominance of the secondary flow field close to the hub, with negligible axial component visible. Figure 5-25a presents the AD case, while Figure 5-25b presents the SD with purge. The pitch-wise migration of the HSV-PS is driven by the strong cross-passage pressure gradient seen in the distribution of pressure on the endwall, visible for both cases. Figure 5-25 identifies the locations of the saddle point (S_p), nodal lines of separation (N_s) and attachment point (N_a).

The S_p moves due to the presence of purge flow, as indicated by the lines of constant pitch and axial coordinate. This modest shift is accompanied by a more significant change of pattern near the leading edge. Figure 5-25a shows a simple N_{s1} line from the S_p to

the suction side of the blade, indicating the presence of the HSV-SS. In Figure 5-25b, however, the HSV-SS is less well defined, agreeing with the previous assessment of the HSV-SS suppression due to egress. Figure 5-25b shows N_{s2} extending upstream in to the seal chute, which is attributed to the change of geometry rather than the presence of egress.

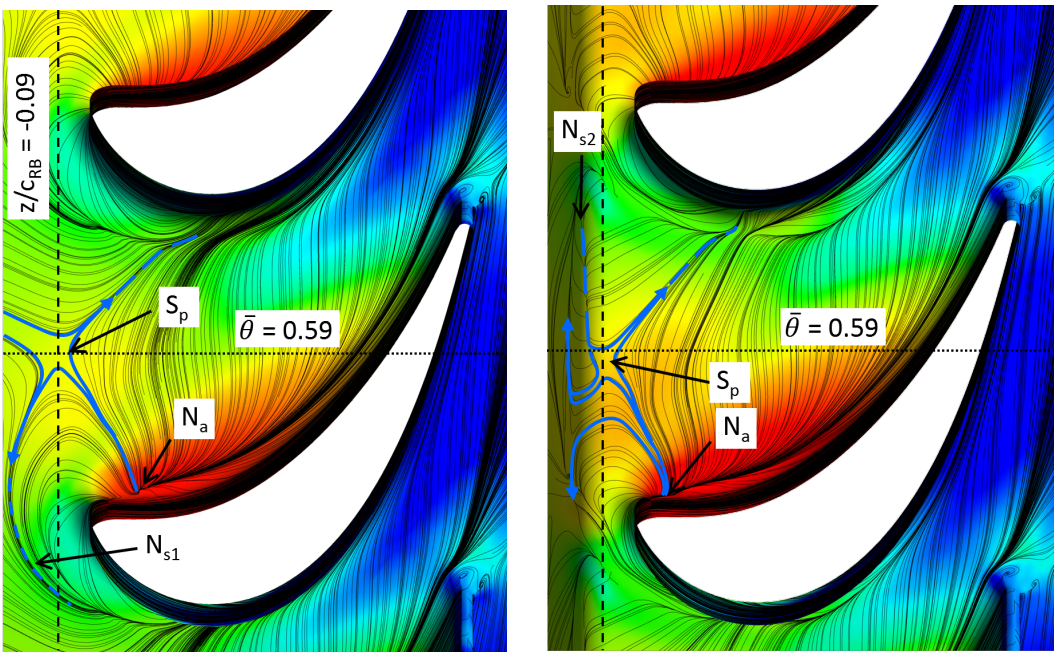

Figure 5-25: Surface streaklines with limiting lines superimposed over a map of the pressure on the endwall (shown as coloured contours): (a) AD and (b) SD with superposed flow (1.7% MF).

The evolution of the stage efficiency for the SD with superposed flow, over the first computational revolution, can be seen in Figure 5-26. Both instantaneous (red) and moving, sector averaged data (blue) are presented. An initial transient lasts 0.4 revolutions, followed by increasingly periodic behaviour. True periodicity is present from 0.8 revolutions. The periodic behaviour now shows peaks corresponding to the expected vane-passing frequency, which suggests a dominance of the vane frequency. However, the non-sinusoidal shape indicates that additional frequencies are still present in the signal, visible in the 0.5 to 0.6 revolution range where the vane-blade interaction frequency is dominant. The moving average stage efficiency remains constant at 80.48% from 0.7 revolutions, with fluctuations in instantaneous efficiency of ±0.18% around the mean value. This represents a reduction in overall efficiency of 1.77% that can be attributed directly to the presence of superposed purge flow. In addition, the unsteady fluctuations were seen to significantly increase in

magnitude (from ±0.05% to ±0.18% around the mean value).

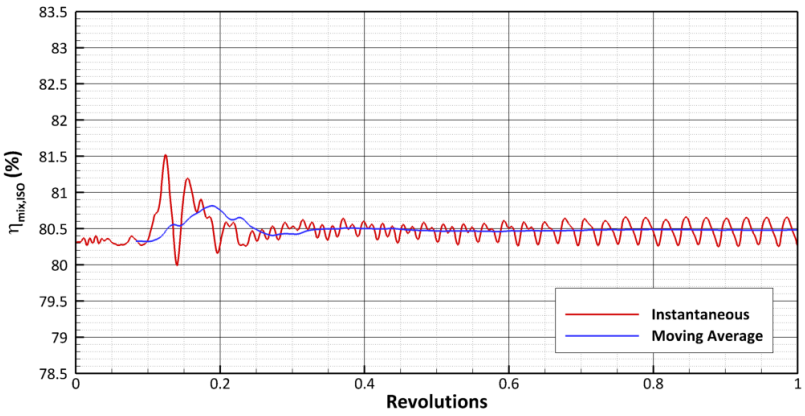

Figure 5-26: Time trace of $\eta_{mix,ISO}$ for SD case with superposed flow over the first revolution. Instantaneous data in red, sector-pass average in blue.

5.4 Implications for Endwall Contouring Design

Understanding the interaction mechanisms between purge and mainstream flows in gas turbines is critical when attempting to design endwall contours. Endwall contouring is a technique used to manipulate the local pressure and velocity fields immediately downstream of the rim-seal and throughout the blade passage in order to reduce aerodynamic loss. In addition, recent research – including that by the author [13] – has sought to use endwalls, designed in combination with the rim-seal, to improve the performance of the secondary flow system in addition to maintaining the aerodynamics in the mainstream gas-path.

Primarily, it is hoped that the work presented here, characterising the interaction effects in the presence of a non-contoured endwall, will be useful to designers and researchers investigating the more complex interaction mechanisms when contouring is introduced. Secondly, it has been demonstrated that the size of the computational domain has a marked effect on the unsteadiness seen in the flow field. Reducing unnecessary unsteadiness is strongly desirable when predicting the total-to-total stage efficiency gains created by contoured endwall designs.

5.5 Summary

The flow field for the cylindrical, or baseline case, has been described in detail for two representations of the LAR stage. Both stator and rotor domains were detailed for the Annulus Domain. The stator in particular provided a relatively simple flow field which reproduced the flow features presented in Chapter 2 and was thus a useful test for their visualisation without the complexity added by rotation, geometric influences or superposed purge flow.

The rotor domain showed large secondary flow features, as identified using surface streaklines. Sieverding and Van den Bosche's boundary layer streamline technique was particularly useful in identification of the HSV formation as well as the convection of the HSV-SS and HSV-PS through the blade passage. This revealed that the HSV-SS and the HSV-PS become entwined for the cases without purge, in agreement with previously published results. The introduction of purge flow complicates this picture.

The use of streamlines released from the inlet midspan reveals the impact of secondary flows on the expected quasi-2D flow. Spanwise migration was found to be towards the shroud near the blade suction surface and towards the hub near the pressure surface for all cases, including the non-rotating stator flow field. The migration was found to increase marginally when the geometry included the seal geometry and significantly when purge flow was present, in agreement with the findings of Schuepbach *et al.* [47].

The cause of the significant radial displacement was found to be the presence of a large, coherent egress vortex. This was successfully visualised using CO_2 mass fraction, indicating that the plume was located near the suction side of the blade and coincident with a region of low pressure. In the experimental campaign for the LAR this visualisation will be possible using PLIF and these CFD simulations will be able to be validated using that technique.

The CO_2 plume position is in conflict with the findings of Schrewe *et al.* [46] who found the plume entrained in the HSV-PS. However, the visualisation method used in the present work was not able to capture the strength of the underlying vortex as the plume widens in mass fraction terms where the vortex is stretched. It was further found in the present work that the egress plume suppressed the HSV-SS and strengthened the HSV-PS, which is in agreement with the findings of Schuepbach *et al.* [48]. The plume and HSV-PS were found to merge once the HSV-PS had migrated across the passage.

Chapter 6

Contoured Endwall Design

A significant proportion of the loss arising from endwall flows is entropy generation in the boundary layers. Another key component of loss comes from the stream-wise vorticity inherent in the secondary flow structures. Streamwise vorticity promotes secondary kinetic energy (the component of kinetic energy normal to the direction of the passage flow), which decays through the passage. The decay of secondary kinetic energy creates entropy – or loss.

Further mixing losses originate from the re-introduction of cooling air, bled from the compressor, into the mainstream flow in the turbine. Cooling air, which is used to purge the disc cavities, emerges from a rim-seal (see Figure 5-19) immediately upstream of the blade endwall. Flow emerging from the rim-seal is known as egress. The interaction of egress flow with the secondary flow field in the turbine annulus can enhance the secondary features; the egress plume increases the strength of the HSV-PS and passage vortex as seen in Chapter 5.

Designers use geometric shaping of the turbine endwalls to minimise secondary flow loss; this process is known as EndWall Contouring (EWC). The objective of EWC is to manipulate, and control, the annulus pressure field such that the growth of passage flow features is reduced. More recently, the interaction between EWC and the upstream rim-seal has become an increasingly important consideration – this has been established in the literature in Section 2.2.4 and 2.4.

This chapter builds on the work published in Schreiner *et al.* [13], where a novel

approach to endwall design is described in detail. Due to the length of that publication, not all endwall designs were presented. This work contains a number of additional endwall designs and thus the numbering system used in the paper has been adapted to include these additional designs.

6.1 Feature-based Approach

EWC has been implemented by a number of authors, predominantly using an optimisation tool to achieve a reduction in loss or total pressure drop across the stage. As shown by Regina *et al.* [68], the gains obtained in this manner are not robust in the context of changing purge flow conditions.

The present study takes a novel approach, implementing specific, discrete features in the blade passage in the presence of rim-seal leakage flow. Each feature has a desired impact and simulations were used to obtain an understanding of the influence of the control parameters. In some cases the engine designer will want to maintain the stage reaction between their non-contoured and contoured endwall designs, which will necessitate keeping the throat area fixed. This approach is applied in all endwall geometries presented here.

The naming convention used for contoured endwall designs in this study is the prefix EW for EndWall, followed by a three digit number, starting from 001. A suffix letter has been used to modify the numbering system used in [13], applied where additional designs of a family exist. The three geometric features considered in this study are: a suction-side trough, a pressure-side trough and a leading-edge feature. The basis for including each of these features will now be considered in turn. The baseline or cylindrical hub is shown in Figure 6-1 with the possible endwall extents (-0.1 < s < 0.1) indicated using coloured contours. For the baseline, this contains the entirety of the blade root fillet above the hub and the outer portion of the chute seal below the hub. These limits were imposed due to manufacturing constraints.

Controlling parameters for the features are shown in Figure 6-2 and are primarily:

1. Trough pitchwise position (θ_{SSTR} or θ_{PSTR} = θ/θ_{RB}) measured from the respective surface;
2. Trough depth (d);

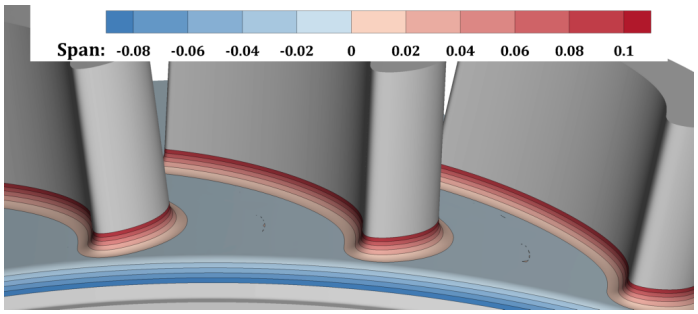

Figure 6-1: Isometric view of the baseline rotor, coloured by spanwise extent (-0.1 < s < 0.1)

3. Leading-Edge Feature angle (α_{LEF}), measured to the axial direction and
4. Leading-Edge Feature height (h).

These parameters have been used to control the underlying endwall features in the following results and are non-dimensionalised using span (s) and blade passage azimuthal extent (θ_{RB}). The blending of each discrete feature to achieve a continuous and smooth surface required the use of fillet functions within a proprietary CAD package. This is noted in more detail below.

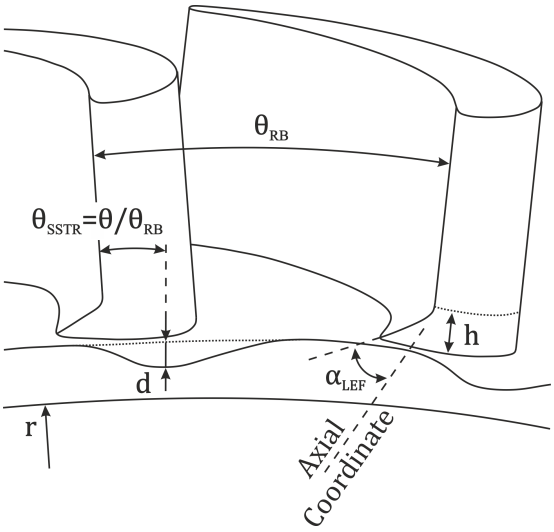

Figure 6-2: Controlling parameters for the Suction-Side TRough and Leading-Edge Feature

6.1.1 Suction-side Trough

The egress plume documented in [12], and described in more detail in Section 5.3, was identified as a flow structure that contributed strongly to losses in the stage; the egress plume was shown to promote radial migration of the HSV-SS. In order to control the pitchwise position and radial migration of this structure, a Suction-Side TRough (SSTR) was proposed, located near to the suction-surface of the blade.

This trough was intended to provide a channel through which to guide the egress plume, subsequently reducing its influence up the span of the RB. Controlling parameters for this feature include the pitchwise location of maximum depth as a fraction of local pitch ($\theta_{SSTR} = \theta/\theta_{RB}$) and the maximum depth below a cylindrical baseline as a fraction of span (d/s), as shown in Figure 6-2. The trough was constrained to return to the baseline endwall shape at, or before, the throat. Two-variants of this feature can be seen in Figure 6-3a and b, identified as EW001 and EW002.

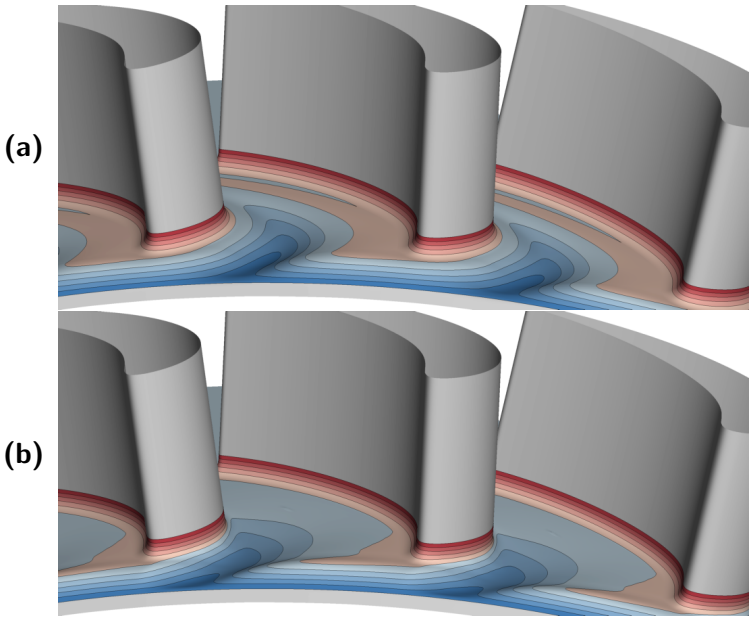

Figure 6-3: Isometric view of the Suction-Side TRough rotors, coloured by spanwise extent (-0.1 < s < 0.1) for (a) EW001 and (b) EW002

6.1.2 Pressure-side Trough

The *Pressure-Side TRough* (PSTR) was proposed as a method to increase the relative prominence of any leading-edge features (i.e. locally increasing the height of a leading-

edge ridge). It was also intended to provide some control of the cross-passage pressure gradient. This feature can be seen applied to four endwalls in Figure 6-4. Here, the controlling parameters again include $\theta_{PSTR} = \theta/\theta_{RB}$ and d/s.

EW003A (Figure 6-4a) utilised a very shallow trough extending across half the pitch. EW003B (Figure 6-4b) increased the depth of this feature and moved the minimum towards the pressure surface. Both troughs were intended to increase the local prominence of other features and provide a modest control of the cross-passage pressure gradient. EW003C (Figure 6-4c) is an evolution of EW002 and EW003B, combining a PSTR (EW003B) and SSTR (EW002). EW003D (Figure 6-4d) combined the leading-edge feature of EW004A (Figure 6-5a) with EW003C.

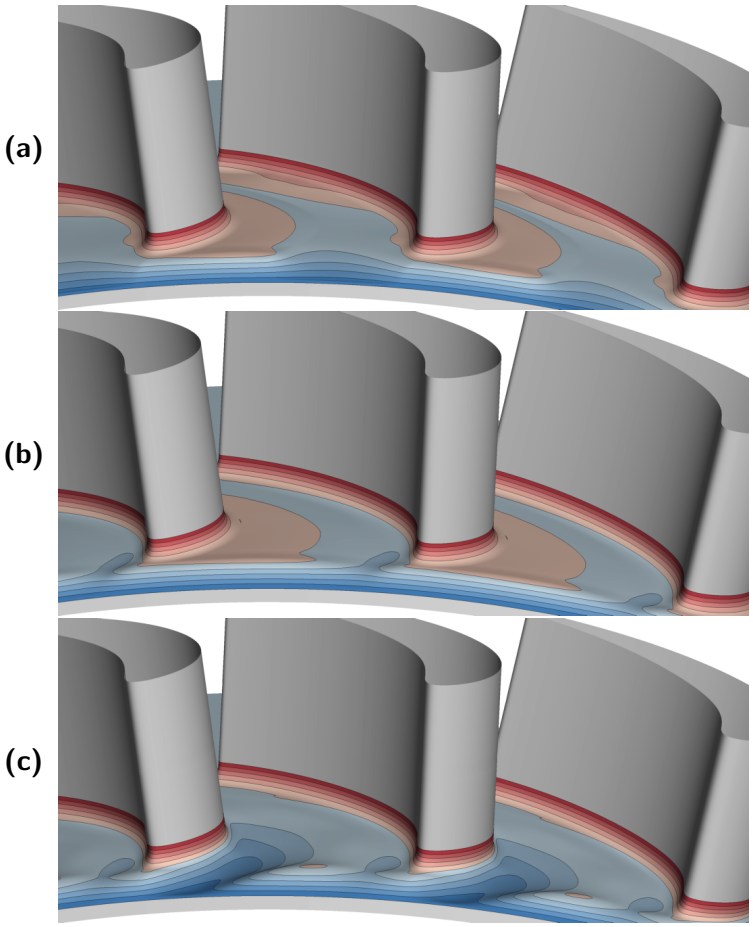

Figure 6-4: Isometric view of the rotor, coloured by spanwise extent (-0.1 < s < 0.1) for Pressure-Side TRough designs: (a) EW003A, (b) EW003B, (c) EW003C, and (d) EW003D

(d)

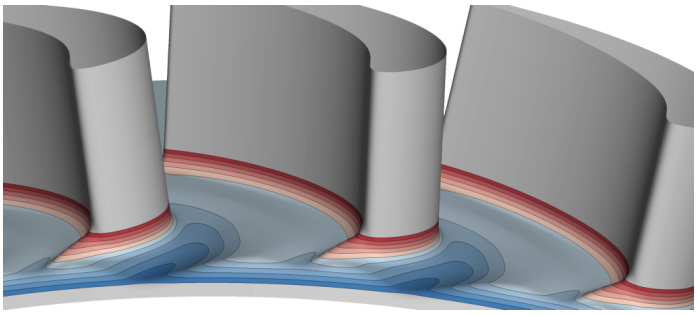

Figure 6-4: Isometric view of the rotor, coloured by spanwise extent (-0.1 < s < 0.1) for Pressure-Side TRough designs: (a) EW003A, (b) EW003B, (c) EW003C, and (d) EW003D

6.1.3 Leading-Edge Feature

The roll-up of the incoming boundary layer at the RB LE causes the formation of a HSV, shown throughout Chapter 5 as being present for all cases. Each leg of the HSV is convected downstream on either side of the blade, with the trajectories being dependent on the presence of the egress plume. In order to control the formation of the horseshoe vortex a *Leading-Edge Feature* (LEF) was proposed.

The aim of this feature is to create a more gradual transition between cylindrical hub and blade surface, enhancing that offered by a simple fillet radius. Examples of this feature can be seen in Figure 6(e) through (i). Controlling parameters for the LEF included the angle between the ridge-line of the feature and the axial co-ordinate (α_{LEF}) and the maximum height above the cylindrical baseline as a fraction of span (h/s) as shown in Figure 6-2. Section 6.1.3 examines EW004A, EW004B, 005 & 006, which introduce LEFs to the EW002 SSTR. Following this, EW007A and 008 combine the beneficial aspects from all three component features and are considered in Section 6.5

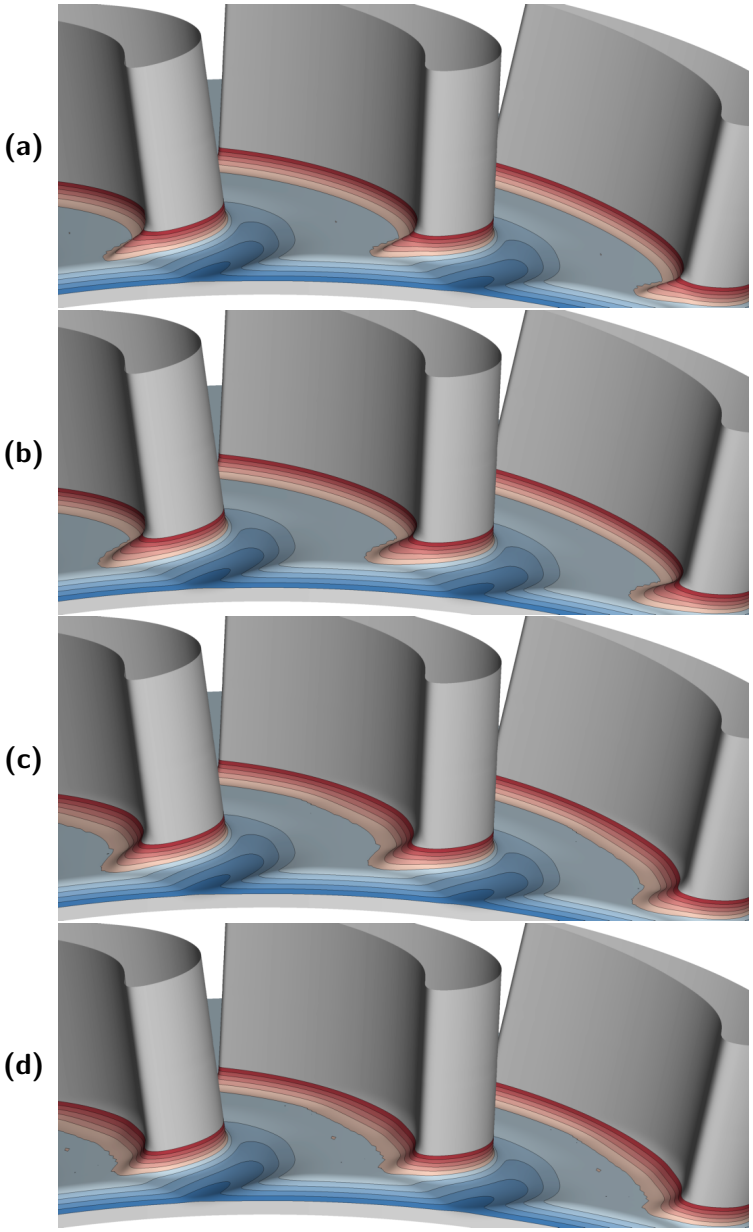

Figure 6-5: Isometric view of the rotor, coloured by spanwise extent (-0.1 < s < 0.1) for Leading-Edge Feature endwalls (a) EW004A, (b) EW004B, (c) EW005, and (d) EW006

6.2 Endwall Generation

Endwall geometry was created using a multi-step, multi-software approach due to the complexity of the surfaces and the difficulties arising from the introduction of the blade root fillet. The endwall design tool of Wood *et al.* [115] provided an initial framework for generating features, which were then manipulated in 3D CAD. The design process was iterative, requiring that each new design be informed by previous studies.

In general the process was as follows:

1. Determine egress plume location and pressure distribution for region between seal chute and BLE (see Figure 5-19).
2. Determine incoming flow angle distribution across span (see Figure 6-6).
3. Position SSTR so as to reduce the pressure locally, encouraging egress at a specified location (Figures 6-7 and 6-8).
4. Align LEF with incoming flow (Figure 6-9).
5. Create blade root fillet.

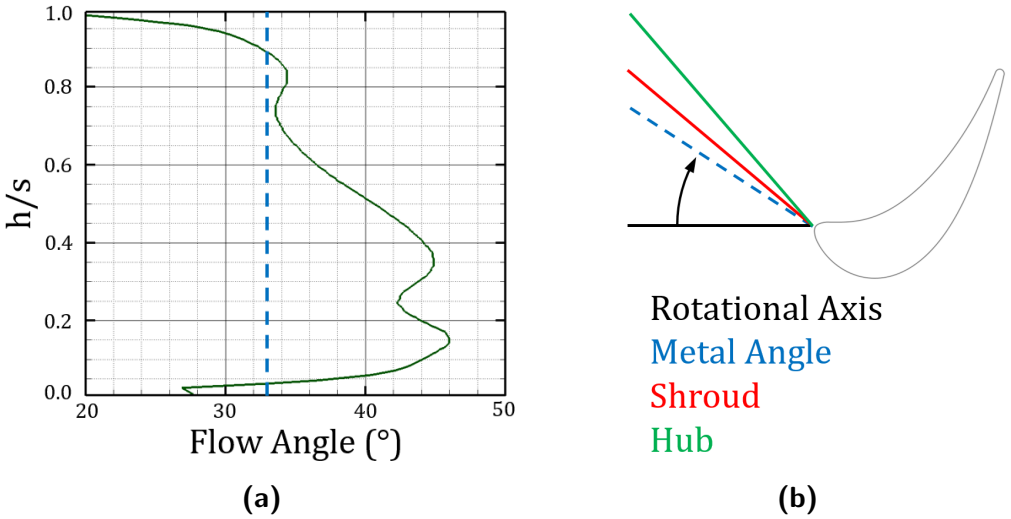

(a) **(b)**

Figure 6-6: Flow angle distribution across span (a) and (b) comparison of hub, shroud and metal angles

A summary of all the endwalls utilised is provided at the end of this chapter, their controlling parameters and a description of their form.

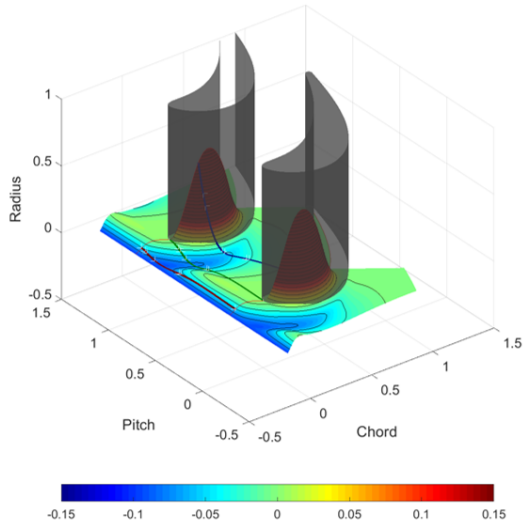

Figure 6-7: Initial positioning of SSTR using Wood's [115] tool

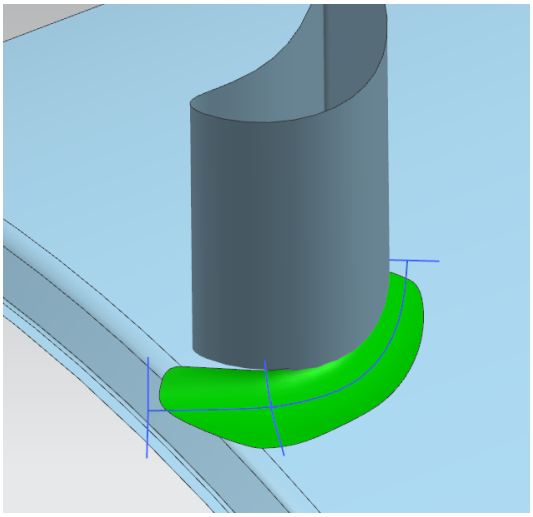

Figure 6-8: Creation of SSTR using 3D CAD

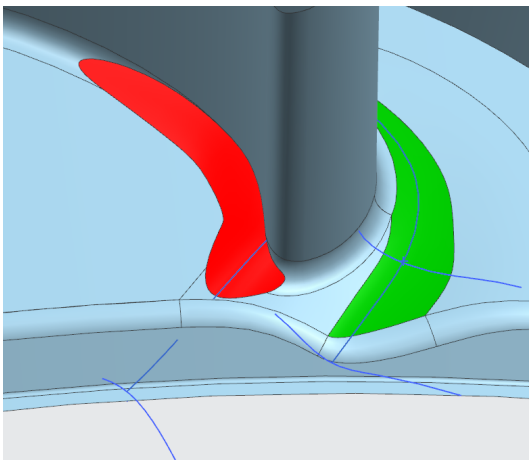

Figure 6-9: Creation of LEF using 3D CAD

6.3 Effect of Trough Features

The performance of trough and leading-edge features will be presented sequentially. Insight acquired from this feature-based study was then used to inform the design of an improved endwall (Section 6.5). All results are presented for the fully purged case, that is $\phi_0 = 0.0134$.

Figure 6-10a shows the path of CO_2 (egress) as it emerges from the seal gap and passes through the blade passage; this simulation is for the baseline cylindrical endwall and is essentially a repeat of Figure 5-19 for convenience, along with the axial plane locations. The planar location of each contour is shown on a cascade view of the stage (inset), with the first plane being located at the mid-plane of the seal and the second plane at the RB LE. A detailed discussion of the egress path and its interaction with the mainstream flow for the baseline (non-contoured) geometry is presented in Section 5.3. The data is included here in order to aid direct comparison with the contoured geometries that form the basis of this study.

At the first plane, there is CO_2-egress across the whole pitch, with the highest concentration emerging close to the suction-surface of the RB; a second, narrower peak in concentration occurs at the leading-edge of the blade. The primary plume of CO_2 (identified as 'D' in the figure) forms a large vortical structure, as demonstrated in Section 5.3, which is convected downstream. The radial migration of the plume is visible from the third plane onwards. A secondary feature, highlighted as 'B', is the entrainment of a small amount of CO_2 in the HSV-PS. The interaction of these flows is highly unsteady but periodic in nature, coinciding with the NGV passing frequency in the rotating domain. The CO_2 plume traces a helical path in the time-resolved results, leading to an apparently large vortex in the time-averaged sense.

Figure 6-10b and c present the path of CO_2-egress through the blade passage for the two endwalls featuring solely an SSTR. EW001 shows a redistribution of the CO_2 in the seal region, with a significant region of low concentration forming circumferentially adjacent to the egress plume. Additionally, the second egress peak (introduced above) appears to have been strengthened for this case. EW002 shows a more evenly distributed CO_2 with pitch when compared to the baseline endwall; the magnitude of the second peak in CO_2 also reduces.

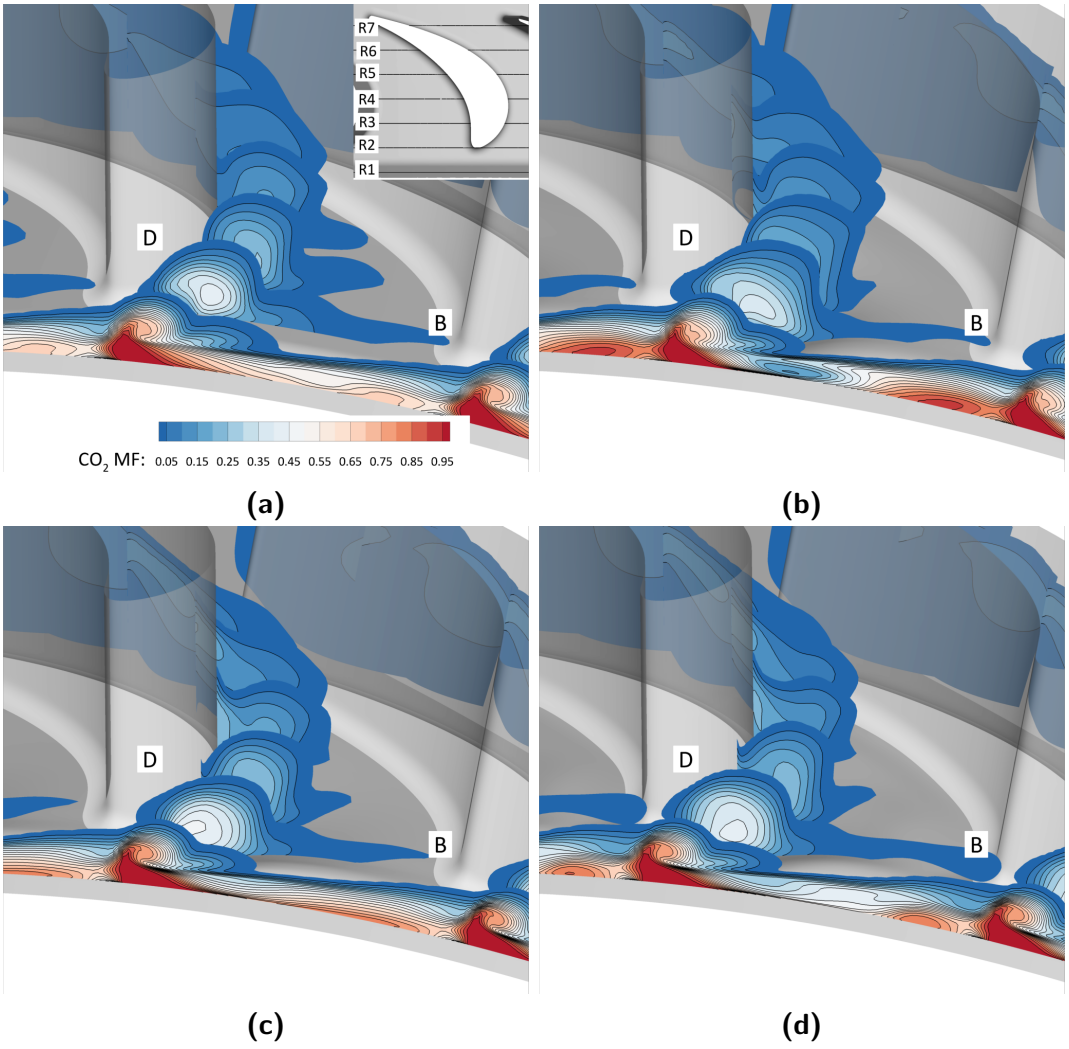

Figure 6-10: Contours of CO_2 MF (where > 9%) through the turbine blade passage for (a) baseline, (b) EW001, (c) EW002 and (d) EW003C

Figure 6-10d presents the path of CO_2-egress for EW003C; EW003C introduces a PSTR to EW002. Here, the pitchwise redistribution of CO_2 seen with EW002 has been reversed, bearing more similarity to the baseline case. However, the entrainment of CO_2 into the HSV-PS (feature 'B') has been enhanced, an unintended negative effect. It is believed that this increase of CO_2 concentration in the HSV-PS is responsible for the 0.17% drop in efficiency between EW002 and EW003C, documented in Table 6.1. While all trough features reduced the unsteady fluctuations in stage efficiency relative to the baseline, the influence on stage efficiency itself was either negligible or adverse.

Figure 6-11 quantifies the radial and pitchwise position of the CO_2 plume at the RB LE. Overlaid on the CO_2 plume at each location are radial bands at 0.05 s increments, along with lines of constant θ (0.1 θ_{RB} or 1° increments), forming a polar coordinate grid. Compared to the baseline (6-11a), the three endwalls can be seen to move the CO_2 plume by varying degrees. EW001 (6-11b) reduces the radial extent of the plume and moves it away from the suction-side of the blade. EW002 (6-11c) also reduces the radial migration, to a greater extent than EW001, but moves the plume towards the suction-side of the blade. This result is consistent with the relative positions of the two SSTRs (see Table 6.1).

EW003C (6-11d), however, appears to increase the radial migration of the egress plume when compared to EW002. The pitchwise location of the plume for EW003C is closest to that seen with the baseline configuration, suggesting that the introduction of the PSTR has acted to counteract the influence of the SSTR.

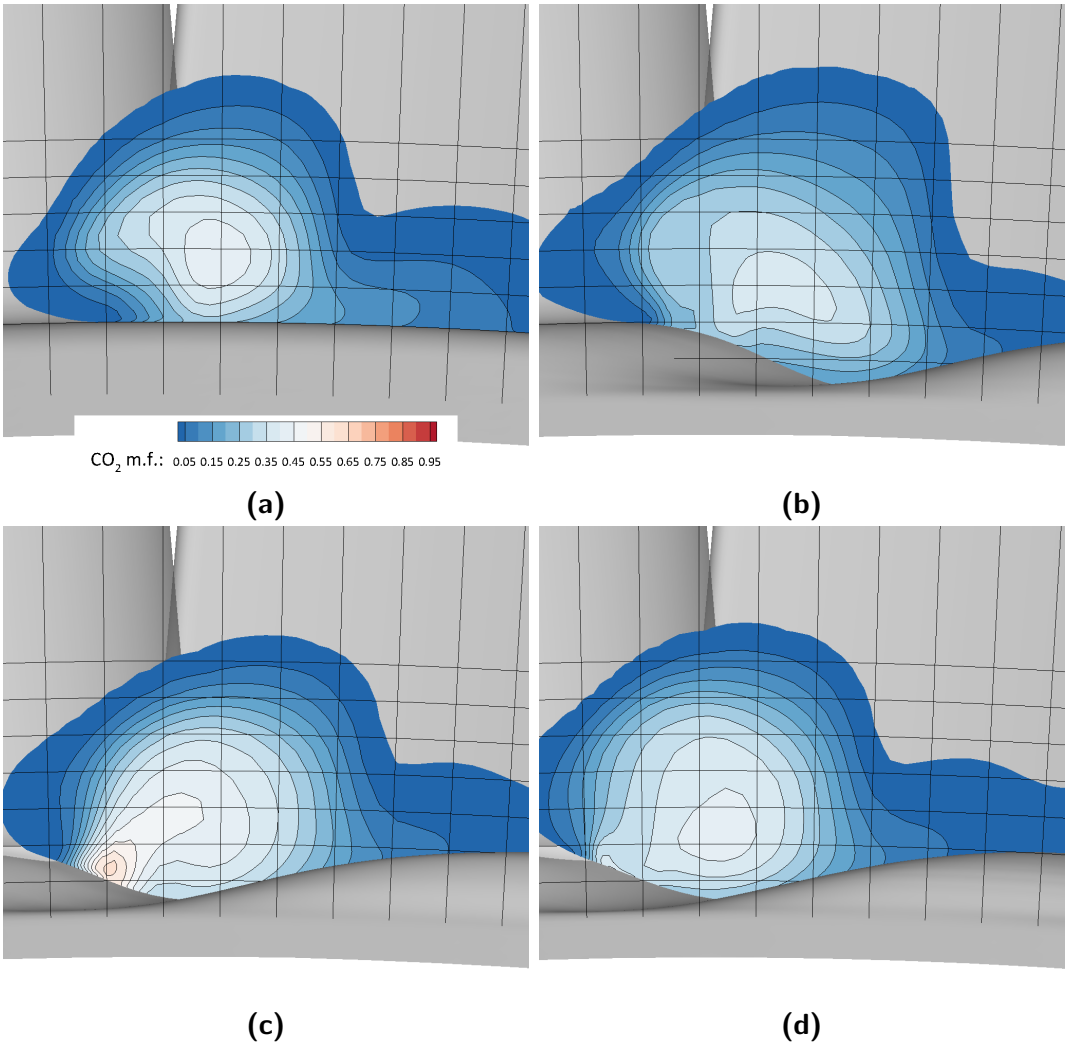

Figure 6-11: Position of the CO_2 plume at $z/c_{RB} = 0$ for (a) baseline, (b) EW001, (c) EW002 and (d) EW003C

The effect of the trough features on the cross-passage pressure gradient is shown in Figure 6-12a and b for SSTR and PSTR endwalls respectively. Data is presented for an axial plane at 0.37 c_{RB} and limited to the hub surface and blade root fillet only. Pitchwise position is taken as $\overline{\theta}_{RB} = \theta/\theta_{RB}$, which reduces to a range of less than 1 in the passage due to the presence of the blades.

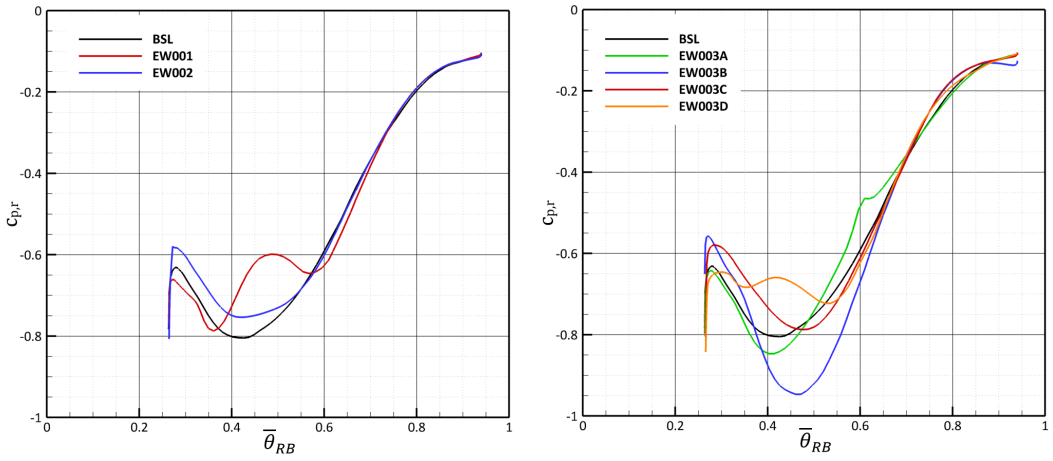

Figure 6-12: Effect of trough feature on the cross-passage pressure gradient at the 0.37 c_{RB} for (a) SSTRs and (b) PSTRs

In Figure 6-12a, both SSTR endwalls (EW001 and EW002) are seen to have only a negligible influence near the pressure surface, as expected. Closer to the suction side, the pressure distribution is heavily modified by the trough feature and both endwalls increase the minimum value of $C_{p,r}$. EW001 introduces a secondary peak, while EW002 does not. Neither significantly affect the cross-passage pressure *gradient* across the bulk of the passage.

In Figure 6-12b, all PSTR endwalls (EW003A through D) are also seen to have only a negligible influence near the pressure surface. In contrast, both EW003A and EW003B have a strong effect close to the suction surface, where no contouring is present. This was unexpected and undesirable. Indeed, EW003B shows a significant increase in the cross-passage *gradient*, achieved by reducing the minimum $C_{p,r}$ and moving its location towards the PS. EW003A introduces a mid-passage kink to the curve, possibly suggesting a non-smooth transition from trough to cylindrical endwall. EW003C, combining PSTR and SSTR, provides a pressure distribution close to the baseline, agreeing with the previous observation that the introduction of the PSTR has negated any impact due to the SSTR.

This conclusion led to the abandonment of the PSTR.

Following the analysis of these endwalls, in which EW002 exhibited the greatest reduction in unsteady fluctuations in stage efficiency, EW002 was selected for further development. Three different leading-edge features were introduced to EW002, with designs numbered EW004A to 006. Owing to the poor performance of the PSTR in controlling the cross-passage pressure gradient, no further iterations of this feature were considered.

6.4 Effect of Leading-Edge Features

Four geometries with LEFs were investigated, including variations in slenderness and radial extent (see Figure 6-5a to d). The angle (with respect to the axial coordinate) and the spanwise extent of the feature is given in Table 6.1

In order to quantify the losses through each blade passage, the entropy generation rate formulation of Zlatinov et al. [51] was used. This is defined in Equation 2.9 but is expanded here in Cartesian coordinates:

$$\dot{S}'''_{visc} = \frac{\mu_{eff}}{T}\left(\begin{array}{l} 2\big[\big(\frac{\partial u}{\partial x}\big)^2+\big(\frac{\partial v}{\partial y}\big)^2+\big(\frac{\partial w}{\partial z}\big)^2 \\ +\big(\frac{\partial u}{\partial z}+\frac{\partial w}{\partial x}\big)^2+\big(\frac{\partial u}{\partial y}+\frac{\partial v}{\partial x}\big)^2+\big(\frac{\partial v}{\partial z}+\frac{\partial w}{\partial y}\big)^2 \\ -\frac{2}{3}\big(\frac{\partial u}{\partial x}+\frac{\partial v}{\partial y}+\frac{\partial w}{\partial z}\big)^2 \end{array}\right) \tag{6.1}$$

Here, effective viscosity (μ_{eff}) is the sum of the dynamic viscosity (μ) and the eddy viscosity (μ_{eddy}). The final term ($-\frac{2}{3}(\frac{\partial u}{\partial x}+\frac{\partial v}{\partial y}+\frac{\partial w}{\partial z})^2$) is simply the divergence of the velocity field and is exactly zero for an incompressible flow field such as found in the LAR. The remaining terms are temperature and the shear strain rate, that is the deformation of the fluid at a point over time. Thus the only contribution to viscous entropy generation in an incompressible fluid are the the shear stresses.

Figure 6-13 presents results for baseline geometry. The integral of entropy generated is shown on a series of axial planes throughout the rotating domain, at a spacing of 0.005 c_{RB}. The planes were clipped at $r/s \geq$ -0.125 in order to exclude the wheelspace, but allow for the maximum depth of all contoured endwalls and include the seal gap region. This radial clip extent can be seen in the rotor cross section at the top of Figure 6-13. A region of high entropy generation can be seen at $z/c_{RB} =$ -0.2, corresponding to the stator platform trailing edge where locally high-shear exists with respect to the mainstream. A

second distinct peak is located at $z/c_{RB} = 0$: the RB LE. Downstream of the RB LE, entropy continues to be generated. This parameter can be non dimensionalised as using:

$$\frac{\widetilde{T}_{0,3}}{\frac{1}{2}(\frac{\rho w^3}{c_{RB}})_{in}} \tag{6.2}$$

where $\widetilde{T}_{0,3}$ is the effective total temperature at the RB TE and the remaining variables (density and axial velocity) are assessed at the RB LE.

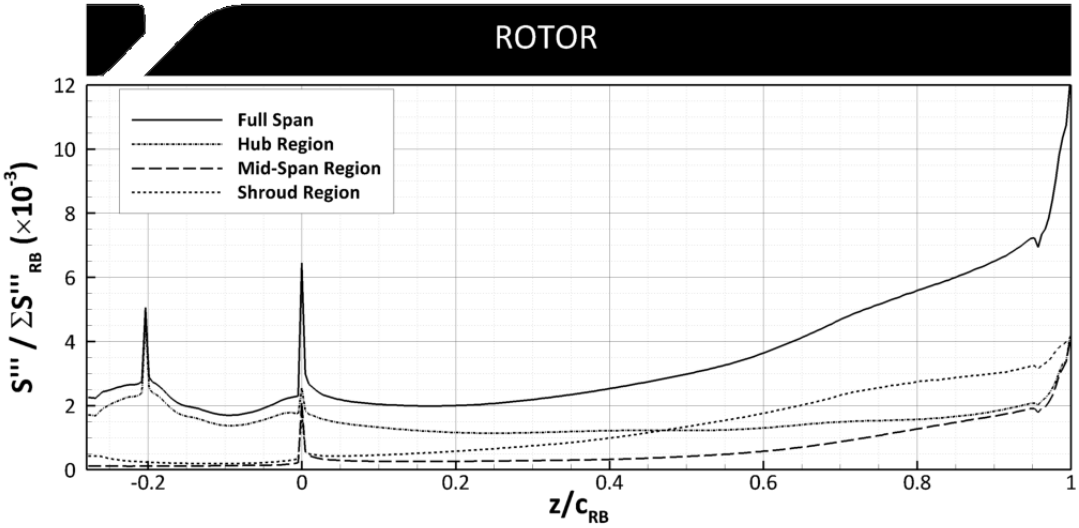

Figure 6-13: Axial development of entropy generation, baseline endwall

In addition, the span has been broken down in to three sub-zones of equal area: hub, mid span and shroud. This allows the predominant loss-generating mechanisms to be identified. Upstream of the RB LE, loss generation is dominated by the hub region until $z/c_{RB} = 0.48$. Downstream of mid-chord, the dominant region becomes the shroud. This indicates that the tip losses are high. As the implementation of contoured endwalls is not expected to reduce the losses in the tip region, only losses occurring close to the hub are considered relevant to their design.

Figure 6-14 presents the axial development of entropy from z/c_{RB} = -0.2 to 1.0, covering the hub region only. Here, data for the baseline (solid, black), EW002 (dashed, black) and the three endwalls with LEFs added to EW002 (colours) are shown. Four key regions are annotated, with an additional enlarged view of the leading-edge region of the blade shown inset.

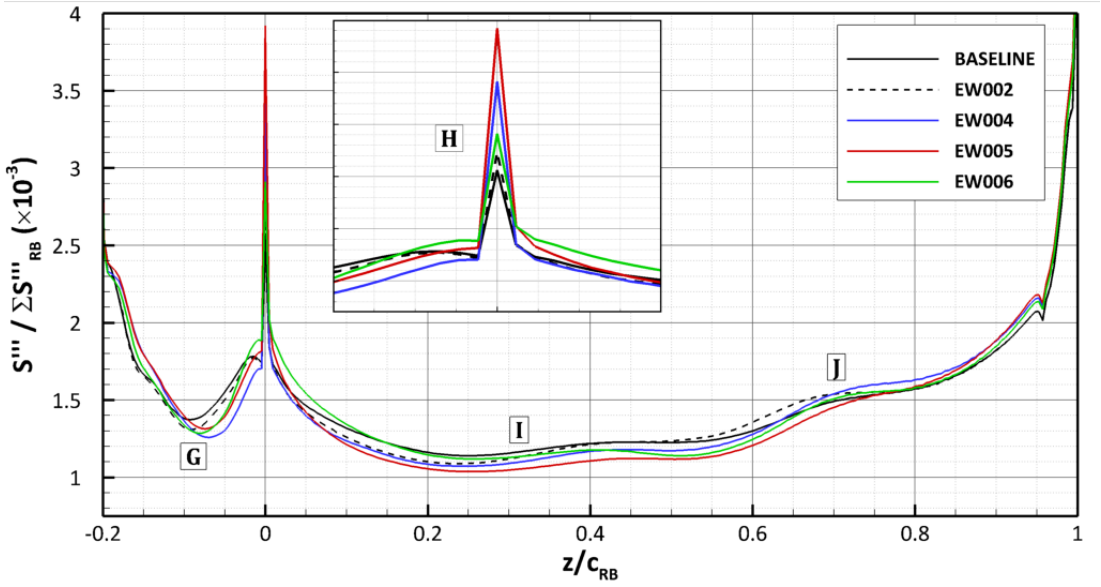

Figure 6-14: Axial development of entropy generation in the hub region for selected endwalls

Annotation 'G' draws attention to the entropy generation immediately upstream of the RB LE, from z/c_{RB} = -0.2 to 0. This region includes the chute region of the seal, but excludes any of the stator hub surfaces. The magnitude of loss in this region is low, with contributions of 0.015% of the total loss at each planar location. However, significant changes are noted in this region for each endwall. EW002 causes decreased loss in comparison to the baseline, while the introduction of a LEF appears to enhance this effect. It is believed that this is evidence of the LEF weakening the roll-up of the HSV, which extends as far upstream as -0.1 c_{RB} for the baseline case.

Annotation 'H', shown on the inset, focuses on the loss at the leading-edge of the RB. Here, a surprising result is found, with all three endwalls including LEFs (EWC004A-006) resulting in a higher loss peak at the RB LE than the baseline. It should be noted that EW002 also causes a slight increase (0.015%) compared to the baseline.

Downstream of the RB LE, Annotation 'I' indicates a region of lower entropy generation. The EWCs, excluding EW006, closely track the baseline loss until 0.05 c_{RB}, before dropping away; by 0.2 c_{RB} the loss generation rate is substantially less than the baseline. In contrast, EW006 initially generates higher entropy throughout this region. Losses in this region are due to both the HSV-SS and HSV-PS, as well as the mixing out of the egress plume; the contoured endwalls minimise these losses well.

Annotation 'J' indicates the transition point for the HSV-PS which travels across the blade passage and becomes entwined with the HSV-SS of the adjacent RB. The vortex strands, known as the passage vortex, gradually move off the hub and migrate radially. This migration occurs further upstream in the baseline case, relative to the contoured endwalls. Further downstream, from 0.8 c_{RB}, the losses are indistinguishable, indicating that the benefits due to the contoured endwall have been exhausted in the near hub region.

Overall, the introduction of a leading-edge feature to an endwall with an SSTR has a net beneficial impact of at least 0.1%, summarised in Table 6.1. The greatest improvement in efficiency was 0.23% seen for EW005; EW005 exhibited the most prominent leading-edge feature. However, it was noted that reducing the radial extent of this feature led to a significant reduction in the unsteadiness. Based on the results discussed in Sections 6.3 and 6.4, an improved design was conceptualised, making use of the insight derived from the earlier simulations.

6.5 Improved Endwalls

Three further endwall concepts were generated (EWC007A, 007B and 008 shown in Figure 6-15a to c); all endwalls included an SSTR and a leading-edge feature, but excluded a PSTR. The radial extent of the geometric features is enhanced in EW007A relative to EW008. EW007B represents a more axially aligned LEF compared to both EW007A and EW008, which results in a deeper, wider trough opening.

The SSTR, present in both endwall designs, differs from the SSTR featured in EW002 (presented in Section 5.1); the trough minima are shifted away from the suction-surface of the blade. The original objective for an SSTR was to control the position of the CO_2-egress plume, which both EW001 and EW002 demonstrated. However, in the development of the improved endwalls it was noted that moving the SSTR away from rather than towards the suction surface, resulted in an improved stage efficiency. The interaction between the HSV-SS and CO_2 egress plume is explored in detail in Section 5.3.

The LEF, geometrically consistent between EW007A and EW008, bar the radial extent, was extended in length upstream of the RB relative to EW002. The extended LEF created a more gradual rise to the leading-edge of the blade from the trough minimum. For EW007B, this feature was aligned more with the axial direction rather than the incoming flow, resulting in a shorter, more abrupt rise from the trough. It was found that while EW007B did increase

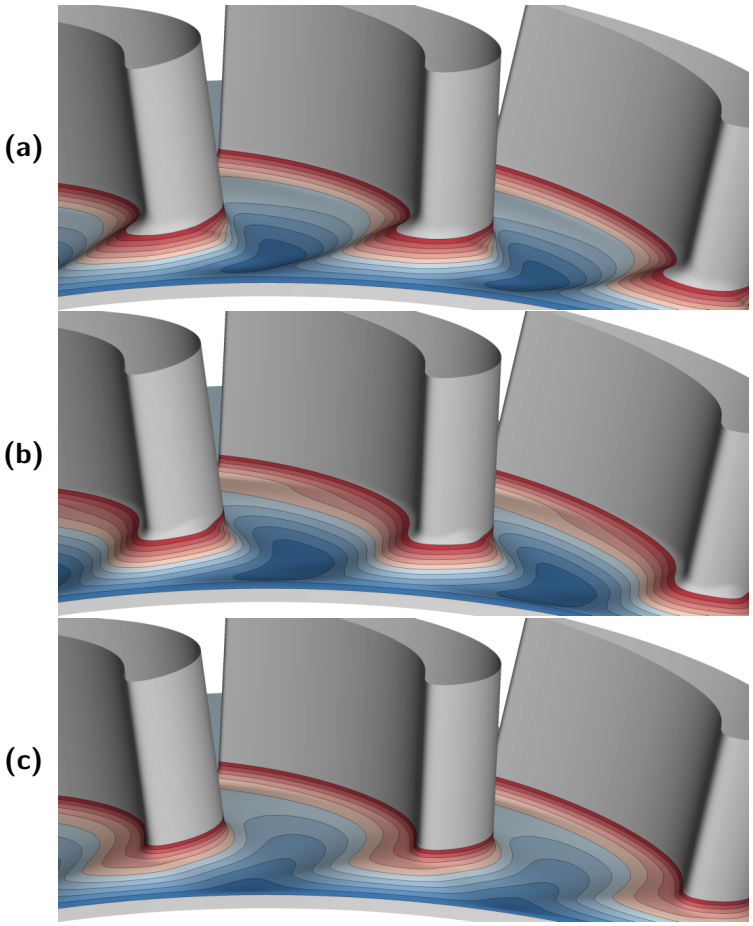

Figure 6-15: Isometric view of the rotor, coloured by spanwise extent ($-0.1 < s < 0.1$) for improved endwalls (a) EW007A, (b) EW007B and (c) EW008

stage efficiency to 80.63%, the concordant increase in unsteady fluctuation to ±0.6% was unacceptably high and the design was discarded.

Figure 6-16 presents contours of non-dimensionalised entropy generation rate according to the formulation given by Equation 2.9. In part 6-16a - the baseline case - entropy is generated in the seal region across the entire blade pitch (shown in the first axial plane). This is a region of high shear between the purge and mainstream flows; in regions of high shear, large losses are expected. The peak magnitude, annotated as 'L', is found to align with the egress plume (shown in Figure 5-19 and Figure 6-10a). Moving downstream, the egress plume, which interacts with the HSV-SS, is visible as a region of loss (marked as 'K'). This region of loss appears close to the suction-surface of the blade and becomes increasingly wall-bound with axial position through the passage. Additionally, the development of the

HSV-PS is clear (annotated 'M'), as it moves across the passage.

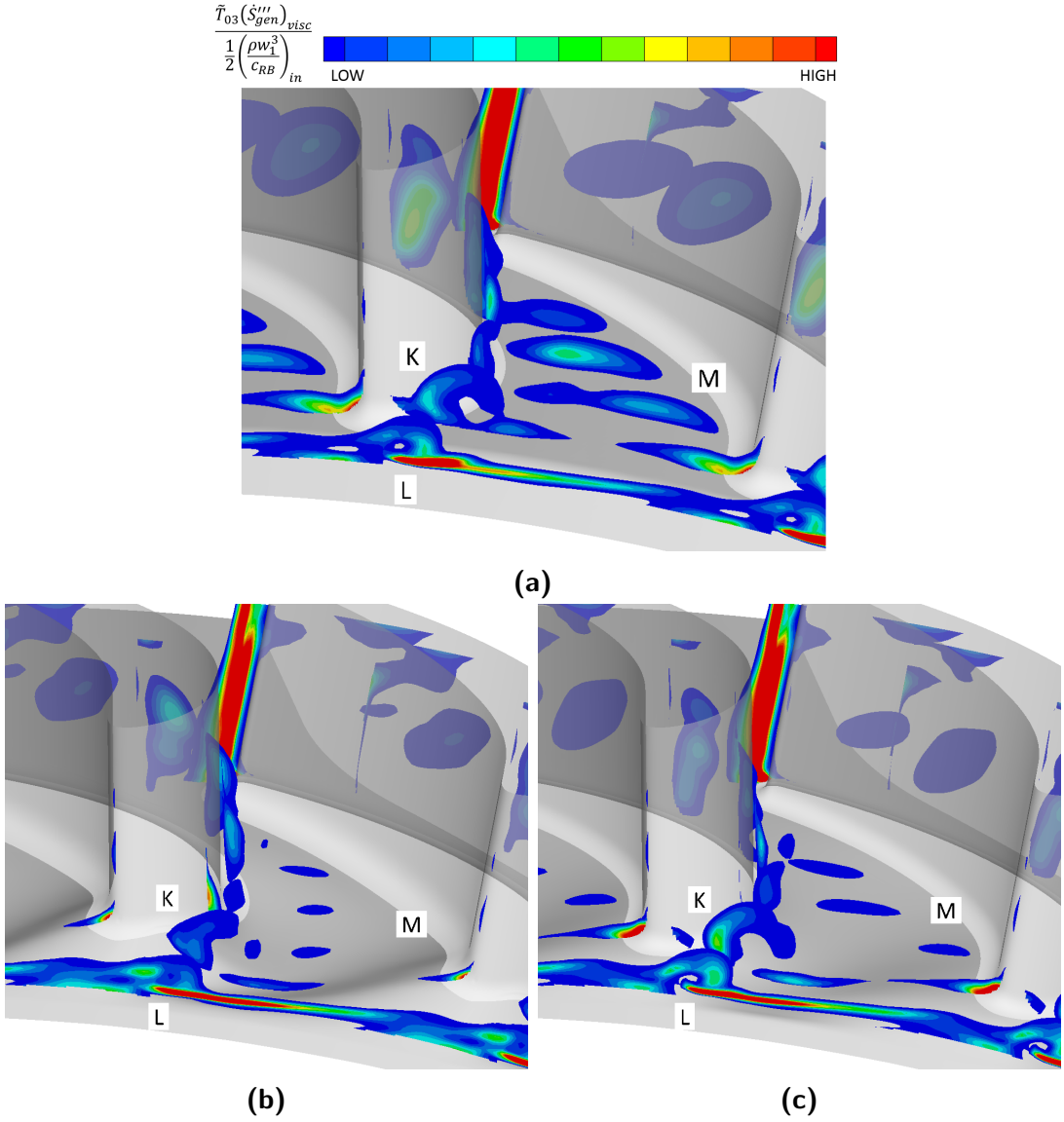

Figure 6-16: Contours of non-dimensionalised $\dot{S}'''_{visc}$ for (a) baseline, (b) EW007A and (c) EW008

In Figure 6-16b, the flow field in the presence of EW007A shows significant differences. The ejection point for the egress plume is still present as a region of loss, 'L', however the peak magnitude occurs at a pitchwise position further away from the suction-surface of the blade. This is expected due to the location of the trough, drawing the plume away from the blade leading-edge. The HSV-SS is still visible (K), though the size and strength appears greatly reduced. Finally, the HSV-PS is barely detectable in the entropy production (M),

suggesting a much reduced secondary flow loss.

Finally, in part c of Figure 6-16, the entropy contours are shown for EW008. As discussed above, this endwall has the same geometrical features as EW007A, but with reduced radial extent. Perhaps predictably, the flow field shows very similar features: circumferential translation of the peak egress (L), reduced loss in the HSV-SS (K) and reduced strength of the HSV-PS (M). The relative impact of these flow-features is, however, reduced in comparison with EW007A; this is reflected in Table 6.1

Figure 6-17 presents streaklines on the hub surface for the baseline and improved endwalls. In part (a), the attachment point (N_a) can be seen on the pressure-surface of the blade, downstream of the leading-edge. The saddle point (S_p) lies approximately at the mid-pitch position, further upstream of the LE; the position of the saddle point relative to the blade indicates a strong roll-up of the HSV. The separation line (N_s) runs from the saddle point to the seal region at a very large angle to the machine axis.

Figure 6-17b shows that EW007A has significantly reduced the size and extent of the HSV, with the saddle point very close to the pressure-surface, immediately downstream of the blade leading-edge. The line of separation is more inclined to the machine axis, while the attachment point has not moved significantly. The same is true of EW007B (seen in Figure 6-17c), where the saddle point is significantly closer to the BLE in comparison to the baseline. Additionally, the streaklines crossing the passage show a consistent axial component to the flow even near the hub. This reduction in HSV strength reflected in the improved stage efficiency obtained by both EW007A and EW007B, although EW007B fails to address the unsteady fluctuations and causes an increase. Part (d) shows that EW008 has not reduced the size of the HSV to the same extent as EW007A, but the streaklines still indicate a reduced roll-up of the HSV compared to the baseline.

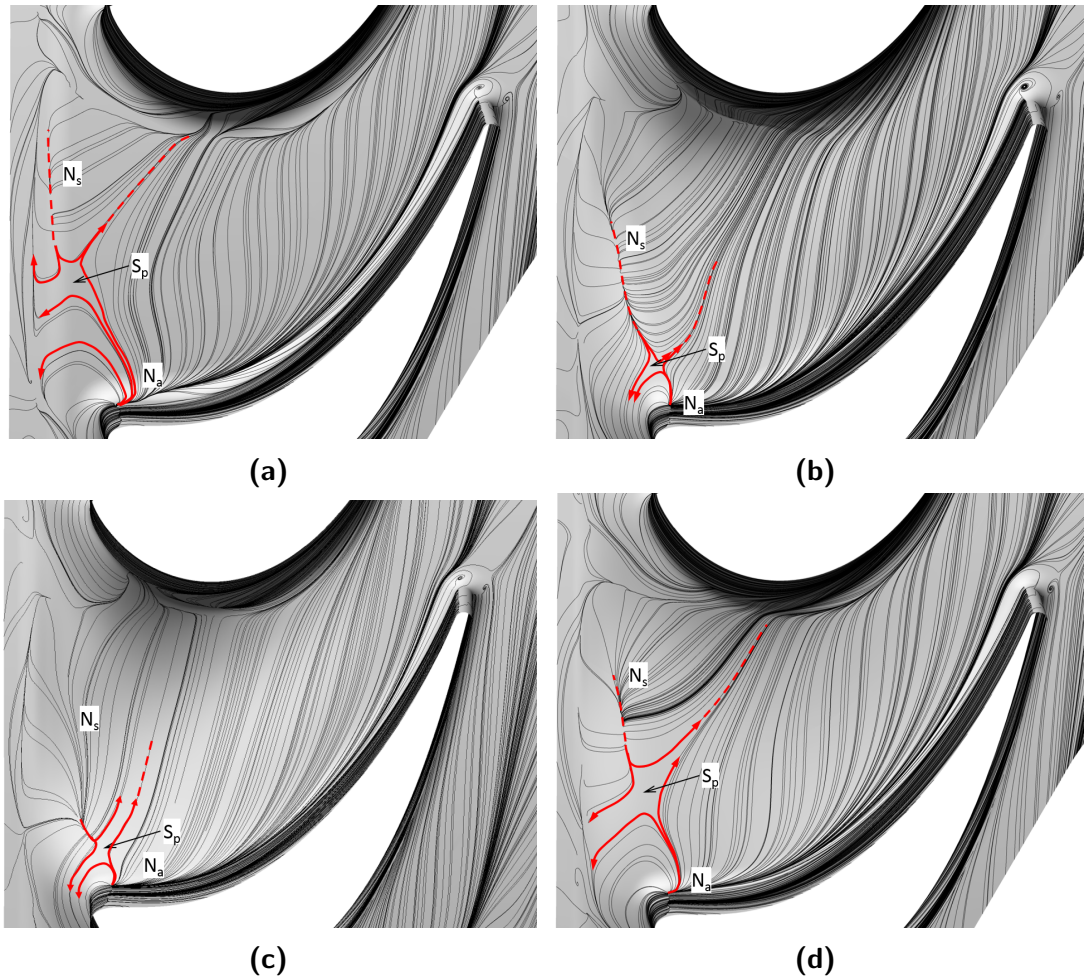

Figure 6-17: Surface streaklines on the rotor hub with limiting lines identified for (a) baseline, (b) EW007A, (c) EW007B and (d) EW008

6.6 Summary

A novel method for endwall designs has been outlined and specific geometric features have been identified according to their desired impact. By applying these features to a known flow field in the presence of purge flow, significant improvement to stage efficiency was achieved. The mechanism by which each feature acts has also been identified.

The suction-side troughs were found to provide a modest control of the egress plume position, with radial and pitchwise displacement possible. This feature also had a beneficial impact on the unsteady fluctuations in stage efficiency. The pressure side trough was found to have a net negative effect, spoiling the effect of the suction-side trough.

Introduction of the leading-edge feature improved the stage efficiency of all designs. This is true even for the case of EWC003D, which included a pressure-side trough. The LEF was able to eliminate the detrimental effect of the PSTR. The mechanism by which the LEF improves stage efficiency is by reduction of the HSV and thus the secondary losses throughout the passage.

Visualising the $\eta_{mix,ISO}$ data from Table 6.1, Figure 6-18 provides a clear summary of all the endwalls presented in this study. Symbols for endwalls featuring troughs are shown as triangles; endwalls with leading-edge features are shown as circles; the improved endwalls are shown as diamonds.

General trends can be identified, such as the addition of a LEF to EW002, resulting in EW004A and EW005, demonstrating an increased stage-efficiency, but with increasing unsteadiness as a result. The move from EW005 to EW006 reduced the fluctuations but with an associated penalty in overall efficiency.

The combination of an SSTR and a leading-edge feature resulted in an improvement in stage efficiency of up to 0.4% relative to the baseline endwall; most endwall concepts were shown to reduce the unsteadiness.

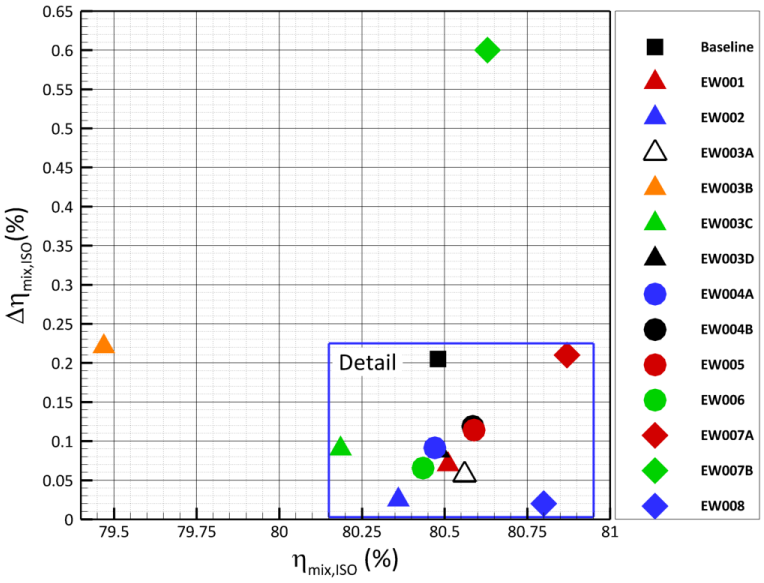

(a)

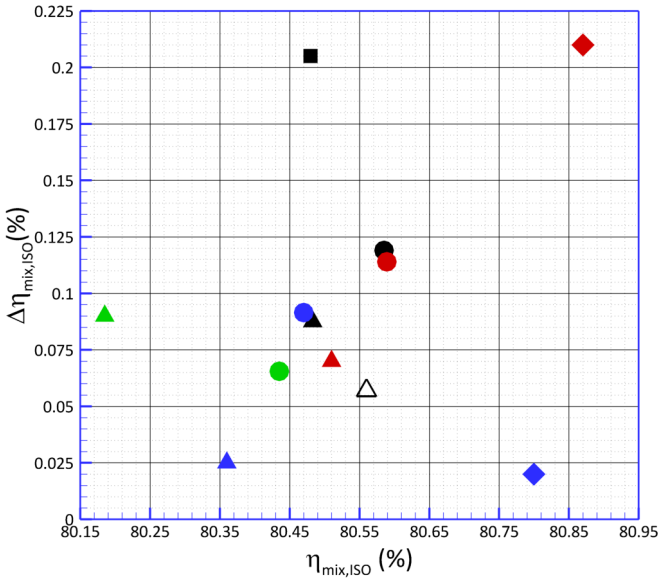

(b)

Figure 6-18: Stage efficiency and unsteady fluctuation in efficiency for all endwall designs (a) and selected detail (b). Symbols: baseline (■); troughs (▲); leading-edge features (●) and improved endwalls (◆)

EW	SSTR		PSTR	LEF		Description	$\eta_{mix,ISO}$	
	θ_{SSTR}	d/s	θ_{PSTR}	α_{LEF}	h/s		%	Δ
001	0.3	0.08	-	-	-	Deep trough near mid-pitch	80.51	0.070
002	0.2	0.08	-	-	-	Deep trough near SS	80.36	0.025
003A	-	-	0.8	-	-	Wide, shallow trough	80.56	0.057
003B	-	-	0.9	-	-	Narrower, deeper trough	79.47	0.221
003C	0.2	0.08	0.9	-	-	EW002 combined with EW003B	80.19	0.090
003D	0.2	0.08	0.9	55°	0.09	EW003C with slender LEF	80.48	0.088
004A	0.2	0.08	-	55°	0.09	EW002 with slender LEF	80.47	0.092
004B	0.2	0.08	-	55°	0.09	EW002 with broad LEF	80.59	0.119
005	0.2	0.08	-	55°	0.09	EW004B with PS blend	80.59	0.114
006	0.2	0.08	-	55°	0.05	EW005 with reduced extent	80.43	0.080
007A	0.4	0.08	-	60°	0.125	Improved endwall, maximum extent	80.87	0.210
007B	0.4	0.08	-	45°	0.125	Improved endwall, axial LEF	80.63	0.600
008	0.4	0.08	-	60°	0.09	Improved endwall, reduced extent	80.80	0.020

Table 6.1: Selected endwall design parameters, descriptions and $\eta_{mix,ISO}$ data

Chapter 7

Conclusions and Future Work

This chapter relates the findings presented in this work to the research aims and objectives, where the key aim was to develop contoured endwalls that offer improved aerodynamic performance in the presence of purge flow. In order to achieve this the new Large Annulus Rig has been designed and developed in order to investigate the fluid dynamics of the interaction between main gas path flow and purge gas egress. The design challenge presented by the inlet was solved using CFD, thereby providing well-conditioned flow at the nozzle guide vane. The rig has been modelled computationally with a periodic, three-dimensional mesh and results obtained using an Unsteady Reynolds-Averaged Navier-Stokes solver. The influence of various geometric representations has been explored at length, building up a picture of the unsteady, three-dimensional flow field. This allowed the isolation and identification of the underlying secondary flow structures in the absence of purge gas and, subsequently, in the presence of purge gas.

This understanding of the secondary flow features and the purge gas egress plume was used to inform the development of contoured endwalls. The novel approach, using specific features to control the vortical structures, was developed and iteratively applied to understand the sensitivities. These trough and extension features were then combined to obtain improved, but not optimised, endwalls.

7.1 Conclusions

7.1.1 Large Annulus Rig

- A computational model of a radial diffuser, transitioning from existing pipework to the desired annulus position, was generated in order to assess the flow condition at the nozzle guide vane of the LAR. The baseline design was found to have recirculating flow at the desired vane position, an unacceptable inlet condition for the stage.
- The addition of a small settling chamber and a conical diffuser to the baseline was found to eradicate recirculation at the vane leading edge, but not sufficient to provide an flat radial velocity profile.
- A baffle plate with blockage ratio of 0.5 was found to significantly flatten the velocity profile and reduce the total pressure drop of the design. The addition of a second baffle further flattened the velocity profile with an additional reduction in total pressure drop. The penalty for the inclusion of baffle plates was the increase in overall inlet length due to the space required between the plates.
- Further improvements to the velocity profile were achieved by implementing a shaped nose to direct the flow. The selected design demonstrated a velocity profile with a slight bias towards the shroud.
- Experimental validation of the inlet design demonstrated that the inlet performs as expected with well conditioned flow delivered to the turbine stage.

7.1.2 Computational Method

- A computational model of the 1-stage axial turbine was created, based on the geometry of a new LAR experimental testing facility developed to investigate the performance of endwall contours in the presence of purge flow. The boundary conditions were selected in collaboration with industrial partners, with a total pressure profile specified at main gas path inlet. A velocity profile with mass flow rate was specified at the purge gas inlet. A multi-component fluid model was employed for the combination of air in the main gas path and 100% CO_2 purge gas. Computations were conducted using steady and unsteady RANS methods. The computational model was validated by direct comparison with data for a cylindrical baseline endwall, collected from the experimental facility.

- Sensitivity to spatial discretisation was investigated using established guidelines in the literature and the medium grid was demonstrated to be sufficiently refined. Temporal discretisation was investigated using a pragmatic approach as no published guidelines were available, with the selected timestep justified by comparing time-averaged parameters at the end of two revolutions.

- The CFD model was validated by comparing predictions of the vane loading and circumferential distribution of pressure in the annulus with data collected from the experimental facility.

- Computational grids were generated for four geometric representations of the LAR: Annulus Domain, Chute Domain, Stub Domain and Full Wheelspace domain. The influence of the size of computational domain was demonstrated by monitoring pressure and total-to-total stage efficiency as a function of time. The interaction between the mainstream gas path and the purge flow was found to be directly linked to increased unsteadiness in the monitored parameters. In order to limit unnecessary unsteadiness in the simulations, the domain was limited to the rim-seal and turbine annulus, neglecting the full wheel-space between the stator and rotor disc.

- The sector size took advantage of the 2:3 periodicity of the vane and blade count, resulting in small sector model. A double sector with 4 vanes and 6 blades was also tested and was shown to have no impact on the unsteadiness or the stator hub pressure circumferential distribution.

- The spoiling effect of purge gas on the stator hub pressure circumferential distribution was demonstrated by comparing results with varying purge flow rates. The removal of purge flow was also found to remove the chaotic unsteadiness seen in the Full Wheelspace Domain.

7.1.3 Effect of Egress

- The baseline secondary flow-field was characterised using the Annulus Domain without a superposed purge flow. Sieverding and Van den Bosche's streamline technique was used to successfully identify the secondary flow structures in the stator and relate them to the vortical structures predicted by the literature, specifically the two legs of the Horseshoe Vortex (Pressure-Side and Suction-Side) and the passage vortex.

However, the point at which the HSV-PS evolves into the PV is not exceptionally clear and vorticity contours reveal that these structures are weak in the stator.

- Analysis of the rotor using midspan streamlines revealed radial deviations from the expected quasi-2D flow. This was interpreted as the presence of large secondary flow structures deflecting the midspan flow due to their presence and migration. Sieverding and Van den Boshe's streamlines supported this assertion by allowing identification of the structures and showing their radial migration to be large.

- Contours of vorticity also revealed that the classical secondary flow structures were present. The HSV formed at the leading-edge of the blade due to the roll-up of the incoming boundary layer and is visible with two lobes of opposite sense of rotation. The HSV was bifurcated by the blade before being convected downstream by the mainstream flow, forming the Pressure-Side and Suction-Side legs of the HSV. The HSV-PS rotates in the same sense as the rotor; the HSV-SS, while weak, was found to have the opposite sense of rotation once the vortex was turned around the leading-edge of the blade.

- A Stub Domain flow field without superposed flow was analysed to assess the effect of rim seal geometry on the flow field. Midspan streamlines and those released in the boundary layer allowed the identification of the same structures seen previously. Slight changes to the HSV-SS formation indicated that the seal geometry had an effect.

- The presence of the rim seal and outer wheelspace caused both ingress and egress across the seal gap. This was identified using radial velocity contours and was due to the disc pumping effect of the rotor.

- Further, the effect of the superposition of purge gas was assessed. Midspan streamlines highlighted an increased radial migration of the secondary flows and signalled the significantly changed flow field due to purge gas egress.

- The egress of purge gas from the rim seal was tracked through the blade passage using contours of CO_2 mass fraction. The plume was found to exit across the seal gap but become concentrated as a coherent vortical structure close to the blade suction surface. The plume is convected downstream by the bulk flow, interacting with the secondary flows. This will be replicated experimentally on the LAR in future using PLIF, allowing for future validation of these results.

- When purge flow was introduced through the upstream rim-seal, the interaction of the egress plume with the mainstream flow was seen to strengthen the secondary flow structures in the blade passage. Specifically, the egress plume enhanced the HSV-PS as the latter reached the suction-side of the adjacent blade. The enhancement of the HSV-PS, which was enabled by the egress plume rotating in a consistent sense of direction, subsequently increased the radial migration of the passage vortex relative to the unpurged case. In addition, the HSV-SS was shown to be overwhelmed by a strong egress plume, which rotates in the opposite to the HSV-SS.

- Results presented in this thesis have been used to support the experimental campaign, providing *a priori* knowledge of the location of flow structures in the blade passage.

7.1.4 Contoured Endwall Design

- A novel feature-based approach to the design of contoured endwalls has been outlined and explored; each endwall included discrete geometric features in the passage.

- Unsteady computations revealed that the introduction of a suction-side trough allowed for the path of the egress flow to be controlled. In addition, the containment of the egress plume within the trough was found to have a beneficial influence on the unsteady fluctuations of stage efficiency.

- The inclusion of a pressure-side trough was found to have a net negative effect on stage efficiency. It was also found to have a spoiling effect on the ability of a suction-side trough to control the position of the egress plume.

- The presence of a leading-edge feature was used to improve overall stage efficiency by reducing the size of the leading-edge horseshoe vortex and subsequently the strength of the hub-bound secondary flows. However, the magnitude of unsteady fluctuations was found to increase for leading-edge features with a large radial extent.

- Through the use of an appropriately sized leading-edge feature, stage efficiency improvements could be achieved without the concordant increase in unsteady fluctuations of efficiency.

- The combination of suction-side trough and a leading-edge feature resulted in an improvement in stage efficiency of up to 0.4% relative to the baseline endwall.

7.2 Future Work

While the novel endwall contouring technique has been successfully demonstrated, a number of open avenues for research remain. A set of possible research direction are presented here.

- The improved endwall design was shown to improve stage efficiency. It should also be demonstrated the aerodynamic performance of the improved endwall design is robust using computations over a range of purge flow rates. This should also be demonstrated for "off-design" conditions with varying flow coefficient and would be complemented by experimental validation work. Computations should be unsteady and assess the impact of these factors on the criteria used throughout this work.

- The novel endwall features should be applied to a different turbine stage with smaller or larger secondary flow structures. This would demonstrate the relative performance gains possible given a different datum design. The initial choice of engine-representative blading with large secondary flows was intended to enable easier detection in the LAR, but this may have unintentionally increased the interaction phenomena and this is an unknown factor.

- Different rim seal configurations and vane-to-blade spacing should be included with the improved endwall design and existing blading. This would allow the circumferential pressure distribution to be changed and thus the egress plume to be manipulated using the primary driver for ingress. A robust endwall design should be insensitive to these effects.

- Endwall contouring should be applied in the stator vane passage to further manipulate the pressure distribution. This would also provide a modified secondary flow field to be passed from the stator domain to the rotor domain, in turn modifying the interaction of boundary layers, egress plume and secondary flow structures. This study focused on providing a common stator flow field to the rotor, however, this may not be desirable.

- There should also be attention applied to tracking the NGV secondary flow features through the rotor passage in the numerical results. The interaction of these structures with the rotor potential field will have an influence on the location and periodicity of the egress plume. This should be complemented with time-accurate experimental data for validation purposes.

- Optimisation of the improved endwall is possible using the framework and parametrisation provided. However, single objective function optimisation can lead to designs which are sensitive to off-design conditions and care should be taken in choosing the desired function. Multi-objective function optimisation is likely to be more robust and the choice of objective functions requires attention..
- Application of advanced CFD techniques such as Delayed Detached Eddy Simulation (DDES) should be considered for future calculations. As computational power increases it is possible to simulate larger and larger grid sizes in a timely manner. For RANS and URANS, there is a limit to the usefulness of an infinitely fine grid but this is not the case for DDES or LES.
- The presence of large scale structures in the wheelspace at lower purge flow rates should be investigated using full wheelspace and 360° annulus calculations. This would provide a more comprehensive understanding of the fluctuations found in the wheelspace.

Bibliography

[1] slender adj. (and adv.) *Oxford English Dictionary*. Oxford University Press. URL: http://www.oed.com/view/Entry/181674 (visited on 18/12/2018).

[2] Hunt R. J. *The History of the Industrial Gas Turbine (Part 1 The First Fifty Years 1940-1990)*. Report 582. Institution of Diesel and Gas Turbine Engineers, 2011.

[3] Saravanamuttoo H. I. H., Rogers G. F. C. and Cohen H. *Gas Turbine Theory*. 5th ed. Harlow: Harlow : Longman, 2001.

[4] Cumpsty N. *Jet Propulsion*. Cambridge: Cambridge University Press, 2003.

[5] *The Jet Engine*. 5th ed. Derby: Rolls-Royce, 1996.

[6] Scobie J. A. 'An Experimental Study of Gas Turbine Rim Seals'. PhD Thesis. 2014.

[7] Regina K., Kalfas A. I. and Abhari R. S. 'Experimental Investigation of Purge Flow Effects on a High Pressure Turbine Stage'. In: *Proceedings of the ASME Turbo Expo 2012: Turbine Technical Conference and Exposition, 11-15 June 2012, Copenhagen, Denmark*. Vol. 8. ASME, 2012, pp. 1509–1519. DOI: 10.1115/GT2012-69466.

[8] Mirzamoghadam A. V., Heitland G., Morris M. C., Smoke J., Malak M. and Howe J. '3D CFD ingestion evaluation of a high pressure turbine rim seal disk cavity'. In: *Proceedings of ASME Turbo Expo 2008: Power for Land, Sea and Air, 9-13 June 2008, Berlin, Germany*. Vol. 4. ASME, 2008, pp. 1443–1452. DOI: 10.1115/GT2008-50531.

[9] Dorfner C., Hergt A., Nicke E. and Moenig R. 'Advanced non-axisymmetric endwall contouring for axial compressors by generating an aerodynamic separator - Part I: Principal cascade design and compressor application'. In:

Proceedings of ASME Turbo Expo 2009: Power for Land, Sea and Air, 8-12 June 2009, Orlando, Florida. Vol. 7. ASME, 2009, pp. 113–120. DOI: 10.1115/GT2009-59383.

[10] Rose M. G. 'Non-axisymmetric endwall profiling in the HP NGV's of an axial flow gas turbine'. In: *Proceedings of the International Gas Turbine and Aeroengine Congress and Exposition, 13-16 June 1994, The Hague, Netherlands*. ASME, 1994, pp. 1–8. DOI: 10.1115/94-GT-249.

[11] Denton J. D. 'Loss Mechanisms in Turbomachines'. In: *Journal of Turbomachinery* 115.4 (1993), pp. 621–656.

[12] Schreiner B. D. J., Wilson M., Li Y. S. and Sangan C. M. 'Effect of purge on the Secondary flow-field of a Gas Turbine Blade-row'. In: *Journal of Turbomachinery* (2019).

[13] Schreiner B. D. J., Wilson M., Li Y. S. and Sangan C. M. 'Design of Contoured Turbine Endwalls in the presence of Purge Flow: A Feature-Based Approach'. In: *Proceedings of ASME Turbo Expo 2019: Turbomachinery Technical Conference and Exposition, 17-21 June 2019, Phoenix, Arizona*. ASME, 2019.

[14] Jones R. R., Pountney O. J., Cleton B. L., Wood L. E., Schreiner B. D. J., Carvalho Figueiredo A. J., Scobie J. A., Cleaver D. J., Lock G. D. and Sangan C. M. 'A New Single-Stage Turbine Facility For Investigating Non-Axisymmetric Contoured Endwalls In The Presence Of Purge Flow'. In: *Proceedings of ASME Turbo Expo 2019: Turbomachinery Technical Conference and Exposition, 17-21 June 2019, Phoenix, Arizona*. ASME, 2019.

[15] Dixon S. L. and Hall C. A. *Fluid Mechanics and Thermodynamics of Turbomachinery*. 6th ed. Boston: Butterworth-Heinemann, 2010.

[16] Horlock J. H. and Denton J. D. 'A Review of Some Early Design Practice Using Computational Fluid Dynamics and a Current Perspective'. In: *Journal of Turbomachinery* 127.1 (2005), pp. 5–13. DOI: 10.1115/1.1650379.

[17] Ainley D. G. and Mathieson G. C. R. *A Method of Performance Estimation for Axial Flow Turbines*. Report. Aeronautical Research Council, 1951.

[18] Craig H. R. M. and Cox H. J. A. 'Performance Estimation of Axial Flow Turbines'. In: *Proceedings of the Institution of Mechanical Engineers* 185.1 (1970), pp. 407–424. DOI: 10.1243/PIME_PROC_1970_185_048_02.

[19] Kacker S. C. and Okapuu U. 'A Mean Line Prediction Method for Axial Flow Turbine Efficiency'. In: *Journal of Engineering for Power* 104.1 (1982), pp. 111–119. DOI: 10.1115/1.3227240.

[20] Wilson D. G. 'New Guidelines for the Preliminary Design and Performance Prediction of Axial-Flow Turbines'. In: *Proceedings of the Institution of Mechanical Engineers, Part A: Power and Process Engineering* 201.4 (1987), pp. 279–290. DOI: 10.1243/PIME_PROC_1987_201_035_02.

[21] Denton J. D. and Dawes W. N. 'Computational fluid dynamics for turbomachinery design'. In: *Proceedings of the Institution of Mechanical Engineers, Part C: Journal of Mechanical Engineering* 213.2 (1999), pp. 107–124. DOI: 10.1243/0954406991522211.

[22] Sieverding C. H. 'Recent Progress in the Understanding of Basic Aspects of Secondary Flows in Turbine Blade Passages'. In: *Journal of Engineering for Gas Turbines and Power* 107.2 (1985), pp. 248–257. DOI: 10.1115/1.3239704.

[23] Langston L. S. 'Secondary Flows in Axial Turbines A Review'. In: *Annals of the New York Academy of Sciences* 934.1 (2001), pp. 11–26. DOI: 10.1111/j.1749-6632.2001.tb05839.x.

[24] Simon T. W. and Piggush J. D. 'Turbine Endwall Aerodynamics and Heat Transfer'. In: *Journal of Propulsion and Power* 22.2 (2006), pp. 301–312. DOI: 10.1016/j.ijms.2006.05.001.

[25] Sharma O. P. and Butler T. L. 'Predictions of Endwall Losses and Secondary Flows in Axial Flow Turbine Cascades'. In: *Journal of Turbomachinery* 109.2 (1987), pp. 229–236. DOI: 10.1115/1.3262089.

[26] Anderson S. D. and Eaton J. K. 'Reynolds stress development in pressure-driven three-dimensional turbulent boundary layers'. In: *Journal of Fluid Mechanics* 202 (1989), pp. 263–294. DOI: 10.1017/S0022112089001187.

[27] Johnston J. P. and Flack K. A. 'Review: Advances in Three-Dimensional Turbulent Boundary Layers With Emphasis on the Wall-Layer Regions'. In: *Journal of Fluids Engineering* 118.2 (1996), pp. 219–232. DOI: 10.1115/1.2817367.

[28] Horlock J. H. and Perkins H. J. 'Annulus Wall Boundary Layers in Turbomachines'. In: *AGARDograph* AG-185 (1974).

[29] Baker C. J. 'The turbulent horseshoe vortex'. In: *Journal of Wind Engineering and Industrial Aerodynamics* 6.1-2 (1980), pp. 9–23. DOI: 10.1016/0167-6105(80)90018-5.

[30] Baker C. J. 'Vortex Flow around the Bases of Obstacles'. PhD Thesis. 1978.

[31] Eckerle W. A. and Langston L. S. 'Horseshoe Vortex Formation Around a Cylinder'. In: *Journal of Turbomachinery* 109.2 (1987), pp. 278–285. DOI: 10.1115/1.3262098.

[32] Langston L. S., Nice M. L. and Hooper R. M. 'Three-Dimensional Flow Within a Turbine Cascade Passage'. In: *Journal of Engineering for Power* 99.1 (1977), pp. 21–28. DOI: 10.1115/1.3446247.

[33] Sieverding C. H. and Van den Bosche P. 'The use of coloured smoke to visualize secondary flows in a turbine-blade cascade'. In: *Journal of Fluid Mechanics* 134 (1983), pp. 85–89. DOI: 10.1017/S0022112083003237.

[34] Snedden G., Dunn D., Ingram G. and Gregory-Smith D. 'The application of non-axisymmetric endwall contouring in a single stage, rotating turbine'. In: *Proceedings of ASME Turbo Expo 2009: Power for Land, Sea and Air, 8-12 June 2009, Orlando, Florida*. Vol. 7. ASME, 2009, pp. 831–840. DOI: 10.1115/GT2009-59169.

[35] Snedden G., Dunn D., Ingram G. and Gregory-Smith D. 'The performance of a generic non-axisymmetric end wall in a single stage, rotating turbine at on and off-design conditions'. In: *Proceedings of the ASME Turbo Expo 2010: Power for Land, Sea and Air, 14-18 June 2010, Glasgow, UK*. Vol. 7. ASME, 2010, pp. 1069–1080. DOI: 10.1115/GT2010-22006.

[36] Wang H. P., Olson S. J., Goldstein R. J. and Eckert E. R. G. 'Flow Visualization in a Linear Turbine Cascade of High Performance Turbine Blades'. In: *Journal of Turbomachinery* 119.1 (1997), pp. 1–8. DOI: 10.1115/1.2841006.

[37] Childs P. R. N. *Rotating flow*. Amsterdam: Elsevier, 2011.

[38] Owen J. M. and Rogers R. H. *Flow and Heat Transfer in Rotating-Disc Systems Volume 1: Rotor-Stator Systems*. Rotor-stator systems Research Studies. 1989.

[39] Daily J. W. and Nece R. E. 'Chamber Dimension Effects on Induced Flow and Frictional Resistance of Enclosed Rotating Disks'. In: *Journal of Basic Engineering* 82.1 (1960), pp. 217–230. DOI: 10.1115/1.3662532.

[40] Owen J. M. 'Prediction of Ingestion Through Turbine Rim Seals Part I: Rotationally induced ingress'. In: *Journal of Turbomachinery* 133.3 (2011). DOI: 10.1115/1.4001177.

[41] Elliott B., Sayma A. and Imregun M. 'Design of Damped High Pressure Turbine Blade Subject to Low Engine Order Forcing'. In: *Evaluation, Control and Prevention of High Cycle Fatigue in Gas Turbine Engines for Land, Sea and Air Vehicles*. NATO Research and Technology Organization, 2005.

[42] Owen J. M. 'Prediction of Ingestion Through Turbine Rim Seals Part II: Externally Induced and Combined Ingress'. In: *Journal of Turbomachinery* 133.3 (2010), pp. 031006–031006. DOI: 10.1115/1.4001178.

[43] Phadke U. P. and Owen J. M. 'Aerodynamic aspects of the sealing of gas-turbine rotor-stator systems. Part 2: The performance of simple seals in a quasi-axisymmetric external flow'. In: *International Journal of Heat and Fluid Flow* 9.2 (1988), pp. 106–112. DOI: 10.1016/0142-727X(88)90061-6.

[44] Johnson B. V., Mack G. J. and Paolillo R. E. 'Turbine rim seal gas path flow ingestion mechanisms'. In: *30th AIAA/ASME/SAE/ASEE Joint Propulsion Conference and Exhibit, 27-29 June 1994, Indianapolis, Indiana*. AIAA, 1994. DOI: 10.2514/6.1994-2703.

[45] Barigozzi G., Franchini G., Perdichizzi A., Maritano M. and Abram R. 'Purge flow and interface gap geometry influence on the aero-thermal performance of a rotor blade cascade'. In: *International Journal of Heat and Fluid Flow* 44 (2013), pp. 563–575. DOI: 10.1016/j.ijheatfluidflow.2013.08.012.

[46] Schrewe S., Werschnik H. and Schiffer H. P. 'Experimental analysis of the interaction between rim seal and main annulus flow in a low pressure two stage axial turbine'. In: *Journal of Turbomachinery* 135.3 (2013). DOI: 10.1115/1.4023015.

[47] Schuepbach P., Abhari R. S., Rose M. G., Germain T., Raab I. and Gier J. 'Effects of suction and injection purge-flow on the secondary flow structures

of a high-work turbine'. In: *Journal of Turbomachinery* 132.2 (2010). DOI: 10.1115/1.4000485.

[48] Schuepbach P., Abhari R. S., Rose M. G. and Gier J. 'Influence of rim seal purge flow on the performance of an endwall-profiled axial turbine'. In: *Journal of Turbomachinery* 133.2 (2011). DOI: 10.1115/1.4000578.

[49] Morgan C. E., Babinsky H. and Harvey J. K. 'Vortex detection methods for use with PIV and CFD Data'. In: *47th AIAA Aerospace Sciences Meeting including the New Horizons Forum and Aerospace Exposition, 5-8 January 2009, Orlando, Florida*. AIAA, 2009. DOI: 10.2514/6.2009-74.

[50] Hunt J. C. R., Wray A. A. and Moin P. 'Eddies, Streams and Convergence zones in Turbulent Flows'. In: *Centre for Turbulence Research Proceedings of the Summer Program*. 1988.

[51] Zlatinov M. B., Tan C. S., Montgomery M., Islam T. and Seco-Soley M. 'Turbine hub and shroud sealing flow loss mechanisms'. In: *Proceedings of the ASME Turbo Expo 2011, 6-10 June 2011, Vancouver, Canada*. Vol. 7. ASME, pp. 947–959. DOI: 10.1115/GT2011-46718.

[52] Manwaring S. R. and Wisler D. C. 'Unsteady Aerodynamics and Gust Response in Compressors and Turbines'. In: *Journal of Turbomachinery* 115.4 (Oct. 1993), pp. 724–740. ISSN: 0889-504X. DOI: 10.1115/1.2929308.

[53] Ingram G. L. 'Endwall Profiling for the Reduction of Secondary Flow in Turbines'. PhD Thesis. 2003.

[54] Snedden G. C. 'The Application of Non-Axisymmetric Endwall Contouring in a 1 Stage, Rotating Turbine'. PhD Thesis. 2011.

[55] Hartland J. C., Gregory-Smith D. G. and Rose M. G. 'Non-axisymmetric endwall profiling in a turbine rotor blade'. In: *International Gas Turbine and Aeroengine Congress and Exhibition, 2-5 June 1998, Stockholm, Sweden*. ASME, 1998. DOI: 10.1115/98-GT-525.

[56] Hawes C., Williams R. and Ingram G. 'Investigating endwall-blade fillet radius variation to reduce secondary flow losses'. In: *11th European Conference on Turbomachinery Fluid Dynamics and Thermodynamics, ETC11, 23-27 March 2015, Madrid, Spain*. Euroturbo, 2015.

[57] Germain T., Nagel M., Raab I., Schuepbach P., Abhari R. S. and Rose M. 'Improving Efficiency of a High Work Turbine Using Nonaxisymmetric Endwalls Part I: Endwall Design and Performance'. In: *Journal of Turbomachinery* 132.2 (2010), pp. 021007–021007. DOI: 10.1115/1.3106706.

[58] Harvey N. W., Rose M. G., Taylor M. D., Shahpar S., Hartland J. and Gregory-Smith D. G. 'Nonaxisymmetric turbine end wall design: Part I - Three-dimensional linear design system'. In: *Journal of Turbomachinery* 122.2 (2000), pp. 278–285. DOI: 10.1115/1.555445.

[59] Hartland J. C., Gregory-Smith D. G., Harvey N. W. and Rose M. G. 'Nonaxisymmetric Turbine End Wall Design: Part II - Experimental Validation'. In: *Journal of Turbomachinery* 122.2 (2000), pp. 286–293. ISSN: 0889-504X. DOI: 10.1115/1.555446.

[60] Gregory-Smith D. G., Ingram G., Jayaraman P., Harvey N. W. and Rose M. G. 'Non-axisymmetric turbine end wall profiling'. In: *Proceedings of the Institute of Mechanical Engineers Part A : Journal of Power and Energy.* 215.6 (2001), pp. 721–734. DOI: 10.1243/0957650011539027.

[61] Brennan G., Harvey N. W., Rose M. G., Fomison N. and M. D. Taylor. 'Improving the Efficiency of the Trent 500-HP Turbine Using Nonaxisymmetric End Walls—Part I: Turbine Design'. In: *Journal of Turbomachinery* 125.3 (2003), pp. 497–504.

[62] Rose M. G., Harvey N. W., Seaman P., Newman D. A. and McManus D. 'Improving the Efficiency of the Trent 500 HP Turbine using Non-Axisymmetric End Walls Part II: Experimental Validation'. In: *Proceedings of ASME Turbo Expo 2001, 4-7 June 2001, New Orleans, Louisiana*. ASME, 2001. DOI: 10.1115/2001-GT-0505.

[63] Ingram G., Gregory-Smith D., Rose M., Harvey N. and Brennan G. 'The Effect of End-Wall Profiling on Secondary Flow and Loss Development in a Turbine Cascade'. In: *Proceedings of the ASME Turbo Expo 2002, 3-6 June 2002, Amsterdam, The Netherlands*. Vol. 5. ASME, 2002, pp. 135–145. DOI: 10.1115/GT2002-30339.

[64] Gregory-Smith D., Bagshaw D., Ingram G. and Stokes M. 'Using Profiled Endwalls, Blade Lean and Leading Edge Extensions to Minimize Secondary

Flow'. In: *Proceedings of the ASME Turbo Expo 2008: Power for Land, Sea and Air, 9-13 June 2008, Berlin, Germany*. Vol. 6. ASME, 2008, pp. 1301–1311. DOI: 10.1115/GT2008-50811.

[65] Poehler T., Gier J. and Jeschke P. 'Numerical and experimental analysis of the effects of non-axisymmetric contoured stator endwalls in an axial turbine'. In: *Proceedings of the ASME Turbo Expo 2010: Power for Land, Sea and Air, 14-18 June 2010, Glasgow, UK*. Vol. 7. ASME, 2010, pp. 1549–1559. DOI: 10.1115/GT2010-23350.

[66] Niewoehner J., Poehler T., Jeschke P. and Guendogdu Y. 'Investigation of nonaxisymmetric endwall contouring and three-dimensional airfoil design in a 1.5 stage axial turbine-part II: Experimental validation'. In: *Journal of Turbomachinery* 137.8 (2015). DOI: 10.1115/1.4029477.

[67] Panchal K., Abraham S., Ekkad S. V., Ng W., Brown B. J. and Malandra A. 'INVESTIGATION OF EFFECT OF END WALL CONTOURING METHODS ON A TRANSONIC TURBINE BLADE PASSAGE'. In: *Proceedings of the ASME Turbo Expo 2012: Turbine Technical Conference and Exposition, 11-15 June 2012, Copenhagen, Denmark*. Vol. 7. ASME, 2012, pp. 523–534. DOI: 10.1115/GT2011-45192.

[68] Regina K., Kalfas A. I., Abhari R. S., Lohaus A., Voelker S. and Auf Dem Kampe T. 'Aerodynamic robustness of end wall contouring against rim seal purge flow'. In: *ASME Turbo Expo 2014: Turbine Technical Conference and Exposition, 16-20 June 2014, Dusseldorf, Germany*. Vol. 2C. ASME, 2014. DOI: 10.1115/GT2014-26007.

[69] Jain S., Roy A., Ng W., Ekkad S., Lohaus A. S. and Taremi F. 'Aerodynamic performance of a transonic turbine blade passage in presence of upstream slot and mateface gap with endwall contouring'. In: *ASME Turbo Expo 2014: Turbine Technical Conference and Exposition, 16-20 June 2014, Dusseldorf, Germany*. Vol. 2C. ASME, 2014. DOI: 10.1115/GT2014-26475.

[70] White F. M. *Fluid Mechanics*. 7th ed. Boston: McGraw-Hill, 2010.

[71] Wu C.-H. *A General Through-Flow Theory of Fluid Flow wirh Subsonic or Supersonic Velocity in Turbomachines of Arbitrary Hub and Casing Shapes*. Report. NACA, 1951.

[72] Montomoli F., Hodson H. P. and Lapworth L. 'RANS-URANS in axial compressor, a design methodology'. In: *Proceedings of the Institution of Mechanical Engineers, Part A: Journal of Power and Energy* 225.3 (2011), pp. 363–374. DOI: 10.1177/2041296710394267.

[73] Versteeg H. and Malalasekra W. *An Introduction to Computational Fluid Dynamics: The Finite Volume Method*. 2nd ed. New Delhi: Pearson, 2008.

[74] Kundu P. K., Cohen I. M. and Dowling D. R. *Fluid Mechanics*. 5th ed. Waltham, MA: Elsevier, 2012.

[75] Anderson J. D. *Computational Fluid Dynamics: The Basics with Applications*. New Delhi: McGraw-Hill, 2012.

[76] Wilcox D. C. *Turbulence Modelling for CFD*. 2nd ed. La Canada: DCW Industries, 2000.

[77] Pope S. B. *Turbulent Flows*. Cambridge: Cambridge University Press, 2000.

[78] Spalart P. R. and Allmaras S. R. 'A One-Equation Turbulence Model for Aerodynamic Flows'. In: *AIAA 30th Aeropace Sciences Meeting and Exhibit, 6-9 January 1992, Nevada*. AIAA, 1992. DOI: 10.2514/6.1992-439.

[79] Menter F. R. 'Two-equation eddy-viscosity turbulence models for engineering applications'. In: *AIAA Journal* 32.8 (1994), pp. 1598–1605. DOI: 10.2514/3.12149.

[80] Denton J. D. 'Some limitations of turbomachinery CFD'. In: *Proceedings of the ASME Turbo Expo 2010: Power for Land, Sea and Air, 14-18 June 2010, Glasgow, UK*. Vol. 7. ASME, 2010, pp. 735–745. DOI: 10.1115/GT2010-22540.

[81] Jia W. and Liu H. 'Numerical investigation of the effect of rim seal on turbine aerodynamic design parameters and end wall flows in low-aspect ratio turbine'. In: *Computers and Fluids* 74 (2013), pp. 114–125. DOI: 10.1016/j.compfluid.2012.12.020.

[82] Holmes D. G., Moore B.J. and Connell S. D. 'Unsteady vs. Steady Turbomachinery Flow Analysis: Exploiting Large-Scale Computations to Deepen Our Understanding of Turbomachinery Flows'. In: *SciDAC Conference, July 2011, Denver, Colorado*. 2011.

[83] O'Mahoney T., Hills N. and Chew J. 'Sensitivity of LES results from turbine rim seals to changes in grid resolution and sector size'. In: *Progress in Aerospace Sciences* 52 (2012), pp. 48–55. DOI: 10.1016/j.paerosci.2011.09.003.

[84] Sandberg R. D., Michelassi V., Pichler R., Chen LW. and Johnstone R. 'Compressible Direct Numerical Simulation of Low-Pressure Turbines Part I: Methodology'. In: *Journal of Turbomachinery* 137.5 (2015). DOI: 10.1115/1.4028731.

[85] Bayley F. J. and Owen J. M. 'The Fluid Dynamics of a Shrouded Disk System With a Radial Outflow of Coolant'. In: *Journal of Engineering for Power* 92.3 (July 1970), pp. 335–341. DOI: 10.1115/1.3445358.

[86] Barringer M., Coward A., Clark K., Thole K. A., Schmitz J., Wagner J., Alvin M. A., Burke P. and Dennis R. 'The Design of a Steady Aero Thermal Research Turbine (START) for Studying Secondary Flow Leakages and Airfoil Heat Transfer'. In: *ASME Turbo Expo 2014: Turbine Technical Conference and Exposition, 16-20 June 2014, Dusseldorf, Germany*. June 2014. DOI: 10.1115/GT2014-25570.

[87] Carvalho Figueiredo A. J., Jones R. R., Pountey O. J., Scobie J. A., Lock G. D., Sangan C. M. and Cleaver D. J. 'Volumetric velocimetry measurements of film cooling jets'. In: *Journal of Engineering Gas Turbines and Power* 141.3 (2018).

[88] Dean W. R. 'XVI. Note on the motion of fluid in a curved pipe'. In: *The London, Edinburgh, and Dublin Philosophical Magazine and Journal of Science* 4.20 (1927), pp. 208–223. DOI: 10.1080/14786440708564324.

[89] Dean W. R. 'Fluid Motion in a Curved Channel'. In: *Proceedings of the Royal Society of London A: Mathematical, Physical and Engineering Sciences* 121.787 (1928), pp. 402–420. DOI: 10.1098/rspa.1928.0205.

[90] Du P. and Agarwal R. K. 'Drag Prediction of NASA Common Research Models Using Different Turbulence Models'. In: *35th AIAA Applied Aerodynamics Conference*. 2017. DOI: 10.2514/6.2017-4233.

[91] Zore K., Shah S., Stokes J., Sasanapuri B. and Sharkey P. 'ANSYS CFD Study for High Lift Aircraft Configurations'. In: *2018 Applied Aerodynamics Conference*. 2018. DOI: 10.2514/6.2018-2844.

[92] Georgiou D. P., Milidonis K. F. and Geniketzidis A. I. 'Comparisons between experimental measurements and RANS-based simulations on the aerodynamics of a horseshoe vortex configuration'. In: *11th European Conference on Turbomachinery Fluid Dynamics and Thermodynamics, ETC11, 23-27 March 2015, Madrid, Spain*. Euroturbo, 2015.

[93] Anderson M. G. 'Fluent CFD Versus Sovran and Klomp Diffuser Data Benchmark Study'. In: *46th AIAA Aerospace Sciences Meeting and Exhibit*. 2008. DOI: 10.2514/6.2008-665.

[94] Selvanayagam J, Aliaga C. and Stokes J. 'CFD Simulation of S-Duct Test Case Using ANSYS FLUENT'. In: *AIAA Propulsion and Energy 2019 Forum*. 2019. DOI: 10.2514/6.2019-3847.

[95] ANSYS Inc. 'ANSYS Academic Research Fluent'. In: *Release 15.0* Help System ().

[96] Stern F., Wilson R. V., Coleman H. W. and Paterson E. G. 'Comprehensive Approach to Verification and Validation of CFD Simulations – Part 1: Methodology and Procedures'. In: *Journal of Fluids Engineering* 123 (2001), pp. 793 –802.

[97] Roache P. J. 'Perspective: A Method for Uniform Reporting of Grid Refinement Studies'. In: *Journal of Fluids Engineering* 116 (1994), pp. 405–413.

[98] Celik I. B., Chia U., Roache P. J. and Freitas C. J. 'Procedure for Estimation and Reporting of Uncertainty Due to Discretization in CFD Applications'. In: *Journal of Fluids Engineering* 130.7 (2008).

[99] Sangan C. M. 'Measurement of Ingress through Gas Turbine Rim Seals'. PhD Thesis. 2011.

[100] Sovran G. and Klomp E. D. 'Experimentally Determined Optimum Geometries for Rectilinear Diffusers with Rectangular, Conical or Annular Cross-Section'. In: *The Symposium on the Fluid Mechanics of Internal Flow*. Ed. by G. Sovran. Elsevier, 1967.

[101] Coull J. D., Atkins N. R. and Hodson H. P. 'Winglets for Improved Aerothermal Performance of High Pressure Turbines'. In: *Journal of Turbomachinery* 136.9 (2014), pp. 091007–091007. DOI: 10.1115/1.4026909.

[102] Da Soghe R., Innocenti L., Andreini A. and Poncet S. 'Numerical Benchmark of Turbulence Modeling in Gas Turbine Rotor-Stator System'. In: *Proceedings of the ASME Turbo Expo 2010: Power for Land, Sea and Air, 14-18 June 2010, Glasgow, UK*. 2010. DOI: 10.1115/GT2010-22627.

[103] Blazek J. *Computational Fluid Dynamics: Principles and Applications*. 2nd ed. Amsterdam: Elsevier, 2005.

[104] Berggren M., Ekstrom S-V. and Nordstrom J. 'A Discontinuous Galerkin Extension of the Vertex-Centered Edge-Based Finite Volume Method'. In: *Communications in Computational Physics* 5.2-4 (2008), pp. 456–468.

[105] Morton K. W. and Sonar T. 'Finite Volume Methods for Hyperbolic Conservation Laws'. In: *Acta Numerica* 16 (2007).

[106] ANSYS Inc. 'ANSYS Academic Research CFX'. In: *Release 17.0* Help System ().

[107] Spalart P. R. and Shur M. 'On the sensitization of turbulence models to rotation and curvature'. In: *Aerospace Science and Technology* 1.5 (1997), pp. 297–302.

[108] Smirnov P. E. and Menter F. R. 'Sensitization of the SST Turbulence Model to Rotation and Curvature by Applying the Spalart–Shur Correction Term'. In: *Journal of Turbomachinery* 131 (2009).

[109] Coull J. D. 'Endwall Loss in Turbine Cascades'. In: *Journal of Turbomachinery* 139.8 (2017). DOI: 10.1115/1.4035663.

[110] Dunn D., Snedden G. and Von Backström T. 'Unsteady Effects of a Generic Non-Axisymmetric Rotor Endwall Contour on a 1 1/2 Stage Turbine Test Rig at Off Design Conditions'. In: *ASME Turbo Expo 2014: Turbine Technical Conference and Exposition, GT 2014, June 16, 2014 - June 20, 2014*. Vol. 2D. Proceedings of the ASME Turbo Expo. American Society of Mechanical Engineers (ASME), International Gas Turbine Institute. DOI: 10.1115/GT2014-25524.

[111] Jakoby R., Zierer T., Lindblad K., Larsson J., deVito L., Bohn D.E., Funke J. and Decker A. 'Numerical Simulation of the Unsteady Flow Field in an Axial Gas Turbine Rim Seal Configuration'. In: *ASME Turbo Expo 2004: Power for Land, Sea, and Air, 14-17 June 2004, Vienna, Austria*. ASME, 2004. DOI: 10.1115/GT2004-53829.

[112] Slater J. W. *Examining Spatial (Grid) Convergence*. 2008. URL: https://www.grc.nasa.gov/WWW/wind/valid/tutorial/spatconv.html (visited on 14/03/2019).

[113] Slater J. W. 'Verification Assessment of Flow Boundary Conditions for CFD Analysis of Supersonic Inlet Flows'. In: *AIAA/ASME/SAE/ASEE Joint Propulsion Conference and Exhibit, 8-11 July 2001, Utah*. AIAA, 2001.

[114] LeVeque R. J. *Numerical Methods for Conservation Laws*. 2nd ed. Basel: Birkhauser Verlag, 1992.

[115] Wood L. E., Jones R. R., Poutney O. J., Scobie J. A., Rees D. A. S. and Sangan C. M. 'A General Design Framework For The Generation Of Contoured Endwalls'. In: *Proceedings of ASME Turbo Expo 2019: Turbomachinery Technical Conference and Exposition, 17-21 June 2019, Phoenix, Arizona*. ASME, 2019.